

DOCTORAL THESIS

Time-Domain and Spectroscopic studies of Active Galactic Nuclei

Author: Saikruba Krishnan

Supervisor: Dr. hab. Alex G. Markowitz

*A thesis submitted in fulfillment of the requirements
for the degree of Doctor of Philosophy
in
Astronomy*



Nicolaus Copernicus Astronomical Center
of the Polish Academy of Sciences

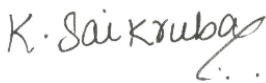
February 5, 2023

Declaration of Authorship

I, Saikruba Krishnan, declare that this thesis titled, "Time-Domain and Spectroscopic studies of Active Galactic Nuclei", submitted in fulfillment of the requirements for the Degree of Doctor of Philosophy represents my own work. I confirm that:

- This work was done as part of the research degree at the Nicolaus Copernicus Astronomical Center of the Polish Academy of Sciences.
- I declare that this work has not been included in any other thesis, dissertation, or report previously submitted to this institute or to any other institution for a degree, diploma, or other qualification.
- Where I have consulted the published work of others, this is always clearly attributed.
- I have acknowledged all main sources of help.

Signed:



Date: February 5, 2023

Abstract

The discovery of supermassive black holes in the centres of galaxies is one of astronomy's most important discoveries. In particular, those systems in which matter is accreting onto the black hole or outflowing – Active Galactic Nuclei (AGN) – serve as laboratories for extreme physical conditions for a black hole — host galaxy co-evolutionary processes. AGN continuum emission can vary significantly across timescales ranging from ks to years; the study of this continuum variability can elucidate characteristic timescales that provide insight into accretion flow or jet physics. The similarities in broadband spectral and timing properties between Seyfert AGN & black hole X-ray binaries (BHXBs) suggest that both classes of systems have similar accretion processes, scaled by mass, luminosity, and timescale. However, AGN duty cycles are considerably longer in comparison to BHXBs and the accretion process likely occurs in an episodic nature. We observe some Seyferts undergoing extreme variations in X-ray/optical flux and optical spectral type, driven by strong accretion changes. These objects are likely undergoing a change between different accretion states. Multi-wavelength observations of these transients provide a way to study their evolving accretion flow structure and understand their transient behaviour. There are still unanswered questions about accretion in both persistent and rapidly-evolving AGN, such as how AGNs exhibits structural changes in accretion flow as a function of system parameters, how quickly the X-ray corona, disc, and broad line region (BLR) can evolve in response to changes in the global accretion supply, what is the typical AGN duty cycle, and do supermassive and stellar-mass black holes exhibit identical accretion flows and variability mechanisms. I have conducted studies to try to address these issues in the thesis.

In my thesis, the first project is to study the detection of periodic/quasi-periodic signals (QPOs) in red noise-dominated AGN light curves using selected statistical tools (Auto-Correlation Function and Phase Dispersion Minimization). The efforts to locate periodic signals (either strictly- or quasi-periodic) in both Seyfert AGN and blazars have involved studies using light curves spanning the EM spectrum. However, statistically robust detections of strictly- or quasi-periodic oscillations (SPOs or QPOs) remain a challenge due to limited data quality. Specifically, it is challenging to separate “narrow-band” SPO/QPO signals from the red noise “continuum.” The periodogram can be used to identify QPO signals. However, alternate statistical methods are generally employed for the detection of periodic/QPO signals in AGN with sparsely sampled data points, such as the Auto-Correlation Function (ACF), Phase Dispersion Minimization (PDM), wavelet analysis, sinusoidal fitting, etc. Generally, QPOs claimed in AGN using these alternate methods are non-repeatable in additional observations, and are based on improper usage of statistical tools or improper calibration of the “false alarm probability.” Given the community's access to large databases of monitoring light curves via large-area monitoring programmes, our goal is to provide guidance to those searching for QPOs via data trawls and enhance statistically significant & robust QPO detections. We perform Monte Carlo simulations to empirically test QPO detection feasibility in the presence of red noise. We simulate evenly-sampled pure red noise light curves to estimate false alarm probabilities; false positives in both tools tend to occur towards timescales longer than (very roughly) one-third of the light curve duration. We simulate QPOs

mixed with pure red noise and determine the true-positive detection sensitivity; in both tools, it depends strongly on the relative strength of the QPO against the red noise and on the steepness of the red noise PSD slope. We find that extremely large values of peak QPO power relative to red noise (typically $\sim 10^{4-5}$) are needed for a 99.7 per cent true-positive detection rate. Given that true-positive detections using the ACF or PDM are generally rare to obtain, we conclude that period searches based on the ACF or PDM must be treated with extreme caution when the data quality is not good. We consider the feasibility of QPO detection in the context of highly-inclined, periodically self-lensing supermassive black hole binaries.

My second work in the thesis focuses on AGNs undergoing extreme variations in X-ray/optical flux and optical spectral type, driven by strong accretion changes. We explore the multi-wavelength nature of a continuum flare in a Seyfert galaxy; the eROSITA all-sky X-ray survey showed that its X-ray flux increased by ~ 6 over six months; concurrent optical photometric monitoring with ATLAS showed a simultaneous increase by a factor of 4. We complemented the eROSITA and ATLAS data by triggering a multi-wavelength follow-up monitoring program (XMM-Newton, NICER; optical spectroscopy) to study the evolution of the accretion disk, broad-line region, and X-ray corona. During the campaign, X-ray and optical continuum flux subsided over \sim six months. Our campaign includes two XMM-Newton observations, one taken near the peak of this flare and the other one when the flare had subsided. The soft X-ray excess from both XMM-Newton observations was power law-like (distinctly non-thermal); using a simple power-law, the photon index varies from a steep value of $\Gamma \sim 2.7$ at the flare peak to a relatively flatter value of $\Gamma \sim 2.2$ later. We successfully model the broadband optical/UV/X-ray SED at both flare peak and post-flare times with models incorporating thermal disk emission in the optical/UV and warm thermal Comptonization in the soft X-rays. In the context of the AGNSED model, the accretion rate falls by ~ 2.8 , and the radii of the hot and warm Comptonizing regions increase from the flaring state to the post-flare state. Additionally, from the optical spectral observations we found the broad He II $\lambda 4686$ emission line fades significantly as the optical/UV/X-ray continuum fades, and the broad He II line flux tracked the evolution in the >54 eV continuum, and is consistent with an origin in the inner BLR. A likely explanation for the flare is that a sudden strong increase in local accretion rate in this source manifested itself via an increase in accretion disk emission and in thermal Comptonization emission in the soft X-rays, followed by a decrease in accretion and Comptonized luminosity.

Abstract (in Polish)

Odkrycie supermasywnych czarnych dziur w centrach galaktyk jest jednym z najważniejszych odkryć w astronomii. W szczególności te układy, w których materia gromadzi się na czarnej dziurze lub odpływa – Aktywne Jądra Galaktyk (AGN) – służą jako laboratoria ekstremalnych warunków fizycznych dla procesów ewolucyjnych galaktyk macierzystych wokół czarnej dziury. Emisja kontinuum AGNów może się znacznie różnić w skalach czasowych od kilosekund do lat; badanie tej zmienności kontinuum może wyjaśnić charakterystyczne skale czasowe, które zapewniają wgląd w przepływ akrecji lub fizykę dżetów. Podobieństwa w szerokopasmowych właściwościach widmowych i czasowych między galaktykami Seyferta, a rentgenowskimi układami podwójnymi czarnych dziur (BHXRBS) sugerują, że obie klasy systemów mają podobne procesy akrecji, skalowane pod względem masy, jasności i skali czasowej. Jednak cykle pracy AGN są znacznie dłuższe w porównaniu z BHXRBS, a proces akrecji prawdopodobnie ma charakter epizodyczny. Obserwujemy niektóre galaktyki Seyferta, które przechodzą ekstremalne zmiany strumienia rentgenowskiego/optycznego i typu widma optycznego, napędzane silnymi zmianami akrecyjnymi. Obiekty te prawdopodobnie przechodzą zmianę między różnymi stanami akrecji. Obserwacje tych transjentów na różnych długościach fal umożliwiają badanie ich ewoluującej struktury przepływu akrecyjnego i zrozumienie ich przejściowego zachowania. Wciąż bez odpowiedzi pozostają pytania dotyczące akrecji zarówno w trwałym, jak i szybko ewoluującym AGNach, takie jak sposób, w jaki AGN wykazuje zmiany strukturalne w przepływie akrecji w funkcji parametrów systemu, jak szybka korona rentgenowska, dysk i obszar szerokich linii (BLR) może ewoluować w odpowiedzi na zmiany w globalnym przepływie akrecji, jaki jest typowy dla zakresu zmienności czasowej AGN, i czy supermasywne i masywne czarne dziury wykazują identyczne przepływy akrecji i mechanizmy zmienności. Przeprowadziłam badania, aby odnieść się do tych zagadnień w mojej pracy doktorskiej.

Pierwszym projektem w mojej pracy doktorskiej dotyczy badań detekcji sygnałów okresowych/quasi-okresowych (QPO) w krzywych blasku AGN zdominowanych przez czerwony szum przy użyciu wybranych narzędzi statystycznych (funkcja autokorelacji i minimalizacja dyspersji faz). Starania mające na celu zlokalizowanie sygnałów okresowych (ściśle lub quasi-okresowych) zarówno w galaktykach Seyferta, jak i blazarach obejmowały badania z wykorzystaniem krzywych blasku obejmujących widmo elektromagnetyczne. Jednak statystycznie solidne wykrywanie oscylacji ściśle lub quasi-okresowych (SPO lub QPO) pozostaje wyzwaniem ze względu na ograniczoną jakość danych. W szczególności trudne jest oddzielenie „wąskopasmowych” sygnałów SPO/QPO od „kontinuum” czerwonego szumu. Periodogram może być wykorzystany do identyfikacji sygnałów QPO. Jednak alternatywne metody statystyczne są generalnie stosowane do wykrywania sygnałów okresowych/QPO w AGNach w danych z rzadko rozmieszczonymi punktami, są to metody takie jak funkcja autokorelacji (ACF), minimalizacja dyspersji faz (PDM), analiza falkowa, dopasowanie sinusoidalne itp. Ogólnie rzecz biorąc, QPO stwierdzone w AGN przy użyciu tych alternatywnych metod nie są powtarzalne w dodatkowych obserwacjach i opierają się na niewłaściwym użyciu narzędzi statystycznych lub niewłaściwej kalibracji „prawdopodobieństwo fałszywego alarmu”. Biorąc pod uwagę dostęp społeczności do dużych baz danych monitorowania krzywych blasku za pomocą programów do monitorowania dużych obszarów, naszym celem

jest zapewnienie wskazówek osobom poszukującym QPO w dużej ilości danych i ulepszenie statystycznie znaczących & solidnych detekcji QPO. Przeprowadzamy symulacje Monte Carlo, aby empirycznie przetestować wykonalność wykrywania QPO w obecności czerwonego szumu. Symulujemy równomiernie próbkowane krzywe zmian blasku czystego czerwonego szumu, aby oszacować prawdopodobieństwo fałszywych alarmów; fałszywe alarmy w obu narzędziach mają tendencję do występowania w skalach czasowych dłuższych niż (z grubsza) jedna trzecia czasu trwania krzywej blasku. Symulujemy QPO zmieszane z czystym czerwonym szumem i określamy prawdziwą dodatnią czułość wykrywania; w obu narzędziach zależy to silnie od względnej siły QPO w stosunku do szumu czerwonego i od stromości nachylenia funkcji PSD szumu czerwonego. Odkryliśmy, że bardzo duże wartości szczytowej mocy QPO w stosunku do czerwonego szumu (zwykle $\sim 10^{4-5}$) są potrzebne do 99.7% wskaźnika prawdziwych dodatnich detekcji. Biorąc pod uwagę, że prawdziwe pozytywne wykrycia przy użyciu ACF lub PDM są na ogół rzadkie, dochodzimy do wniosku, że wyszukiwanie okresów oparte na ACF lub PDM należy traktować z najwyższą ostrożnością, gdy jakość danych nie jest dobra. Rozważamy wykonalność wykrywania QPO w kontekście bardzo nachylonych, okresowo samosoczewkujących układów podwójnych supermasywnych czarnych dziur.

Moja drugi projekt w tej pracy doktorskiej koncentruje się na AGNach przechodzących ekstremalne zmiany strumienia rentgenowskiego/optycznego i typu widma optycznego, napędzane przez silne zmiany akrecyjne. Badamy naturę rozbłysku kontinuum w galaktyce Seyferta dla różnych długości fali; przegląd rentgenowski całego nieba eROSITA wykazał, że jego strumień rentgenowski wzrósł o ~ 6 w ciągu sześciu miesięcy; jednoczesne optyczne monitorowanie fotometryczne z ATLAS wykazało jednoczesny wzrost o współczynnik 4. Uzupełniliśmy dane eROSITA i ATLAS, uruchamiając program monitorowania wielu długości fal (XMM-Newton, NICER; spektroskopia optyczna) w celu zbadania ewolucji dysku akrecyjnego, obszaru szerokich linii i korony rentgenowska. Podczas kampanii strumień promieniowania rentgenowskiego i optycznego w kontinuum opadł w ciągu \sim sześciu miesięcy. Nasza kampania obejmuje dwie obserwacje XMM-Newton, jedną wykonaną w pobliżu szczytu tego rozbłysku, a drugą, gdy rozbłysk zmniejszył jasność. Nadmiar miękkiego promieniowania rentgenowskiego z obu obserwacji XMM-Newton był podobny do prawa potęgowego (wyraźnie nietermiczny); korzystając z prostego prawa potęgowego, indeks fotonów zmienia się od stromej wartości $\Gamma \sim 2.7$ w szczycie rozbłysku do względnie płaskiej wartości $\Gamma \sim 2.2$ później. Z powodzeniem wymodelowaliśmy szerokopasmowy optyczny/UV/rentgenowski SED zarówno w czasie szczytu rozbłysku, jak i po rozbłysku, z modelami obejmującymi emisję dysku termicznego w zakresie optycznym/UV i komptonizację termiczną w miękkim promieniowaniu rentgenowskim. W kontekście modelu AGNSED tempo akrecji spada o ~ 2.8 , a promienie gorących i ciepłych regionów komptonizujących rosną od stanu rozbłysku do stanu po rozbłysku. Dodatkowo, z optycznych obserwacji spektralnych odkryliśmy, że szeroka linia emisyjna He II $\lambda 4686$ znacznie zanika wraz z zanikaniem kontinuum optycznego/UV/rentgenowskiego, a szeroki strumień linii He II podążał za ewolucją w kontinuum > 54 eV i jest zgodny z promieniem wewnętrznym BLR. Prawdopodobnym wyjaśnieniem rozbłysku jest to, że nagły, silny wzrost lokalnego tempa akrecji w tym źródle objawił się wzrostem emisji dysku akrecyjnego i termicznej emisji komptonowskiej w miękkim promieniowaniu rentgenowskim, po czym nastąpił spadek akrecji i komptonizowanej jasności.

Acknowledgements

First and foremost, I would like to thank my Ph.D. advisor Dr. Alex Markowitz for giving me this amazing opportunity to do my Ph.D. at CAMK. I consider myself fortunate to have had a mentor who, despite his busy schedule, was always available for guidance and help. I really admire his hard work, and I am grateful for the opportunity to have worked with him. I want to thank my co-supervisor Prof. Alex Czerny for playing a big part in my first project. He was always there for advice/suggestions and has always been a cheerful company. I would like to thank my collaborators, Dr. Mirko Krumpel and Dr. J. Wilms, for having the German eROSITA collaboration work to be a part of my Ph.D. thesis. I would like to particularly thank Dr. David Homan for his time and help in working on the optical spectral analysis related to our project. I am personally grateful and thankful to my fellow group mate and friend Tathagata Saha who had always encouraged me to work consistently and was always available for any science discussions/work-related help. I would like to thank my best friend Prasad for his constant support right through my Masters. He plays a very big role in my career. I am thankful for all the dear friends I have met during my stay in Poland who made it a very beautiful and memorable chapter of my life. I will never find sufficient words to fully express my gratitude to my parents, particularly my brother Hariharan, who has given me their unrelenting support throughout my life.

Contents

Declaration of Authorship	iii
Abstract	v
Acknowledgements	xi
List of Figures	xviii
List of Tables	xix
1 Introduction	1
1.1 Historical background	1
1.2 AGN structure	3
1.3 AGN Unification model	6
1.4 Components of AGN continuum spectra	8
1.5 X-ray spectral properties of AGN	11
1.5.1 Primary Emission	11
1.5.2 Reprocessed Emission	12
1.5.3 Absorption features	13
1.5.4 The soft excess	13
1.6 Studies on variability in AGN	14
1.6.1 Characteristic timescales	14
1.6.2 Stochastic variability due to persistent accretion	15
1.6.3 Periodic/Quasi-Periodic Oscillations in AGN	16
1.6.4 Extreme variability in AGN	18
1.7 Thesis Overview	21
2 Detection of periodic signals using statistical tools	23
2.1 Methodology: Light-curve simulation and input PSD models	23
2.2 ACF for QPO detection	26
2.2.1 The behaviour of the ACF for pure Lorentzian processes	27
2.2.2 The behaviour of the ACF for pure red noise power-law processes	28
Unbroken power law model	28
Broken power-law model	31
False Alarm Probabilities	32
2.2.3 ACFs for QPOs mixed with red noise	33

	False negatives and detection inaccuracy errors	34
2.3	PDM for QPO detection	36
2.3.1	PDM test for Lorentzian profile:	38
2.3.2	The behavior of the PDM for pure red noise processes	39
	Unbroken and broken power-law models	39
	False Alarm Probabilities	40
2.3.3	The behaviour of PDM for QPOs mixed with red noise	41
	False negatives and detection inaccuracy errors	42
2.4	Realistic uneven Sampling test using PDM	44
2.4.1	PDM test for Lorentzian profile with uneven sampling	44
2.4.2	The behaviour of the PDM for pure red noise processes with uneven sampling	45
2.4.3	The behaviour of PDMs for QPOs mixed with red noise	47
2.5	Discussion	48
2.5.1	Some of the claims in the literature and basic pitfalls regarding ACF and PDM usage	51
	General issues with ACF, with a few select examples:	52
	General issues with PDM, with a few select examples:	52
2.5.2	Application to the detection of periods for selected physical situations	53
	Highly-inclined self-lensing SMBH binaries	54
3	An X-ray flaring event and a variable soft X-ray excess detected with eROSITA	57
3.1	X-ray Instrumentation	58
3.1.1	eROSITA	58
3.1.2	XMM-Newton	59
3.1.3	NICER	60
3.2	Source detection, follow-up observations, and data reduction	60
3.2.1	eROSITA data reduction and results	60
3.2.2	XMM-Newton data reduction	61
3.2.3	NICER data reduction	62
3.2.4	Optical & IR photometry	63
3.2.5	Optical spectroscopic observations	63
	Continuum variability overview	63
3.3	X-ray data analysis	64
3.3.1	XMM-Newton observations	64
3.3.2	NICER observations	68
3.3.3	eROSITA observations	69
3.4	Modeling the optical to X-ray SED	69
3.4.1	Warm Comptonization with AGNSED	70
3.4.2	Double Comptonization with THCOMP*ZBBODY	73
3.5	Optical spectroscopic analysis	74
3.6	Discussions	76
3.6.1	Summary of main observations:	76

3.6.2	Origin of the soft-excess	77
3.6.3	Determining the possible origin of the flare: Characteristic variability timescales	79
3.6.4	Disk instability models	79
3.6.5	Tidal Disruption Event	80
3.6.6	Alternative models	81
3.6.7	Diagnostics of the Broad Line Region	81
4	Conclusions	85
4.1	Summary and conclusions on the study of detection of periodic signals using the statistical tools: ACF & PDM	85
4.2	Summary and conclusions on the results on the multi-wavelength campaign on a flaring Seyfert detected with eROSITA	88
5	Acknowledgements	91

List of Figures

1.1	Schematic representation of the unification model of AGN	7
1.2	Schematic representation of an AGN spectral energy distribution (SED)	9
1.3	The typical X-ray spectrum of AGN	12
1.4	VLA image of microquasar SS 433	17
1.5	Examples of Changing-Look and Changing Obscuration AGN	19
2.1	The mean & dispersion values of $\tau_{1,2}$ vs $r_{\text{corr1,corr2}}$ respectively	28
2.2	Illustration on the ACFs of pure red-noise light curves	29
2.3	The distribution of τ_1 vs r_{corr1} for pure red noise simulations	30
2.4	False Alarm Probabilities of the ACF	32
2.5	True positive detections along with false negatives and detection inaccuracy errors when using ACF	34
2.6	Illustration of false negatives and detection inaccuracy errors in ACF	36
2.7	The PDM periodogram and the distribution of the PDM parameters for Lorentzian profile	37
2.8	The PDM periodogram of pure red noise light curves	39
2.9	False Alarm Probabilities of PDM	41
2.10	Illustration of PDM periodogram for QPO mixed with red noise describing criteria for true positive detection	42
2.11	True positive detections along with false negatives and detection inaccuracy errors when using PDM	43
2.12	The PDM periodogram of pure red noise lightcurves for different sampling patterns	45
2.13	The PDM periodogram of pure red noise light curves with irregular sampling patterns along with sun gaps	46
2.14	Sample light curve of QPO mixed with red noise having no significant true positive detection in ACF & PDM even with apparent trends	49
3.1	eROSITA telescope consisting of seven identical Wolter-I geometry mirror modules. Image credits: MPE/Predehl et al. (2021).	59
3.2	Multi-wavelength light curves of the flaring event	61
3.3	Follow-up XMM-Newton X-ray spectrum of J0408–38	65
3.4	Follow-up NICER X-ray spectrum of J0408–38	68
3.5	Simple red-shifted power-law model fit to the eRASS X-ray spectra along with the residuals	70
3.6	optical to X-ray SED fits of JO408-38	71

3.7	Overview of optical spectra of J0408–38	74
3.8	Line fitting of the optical emission line components using <code>lmfit</code>	75

List of Tables

2.1	The mean and dispersion of the time lag of the peaks in ACF for pure Lorentzian signals	27
2.2	The 99.9 per cent contour limits of θ_{\min} and trial frequency $\nu_{\theta_{\min}}$ for the Lorentzians at the three test frequencies.	38
2.3	The values of RMS/mean estimated from the light curves of highly-inclined SMBH binary systems, based on the flare emission profiles in DD18.	53
3.1	Observation log of the X-ray data from the eROSITA detected ignition event along with the X-ray follow-up observational campaign	60
3.2	Simultaneous fit of <i>XMM-Newton</i> spectra of the two XMM observations over the energy range of 0.2–10 keV.	66
3.3	Model fit of the two NICER spectra over the energy range of 0.4–5 keV.	67
3.4	Model fit of the five eRASS spectra over the energy range of 0.2–3 keV	69
3.5	The best-fitting parameters of two broad-band SEDs for J0408–38, using two models	72
3.6	Results from the spectral line fitting procedure	75

List of Abbreviations

AGN	Active Galactic Nuclei
SMBH	Super Massive Black Hole
BHXB	Black Hole X-ray Binary
ISCO	Innermost Stable Circular Orbit
UV	Ultra Violet
FUV	Far Ultra Violet
NIR	Near Infra Red
NLR	Narrow Line Region
BLR	Broad Line Region
RIAF	Radiatively Inefficient Accretion Flow
ADAF	Advection Dominated Accretion Flow
QPO	Quasi Periodic Oscillations
CLAGN	Changing Look Active Galactic Nuclei
COAGN	Changing Obscuration Active Galactic Nuclei

Physical Constants

Speed of Light	$c = 2.997\,924\,58 \times 10^8 \text{ m s}^{-1}$
Gravitational constant	$G = 6.6743 \times 10^{-11} \text{ m}^3 \text{ Kg}^{-1} \text{ s}^{-1}$
Gravitational constant	$G = 6.6743 \times 10^{-11} \text{ m}^3 \text{ Kg}^{-1} \text{ s}^{-1}$
Boltzmann constant	$k = 1.380\,649 \times 10^{-23} \text{ m}^2 \text{ Kg s}^{-1} \text{ K}^{-1}$
mass of proton	$m_p = 1.672\,622 \times 10^{-27} \text{ Kg}$
Thompson cross-section	$\sigma_T = 6.652\,459 \times 10^{-29} \text{ m}^2$

Chapter 1

Introduction

Contents

1.1	Historical background	1
1.2	AGN structure	3
1.3	AGN Unification model	6
1.4	Components of AGN continuum spectra	8
1.5	X-ray spectral properties of AGN	11
1.5.1	Primary Emission	11
1.5.2	Reprocessed Emission	12
1.5.3	Absorption features	13
1.5.4	The soft excess	13
1.6	Studies on variability in AGN	14
1.6.1	Characteristic timescales	14
1.6.2	Stochastic variability due to persistent accretion	15
1.6.3	Periodic/Quasi-Periodic Oscillations in AGN	16
1.6.4	Extreme variability in AGN	18
1.7	Thesis Overview	21

1.1 Historical background

From a historical perspective, Fath (1909) obtained the first optical spectra of active galactic nuclei (AGN) at the Lick Observatory for the “nebula” NGC 1068 and reported the existence of strong emission lines identical to spectra of gaseous nebulae. These lines were speculated to be emissions from unresolved solar-type stars or nearby gaseous objects. A few years later, the same nebula was observed by Slipher (1917) at Lowell Observatory with improved spectral resolution; Slipher reported the presence of broad emission lines in the spectrum. Seyfert (1943) systematically examined six spiral galaxies with bright nuclei and found that their optical spectra were characterized by strong broad (thousands of km s^{-1} FWHM) nuclear emission lines and classified them as ‘Seyfert galaxies’. These galaxies were radio-quiet and displayed low optical luminosities. From the first radio surveys, it was found that the position of some of the radio emitters was congruent with star-like point objects. Bolton et al. (1949) were the first to associate identified radio sources

to optical objects (identified Taurus A, Centaurus A, and Virgo A with the Crab Nebula, NGC 5128, and M87 respectively). This result was followed by Baade et al. (1954) where the authors identified two of the sources of Seyfert galaxies as radio objects. The term “quasi-stellar radio sources” (now known as quasars) was coined to describe these objects whose spectra displayed strong and broad emission lines similar to Seyfert galaxies. A major breakthrough occurred in 1963 when Maarten Schmidt studied the optical spectrum of the radio source 3C 273 and determined that it had a large redshift of $z = 0.158$ (Schmidt 1963). He suggested that such a large red shift implied that the source was extragalactic and the emission should have originated from a very small nuclear region of less than 1 kpc having the total radiated energy of at least 10^{59} ergs.

Soon after quasars were discovered, the hypothesis that a supermassive black hole (SMBH) is the primary engine driving them was put forth. Such enormous luminosity of quasars at great distances and the mass-to-energy conversion efficiencies suggest that the physical processes should be from accretion onto SMBHs (Hoyle et al. 1963; Salpeter 1964; Soltan 1982). The observations of active nuclei currently span the whole spectrum of electromagnetic radiation, including radio, IR, UV, X-ray, and gamma-rays. The resolution of observations likewise increased, with interferometry achieving the maximum resolution. In recent years, the existence of a supermassive black hole at the center of our galaxy has been confirmed observationally. Observations of gas or stars rotating rapidly within a small region around a central body provided dynamical evidence for the presence of SMBHs at galaxies’ centers. The observation of rotating gas near the center of NGC4258 indicated the presence of SMBH of mass $\sim 3.6 \times 10^7 M_{\odot}$ in a region < 0.13 pc radius (Miyoshi et al. 1995; Herrnstein et al. 1999). Strong evidence for the presence of the SMBH at the centre of the Milky Way galaxy comes from tracking individual stars in the central 0.1 pc region by the GRAVITY collaboration (Eckart et al. 1996; Eckart et al. 1997; Ghez et al. 1998). In recent years, the community has obtained the highest spacial-resolution images of the immediate regions around two supermassive black holes, using the Event Horizon Telescope: one at the centre of M87, a nearby elliptical galaxy, and the black hole at the centre of the Milky Way galaxy (Sagittarius A*).

The accretion process that powers AGN feeds and grows the SMBH at the centre, and produces a lot of luminosity via high efficiency in such a compact region. The Shakura et al. (1973) geometrically-thin, optically-thick, radiatively-efficient accretion disk, which converts gravitational potential energy into large amounts of optical/UV/EUV emission, plays a major role here. Studies have been conducted to explore a possible correlation between numerous characteristics of the host galaxies and black hole mass. There are scaling relations between the mass of SMBH and that of the spheroidal component of galaxies in the local universe suggesting common evolution (Ferrarese et al. 2000; McConnell et al. 2013). AGN can be involved in radiative feedback that may impact the host galaxy’s evolution mechanical feedback via big radio jets/lobes (e.g., King 2003; Hopkins et al. 2010).

1.2 AGN structure

In this Section, we provide a quick summary of the key elements of the AGN structure as provided by the model that is most generally accepted by the community, although there remain open questions on some components, such as their detailed morphology, and behavior as a function of luminosity. To determine the mechanisms generating their observable emission, it is essential to comprehend the various AGN components.

Black Hole

A supermassive black hole serves as the AGN's central engine. Black holes are regions of space-time where a massive quantity of matter is compacted into a relatively tiny space to the point that an event horizon—a surface from which electromagnetic radiation and particles cannot escape—is generated (Rindler 1956). Black holes themselves (e.g., isolated, non-accreting) are impossible to observe since they don't directly emit anything. However, it is possible to infer their properties and existence by observing and studying phenomena associated with black holes' impact on their surroundings, e.g., their gravitational influence on the stars or gas (in the form of disks) orbiting them. Einstein's general theory of relativity provides a theoretical description of black holes, offering analytical solutions for non-rotating and rotating objects with or without a charge (Carroll 2004). The resulting observations — kinematic measurements of stellar or gaseous velocity dispersion (e.g., Kormendy et al. 1995), suggest that masses of SMBHs can be up to $10^{10}M_{\odot}$. This mass range has also been long-supported by models of quasar growth (Soltan 1982). Typically black holes are categorised as stellar-mass black holes ($< 100 M_{\odot}$), intermediate-mass black holes ($10^2 - 10^5 M_{\odot}$), and supermassive black holes ($> 10^5$). Gravitational-wave astronomy has opened a new window for looking at and studying black holes by measuring gravitational wave signals (space-time ripples) produced in binary merger events (Abbott et al. 2016a; Abbott et al. 2017; Abbott et al. 2016b; Abbott et al. 2020a; Abbott et al. 2020b). Gravitational waves from the merger of supermassive black-hole mergers will be in reach of as well in a space-based detector (Berti 2006; Kocsis et al. 2008).

The no-hair theorem states that a black hole may be entirely described by three quantities: mass, electric charge, and angular momentum. For non-rotating black holes, also called Schwarzschild black holes, the event horizon is described by (Carroll 2004),

$$R_S = \frac{2GM_{BH}}{c^2} \quad (1.1)$$

where, M is the mass of black hole, c represents the the speed of light, and G represents the gravitational constant. A rotating black hole possesses angular momentum J described with a dimensionless parameter, $a = Jc/GM_{BH}$, known as the Kerr parameter that takes values between -1 and 1. The radius of event horizon is given by $r_{\pm} = 1 \pm (1 - a^2)^{1/2}$, in units of GM_{BH}/c^2 (Carroll 2004). The case of $a = 0$ represents a non-rotating case with a Schwarzschild radius. Theoretically, $a = 1$ represents a maximally rotating black hole. However, the maximum value is likely to be $a = 0.998$ (Thorne 1974), a spinning black hole captures photons with negative angular momentum (with respect to the disk) at a rate that increases as a goes up, preventing maximal

spin-up to $a = 1.0$. According to general relativity, not all orbits around are stable. There exists an inner-most stable circular orbit referred to as ISCO for non-rotating black holes at $r = 3R_S$ (Carroll 2004; Poisson et al. 2014). For rotating black holes, its complex and the location of the ISCO depends on both J and the direction of gas motion (Dauser et al. 2010).

Accretion Disk

An accretion disk is a structure formed naturally by orbiting gas, plasma, and dust around a massive central object. These disks are found around proto-stars (e.g., Lee et al. 2018), accretion binaries (e.g., Zola et al. 2001), and supermassive black holes located at their respective galactic centre. In the disk, the gas is spiralling. The in-falling matter's gravitational energy converts into kinetic energy and heat, making the disk luminous. The material in an accretion disc surrounding a black hole is hot enough to produce significant energetic emissions.

The accretion luminosity of AGN is $L_{ac} = \eta \dot{M} c^2$, where \dot{M} is the accretion rate, and η is mass to luminosity conversion efficiency (Peterson 1997). Another useful quantity associated with AGNs is the Eddington luminosity. It corresponds to when the inward gravitational force is equal to the outward radiation pressure and represents the system's maximum achievable brightness. It is given by,

$$L_{Edd} = \eta \dot{M}_{Edd} c^2 = \frac{4\pi c G M_{BH} \mu m_p}{\sigma_T} \quad (1.2)$$

where \dot{M}_{Edd} represents the Eddington accretion rate, m_p is the proton mass, and μ is the mean molecular weight. σ_T is the Thomson cross section for an electron (Peterson 1997). The ratio of accretion luminosity and Eddington luminosity is referred to as the Eddington ratio λ_{Edd} . It measures how powerful an AGN is relative to its Eddington luminosity. For example, the sources exhibiting $\lambda_{Edd} \gtrsim 1$ are typically referred to as "high-accretion" rate AGN. Additionally, a dimensionless mass accretion rate can be defined, given by $\dot{m} = \frac{\dot{M}}{\dot{M}_c}$, where $\dot{M}_c = \frac{\dot{M}_{Edd}}{\eta}$ is the critical accretion rate (Wallinder 1993).

Several factors determine the geometry of the accretion disk. Depending on the column density, the gas's ionization level, and the mass accretion rate, the disk can be thin, slim, or thick (Wallinder 1993). When the accretion rate is moderate ($\sim 0.01 < \dot{m} < \sim 1$), the preferred solution is a geometrically-thin, optically-thick, radiatively efficient "alpha disk" (Shakura et al. 1973). As \dot{m} approaches and surpasses unity, the disc may become geometrically thick owing to photon-trapping, resulting in the so-called "slim" disk, in which dissipated energy is transferred radially inward (Abramowicz et al. 1988). When the accretion rate is below a particular critical value (of the order of $\dot{m} \sim 10^{-2} - 10^{-3}$), the inner accretion flow may be dominated by a geometrically thick, optically-thin, and radiatively-inefficient flow (Narayan et al. 1994; Esin et al. 1998).

Optical Broad & Narrow line regions

In the optical/UV/NIR bands, emission lines are produced predominantly by photoionization processes and originate in the medium containing partly ionized gases. When photons pass through a cloud of gas, on collision with the atoms, they induce ionization or excitation, wherein the electrons transit from the ground state to the excited state. However, the de-excitation may not produce photons of the same energy as some portion getting used up in inter-atomic collisions due to the bulk motion of the gas. Thus in the spectrum, line widths appear to be Doppler-broadened. In AGN, two distinct sets of emissions lines have been observed and are considered to emerge from two different regions around the AGN, the narrow-line and the broad-line regions.

The Narrow line region (NLR) is distant from SMBH and is at parsec distance, whereas the Broad-line region (BLR) is closer to SMBH and is light days away. The broad line region has a higher density and particle velocity. It has been inferred that the densities in broad line regions are generally in the order of 10^{8-9} cm^{-3} , while typical cloud velocities, as determined using line widths, are typically in the range of $3000-10000 \text{ km s}^{-1}$ (e.g., Blandford et al. 1982a; Netzer et al. 1997). Reverberation mapping indicates that the BLR is generally light days to light weeks away from the SMBH. Gas in the narrow line region is less dense, with average densities of 10^{3-6} cm^{-3} and line widths of a few hundred km s^{-1} . Furthermore, certain NLRs have been spatially resolved by ground-based observations in many of the nearest Seyferts and are commonly 100-300 pc in size (e.g., in the optical/NIR by Kakkad et al. 2018, and in X-rays using Chandra by Young et al. 2001). Narrow lines are generated farther away in substantially lower-density and temperature regions. All forbidden lines originate from NLR and are suppressed in BLR due to collisions resulting from high densities typically found in BLR clouds.

Corona

The corona is a very hot (on the order of 10^9 K) plasma of electrons. It is the most ambiguous emission component, and uncertainties prevail regarding its location and morphology. Various models posit the corona as being the skin of an accretion disk (Nayakshin 2000), associated with an advection-dominated accretion flow (Esin et al. 1997), forming the base of a jet (Markoff et al. 2005; also popularly called the "lamppost" configuration) or a combination of multiple modes (Wilkins et al. 2017). In the corona, soft (optical/UV/EUV) photons are created thermally from the accretion disc and are upscattered several times in the corona because of Compton scattering. This produces X-ray emission that mimics a power law across a broad range of frequencies (Titarchuk et al. 1995; Beloborodov 1999).

Various studies (e.g., frequency-dependent X-ray timing studies; Wilkins et al. 2022) are underway to understand better its shape, location, relationship to the disk, and whether it is static or part of continually-replenished outflow.

Torus

Infrared interferometric observations have revealed evidence for the presence of torus of size typically pc-scale to tens of milli-pcs and provide the necessary resolution to study its distribution

and properties (e.g., Kishimoto et al. 2009; Tristram et al. 2009; Kishimoto et al. 2011). The torus is an annular region composed of dusty gas, it is commonly invoked to describe the orientation-dependent Seyfert type 1/2 unification scheme. It primarily emits infrared radiation after absorbing radiation from the disk. The densities range between $10^4 - 10^6 \text{ cm}^{-3}$ (Netzer 2006). The temperature reaches up to 1000 - 1500K (Elitzur 2006; Netzer 2015), and velocities of about 10^3 km s^{-1} (Bannikova et al. 2021). It is considered to be composed of a dusty phase and a gaseous phase. The gas phase is predominantly neutral and lowly-ionized gas, including molecular gas. The dust sublimation radius determines the inner edge of the dusty torus. Moreover, reverberation mapping of the thermal continuum emission in Seyferts indicates that warm dust gas extends to 10-80 light days, just beyond the BLR's outermost boundaries (Suganuma et al. 2006).

It is speculated that the dusty torus and BLR form a single radially extended structure that straddles the dust sublimation zone (Netzer et al. 1993; Gaskell et al. 2008; Elitzur 2012). The conventionally accepted model for its morphology is that of a continuous "donut". However, the single-density torus is clearly an oversimplified approximation. In recent years, infrared interferometric data (e.g., Packham et al. 2005; Tristram et al. 2007; Burtscher et al. 2013; López-Gonzaga et al. 2016) and X-ray variability due to individual clouds transiting the line of sight to the corona (e.g., Risaliti et al. 2002; Markowitz et al. 2014) has provided convincing evidence that the torus structure is likely to be clumpy, composed of a large number of optically-thick clouds (of the order 10^5 or 10^6), with an average of \sim several along a given line of sight (e.g., Krolik et al. 1988).

Jets

AGN jets are collimated outflows propelled close to the galaxy's supermassive black hole. The jets are likely to be powered by the spin of the black hole (Blandford et al. 1977) or through the energy extracted from the magnetized accretion disk (Blandford et al. 1982b). They can be perhaps tightly collimated by twisting magnetic field lines anchored to the accretion disk. The jets extend over large distances from greater than pc scales to kpcs, sometimes Mpcs. These are launched close to the accretion disk and are usually along the system's symmetry axis. Additionally, it is believed that the radio lobes seen in galaxies are powered by the jets that originate from the centres of galaxies (Rees 1966; Adams et al. 2004). The jets have been seen only in a small proportion of galaxy or AGN samples. The fraction of radio-loud sources can range from < 1 percent to about 20-30 percent depending on parameters such as the galaxy's mass and black hole's mass (Best et al. 2005; Rusinek-Abarca et al. 2021).

1.3 AGN Unification model

AGN emit powerful radiation over the entire electromagnetic spectrum and with each technological advancement, they were discovered and classified into different classes depending on their emission at different wavelengths. As a result, multiple classifications may apply to an individual AGN. The purpose of classification is to uncover patterns in behavior that lead to physical insights. One classic unification approach is based through the torus inclination to the line of sight and the source luminosity (Antonucci et al. 1985; Antonucci 1993; Urry et al. 1995, Urry 2003). The

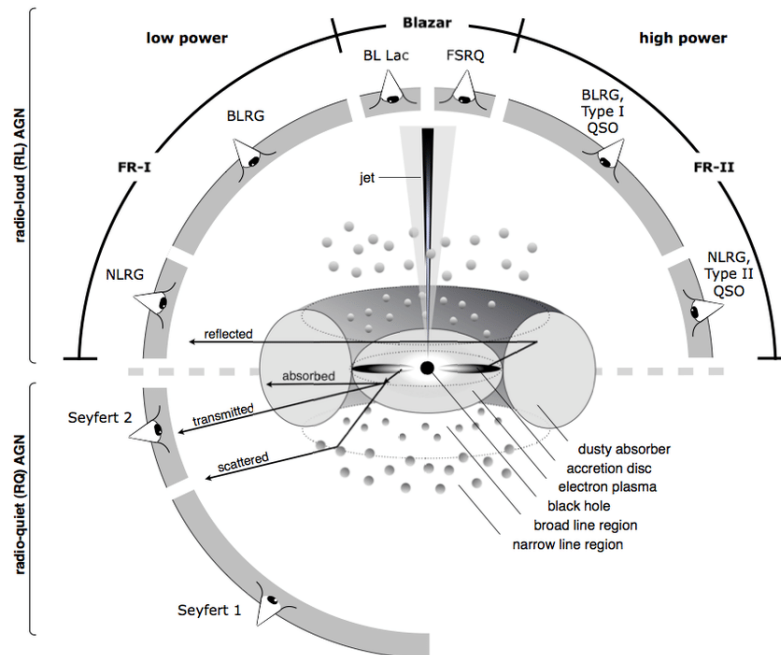


FIGURE 1.1: Schematic representation of the different AGN phenomena in the unification model, where the AGN type depends on the viewing angle and the presence/absence of significant jet emission. Image credits: Beckmann et al. (2012) made by Marie-Luise Menzel (MPE)

basic unified model is illustrated in Fig. 1.1 highlighting some of its main components discussed in detail Section 1.2. This basic model provides an explanation for classification based on the width of the optical emission lines, where both Type 1 and Type 2 AGN have narrow emission lines, and Type 2 AGN have no broad emission lines in their optical spectra. This classification between Type 1 and 2 Seyferts is explained by a dusty torus surrounding the SMBH, obscuring the broad-line region (BLR) and central continuum source from the observer. When the torus is viewed at face-on angles with a clear, unobstructed view of the BLR, a broad-line spectrum can be seen. There is evidence of Seyfert 2 galaxies having broad-line components in polarized light (e.g., Antonucci et al. 1985; Heisler et al. 1997; Véron-Cetty et al. 2006). The presence of these hidden BLRs can also be recognized via Doppler-broadened Paschen hydrogen lines in (less-absorbed) near-IR spectra at $\sim 0.8 - 1.9 \mu$. If the same system is studied more closely in an edge-on orientation, where the obscuring torus hides emission from the accretion disc and the BLR, only a narrow-line spectrum will be visible. We also have the intermediate classes (1.2, 1.5, 1.8, and 1.9), since the obscuration is not always complete on the basis of the relative strengths of the broad components of the $H\alpha$ and $H\beta$ (Osterbrock, 1981). The obstruction of the X-ray spectrum is attributed to high columns of neutral gas, and there is a possible correlation to type 1/2 (Shi et al. 2010). Also, some studies favor host galaxy structures like filaments or dusty structures at the kpc scale that dominate optical spectral type instead of the compact torus (Malkan et al. 1998).

Apart from orientation, there are other parameters that can contribute significantly to explaining the AGN diversity, including accretion rate and presence/absence of a relativistic jet (Padovani et al., 2017). The presence or absence of a strong collimated jet is one of the important parameters to determine the specific view of an AGN. It results in the distinction of jetted and non-jetted

AGN, along with substantial modifications to the spectral energy distribution (SED). Face-on observation of a strong jet produces the blazar phenomenon having rapid variability, and relativistic boosted emission can dominate the entire spectrum. Radio structures can also be present in non-jetted AGNs, but the jets are small, weak, and slow in comparison to the jetted sources. Large-scale magnetic field, spin of the BH, accretion mode could contribute to the formation of the jet component (e.g., Sikora 2009; Keenan et al. 2021).

In both Seyferts and BHXRBS, there is a critical value of $L_{\text{bol}}/L_{\text{Edd}}$ that separates two regimes of SED behavior and X-ray spectral variability behavior (Jester 2005; Wu et al. 2008; Ruan et al. 2019) and typically it is $\log(L_{\text{bol}}/L_{\text{Edd}}) \sim -3$ to -2 . Above this critical value, a thick, radiatively efficient disk dominates, with SED and X-ray thermal emission softening as flux rises (Remillard et al. 2006). Below this threshold, the emission is believed to be dominated by a radiatively inefficient flow (RIAF) or advection-dominated accretion flow (ADAF) (Narayan et al. 1994). Additionally, jets tend to be detected preferentially in sources with relatively lower values of $L_{\text{bol}}/L_{\text{Edd}}$, and the Big Blue Bump (thermal emission from the accretion disk) tends to be detected towards higher values of $L_{\text{bol}}/L_{\text{Edd}}$ (Nagar et al. 2005). Such observations are directly analogous to those in BHXBs (Remillard et al. 2006). In addition, there is observational support for the BLR to be present only above a certain accretion rate (Bianchi et al. 2008; Elitzur et al. 2009). The scenario proposed is one where the BLR is an outflowing wind, launched from the accretion disk and constantly replenished by it. However, if the accretion rate is too low there is an insufficient surface density of gas in the disk to support the BLR wind. Finally, X-ray studies of line-of-sight obscuration also support evolution in torus structure as a function of luminosity. Specifically, relatively more luminous AGNs are less likely to experience nuclear obscuration (e.g., Ebrero et al. 2009, Buchner et al. 2017), indicating that AGN-driven outflows may effectively remove gas and dust from their surrounds, thereby altering star formation in their hosts (e.g., King 2003; Hopkins et al. 2010).

1.4 Components of AGN continuum spectra

Active galaxies emit powerful radiation across the whole electromagnetic spectrum ranging from radio frequencies to hard X-rays. The continuum emission from AGN is very complex since it does not emit at the same level throughout the whole wavelength range since each emission is produced by different astrophysical processes that take place in different regions around the black hole. The SED which describes the amount of flux emitted at each wavelength of AGN is shown in Fig. 1.2 adopted from Harrison (2014). In my work, I concentrate primarily on radio-quiet Seyferts and quasars, wherein emission from the disk and corona typically dominates, and jets are lacking. Their SED components are generally common and are discussed below, although not all these properties are observed across all Seyferts/quasars. Blazars, in contrast, are jetted AGN whose jet emission dominates the observed properties, and thus yields a very different SED, as also discussed below.

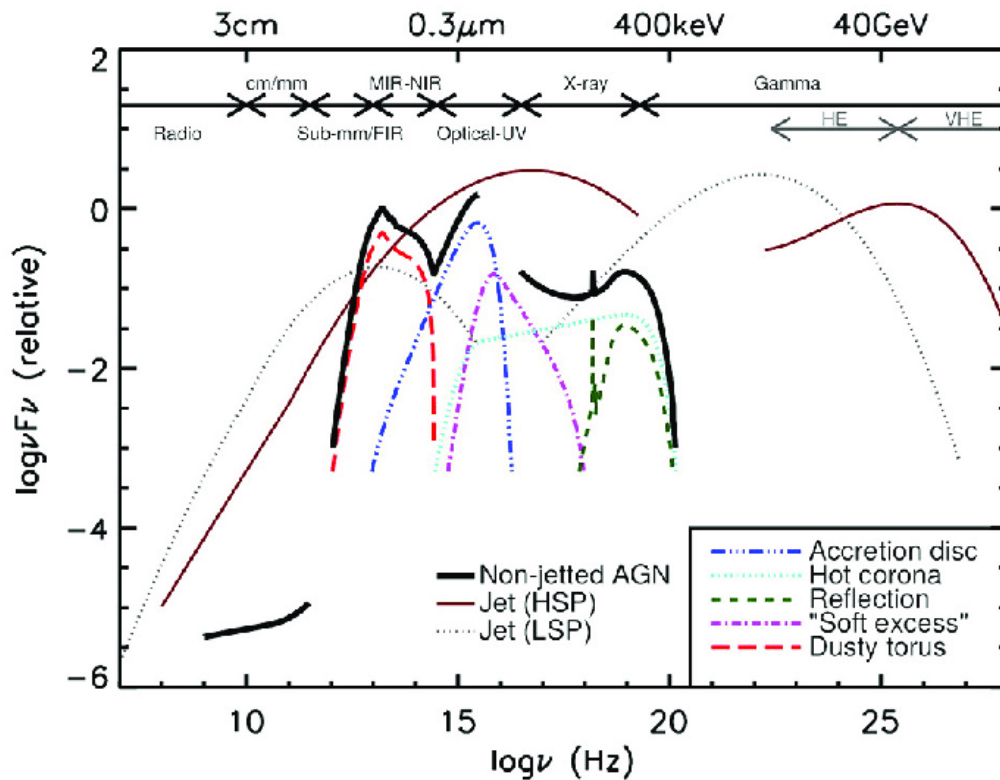


FIGURE 1.2: Schematic representation of an AGN broadband spectral energy distribution (SED). The total emission is represented by black solid lines and the main individual components are represented by different colored curves and explained in detail in Section 1.4 respectively. Image credits: Harrison (2014)

Radio Emission

The radio emission is significantly different for the radio-loud and radio-quiet sources. In the radio-loud AGN, it is non-thermal radiation that comes from the compact core and the extended regions such as the jets, lobes, and hot spots. The emission of jetted AGN is caused due to the relativistic acceleration of charged particles in magnetic fields producing a steep power-law continuum spectrum with typical slopes of $-1.1 < \alpha < -0.4$ (where α is defined by $F_\nu \propto \nu^\alpha$) through synchrotron emission (e.g., Jones et al. 1974; Wilson et al. 1985). This non-thermal continuum spans from radio to the far-infrared through the submillimeter-infrared region and can sometimes extend until the X-rays depending on the orientation of the jet towards the observer and the power of the jet. These well-collimated relativistic jets can extend far beyond the host galaxies. The radio-quiet sources are non-jetted low-power radio emissions and therefore remain unresolved mostly on large scales. The emission could be caused by the inner hot corona or a very short/non-relativistic jet. The radio spectrum is flat and considered to be non-thermal emission (Ho et al. 2001, Barvainis et al. 2005; Anderson et al. 2005) where the SED turns over sharply in the far infrared with a steep slope. However, in both sources since the power emitted in the radio region is small the contribution of the radio emission to the total bolometric luminosity is not significantly high.

Infrared Emission

The source of emission of the infrared (IR) radiation is assumed to be from the dusty torus surrounding the central engine which reprocesses the primary emission. The dust gets heated up by absorbing photons from the accretion disk and re-emits thermal radiation in the IR ranging from $\sim 1\text{--}1000\ \mu\text{m}$. There is typically an IR bump in the spectrum which can occur between ~ 1 to $100\ \mu\text{m}$ due to the dust with temperature ranging between $\sim 10\text{--}1800\ \text{K}$ (e.g. Barvainis 1987; Sanders et al. 1989; Pier et al. 1992; Rowan-Robinson 1995; Polletta et al. 2000) located at a range of distance from the black hole. There is a steep decline towards the longer wavelengths (e.g., Mullaney et al. 2011) since the emission efficiency from the dust decreases and this is sometimes in radio luminous jetted-AGN is associated with non-thermal emission dominated by the synchrotron radiation from the radio regime. The submm/far-infrared emission is produced from cooler dust heated by star formation regions in the host galaxy (Willott et al. 2002; Alexander et al. 2005; Schartmann et al. 2009; Dicken et al. 2009).

Optical/UV emission

In the standard AGN model, the BH is surrounded by the accretion disk which is assumed to be geometrically thin and optically thick producing a thermal multi-color black body spectrum (Shakura et al. 1973; Novikov et al. 1973; Sun et al. 1989; Laor et al. 1989). The temperature of the gas within the accretion disk has a wide range of temperature $T \sim 10^4\text{--}10^5\ \text{K}$ and therefore has the majority of the emission at $\sim 10\text{--}300\ \text{nm}$ (i.e., at UV–optical wavelengths) for a “typical” AGN of black-hole mass $M_{\text{BH}} \sim 10^8 M_{\odot}$ and Eddington ratio of $\lambda_{\text{Edd}} \sim 0.1$. The peak of the quasar emission in the optical-UV continuum is generally called the “big blue bump” (BBB) which is around the Lyman edge ($\lambda = 1216\text{\AA}$) with a break at $\sim 1000\text{\AA}$ (Shields 1978; Malkan et al. 1982). The spectrum is well approximated by a power-law model both at lower and higher frequencies. A substantial part of the BBB is thought to occur in the UV range and due to the Galactic absorption along the line of sight, the peak of the far-UV emission is hard to detect since there is a gap between the far-UV and the soft X-ray band. In addition, in obscured AGN, the continuum emission can be “reddened” by dust residing in the host galaxy along the line of sight.

There are many emission lines present in the quasar spectra, where the broad permitted lines are emitted from the broad line region caused due to the photo-ionization of the gas of velocities $2000\text{--}15000\ \text{km s}^{-1}$ heated by the radiation from the accretion disk and is present between the SMBH and dusty torus. The narrow forbidden lines are from the gas of velocities a few hundred km s^{-1} and are located above the plane of dust. There is another additional feature, the “small blue bump” (Wills et al., 1985) which is a blend of FeII emission lines and Balmer continuum occurring between $\sim 2200\text{--}4000\ \text{\AA}$.

X-ray emission

The higher energy end of the EM spectrum in AGN is observed in X-rays. Only the radio-loud sources show emission until the γ -rays. We have a detailed account of the different X-ray spectral properties of AGN below in Section 1.5.

γ -ray emission

The vast majority of γ -ray detected AGN are all Blazars (with the exception of some Narrow-line Seyferts detected in *Fermi*, indicating that these NLSy1 likely hosts jets). In general, the very high-energy γ -rays are thought to be produced by inverse-Compton emission from jets. It is still an open question whether the inverse-Compton emission originates from the synchrotron photons (synchrotron self-Compton which fits well for BL Lacs' SEDs well, e.g., Moderski et al. 2003; Acciari et al. 2011) or from an external photon field (External Compton process, e.g., Finke 2016).

1.5 X-ray spectral properties of AGN

X-ray emissions from quasars can range from ~ 0.1 keV up to ~ 300 keV and cover a considerable fraction of the bolometric luminosity ($\sim 5 - 40\%$, Ward et al. 1987; Padovani et al. 1988; Vasudevan et al. 2007) ranging from $10^{40} - 10^{47}$ erg s $^{-1}$. It is essential to understand the relationship between X-ray luminosity and bolometric luminosity in order to calculate the AGN bolometric luminosity function and the mass function of the SMBH. It has been shown that the X-ray bolometric luminosity correction decreases with increasing bolometric luminosity (Lusso et al. 2012). Studying the X-ray emission of AGN allows us to get a better understanding of their innermost regions.

There can be different components that can be observed in the X-ray spectra of AGN such as the primary emission, reflection components, soft excess emissions, and absorption features described in detail below.

1.5.1 Primary Emission

The hard X-ray continuum emission (known as the primary emission) in AGN is generally thought to be produced by a Comptonization mechanism, where the low energy optical-UV seed photons produced from the accretion disk undergoes multiple inverse-Compton scattering by hot plasma of temperature ~ 100 keV close to the central SMBH in the corona (e.g. Shapiro et al. 1976; Haardt & Maraschi 1993; Petrucci et al. 2001a,b). The X-ray spectral shape can roughly be approximated by a power law i.e, $F_\nu \propto \nu^{-\Gamma}$ extending from the lowest observable X-ray energies to the hard energies up to ~ 200 keV, where the photon index Γ can range between 1.5 and 2.5 (Nandra et al. 1994; Piconcelli et al. 2005). The power-law continuum often can show an exponential cut-off at high energies $\sim 80 - 300$ keV which could probably produce due to the cut-off in the energy distribution of the electrons producing the X-rays (e.g., Perola et al. 2002; Malizia et al. 2014; Fabian et al. 2015; Fabian et al. 2017). It is possible to determine the parameters of the hot plasma such as the temperature and the optical depth by analyzing these kinds of features in the X-ray continuum. The geometry and location of the hot corona are still uncertain where in one such simple model it is considered to be an extended optically thin slab present above the optically-thick and cold disk (Haardt et al. 1991; Haardt et al. 1994).

The existence of a correlation of the photon index with luminosity and redshift is still debated and unclear with several contradictory results presented over the years (e.g., Zamorani et al. 1981; Avni et al. 1986; Dai et al. 2004; Winter et al. 2009; Corral et al. 2011). The existence of a potential photon

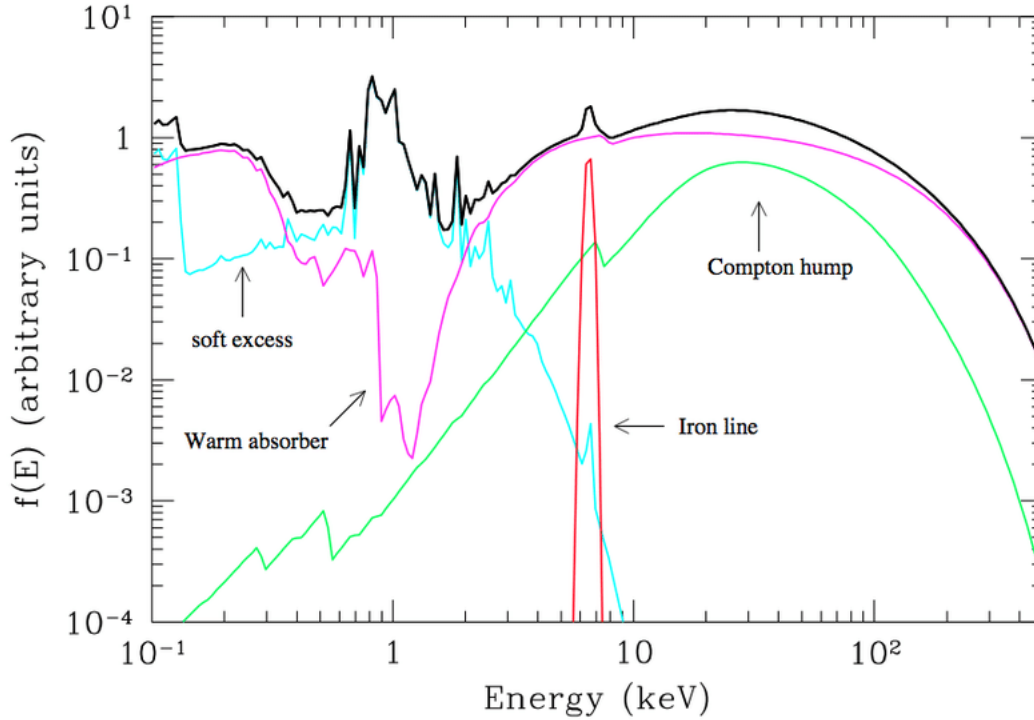


FIGURE 1.3: Schematic representation of the X-ray spectrum (black) of a typical Type 1 AGN along with the different X-ray spectral components such as the primary continuum emission (pink) absorbed at soft energy by warm gas, Compton hump (green), the narrow iron emission line feature (red) and soft excess (cyan). Image credits: Risaliti et al. (2004).

index evolution with redshift is also still unknown; while several studies (e.g., Green et al. 2009) revealed no such correlation. One of the most important and significant correlations was found between the photon index and the Eddington accretion rate where objects with a higher Eddington ratio tend to have steeper slopes (e.g., Shemmer et al. 2006). A likely physical explanation is that higher $L_{\text{bol}}/L_{\text{Edd}}$ implies stronger disk thermal emission, which effectively cools the corona, so the electrons are less energetic and each electron-photon interaction impacts less energy to the photon producing a steeper X-ray slope.

1.5.2 Reprocessed Emission

A part of the primary emission is reprocessed by materials surrounding the central SMBH in the accretion disk or the distant torus giving rise to the ‘reflection’ spectrum whose shape depends on the ionization state (Ionized/neutral gas) of the material (Lightman et al. 1988; Guilbert et al. 1988; Matt et al. 1991; George et al. 1991). It is produced by Compton scattering by free or bound electrons and photoelectric absorption. The main features of the reflection components are the Compton hump peaking at $\sim 20\text{--}40$ keV due to the down scattering of hard X-ray photons and a rollover ~ 6 keV caused due to the photoelectric absorption of the incident radiation at low energy followed by the important feature of the $K\alpha$ iron emission line. At energies below 10 keV, photons can get absorbed and give rise to many fluorescence emission lines which are strongest in Fe- $K\alpha$ occurring between the energies 6.4–7 keV (Matt et al. 1997; Fabian et al. 2000), because iron has the highest cosmic abundance among the heavy metals. It is produced when one of the

two K-shell having the principal quantum number $n = 1$ of the iron atom ejects an electron due to irradiation of the plasma by the X-rays, which is followed by the ejection of L-shell electron (Auger effect, 66% probability) or $K\alpha$ fluorescence effect (34% probability) caused due to the emission of photons at 6.4 keV as electron drops from L-shell into the K-shell.

1.5.3 Absorption features

Absorption features in the X-rays can be caused due to photo-electric absorption and Compton scattering by obscuring cold material present along the line of sight. Compton scattering becomes significant at column densities $N_H \sim \sigma_T^{-1} \simeq 1.25 \times 10^{24} \text{ cm}^{-2}$ where σ_T is the Thompson cross-section. The sources with column densities $N_H \gtrsim 1.25 \times 10^{24} \text{ cm}^{-2}$ are called as Compton-thick sources. The rollover energy below which all X-rays are absorbed is energy-dependent is ~ 6 keV or more for Compton-thick obscured sources. Possible origins of neutral obscuring gas could be due to a pc-scale torus or closer (Maiolino et al. 2001) and/or kpc-scale dusty structures in the host galaxy (Matt 2000; Guainazzi et al. 2001; Guainazzi et al. 2005).

The equivalent width (EW) measures the intensity of the line with respect to the continuum emission. In unobscured sources, the EW of the iron line depends on the fraction of the intrinsic continuum emission absorbed at the line energy. Many Type 1 AGN show narrow $K\alpha$ lines. For $N_H < 10^{23} \text{ cm}^{-2}$, we have $EW(K\alpha) \sim 50\text{--}300$ eV. In Compton thick sources where $N_H > 10^{24} \text{ cm}^{-2}$ we observe $EW(\text{Fe-}K\alpha) \sim 1\text{--}3$ keV against the weak reflected continuum. In this instance, a large portion of the $K\alpha$ line is not being absorbed, but the torus blocks the majority of the continuum radiation.

Warm absorbers: There is evidence of the presence of strong absorption and narrow emission features in the X-ray spectrum due to warm absorbing gas with a range of ionization states, from near-neutral to hydrogenic for medium-Z elements. There is a significant fraction of AGNs that exhibit these features observed with sufficient sensitivity (e.g., George et al. 1998; Blustin et al. 2005; McKernan et al. 2007). The ionized gas have intermediate to large column densities of $N_H \sim 10^{21\text{--}23} \text{ cm}^{-2}$ and ionization states of $\log \xi \sim 0\text{--}4$. The outflow velocities typically span between hundreds to thousands km s^{-1} and are inferred to have radial locations ranging beyond BLR to commensurate with the NLR (e.g., Kaspi et al. 2002; Blustin et al. 2007). We also observe ultrafast outflows, which produce highly blue-shifted absorption lines that indicate relativistic outflows with velocities of order 10^5 km s^{-1} (e.g., Pounds et al. 2003; Reeves et al. 2008; Tombesi et al. 2010; Tombesi et al. 2013). The ionized gas of this medium has typical column densities of $N_H \sim 10^{23\text{--}24} \text{ cm}^{-2}$ and ionization states of $\log \xi \gtrsim 3\text{--}4$.

1.5.4 The soft excess

One of the common AGN spectral features is the extra emission over the power-law continuum observed at energies below $\sim 1\text{--}2$ keV, known as the “soft excess”. The first evidence of the soft excess was found in the HEAO-1 spectrum of Mrk 509 (Singh et al., 1985) and the EXOSAT observations of the Seyfert 1 Mrk 841 (Arnaud et al., 1985). It is present in more than 50% of Seyfert1

galaxies (Halpern 1984; Turner et al. 1989). The origin of the soft excess is not completely understood and is still under debate (Done et al., 2007). For example, in the study of the soft excesses in 17 objects from ROSAT and Ginga by Piro et al. (1997), no single model fitted the emission satisfactorily concluding that the soft excess varies from source to source. Sometimes, the soft excess could be fitted with a black body model with best-fit temperatures of $\sim 0.1\text{--}0.2$ keV. However, this characteristic temperature is significantly high to be related to the exponential wein tail of the “big blue bump”. It is in fact found to be independent of the black hole mass where it remains constant over a wide range of AGN luminosity (e.g., Walter et al. 1993; Gierliński et al. 2004; Crummy et al. 2006), which is in contrast to the standard accretion disk where the effective temperature scales with the black hole mass as $\propto M^{-1/4}$. There are different theoretical models that are used to explain the nature of the soft excess observed in the X-ray spectra: (i) A possible explanation is using a ‘warm Comptonization’ region where the seed disk photons are up-scattered in an optically thick ($\tau > 1$) and warm ($kT \sim 1$ keV) plasma to produce the excess photons at the soft X-ray band (e.g., Porquet et al. 2004; Mehdipour et al. 2011); (ii) Another interpretation is by using the blurred ionized reflection model where the soft excess is produced due to the relativistic blurred reflection of the primary X-ray continuum in an ionized disk (e.g., Ballantyne et al. 2001; Fabian et al. 2005; Crummy et al. 2006; García et al. 2019); (iii) Partial covering ionized absorption models are also used where the soft excess could be produced due to the smearing of wind from the inner disk at relativistic velocities in the vicinity of the black hole (Miller et al. 2008; Turner et al. 2009).

1.6 Studies on variability in AGN

AGN exhibits large variations in luminosity on time scales from hours to years, and across all wavelengths. Studying the continuum variability can reveal distinctive timescales that shed light on the physics of accretion flow or jets and the central regions of the AGN. For many variability mechanisms, system parameters such as black hole mass M_{BH} , brightness, accretion rate relation to Eddington ratio, etc. can govern variability timescales due e.g., size scales that scale linearly with M_{BH} . Multiwavelength monitoring has enabled the study of interband correlations which can potentially yield causal time delays between two time series. Such time delays form the basis of, for example, reverberation mapping of the BLR or accretion disk temperature structure in Seyferts (e.g., Edelson et al. 2019), or can yield insight into blazar jets by linking emission regions (e.g., Tavecchio et al. 1998).

1.6.1 Characteristic timescales

Depending on the type of variability and the underlying physical processes, different timescales will dominate. Below we mention some of the variability timescales associated with standard geometrically thin disks in accreting SMBHs.

Light-crossing time scale: It is the shortest time scale of variability. The time taken by the light to cross a distance R from the central region. It helps to determine the size of the object.

$$t_{lc} = R/c$$

The time taken by a radiative signal to cross the X-ray emitting region at a distance r in light days can be given by re-writing the above equation as,

$$t_{lc} = 0.011M_7 \left(\frac{r}{10R_g} \right) \text{ d} \quad (1.3)$$

where M_7 is the black hole mass in units of $10^7 M_\odot$ and R_g is the Schwarzschild radius.

Dynamical/Orbital timescale: It is the orbital timescale (t_{orb}) of the black hole from Keplers' third law of motion and is proportional to the inverse of the angular frequency.

$$t_{orb} = \left(\frac{r^3}{GM_{BH}} \right)^{1/2} \approx 0.33 (M_{BH}/10^7 M_\odot) (R/10R_s)^{3/2} \text{ d} \quad (1.4)$$

Thermal timescale: Thermal instabilities cause variability at timescales given by,

$$t_{th} = (\alpha)^{-1} \times t_{orb} \approx 5.3 (\alpha/0.01)^{-1} (M_{BH}/10^7 M_\odot) (R/10R_s)^{3/2} \text{ d} \quad (1.5)$$

where α is the viscosity parameter.

Viscous timescale: is the timescale for material to radically drift inward through the disk due to local angular momentum losses.

$$t_{vis} = \left(\frac{H}{R} \right)^{-2} \times t_{th} \approx 53000 \left(\frac{H}{R} \right)^{-2} (\alpha/0.01)^{-1} (M_{BH}/10^7 M_\odot) (R/10R_s)^{3/2} \text{ d} \quad (1.6)$$

where H/R is the ratio of the height of the disk to the radius.

1.6.2 Stochastic variability due to persistent accretion

AGN are characterized by variable emissions that are in the form of aperiodic, stochastic (non-deterministic) fluctuations (e.g., Lawrence et al. 1987). The Power Spectral Density function (PSD) is one of the most common methods for characterizing variability which is a measure of the amount of variability power P as a function of the temporal frequency. The PSD of AGN is usually well represented as a power law over a wide range of frequencies: $P(f) \propto f^{-\alpha}$. The variability on shorter time-scales has the spectral index slope ranging between $\alpha \sim 1-3$ (e.g., McHardy et al. 1987; Vaughan et al. 2003). Hence, such variability processes are referred to as "red noise." In the X-ray band, variability studies have focused on measuring PSDs to search for characteristic variability timescales; if the requisite data quality for a PSD is lacking, one can

measure variability amplitude (root mean square amplitude F_{var} (Vaughan et al. 2003), or mean-normalized excess variance (Nandra et al. 1997). Early works using X-ray light curves obtained from *ASCA* established an anticorrelation between variability amplitude and luminosity (Nandra et al. 1997; Leighly 1999; Turner et al. 1999). The study of this anti-correlation was extended to longer timescales by Markowitz et al. (2001) using *RXTE* observations, where they also showed that the AGNs are more strongly variable on longer time-scales compared to the short time-scales. The broad-band X-ray PSD has breaks in the continuum power-law slope, which is flatter towards the lower frequencies, similar to that observed in X-ray binaries (e.g., Edelson et al. 1999; Uttley et al. 2002) and were the first characteristic variability timescales to be discovered. This break time-scale (T_{B}) was found to linearly scale with black hole mass (Markowitz et al. 2003) and also to be dependent on the accretion rate (McHardy et al. 2006) quantified empirically as follows:

$$\log T_{\text{B}} = 2.1 \log M_{\text{BH}} - 0.98 \log L_{\text{bol}} - 2.32$$

where T_{B} is in days; L_{bol} is the bolometric luminosity which depends on the accretion rate in units of 10^{44} ergs s^{-1} and the black hole mass M_{BH} in units of $10^6 M_{\odot}$. Therefore, break frequencies in the power spectra suggest that the variability is controlled by distinctive characteristic timescales which can provide insight into the accretion flow (e.g., Kelly et al. 2009).

1.6.3 Periodic/Quasi-Periodic Oscillations in AGN

Similarities between black hole X-ray Binaries (BHXBs) and AGNs have been long studied in the literature. There are similarities in the power spectra in both classes of systems (e.g., broadband shapes, and break frequencies scale linearly with black hole mass across 6–7 orders of magnitude). The X-ray/radio luminosity relations, the scaling relations of the black hole jet with the black hole mass (e.g., Sams et al. 1996; Heinz et al. 2003), similarities in the emission and spectral properties – support the idea that both classes of objects should have similar accretion mechanisms. The existence of the fundamental plane linking the radio, X-ray luminosities, and black hole mass was established independently by two groups (Merloni et al. 2003; Falcke et al. 2004). This relation supports the case that variability components present in one class of object may also be present in the other. Several actively accreting BHXB show quasi-periodic oscillations (QPO) in their X-ray PSDs (e.g., Wijnands et al. 1999; Casella et al. 2004; Motta et al. 2015). As source luminosity and the inner disk size evolves, the so-called low-frequency QPOs in BHXBs, which are commonly found at frequencies $f \sim 1\text{--}30$ Hz also evolve, with QPO temporal frequency migrates to higher values as luminosity increases and disk radius becomes smaller. These changes in frequency may be related to Lense-Thirring precession in the inner disk (e.g. Ingram et al. 2012). The high-frequency QPOs ($f \sim 40\text{--}450$ Hz) scale as the inverse of M_{BH} and therefore, they could be an imprint of both spin and the black hole mass (Remillard et al. 1999; Abramowicz et al. 2001).

Studies on light curves across the EM spectrum have been conducted in the quest to find periodic signals (either strictly- or quasi-periodic) in both blazars and Seyfert AGN. According to some interpretations, the innermost accretion disk occasionally shows a “hot spot” of intense localized emission, which can be used to obtain the constraints on the black hole mass or the size of the

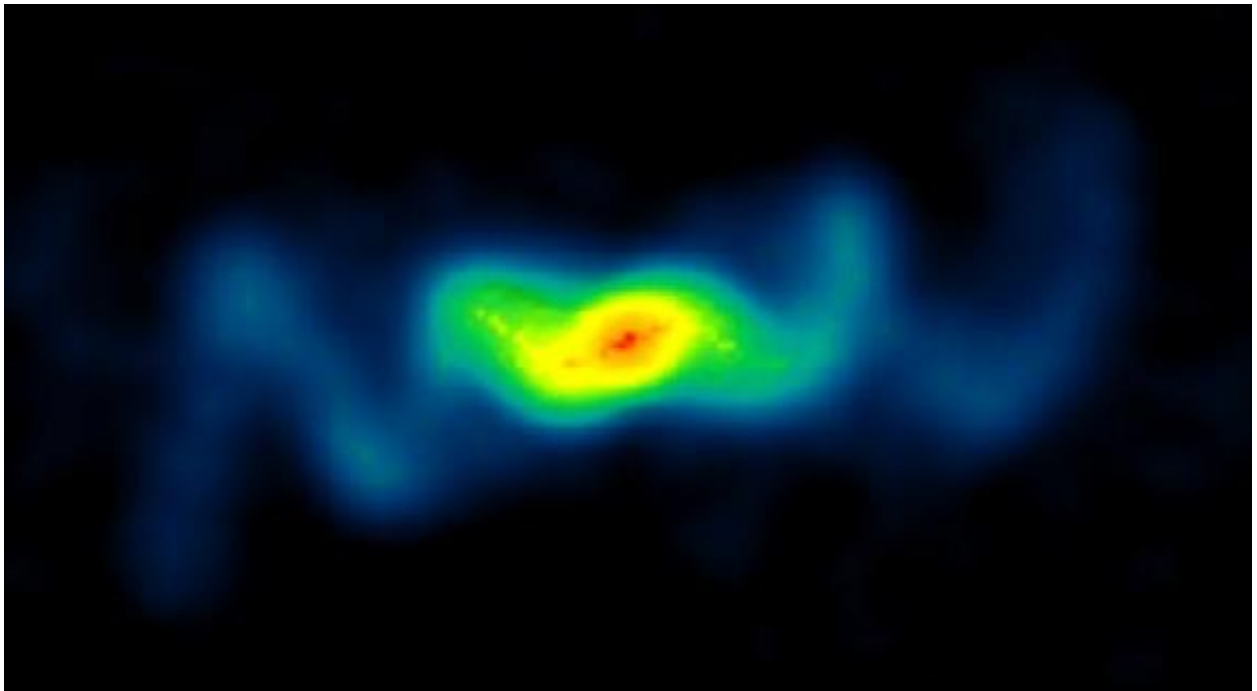


FIGURE 1.4: VLA image of microquasar SS 433, image credits: Blundell & Bowler, NRAO/AUI/NSF

inner disk through the putative hot spot’s orbital motion (e.g. Gupta et al. 2009). In another interpretation, jet precession could cause periodic modulations in luminosity. We resolve the jet in the Galactic microquasar SS433 to be twisted into a helical shape (see the VLA image in Fig. 1.4), due to jet precession. Some claimed periodicities in blazars have thus been attributed to jets precessing in and out along the line of sight (e.g. Carrara et al. 1993; Villata et al. 1999; Li et al. 2009; Sandrinelli et al. 2016) and with some modulations associated with claims of blazars being part of SMBH binary systems (e.g. Lehto et al. 1996; Valtonen et al. 2006). Furthermore, in recent claims of periods for quasars, the luminosity variations attributed due to changes in the mass accretion are interpreted as a result and evidence for gravitationally bound SMBH binary systems (e.g. Liu et al. 2015; Graham et al. 2015; Charisi et al. 2016).

However, due to the poor data quality for AGN, it is still challenging to obtain statistically robust detections of strictly periodic oscillations (SPOs) or quasiperiodic oscillations (QPOs). For instance, searches for QPOs in Seyferts’ broadband X-ray PSDs or periodogram¹ are hindered by their poor frequency resolution, particularly in comparison to the higher-quality X-ray timing data for BHXRBs where QPOs are typically detected (Vaughan et al., 2005). Hence, so far there have been only a few robust X-ray-based claims, such as the QPO observed in RE J1034+396, which persists at a timescale of ~ 1 hr across observations spanning years (Gierliński et al. 2008; Alston et al. 2014) a ~ 2 hr QPO detected in MS 2254.9–3712 (Alston et al. 2015) and a ~ 24 -minute QPO in IRAS 13224–3809 (Alston et al. 2019); for additional detections see Ashton et al. (2021). However, the behavior of the PSD — e.g. distribution and scatter of periodogram points; biases — under a variety of noise processes (white, red, etc.) and in astrophysical contexts is now well-understood (e.g. Fisher 1929; Leahy et al. 1983; Papadakis et al. 1993). Particularly when data quality is high,

¹The periodogram is an estimator of the PSD.

meaning data sampling is relatively continuous (few major gaps) and close to even spacing, the periodogram or PSD is straightforward to use for detections of QPOs (e.g. Vaughan 2005). Otherwise alternate statistical methods are generally employed for the detection of periodic/QPO signals in AGN with sparsely sampled data points, such as the Auto-Correlation Function (ACF), Phase Dispersion Minimization (PDM), wavelet analysis, sinusoidal fitting, etc. Generally, QPOs claimed in AGN using these alternate methods are non-repeatable in additional observations, are based on improper usage of statistical tools, such as simply identifying the highest-amplitude points in a periodogram as outliers (e.g. Webb et al. 1988; Smith et al. 1995; Pihajoki et al. 2013; Ackermann et al. 2015), or improper calibration of the “false alarm probability.” In particular, the presence of stochastic, aperiodic “red noise” is seen at all wavebands and dominates the AGN emission and which tends to bury any possible periodic/quasi-periodic signal, if any present. In addition, pure stochastic red noise processes (no QPO present) are seen to spuriously mimic few-cycle sinusoid-like periods (Kozłowski et al. 2010; Vaughan et al. 2016), which can be misinterpreted as an intrinsic periodic signal. Hence, it is crucial to account for the amount and form of the red noise which can impact the calculation of statistical significances of detection of periods and calibration of false alarm probability while using any statistical tool. Many claims of AGN periodicities in the literature simply made no attempt to account for this red noise “background.” In addition, many claims of AGN periodicities in the literature are few-cycle (e.g. Ackermann et al. 2015; Bon et al. 2016). In either of these scenarios, it is likely the claimed periodicity does not exist, and is merely an artifact of red noise. Finally, the accumulated publications of periods in AGN do not yet exhibit any obvious trend between timescale and system parameters such as M_{BH} or accretion rate relative to Eddington. In contrast, the continuum break timescales in X-ray PSDs and the characteristic frequencies of low-frequency QPOs and broad Lorentzian components in BHXRBs are observed to robustly depend on M_{BH} and/or accretion rate.

1.6.4 Extreme variability in AGN

Over the past few years, researchers have observed a number of accreting SMBHs that undergo extreme variability exhibiting dramatic and consistent changes in their luminosities and spectral properties through large-scale time-domain surveys. These variations are substantially higher than the “normal” stochastic variations associated with persistent accretion in Seyferts and quasars.

Changing Look AGN

At the extremes of variability, the mass accreting onto the SMBHs can be triggered – that is, an accretion flow onto the SMBH establishes itself, and a quiescent galaxy turns into an active one – or halted/shutdown – the accretion gas depletes itself. Therefore, the accretion phases of AGN are likely episodic in nature (Shen 2021). Identification and study of extremely variable AGN events can provide a better understanding of the accretion process and AGN evolution. These AGN are classified as “Changing Look” AGN: a given source switches classification in the optical/UV regime (discussed in Section 1.3), X-rays, or both. In the X-ray band, extreme changes are attributed to the temporal variations in the line-of-sight column density (N_{H}) in the gas near the SMBH and are called Changing Obscuration AGN (CO-AGN). However, in the optical/UV

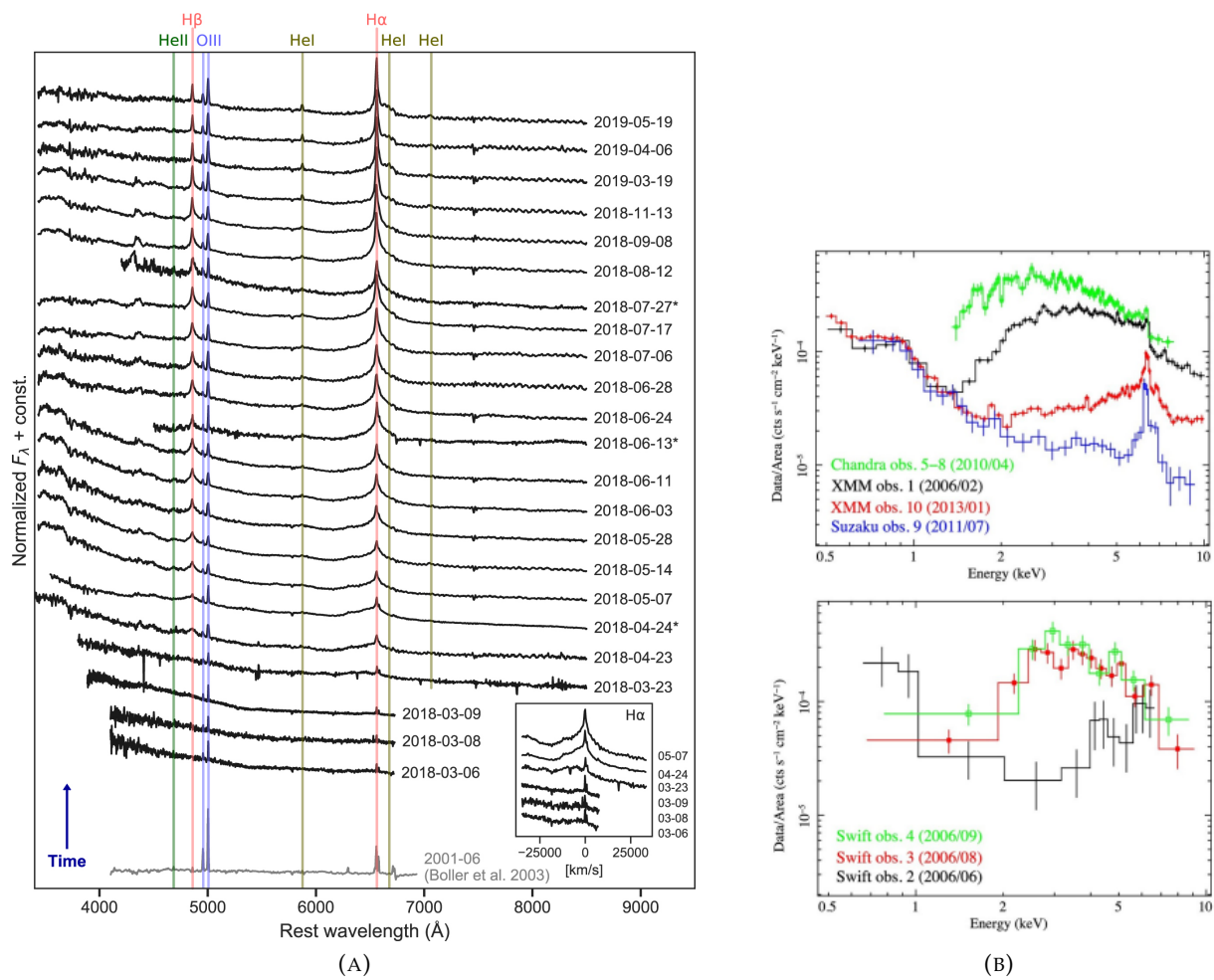


FIGURE 1.5: (A) Example of Changing-Look AGN: 1ES 1927+654 changing from a Type-2 AGN (bottom) to a Type-1 AGN with an intermediate stage of a blue-continuum-dominated from Trakhtenbrot et al. 2019; (B) Example of Changing Obscuration AGN: the progression of the CO-event seen in the X-ray spectrum from least obscured to most obscured phase in Type 1 AGN ESO 323-G77 from Miniutti et al. 2014

these events are typically associated with changes in the accretion rate, which in turn causes drastic changes in the ionizing thermal continuum, accompanied by the appearance/disappearance of the broad optical/UV lines typical of Type 1 AGN (hence the changing “look” moniker used frequently in the literature). We also refer to these objects as Changing State AGN (CS-AGN).

Selected examples of CL-AGN in the literature: The observations of the optical spectra of the Seyfert galaxy NGC 2992 revealed that its type classification was varying between Seyfert Type 1 and Seyfert Type 2 with the appearance and disappearance of the weak broad H α emission line. The source also showed correlated variability between the X-ray continuum flux and the H α behavior. The X-ray was in a high state during the presence of the broad H α line, but it slowly decreased in concert with the disappearing H α line (Gilli et al. 2000; Trippe et al. 2008 and references therein). In other cases, it was discovered that changes in X-ray flux were related to significant X-ray spectral variability with the appearance of a strong soft excess during the brightest periods when correspondingly the broad optical lines are present and disappear during the lowest flux periods as the continuum fades (e.g., Mrk 1018: Noda et al. 2018). There are many

additional similar examples with changes in the broad-line components that cause the optical classification to change (e.g., Shappee et al. 2014; LaMassa et al. 2015). Another peculiar object 1ES 1927+654, was initially a source with no broad emission lines and with no X-ray obscuration (Gallo et al. 2013). It had an optical outburst at the end of 2017, as monitored by ASAS-SN. The spectroscopic follow-up on the source revealed that the source first developed a blue continuum like a quasar followed by the appearance of broad Balmer lines as shown in fig. 1.5 (Trakhtenbrot et al. 2019 and references therein).

There are several CO-AGNs observed in the X-rays to undergo a transition from/to Compton-thick ($N_{\text{H}} \gtrsim 10^{24} \text{ cm}^{-2}$) to/from Compton-thin ($N_{\text{H}} < 10^{24} \text{ cm}^{-2}$). In these cases, there is a dramatical change in the spectral shape from transmission-dominated to reflection-dominated spectra and vice-versa (e.g., Matt et al. 2003; Piconcelli et al. 2007; Ricci et al. 2016). The reprocessed X-ray radiation dominates over the primary X-ray continuum when the column density increases.

Quasi-Periodic Eruptions

Quasi-periodic eruptions (QPEs) are rapid and high-amplitude X-ray flares repeating over a short time scale originating near the centers of low-mass SMBHs in both optically-classified active and inactive galaxies. This phenomenon was first observed by Miniutti et al. (2019) in GSN 069, which exhibited flares every 9 hours, with each flare lasting for \sim an hour. Such variability behaviour is unique and distinct from other known AGN variability behaviours. Since then, QPEs have been detected in four additional sources, such as RX J1301.9+2747 (Giustini et al. 2020), 2MASXJ0249 (Chakraborty et al. 2021). Typically, the X-ray bursts exhibit a regular spectral behaviour, and the main emission component is thermal, and confined to soft X-rays, below 2 keV. During a flare, the thermal emission increases in temperature, and in some sources, there is an additional hard X-ray, power law-like component emerging above 2 keV. The origin of these events, the duration, and their relationship to the physical properties of the inner accretion flow are still unclear. Various models have been proposed to explain the phenomena, mostly focusing on intrinsic changes in the accretion flow and orbital phenomena. For example, Arcodia et al. 2021 detected QPEs from two previously quiescent galaxies. In these galaxies, no sign of black hole activity can be seen in the optical spectra, supporting the conclusion that a pre-existing accretion flow is not required to trigger these events and the periods, amplitudes, and profiles of these QPEs are inconsistent with current models that invoke radiation-pressure-driven instabilities in the accretion disk but instead is driven by an orbiting compact object.

Physical scenarios/models causing CL events

In general, there are two main categories of scenarios proposed to explain CS events: (i) changes in the accretion flow, and consequently the emission properties, caused by instabilities in the accretion disk and (ii) significant perturbations to accretion disks that can be produced due to activity such as tidal disruption events (TDEs).

One of the possible mechanisms for a CS event can be the thermal instability of an accretion disk that has significant localized variations in temperature and which could possibly cause a limited

cycle of outbursts (e.g., Lin et al. 1986). In the example of Mrk 1018, the CL-phenomena is linked to variations in the soft X-ray excess at $\gtrsim 1\text{--}2$ keV caused by changes in the warm corona which possibly evaporates into an advection-dominated accretion flow (ADAF) or ADAF condensates. The spectral hardening of the source from the bright to the faint state is due to huge variations in the mass accretion rate driven by the hydrogen ionization disk instability similar to the state transitions observed in BHXBs. In this scenario, the sound speed is much faster, decreasing the viscous time scale of variability (Noda et al. 2018).

Another potential instability mechanism is the radiation-pressure instability a.k.a the Lightman et al. (1974) instability. Sniegowska et al. (2020) adopted a simple toy model where we consider a narrow, unstable disk where the radiation pressure changes vertically, the model is applied to explain the CL behaviour in NGC 1566, NGC 4151, and NGC 5548. Ross et al. 2018 considers the model where the changes at the innermost circular orbit (ISCO) of the SMBH caused by magnetic-hydrodynamical instability associated with propagating cooling front are capable of decreasing the optical/UV luminosity. Re-brightening of the AGN can happen after the cooling front stops and when the heating front propagates inwards. This model was used to explain the temporal and spectral variations observed in the source SDSS J110057.70-005304.5. In 1ES 1927+654, Scepi et al. (2021) explained the dip in the X-ray luminosity as being due to a change in the accretion rate and inversion in magnetic flux advected onto the SMBH (magnetically arrested disk) which simultaneously resulted in an increase of the optical/UV luminosity.

Major perturbations in the accretion disk could also be due to the tidal disruption of a star passing close to the SMBH (e.g., Merloni et al. 2015). A TDE occurring in an active SMBH can interact with the accretion disk, disrupting the gas in the disk which in turn increases the accretion rate, causing an increase in the flux of the optical/UV emission (e.g., Ricci et al. 2020; Malyali et al. 2021; Li et al. 2022). The impact can create shocks in the disk, causing inflow and energy dissipation that may cause the X-ray corona to vanish (e.g., Chan et al. 2019).

In CO-AGN, although variability in intrinsic column density caused by clouds moving in and out of the line of sight is the most commonly accepted explanation for CO events (e.g., Marchese et al. 2012; Lusso et al. 2013), various other theories have been put out over the years. A possible explanation for the observed N_{H} changes is that they are caused by variations in the material's ionization state, which are connected to changes in the intrinsic AGN luminosity. Lower luminosities allow material that was previously too highly ionized to absorb the X-ray continuum to drop to low ionization levels and absorb continuum photons more efficiently and hence the anti-correlation between N_{H} and X-ray luminosity (e.g., Krolik et al. 2001; Couto et al. 2016).

1.7 Thesis Overview

I summarize each chapter of this dissertation below.

Chapter 2 comprises the first project to study the detection of periodic/quasi-periodic signals in AGN data dominated by stochastic variability using the Auto-Correlation Function (ACF) and

Phase Dispersion Minimization (PDM). In this chapter, we first review our methodology to simulate the AGN light curves that are used to perform the tests. We present the calibration of False Alarm probability rates of the ACF & PDM determined by Monte Carlo simulations of pure red noise light curves for evenly sampled light curves. We present the analysis of the parameter space required for a true positive detection using the ACF and PDM using Monte Carlo simulations for combinations of broad-band red noise of unbroken power-law PSD model and different strengths of QPO signal for evenly sampled data and additionally test the PDM for realistic sampling patterns. We discuss the results in the context of previous claims of periodicities appearing in the literature, and we present suggestions for reducing false-positive claims. Finally, we apply the results to one physical system, namely a highly-inclined SMBH binary system incorporating periodic gravitational lensing, and present the region of parameter space/conditions where we can determine the period with statistical significance using the ACF & PDM. We have published the results of this project in Krishnan et al. (2021).

In **Chapter 3**, we present the study of a flaring event detected in the X-rays with eROSITA on the Russian Spectrum-Roentgen-Gamma (SRG) mission; this work was done as an External Collaborator to the German consortium. This chapter contains the archival & follow-up data sets and data reduction techniques obtained for this source. We present the *XMM-Newton* and *NICER* observations and the results of the analysis. We present the analysis and results from modeling the optical-UV to X-ray SED. We observe the spectral state of the soft excess varying between the X-ray observations taken during the flaring epoch and after the flaring of the source. We overview the analysis from our optical spectroscopic follow-up observations. The optical spectral observations of the source revealed that the emission line HeII $\lambda 4686$ intensely fades, roughly tracking the optical/UV/X-ray continuum. Finally, we discuss the results in the context of broadband thermal Comptonization emission models and discuss the possible origins of the flaring event. The results of this project will be submitted soon to a peer-reviewed scientific journal (possibly in *Astronomy & Astrophysics*).

Chapter 4 contains the conclusions of the analysis from the work presented in Chapters 2 & 3.

Chapter 2

Detection of periodic signals using statistical tools

Contents

2.1 Methodology: Light-curve simulation and input PSD models	23
2.2 ACF for QPO detection	26
2.2.1 The behaviour of the ACF for pure Lorentzian processes	27
2.2.2 The behaviour of the ACF for pure red noise power-law processes	28
2.2.3 ACFs for QPOs mixed with red noise	33
2.3 PDM for QPO detection	36
2.3.1 PDM test for Lorentzian profile:	38
2.3.2 The behavior of the PDM for pure red noise processes	39
2.3.3 The behaviour of PDM for QPOs mixed with red noise	41
2.4 Realistic uneven Sampling test using PDM	44
2.4.1 PDM test for Lorentzian profile with uneven sampling	44
2.4.2 The behaviour of the PDM for pure red noise processes with uneven sampling	45
2.4.3 The behaviour of PDMs for QPOs mixed with red noise	47
2.5 Discussion	48
2.5.1 Some of the claims in the literature and basic pitfalls regarding ACF and PDM usage	51
2.5.2 Application to the detection of periods for selected physical situations	53

2.1 Methodology: Light-curve simulation and input PSD models

In our studies, we simulate light curves assuming different forms of the underlying PSD (continuum shape, presence/absence of QPOs), apply the ACF or PDM to these light curves, and compile the statistics to determine whether QPOs are present or not. The accretion processes in radio-quiet AGN and stellar-mass black-hole X-ray binaries (BHXBs) are strikingly similar with regard to the PSD shape. Thus, it is reasonable to assume that the variability processes in these two classes of objects are also identical. In BHXBs, the broadband continuum is typically modeled using cut-off

power-law models, and the QPOs using broad or narrow Lorentzian components in the X-ray PSDs (e.g., Nowak 2000; Belloni et al. 2002; Pottschmidt et al. 2003; Axelsson et al. 2005; Grinberg et al. 2014; De Marco et al. 2015). However, compared to BHXB X-ray PSDs, the data quality for PSD measurement is usually much poorer for Seyfert AGN (where disk emission dominates) and blazar AGN (where jet emission dominates) at all the wavelengths. For Seyferts, it is often sufficient to use unbroken, broken, or slowly-bending power laws to model broadband X-ray PSDs. One notable exception is the X-ray PSD of the Seyfert 1 Ark~564 fitted with two broad Lorentzian (McHardy et al. 2007). For blazars, broadband PSDs measured at different wavelengths approximately follow simple power-law models (e.g., Goyal et al. 2017; Goyal et al. 2018; Goyal 2019) or bending power-laws (Chatterjee et al., 2018). In this work, all studies are performed considering that the red noise PSD continuum can be represented by a simple power law or occasionally by a broken power law model. This assumption is standard for most AGN data and/or appropriate for comparatively limited dynamic ranges in temporal frequency. However, we suggest the readers investigate other PSD continuum forms and do their own Monte Carlo simulations if necessary. We generate simulated time series comparable to actual AGN light curves using the numerical algorithm described in Timmer et al. (1995). This approach constructs linear time series by randomly varying the phase and amplitude of the Fourier transform of the input data of an arbitrary PSD shape. The algorithm by Timmer et al. (1995) generates light curves with a Gaussian flux distribution. For simulating light curves with arbitrary (non-Gaussian) flux distributions, the readers can employ the procedure in Emmanoulopoulos et al. (2013). We employ the "RMS2/Hz" normalisation of Miyamoto et al. (1991) and van der Klis (1997) for all the input PSD models.

We first examine an "ideal case" of a QPO only, in the absence of any broadband noise, for the ACF and PDM to identify the signatures one may pursue while looking for a QPO. Hence, we consider a narrow Lorentzian component as the input of our model where the PSD is given by

$$P_{\text{Lor}} = \frac{2R^2 Q f_L}{\pi(f_L^2 + 4Q^2(f - f_L)^2)} \quad (2.1)$$

where R is the fractional RMS amplitude (absolute RMS/mean) and f_L is the centroid frequency of the Lorentzian. The width of the Lorentzian is quantified by the "quality factor" Q , where a narrow-peaked Lorentzian will have a relatively higher value of quality factor ($Q \sim f_L/\text{FWHM}$). A strict sinusoidal signal with coherent oscillation has the quality factor $Q = \infty$.

We simulate the light curves corresponding to pure red noise only, modelled with a simple unbroken power-law PSD given by :

$$P_{\text{PL}} = A(f/(10^{-6}\text{Hz}))^{-\beta} \quad (2.2)$$

where A is the amplitude in units of Hz^{-1} at an arbitrary frequency of 10^{-6} Hz; in the X-ray PSDs of Seyferts, power is typical of order 10^{3-4} Hz^{-1} . Therefore, we fix the amplitude at $A = 1.5 \times 10^4 \text{ Hz}^{-1}$. β is the red noise power-law slope, where more positive values correspond to steeper slopes. In the ACF and PDM, we look for signatures that could be mistaken for a QPO due to red

noise by performing tests for a range of PSD power-law slopes β . Such simulations allow us to investigate the false alarm probability corresponding to the Type I errors (false positive detection of a QPO using ACF/PDM) over a range of pure stochastic processes.

We also perform the simulations for QPOs mixed with red noise. The PSD of the variability is modelled as the sum of a broadband power-law continuum and a narrow Lorentzian for a range of power-law slopes and Lorentzian RMS strength. This test allows us to understand the conditions at which one can detect a statistically significant QPO in the presence of red noise.

Numerous claims of QPO reported in the literature, e.g., claims of QPO from SMBH binaries, lack estimates of the quality factor Q and are commonly considered strict periods for simplicity. For example, in self-lensing SMBH binaries, the light curve variations could be periodic even if they do not have constant wave amplitude due to changes in the continuum luminosity of the accretion disk. However, the quasi-periodic components observed in the emissions may have other origins, such as extra variability modes related to the orbital motion or tidal interactions in the binary, or the impacts of periodic streams of matter on the disc. For the precessing jets of blazars, some papers (e.g. Abraham 2000; Britzen et al. 2018) suggest that the precession produces a strictly periodic behaviour in the resultant light curves due to periodic beaming assuming a constant input (pre-beaming) flux. However, it is simple to comprehend how non-sinusoidal behaviour can arise. The flux amplification could depend on the number of individual knots ejected at specific phases of precession, and there could be deviations in the fluxes and ballistic behaviour of individual jet knots.

Since studying all possible QPO signals with varying widths is difficult, we have used a relatively high-quality factor $Q = 30$ in our analysis for modelling something quite close to high-quality periodic signals. P_{rat} is defined as following ratio,

$$P_{\text{rat}} = P_{\text{Lor}}/P_{\text{PL}} = \frac{2R^2Q}{\pi f_L A \left(\frac{f_L}{1.0 \times 10^{-6}} \right)^{-\beta}} \quad (2.3)$$

where $P_{\text{Lor}}(f_L)$ is the power of the Lorentzian at f_L , and $P_{\text{PL}}(f_L)$ is the power in the power-law continuum at that frequency. Below, we test QPO detection thresholds for values of $\log(P_{\text{rat}})$ spanning -1 to 5 .

It is impossible to account for all possible sampling patterns for the light curve. For our initial tests presented in Section 2.2 and Section 2.3, we adopt what we refer to as our “baseline” sampling, which consists of evenly-sampled light curves with a duration of 250 days and having one point per day, corresponding to one representative ground-based optical observing season between 115-day yearly sun gaps.

In lieu of testing potential QPOs at all frequencies between $1/(250 \text{ days})$ and the Nyquist frequency of $1/(2 \text{ days})$, we choose three representative test frequencies f_L : 2.0, 8.0, and 32.0×10^{-7} Hz, corresponding to timescales of 57.9, 14.5, and 3.6 days, and spanning 4.3, 17.2, and 69.0 cycles, respectively; we refer to them low-, medium- and high-frequency (LF, MF, and HF) QPOs (not

to be confused with the LF and HF QPOs routinely identified in the X-ray PSDs of BHXBs near typically 0.1 – 30 Hz and 40–450 Hz, respectively).

Finally, we exclude the effect of Poisson noise, which is the measurement uncertainty associated with photon counting. This noise term corresponds to a constant level of power in the power spectrum and impacts all frequencies. Poisson noise impacts only the high-frequency range in the presence of red noise and the exact range depends on the slope of red noise and the level of power from Poisson noise. Since this power is an additional source of continuum noise, it would lower the true-positive detection likelihood for a given value of P_{rat} , which is defined with respect to the level of red noise at that frequency. Hence, in this regard, our results can be interpreted as a "best case" scenario for true-positive detections. Since each observation has varying Poisson noise levels, red noise PSD shape, etc., it is impossible to test all these scenarios in this work. However, we *strongly* encourage readers to conduct their simulations, taking into consideration the true PSD continuum shape since it is affected by the power due to Poisson noise.

We only test a small number of "representative" sampling patterns. Hence we leave it up to the users to conduct their own Monte Carlo simulations (MCS) based on our work as a guide. For this, consider pure red noise processes (for a range of continuum red noise model shapes, e.g., testing unbroken and broken/bending power-law models as necessary) and mixtures of red noise and QPOs. We also encourage to test your own sampling patterns, candidate QPO frequencies, and signal-to-noise values. Users are particularly suggested to examine appropriate red noise shape ranges (both in power-law continuum slopes and normalizations), QPO test frequencies, and $\log(P_{\text{rat}})$ values.

2.2 ACF for QPO detection

The Cross Correlation Function (CCF) is used to calculate the correlation coefficient of two light curves, which provides a measure of the strength of the correlation as a function of the shift in time. A positive peak indicates that there is a correlation, whereas a negative peak suggests that there is an anti-correlation. When we use the correlation function between the same set of data, it is known as an auto-correlation function. There exists a peak at zero time lag. The successive peaks at different time lags represent the times at which the signal is correlated with itself and this can be interpreted as the period of any underlying periodic/quasi-periodic signal that is present. The ACF for a pure sinusoidal input signal is a simple cosine, where the period is indicated by the first peak and the higher-order harmonics by the successive peaks. However, computing the CCF requires the two light curves to be uniformly sampled. The Discrete Correlation Function approach proposed in Edelson et al. (1988) works well for light curves with uneven sampling. To calculate the unbinned discrete correlation function, we use the following:

$$UDCF_{ij} = \frac{(a_i - \bar{a})(b_j - \bar{b})}{\sigma_a \sigma_b} \quad (2.4)$$

Centroid Frequency f_L (10^{-7} Hz)	τ_1 [d]		τ_2 [d]	
	Mean (μ)	S.D (σ)	Mean (μ)	S.D (σ)
2.0 (LF QPO)	57.84	3.37	116.30	7.83
8.0 (MF QPO)	14.37	0.48	28.93	0.61
32.0 (HF QPO)	3.99	0.045	7.00	0.00

TABLE 2.1: The mean and dispersion of the time values of the fundamental peak (τ_1) and the second peak (τ_2) for pure Lorentzians for 1000 MCS having $Q = 30$ at the three test frequencies for the ACF.

where a_i and b_j are the two data sets for which we want to calculate the correlation, \bar{a} and \bar{b} are the mean values of the respective data set, σ_a and σ_b are their respective standard deviations. To calculate the DCF, the above equation is binned in time for each time lag τ :

$$DCF(\tau) = \frac{1}{M} \sum UDCF_{ij}(\tau) \quad (2.5)$$

where M is the total number of pairs.

A new approach to compute the CCF when the data sets are very sparsely and irregularly sampled is the z -discrete correlation function (ZDCF) (Alexander, 2013). It computes a more precise estimate of the CCF using equal population binning and Fisher's z -transform; the resultant bias is relatively moderate and goes to zero as the number of points increases. We make use of the ZDCF for all our tests and analysis.

For unevenly-sampled data, one may utilise the Interpolated Correlated Function (ICF) and its associated bootstrap error (ICF; White et al. 1994; Peterson et al. 1998). To produce an evenly-sampled light curve, it resamples the data and linearly interpolates between the data points. However, there are risks that the results can be misleading if the interpolation does not accurately mimic the underlying red-noise behaviour, as stated by White et al. (1994). We stick with the ZDCF as we test a wide range of red-noise power-law slopes, including slopes as steep as $\beta = 3$.

2.2.1 The behaviour of the ACF for pure Lorentzian processes

In the "ideal" scenario of strictly periodic sinusoidal oscillations without the inclusion of any red noise variability, the ACF is a cosine, with correlation coefficient $r_{\text{corr}} = 1$, at time lags perfectly corresponding to the period and successive harmonics of the strictly periodic signal. Lorentzian profiles exhibit quasi-regularly spaced peaks near the predicted time lags for successive corresponding harmonics, even for reasonably high values of quality factor ($Q \gtrsim 3$). To measure this dispersion of time values corresponding to the peak τ and r_{corr} , we simulate 1000 light curves (enough to explore the 99.7% confidence limit) for pure Lorentzians with quality factors ranging from 1 to 120. We refer the first peak (period of the signal) after the zero lag as the maximum value of the ACF between the first negative-to-positive crossing and the second peak (second harmonic of the signal) as the maximum value of ACF between the second positive-to-negative crossing. We calculate the 99.9% confidence interval for the parameters τ_1 , τ_2 , $r_{\text{corr}1}$ and $r_{\text{corr}2}$, where 1 and 2 denote the fundamental peak and second peak (second harmonic) respectively. The dispersion

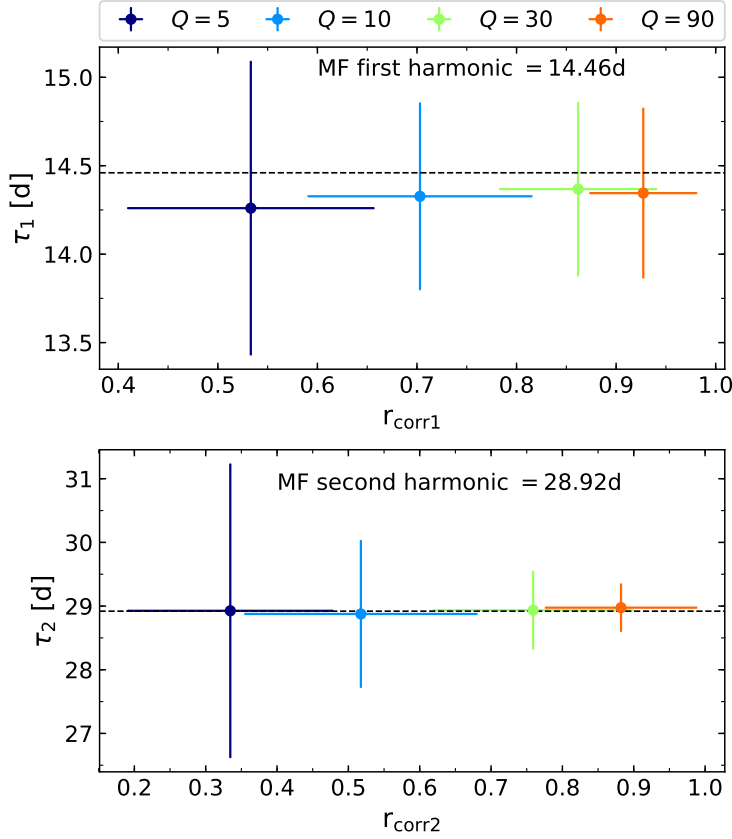


FIGURE 2.1: The mean and dispersion of the times of the fundamental peak (τ_1) & the second peak (τ_2) plotted against their corresponding correlation coefficient values for the MF Lorentzian signal obtained for 1000 MCS for few selected Lorentzian widths for the ACF.

in τ_1 stays almost constant for Q values greater than ~ 20 , as seen in Fig. 2.1. Therefore, we use a large value of $Q = 30$ for all of the tests in our analysis. Table 2.1 shows the dispersions of τ_1 and τ_2 for the LF, MF, and HF QPOs. We can observe that for the LF, MF, and HF cases, the 99.9% limits in τ_1 & τ_2 are within ± 20 , ± 10 , and ± 4 per cent of the input value of Lorentzian frequency (f_L) respectively. These 99.9 per cent confidence contours are used as the limits within to search for the first and second harmonics in our ACF-based search for QPOs mixed with broadband red noise at every different test frequency. We observe that the 99.9 per cent limits of r_{corr1} in the LF case span from 0.1 to 1.0, but they are more confined to values > 0.45 in the MF and HF cases. The limits of r_{corr2} in the LF and MF cases vary from 0.1 to 1.0, whereas they are constrained to values greater than 0.4 in the HF case.

2.2.2 The behaviour of the ACF for pure red noise power-law processes

Unbroken power law model

We construct pure red noise light curves assuming an unbroken power-law PSD model over a broad range of slopes β (0.4–3.0), generated in increments of $\Delta\beta=0.2$ with 1000 realizations at each step.

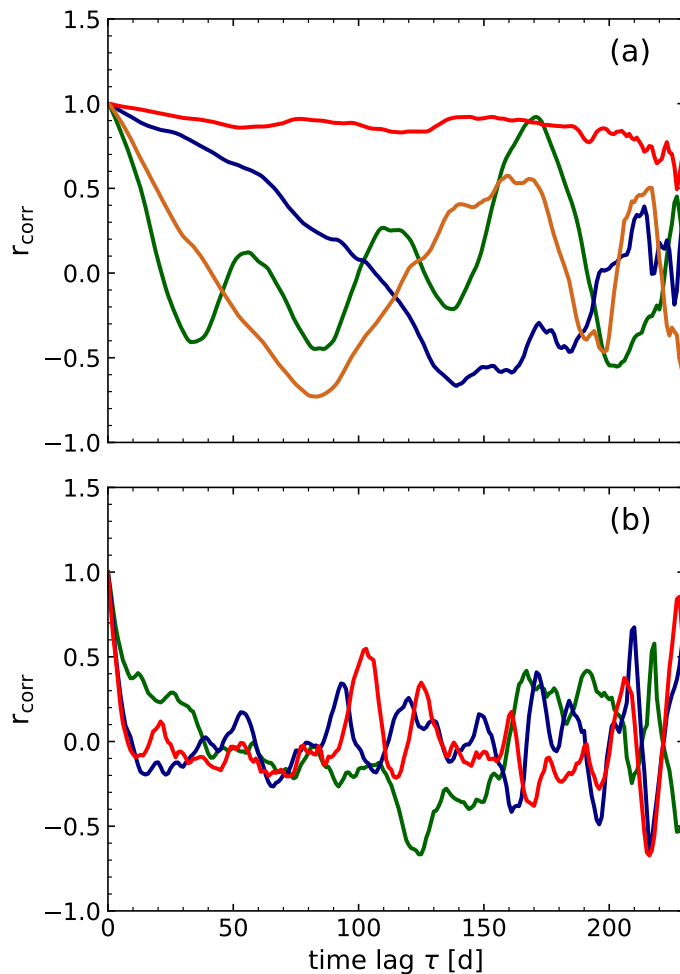


FIGURE 2.2: The ACFs of pure red-noise light curves generated with (a) an underlying unbroken power-law PSD that has a power-law slope of $\beta = 2.2$, and with different random number seeds. Such a pure random stochastic red noise process causes broad bumps and wiggles in the ACFs. For example, consider the green line: the first peak occurs at a time lag of ~ 55 days, with successive peaks near 110 and 165 days. Such a signature is similar to that expected from a quasi-periodic signal. It thus can possibly be misinterpreted as a period, (b) for an input PSD with a broken power-law model, with slope $\beta = 2$ above a temporal frequency of 5.62×10^{-7} Hz breaking to $\gamma = 1$ below it. Again, broad bumps and wiggles are common.

The ACFs of a few selected light curves produced using the same unbroken power-law model of $\beta = 2.2$, but with different random number seeds are shown in Fig. 2.2 (a). In certain ACFs, we notice spurious broad bumps and wiggles, and some of the peaks after the zero lag can attain high r_{corr} values like 0.8 or 0.98. For one specific realization, represented by the green curve in Fig. 2.2 (a), the ACF consists of three broad bumps, in that the second peak and third peak belong to time lags approximately 2 and 3 times the delay of the first peak. A purely stochastic process produced this signature, yet it is close to the one expected for a quasi-periodic signal.

As a preliminary exploration of false positives and the timescales over which they can occur, we adopt the following criteria for false positives: only the ACF that crosses zero level at $r_{\text{corr}} = 0.0$ and rises up to a non-zero value will register a positive detection at the time lag (τ_1) with a maximum value of correlation coefficient ($r_{\text{corr}1}$). In this way, we have the false positives determined

as a function of time lag. Again, to register a second peak, the r_{corr} must decrease from the maximum value corresponding to r_{corr1} , pass through the zero, and then increase once again to peak at a non-zero value. This second positive peak is registered at the corresponding time lag τ_2 at the second maximum correlation coefficient r_{corr2} after the zero lag. For illustration, in Fig. 2.2 (a), the green lines will register false positive detection at time lags corresponding to three peaks, whereas the orange and blue lines will exhibit false positives at time delays corresponding to the first and second peak after crossing zero. However, the ACF in red does not pass through zero and will never register a false positive at any time lag. In the presence of red noise, the ACF and PDM points are highly self-correlated, and estimating the effective number of independent timescales becomes more complex (in contrast to an evenly-sampled periodogram). As a result, we stress that our false-alarm rate tests aim to determine whether or not a pure red noise process can produce *at least one* false signal *at any frequency*. This implies that our computed false-alarm probabilities are conservative, and the likelihood of one signal at one given frequency being real is even lower.

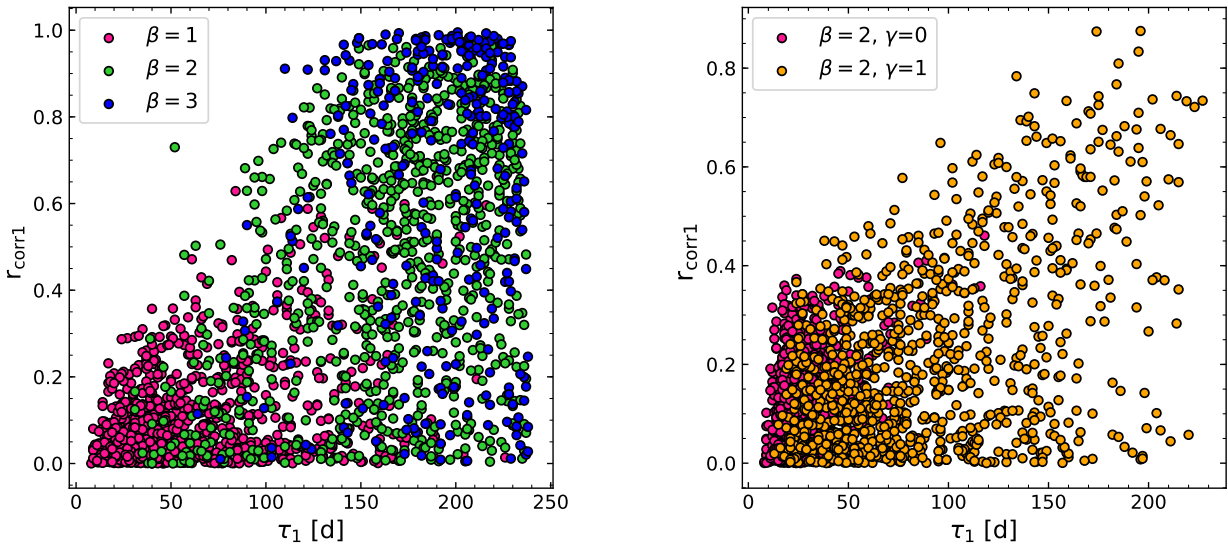


FIGURE 2.3: The distribution of the time scales of the first peak after the zero lag against the corresponding correlation coefficient of false positives detected in ACF for 1000 simulations of pure red noise signals of (left) unbroken PL PSD model for few selected spectral index slopes (right) broken PL PSD model for $\beta = 2.0$ breaking to few selected low frequency slope (γ) below a temporal break frequency of 5.6×10^{-7} Hz.

We illustrate the distribution of false-positive peaks as a function of timescale τ for four chosen values of β in Fig. 2.3. We notice that the 99.9 per cent confidence distributions of the correlation coefficients r_{corr1} & r_{corr2} of the first and second peaks become broader as the slope increases. For example, they have $r_{\text{corr1,2}} < 0.45$ for $\beta \lesssim 0.8, 0.6$ and as the slope increases, it can range anywhere from 0 to as high as 0.9 or greater for $\beta \gtrsim 1.6$. This figure can be used to provide an estimate of the region of $(\tau_1, r_{\text{corr1}})$ space where a false-positive peak is statistically likely or unlikely to occur. For a candidate peak that occurs at τ_1 , say, roughly $83 \text{ d} = 1/3$ of the duration, if $\beta = 1.0$ (2.0), there would there be a high probability (>99.7 per cent) that the signal is genuine only if r_{corr1} is more

than about 0.7 (0.8). For $\tau_1 = 125\text{d}$, 1/2 of the duration, the minimum values of r_{corr1} required to confidently claim a real signal increase to ~ 0.85 for $\beta = 2.0$.

Note that the majority of the false positive peaks (τ_1) for slopes 2.0 and steeper (green and blue points) in Fig. 2.3 occur at timescales longer than the approximately 1/3 duration of the light curve: for $\beta = 1.0, 2.0$, and 3.0 , the fractions of false peaks located at timescales of $> 1/3$ duration are $261/1000 = 26.1$ per cent, $790/857 = 92.2$ per cent, and $316/319 = 99.1$ per cent, respectively. Hence, a straightforward and efficient method to minimize the total number of false-positive detections for very steep red-noise slopes is to exclude any peaks occurring at timescales longer than approximately 1/3 duration. At timescales less than $\sim 1/3$ of the duration, false-positive signals can also be minimized by excluding signals with r_{corr1} and r_{corr2} values that are less than ~ 0.55 and 0.45 , respectively.

We also try to look for peaks without the zero crossings, i.e. the ACF which crosses any non-zero level say at $r_{\text{corr}} = 0.2/0.3/0.4$ and rises up to a maximum value (i.e., $r_{\text{corr1}} > 0.2/0.3/0.4$ respectively) is registered as a positive detection at the corresponding time lag (τ_1). We find that the red noise light curves produce a significantly high percentage of false positives even with a non-zero crossing level. For instance, it exhibits false positives of more than 99.7 per cent (99 per cent) at $\beta \gtrsim 1.2$ (1.0) for the crossing level of $r_{\text{corr}} = 0.2$ (0.3).

Broken power-law model

We construct red noise light curves considering broken power-law models for 1000 realizations. We examine only limited values of high-frequency spectral index slopes β (1.0,2.0,3.0) breaking to lower spectral index slopes γ (0.0,1.0,2.0) below a temporal mid-frequency 5.6×10^{-7} Hz.

In Fig. 2.2 (b), we plot the ACFs of a few selected light curves for a high-frequency slope of $\beta = 2.0$, breaking to low-frequency slope of $\gamma = 1.0$. Similar to the unbroken PL model, we see various bumps and wiggles in the ACF of the broken PL model as well. We present the ACFs of a few chosen light curves with a high-frequency slope of $\beta = 2.0$ breaking to a low-frequency slope of $\gamma = 1.0$, in Fig. 2.2 (b). ACF of the broken PL model exhibits several bumps and wiggles, the same as that of the unbroken PL model. The 99.9 per cent confidence distributions of r_{corr1} become wider with increasing slopes of β and γ independently: for $\beta = 1.0, 2.0$ breaking to $\gamma = 0.0$, has the upper confidence limit of r_{corr1} to be 0.35 and 0.45 respectively. When $\beta = 3.0$, breaking to $\gamma = 1.0, 2.0$, it has the r_{corr} range from 0 to 0.98.

In Fig. 2.3, we plot the distribution of false positives of the first peak after zero lag for the case of $\beta = 2.0$ breaking to $\gamma = 0.0$ and $\gamma = 1.0$. We see that for the case of $\beta = 2.0$ breaking to a flatter spectrum, the majority fraction (99.2 per cent) of the candidate peaks (τ_1) at timescales < 83 d (1/3 duration) and with $r_{\text{corr1}} < 0.4$, while for breaking to a much steeper spectral slope of $\gamma = 1.0$, while it still has the many of the candidate peaks (55.9 per cent) below 1/3 duration, it can still have false positives at longer timescales with high correlation coefficient values of $r_{\text{corr1}} \gtrsim 0.8$. Hence, we conclude that excluding peaks at timescales longer than roughly 1/3 duration of the light curve greatly reduces the false-positive detections for broken-power law PSD models.

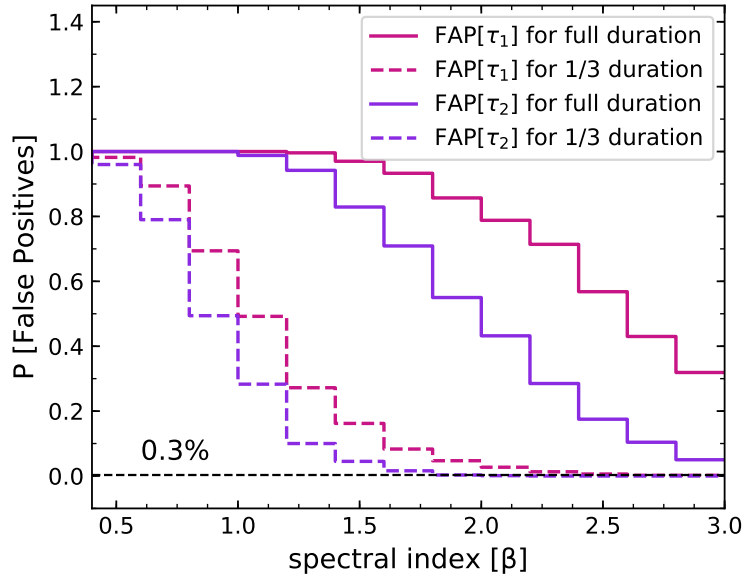


FIGURE 2.4: The rate of false positives detected in pure red noise light curves having unbroken power-law PSD model at different spectral index slopes for the first & second peaks in the ACF while considering the full duration and then while considering just one-third of the total duration.

False Alarm Probabilities

In all our discussions regarding the errors, the null hypothesis, H_0 , is considered to be pure red noise variability, while the alternative hypothesis, H_1 , is a mixture of a QPO and red noise.

Type I Error (false positive): Continuing on the above discussion, we determine how often H_1 is mistakenly inferred true when H_0 is inherently true in the ACF of 1000 MCS of pure red noise light curves. For this, we implement the selection criteria for false positive detections as mentioned in Section 2.2.2. We estimate the probability of false positives of the first and second peaks in the ACF across the time lag independently.

For the unbroken-PL model in Fig. 2.4: On considering the total duration of the light curve, we find that false positives of the first and second peak are detected with $\gtrsim 0.3$ per cent probability for all tested values of the pure red noise slope using the unbroken-PL model. In the case of $\beta \lesssim 1.4$, for instance, a large fraction of the simulated light curves, nearly 99.6 per cent, produce at least one false positive signal. Additionally, we observe that at relatively steeper slopes of $\beta \gtrsim 2.0$, the fractions of the ACF crossing zero and producing a peak become much lower. The ACFs of the steepest slope red noise light curves are relatively wide and usually never cross zero to register a false positive based on our selection criteria. As a result, the probability of identifying a second peak after the zero lag is significantly lower towards the steeper spectral index slopes.

We find that on limiting ourselves to timescales shorter than one-third of the length, the rate of false positives of the first and second peak after the zero lag in the ACFs of the unbroken-PL model is $\gtrsim 0.3$ per cent only at $\beta \gtrsim 2.6, 1.8$ respectively. In addition, we also observe that fewer than 0.3%

of the simulations at all spectral index slopes exhibit correlation values corresponding to τ_1 and τ_2 more than 0.45–0.5.

We tested the following cases for the broken-PL PSD model : (i) $\beta = 3.0$ breaking to three values of $\gamma = 0.0, 1.0, 2.0$; (ii) $\beta = 2.0$ breaking to two values of $\gamma = 0.0, 1.0$ and (iii) $\beta = 1.0$ breaking to $\gamma = 0.0$, below a temporal mid-frequency of 5.6×10^{-7} Hz. The probability of false positives considering the full duration of the light curve in the ACF for the first and second peaks is $> 0.3\%$ for all three scenarios. More than 99.7% of the time, it is possible to get at least one peak at some time lag for the particular cases of $\beta = 1.0, 2.0$, and 3.0 , breaking to $\gamma = 0.0$ and 1.0 . When we limit the timescales to one-third duration in the ACF, the false positives of the first and second peaks remain > 0.3 per cent. However, the associated correlation values are now constrained for all three cases to $r_{\text{corr}1,2} < 0.55$. We observe that specifically for the $\beta = 1.0$ breaking to $\gamma = 0.0$ case, despite taking only one-third of the duration, the probability of false detection for 1000 simulations approaches > 99.7 per cent. At the same time, the correlation coefficient attains a maximum value of $r_{\text{corr}1} < 0.35$.

Therefore, based on the results obtained from the aforementioned tests, we draw the conclusion that one can prevent false-positive detection and achieve substantially low ($< 0.3\%$) false-positive rates for the period of the signal across all spectral index slopes by avoiding searching for ACF peaks at lags shorter than one-third of the lightcurve duration and considering the first peak after the zero lag to have the correlation coefficient greater than 0.45–0.5.

2.2.3 ACFs for QPOs mixed with red noise

We carry out MCS for the sum of a $Q = 30$ Lorentzian and an unbroken power-law red noise continuum, with slopes spanning 0.4–3.0 in steps of $\Delta\beta = 0.2$, and power ratios $\log(P_{\text{rat}})$ ranging from -1 to $+5$ in steps of $\Delta\log(P_{\text{rat}}) = 1$ for $N = 1000$ light curves at each step.

True-positive detections: The criteria for true-positive detections are as follows: we register true-positive detections for the first or second harmonics of the QPO independently only when they fall within their respective anticipated time lag ranges as determined from the "ideal" case of a $Q = 30$ Lorentzian (no red noise) and use just one-third of the ACF when looking for peaks. We also need to verify the 99.7 per cent significance level to claim a genuine detection and rule out the idea that the peaks are caused by the red noise continuum having a broken power-law model form. For this, the corresponding correlation coefficient of the first peak should satisfy $r_{\text{corr}1} > 0.45$.

We remark that we do not conduct tests for the LF QPO signal mixed with red noise since the distribution of $r_{\text{corr}1}$ spans from 0.1–1 even for true Lorentzian. It is quite low, and we cannot restrict it along the correlation coefficient values to statistically eliminate the possibility of true positive detection from false positives (such as the red noise with the broken power law model).

The detection rate of true positives for both the first and second harmonics varies with power-law slope β and $\log(P_{\text{rat}})$. The detection rate decreases as $\log(P_{\text{rat}})$ decreases and/or as the power-law slope β increases. This behaviour is consistent across both the MF and HF QPOs, as presented

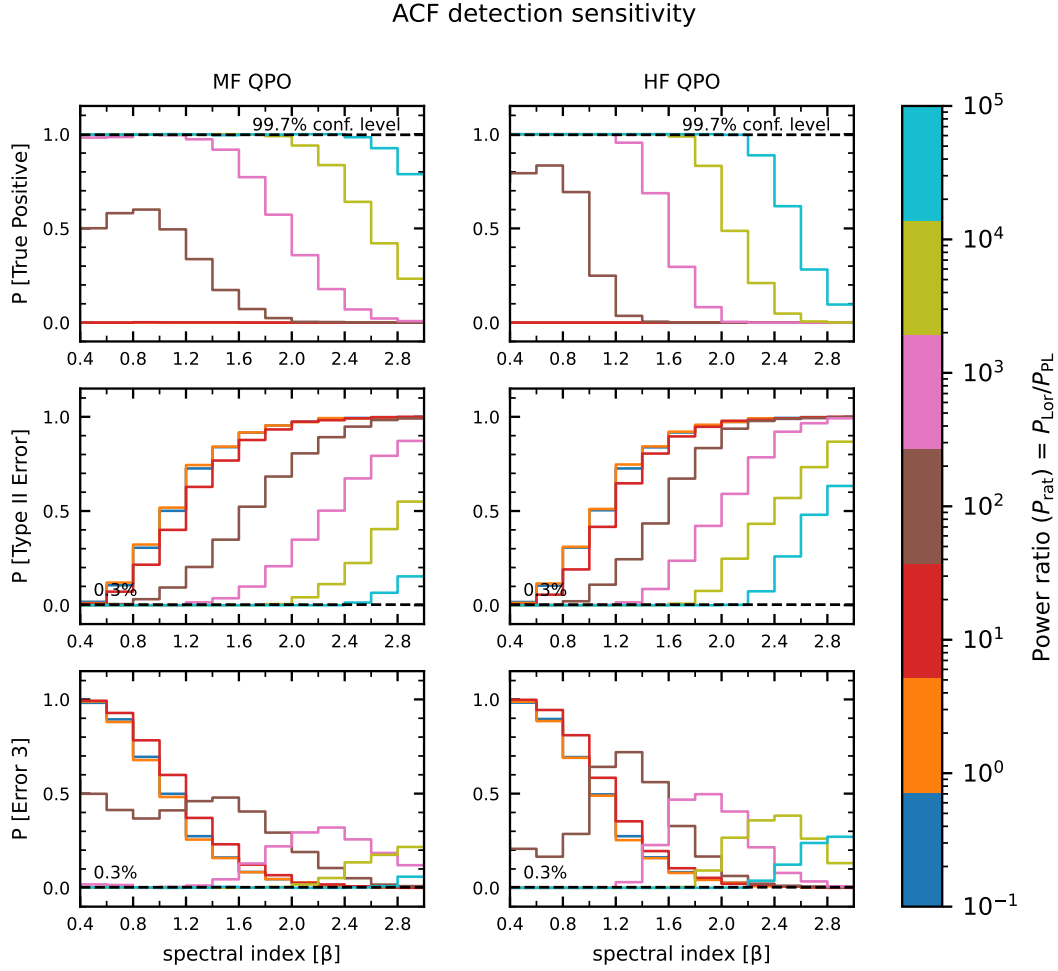


FIGURE 2.5: Top panel: The probability of detecting the first harmonics of the periodic signal in the expected frequency range, Middle panel: The probability of detecting the first harmonics of the quasi-periodic signal in the wrong frequency range, Bottom panel: The probability of detecting false negative of the first harmonics of the quasi-periodic signal all as a function of power ratio $\log(P_{\text{rat}})$ and red noise PSD power-law slope β for the MF & HF QPO mixed with broadband red noise signals on using the ACF.

in Fig. 2.5. One typically requires a very high power ratio to ensure a 99.7% or higher reliability for QPO detection. To register true positives of τ_1 with a 99.7% significance having $r_{\text{corr1}} > 0.45$: in the MF case, $\log(P_{\text{rat}})$ must be 5, or 4 for values of $\beta \lesssim 2.4$, or ~ 1.8 respectively. In the HF case, $\log(P_{\text{rat}})$ must be 5, 4, or 3 for values of $\beta \lesssim 2.2$, ~ 1.6 , or ~ 1.2 respectively. To register true positives of τ_2 having $r_{\text{corr2}} > 0$: for MF case, $\log(P_{\text{rat}})$ must be 5, or 4 for values of $\beta \lesssim 2.4$, or ~ 1.6 respectively (where r_{corr2} is always greater than 0.2). In the HF case, $\log(P_{\text{rat}})$ must be 5, 4, or 3 for values of $\beta \lesssim 2.0$, ~ 1.6 , or ~ 1.0 respectively (where r_{corr2} is always greater than 0.4).

False negatives and detection inaccuracy errors

Type II Error (false negative): H1 is incorrectly inferred to be false in the presence of a QPO.

We determine the number of times the first and second harmonics are never triggered positive (at *any* timescale) in the ACF of the light curves determined independently across the time lag on

using the true-positive detection criteria.

In a light curve consisting of a QPO mixed with red noise, we account for false negatives of the first and second peaks. To calculate the false negatives of the first peak (period), we determine the number of times not even a single peak is detected after the zero lag in the ACF (i.e., it never passes through $r_{\text{corr}} = 0$ and increases). To calculate the false negatives of the second peak, we compute the number of times the ACF never crosses $r_{\text{corr}} = 0$ and rises above it after the first peak at τ_1 of 1000 simulations calculated independently of the timescale of the first lag. For illustration, in Fig. 2.6, we plot two selected ACFs for light curves corresponding to power spectra with MF QPO signal of $\log(P_{\text{rat}}) = 2$ against the red noise continuum having $\beta = 1.8$. Mild features of quasi-periodicity are evident in the ACFs. The ACF shown in red in Fig. 2.6 has no peaks after crossing $r_{\text{corr}} = 0$. It does not satisfy our positive detection criteria and would thus lead to a false negative.

Particularly for the steepest power-law slopes — $\beta > 2$ — the probability of obtaining a false negative is quite high for all but the largest values of P_{rat} . Even for such large values of $\log(P_{\text{rat}})$ and large values of β , the dominating red noise causes the ACF central peak to simply not reach zero and completely overwhelms the cosine-like behavior from the QPO.

For the MF QPO case, negligible false negative probabilities (< 0.3 per cent) for the first and second harmonic are obtained only for values of $\log(P_{\text{rat}}) \sim 2, 3, 4$, and 5 at $\beta \lesssim 0.6, 1.2, 1.8$, and 2.4 , respectively. By the time one reaches $\log(P_{\text{rat}}) \sim 1$, a significant percentage (~ 99.7 per cent) of simulations yield false negatives for the first (second) harmonic at $\beta \gtrsim 2.8$ (2.4). For the HF case, it is a similar story: negligible false negative probabilities for the first and second harmonic are obtained only for values of $\log(P_{\text{rat}}) \sim 2, 3, 4$, and 5 at $\beta \lesssim 0.8, 1.2, 1.6$, and 2.2 , respectively. False negative probabilities for the MF and HF cases are plotted in Fig. 2.5.

Detection inaccuracy error (Error 3): H1 is intrinsically true and registered as true, but the QPO does not satisfy the true positive detection criteria.

We define the detection inaccuracy error as the occurrence of either of the two conditions when a light curve having a QPO mixed with red noise yields a positive detection in the ACF, but: (i) the first (second) harmonic is not in the range of time lags as obtained from the "ideal" situation of a $Q = 30$ Lorentzian (no red noise) obtained from the analysis described in Section 2.2.1 or (ii) the first harmonic within the expected time lag has the corresponding correlation coefficient $r_{\text{corr}1} < 0.45$. For instance, in Fig. 2.6, the ACF in blue represents a light curve with an MF QPO signal of $\log(P_{\text{rat}}) = 2$ against the red noise continuum with $\beta = 1.8$. It features the first peak outside the frequency range expected for the MF QPO and, therefore will be registered as Error 3.

The chance of identifying a QPO at the wrong timescale increases with a decrease in P_{rat} . However, as the power-law slope β increases, the likelihood of correctly identifying a QPO at *any* timescale (within the correct range or outside of it) diminishes (particularly for $\log(P_{\text{rat}}) \lesssim 3$). Hence, the probability of detecting a QPO at the wrong timescale reduces.

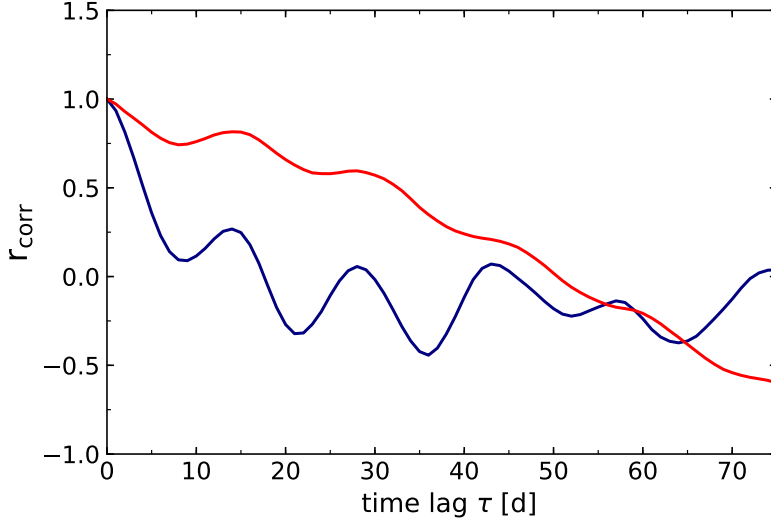


FIGURE 2.6: Two selected ACFs for light curves corresponding to power spectra of MF QPO signal of $\log(P_{\text{rat}}) = 2$ against the red noise continuum having $\beta = 1.8$. Mild features of quasi-periodicity are evident in the ACFs, but these ACF peaks do not satisfy our true positive detection criteria and would thus lead to false negatives (red) and detection inaccuracy errors (blue).

In general, we observe that the chances of detecting the QPO (first peak) at the wrong timescale is extremely low ($\lesssim 0.3\%$) only for $\log(P_{\text{rat}}) \gtrsim 4-5$ and only when avoiding the steepest values of spectral index slope β . When $\log(P_{\text{rat}}) \sim 5$, detection inaccuracy probabilities are $< \sim 0.3$ per cent for nearly all values of β tested: the probabilities exceed ~ 0.3 per cent only for $\beta \sim 3.0$, and $\gtrsim 2.4$ (MF, and HF, respectively). However, when $\log(P_{\text{rat}}) \sim 4$, detection inaccuracy probabilities are $< \sim 0.3$ per cent only when β is $\lesssim 1.8$, and 1.6 (MF, and HF, respectively). When $\log(P_{\text{rat}}) \sim 3$, detection inaccuracy probabilities are $< \sim 0.3$ per cent only when β is $\lesssim 1.2$ for the HF case.

In Fig. 2.5 we present the probabilities of obtaining a detection inaccuracy error for the MF and HF cases.

2.3 PDM for QPO detection

The Phase Dispersion Minimization (PDM) method is a commonly used numerical technique for detecting periodic pulsations in the fluxes of different astronomical objects (Stellingwerf, 1978). The method is suitable particularly for non-sinusoidal waveforms. Consider a time series consisting of N observational points denoted as (x_i, t_i) , where x_i represents the flux or count rate at time t_i . The variance of the flux is

$$\sigma^2 = \frac{\sum (x_i - \bar{x})^2}{N - 1}, (i = 1, \dots, N) \quad (2.6)$$

where \bar{x} denotes the mean of the fluxes. The light curve is segmented into a series of M phase bins based on the trial period ϕ , with each phase bin containing n_j data points identical in phase. The variance of amplitude in each bin is computed using the formula

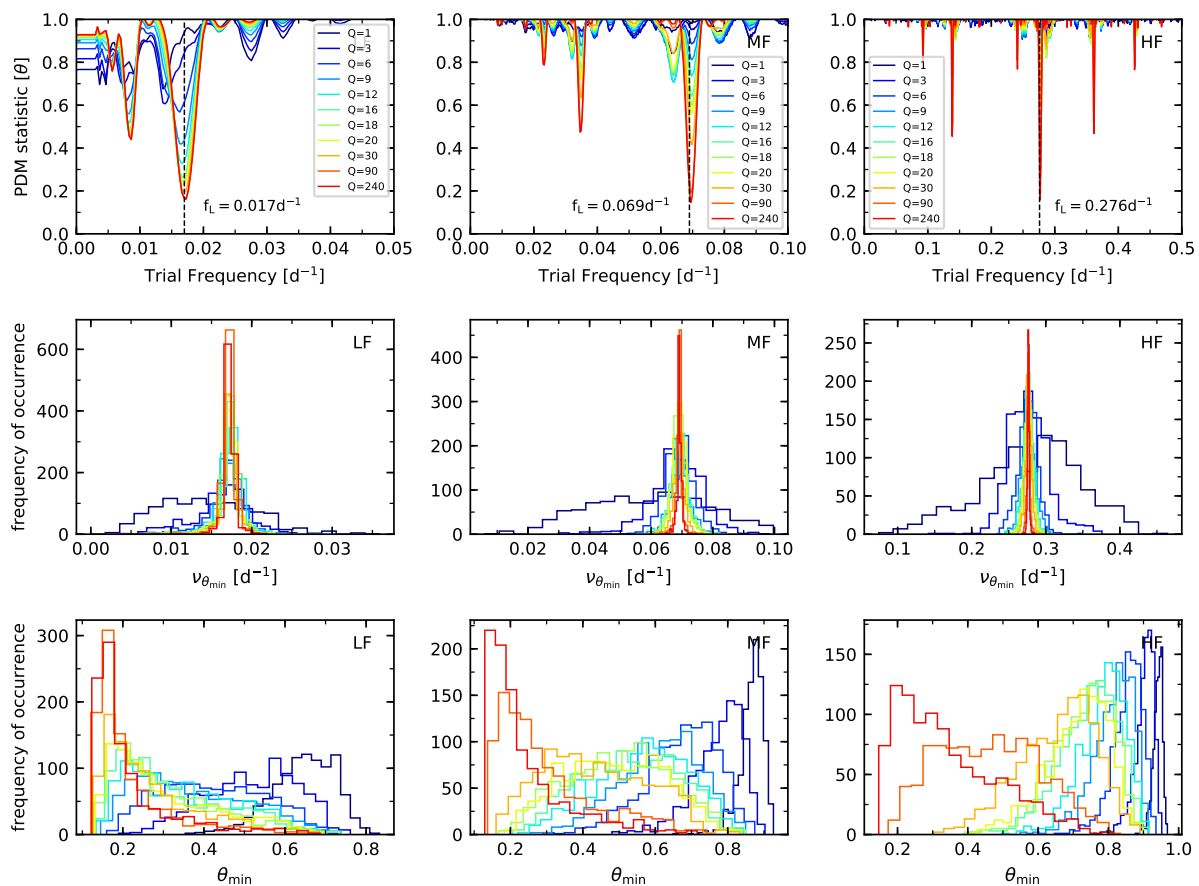


FIGURE 2.7: Top panel: The PDM periodogram showing the characteristic dip at the expected frequency for one realization for different widths of Lorentzian profile at the three test frequencies, Middle panel: The histogram of the frequency $\nu_{\theta_{\min}}$ $[\text{d}^{-1}]$ corresponding to the minimum statistic value θ_{\min} , Bottom panel: The histogram of minimum statistic value θ_{\min} for different widths of Lorentzian profile at the three test frequencies for 1000 MCS when using the PDM.

$$s_j^2 = \frac{\sum (x_{kj} - \bar{x}_j)^2}{n_j - 1}, (j = 1, \dots, M) \quad (2.7)$$

where x_{kj} is the k th data point of the j th phase bin. The overall variance for all the phase bins is computed by

$$s^2 = \frac{\sum (n_j - 1) s_j^2}{\sum n_j - M}, (j = 1, \dots, M) \quad (2.8)$$

The periodogram statistic θ is the ratio of the sample variance and the light curve's overall variance. This ratio is given by $\theta = s^2 / \sigma^2$. It provides the measure of the scatter of sample variance about the mean of the light curve. The scatter of sample variance about the mean will be minimum for a genuine period. Hence we can expect θ to approach zero at that frequency. However, there will be a substantial scatter of the sample variance about the mean for frequencies that do not correspond to a real period where $s^2 \approx \sigma^2$ and the test statistic θ approaches 1. One can plot the test

	upper limit on θ_{\min} (99.9%)	Range of $\nu_{\theta_{\min}}$ [d^{-1}] (99.9%)
LF QPO	0.684	0.0096–0.0216
MF QPO	0.805	0.0608–0.0754
HF QPO	0.883	0.262–0.293

TABLE 2.2: The 99.9 per cent contour limits of θ_{\min} and trial frequency $\nu_{\theta_{\min}}$ for the Lorentzians at the three test frequencies.

statistic θ at each trial frequency and determine the local minimum value θ_{\min} , which indicates the frequency corresponding to the least scatter about the mean light curve. It was demonstrated that the test statistic θ actually follows a beta distribution (Schwarzenberg-Czerny 1997) from which the significance of any detected pulsation can be obtained.

However, the astronomical applications have mainly been restricted to cases when the underlying noise is Poisson (i.e., white noise). The performance of the PDM has not yet been empirically tested for situations with stochastic red noise backgrounds. Hence, it is not clear that simply identifying the local minimum value θ_{\min} automatically indicates that a strictly/quasi-periodic signal exists at that frequency.

2.3.1 PDM test for Lorentzian profile:

We start with the "ideal" scenario of QPOs, described by simple Lorentzians centred at each of our three test frequencies and spans a range of quality factor Q values.

We generated 1000 light curves for each value of Q using our "baseline" sampling pattern, measured their PDMs, and plotted the test statistic θ calculated at each trial period versus frequency; sample PDMs for the LF, MF, and HF are represented in Fig. 2.7. Each exhibits a characteristic dip (θ_{\min}) at the expected frequency ($\nu_{\theta_{\min}}$), in addition to harmonics. Also, the considerably higher values of Q result in narrower dips and lower values of θ_{\min} .

The standard deviation of $\nu_{\theta_{\min}}$ decrease with an increase in Q values. To get θ_{\min} values below ~ 0.3 , for the LF and MF cases, extremely coherent signals with values of Q in the range of 10–20 are typically required. On the other hand, for the HF case, values of Q that are closer to 90 are required.

Henceforth, we consider Lorentzians with $Q = 30$ for all our tests. We determine the 99.9 per cent confidence regions from the MCS representing the distributions of θ_{\min} (upper limits) and $\nu_{\theta_{\min}}$, and this enables us to delineate the region of frequency— θ space where the "ideal" signal occurs. Table 2.2 lists this upper bounds/ranges.

We will later use these confidence ranges as the limits within which to search for signatures of QPOs when we consider mixtures of a QPO and red noise while using the PDM.

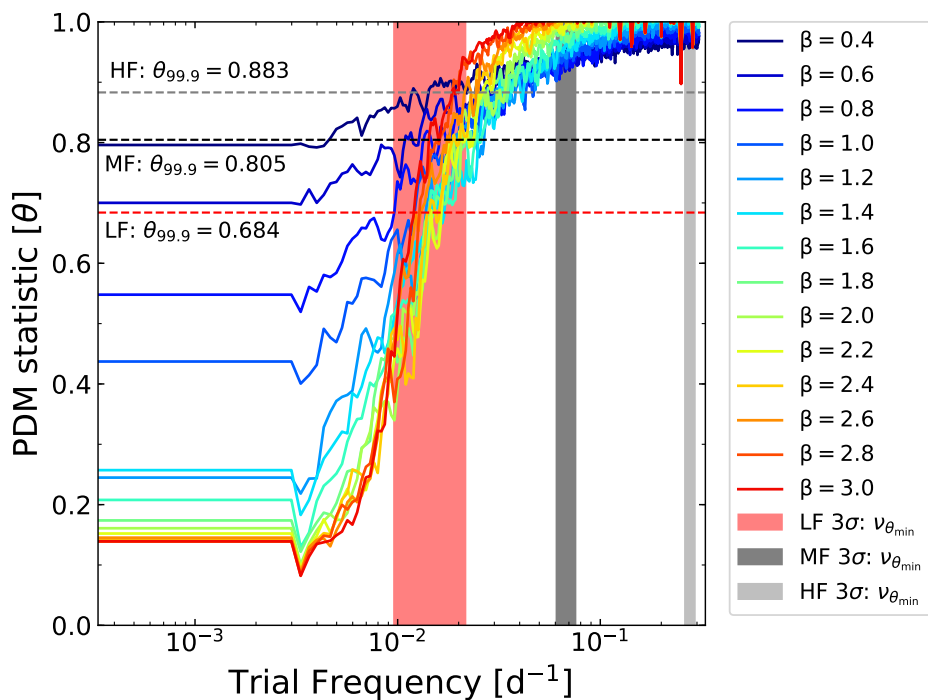


FIGURE 2.8: The overplot of the 99.9 per cent lower limit of the PDM statistic value θ at each test frequency that can be caused due to pure red noise light curves having evenly sampled data for broadband spectral index slopes against the 99.9 per cent contour limits of $\nu_{\theta_{\min}}$ and the upper limit on the θ_{\min} determined for pure Lorentzian signals at the three test frequencies for 1000 MCS within which we expect the characteristic dip to occur for QPOs mixed with red noise.

2.3.2 The behavior of the PDM for pure red noise processes

Unbroken and broken power-law models

We once again create pure red noise light curves for various slopes β (0.4—3.0) in steps of $\Delta\beta=0.2$ for an unbroken power-law PSD model, simulating 1000 light curves at each step, and measuring their PDMs.

We determine the periodogram statistic θ for each light curve over all possible test frequencies. The obtained 99.9 per cent confidence lower bounds on θ at each trial frequency is shown in Fig. 2.8 for the various spectral index slopes. The value of θ is typically greater than 0.9 for all power-law slopes across a wide frequency range, and it is greater than 0.8 even down to ~ 0.02 d^{-1} (i.e., the scatter variance is usually significant above this frequency). However, in the lowest frequency bins (those corresponding to timescales longer than $\sim 1/3$ of the length), θ plunges to 0.6 or lower, with relatively steeper PSD slopes approaching values of θ much below 0.2, and these local minimums resulting from pure red noise may be mistaken for quasi-periodic signals. In fact, we see that the population of pure red noise-only trials that may attain $\theta_{\min} < 0.6$ is greater than 99.7 per cent at $\beta \geq 2.6$ and it is less than 0.3 per cent at $\beta \leq 0.8$. However, if we exclude frequencies from the lowest bin (at about $1/3$ of the duration), we find that the percentage of trials with pure red noise that achieve a $\theta_{\min} < 0.6$ is less than 0.3 per cent almost across all the beta values we tested.

We repeat the test for pure red noise light curves considering broken power-law models for 1000 realizations. We analyze it for just a few selected values of high-frequency spectral index slopes β (1.0, 2.0, and 3.0) that breaks below a temporal mid-frequency of 5.6×10^{-7} Hz to lower spectral index slopes of γ (0.0, 1.0, 2.0). We see that near the lower frequency bins, θ minimizes to values < 0.6 , similar to the unbroken power-law models. The fractions of red noise light curves that could reach $\theta_{\min} < 0.6$ is less than 1 per cent when any value of β breaks to a flatter slope of $\gamma = 0.0$, but the fractions get higher as β increases (> 40 per cent) on breaking to $\gamma = 1.0$ or 2.0. After excluding the lowest bin frequencies (corresponding to $\sim 1/3$ duration), we see that the fraction of pure red noise-only trials that can obtain a value of $\theta_{\min} < 0.6$ is less than 1 per cent for all the combinations of broken power-law PSD model.

It is very evident that low values of θ in a given PDM do not necessarily indicate the existence of a QPO, since red noise may also produce such low values of θ . In particular, however, one must take into account the frequency regime where the minimum occurs before attempting to decide if a given minimum corresponds to a genuine QPO. For example, in Fig. 2.8, we observe that at timescales $\sim 1/7$ – $1/12$ th of the total duration, the 99.9 per cent lower limit of θ_{\min} due to pure red noise ranges between 0.8–0.88, which is below the 99.9 per cent upper limit of θ_{\min} that can be reached by the HF pure Lorentzian signals but they do not occur within their expected frequency range. In fact, we note that the 99.9 per cent lower limit of θ_{\min} caused due to pure red noise never intersects with the 99.9 per cent search contour limits obtained for the MF & HF pure Lorentzian signals because it is always greater than 0.89 around those frequency bins. On the other hand, the pure red noise light curves (e.g., $\beta < 1.2$) can attain $\theta \lesssim 0.6$ within the 99.9 per cent contour limits of $\nu_{\theta_{\min}}$ expected for a pure LF Lorentzian signals. Hence, we will not be able to statistically distinguish a LF QPO signal mixed with red noise causing the minimized θ value.

False Alarm Probabilities

Type I error (false positive): We quantify the frequency at which H1 is wrongly perceived as true when H0 is intrinsically true. For this, we generate 1000 MCS of pure red noise light curves across a wide range of spectral indices. We calculate the rate at which a pure red noise light curve can minimize the test statistic to low values at ANY frequency, with at least one occurrence per realization, and can be falsely registered as a QPO signal.

To calculate the probability of the false positives, we count the number of times θ_{\min} for a given PDM drops below the 99.9 per cent upper confidence limit of θ_{\min} obtained from the "ideal" (Lorentzian-only) scenario of HF QPO, which has the maximum value of 0.88 for each realization of the red noise light curves, to determine the probability of the false positives. For an unbroken power-law model as shown in Fig. 2.9, we observe that the rate of false positives is > 0.3 per cent across all tested values of β . When we neglect the lower frequency bins corresponding to timescale $> 1/3$ duration, even though the rate of false positive is still > 0.3 per cent at all slopes, we observe a decrease in the rate of false positives, particularly in the higher spectral index slopes. We also observe a small increase in the rate of false positives at spectral index slopes of $0.6 \lesssim \beta \lesssim 1.4$, since the red noise exhibits $0.65 < \theta_{\min} < 0.8$ at frequency bins corresponding to timescales of $\sim 1/3$ – $1/9$ duration around these spectral indices. For all examined combinations

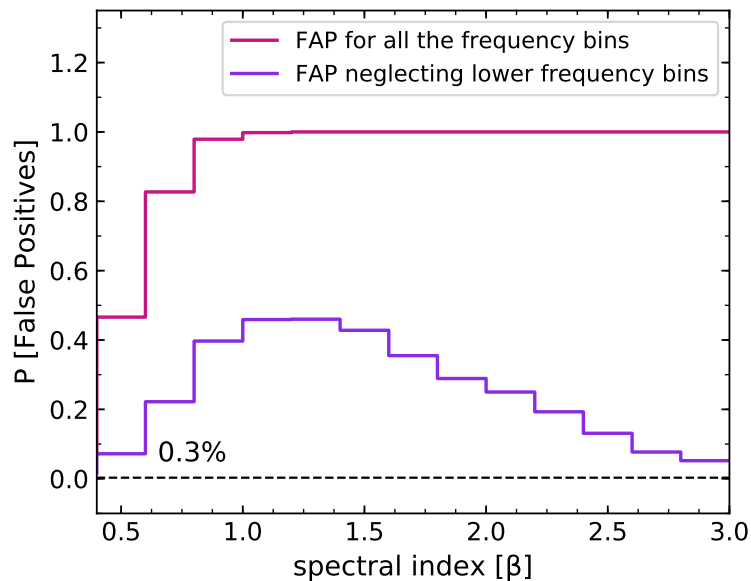


FIGURE 2.9: The rate of false positives detected in pure red noise light curves having unbroken power-law PSD model at different spectral index slopes while using the PDM tested for all the trial frequency bins and then neglecting the lower frequency bins corresponding to timescales $> 1/3$ duration.

of the broken power-law model, that is, $\beta = 1.0, 2.0, 3.0$ breaking to $\gamma = 0.0, 1.0, 2.0$ after the break at the mid-temporal frequency, the rate of false positives come out to be $> 0.3\%$, both before and after omitting the lower frequency bins.

It is essential to note that, after excluding the lower bins, lesser than 0.3 per cent of red noise simulations with unbroken and broken power-law models attain values of $\theta_{\min} \lesssim 0.65$ and 0.5 on using the PDM for all the tested values of slopes, respectively.

2.3.3 The behaviour of PDM for QPOs mixed with red noise

We repeat the MCS procedure for the combination of a $Q = 30$ Lorentzian and an unbroken power-law red noise continuum, with slopes ranging from 0.4 to 3.0 in steps of $\Delta\beta = 0.2$, and power ratios $\log(P_{\text{rat}})$ varying from -1 to $+5$ in steps of $\Delta\log(P_{\text{rat}}) = 1$.

True-positive detections: We record true positive detections when θ_{\min} occurs within the 99.9% confidence interval in θ -frequency space, as determined using the "ideal" (Lorentzian-only) scenarios described above in Section 2.3.1. In Fig. 2.10, for example, we depict the PDM periodogram for a few realizations of light curve containing a MF QPO signal mixed with red noise of $\beta = 2.6$. The green shaded area represents the contour bounds of the "ideal signal" in the θ -frequency space expected for the MF QPO signal, and the black points correspond to the lowest minimum (θ_{\min}) for a given PDM periodogram. Therefore, only the points that fall within this green region will be registered as true positives.

We find that one always needs a large $\log(P_{\text{rat}})$ value, usually > 5 or more, for correctly registering true positives with ~ 99.7 per cent. As illustrated in Fig. 2.11 for the MF QPO, the values

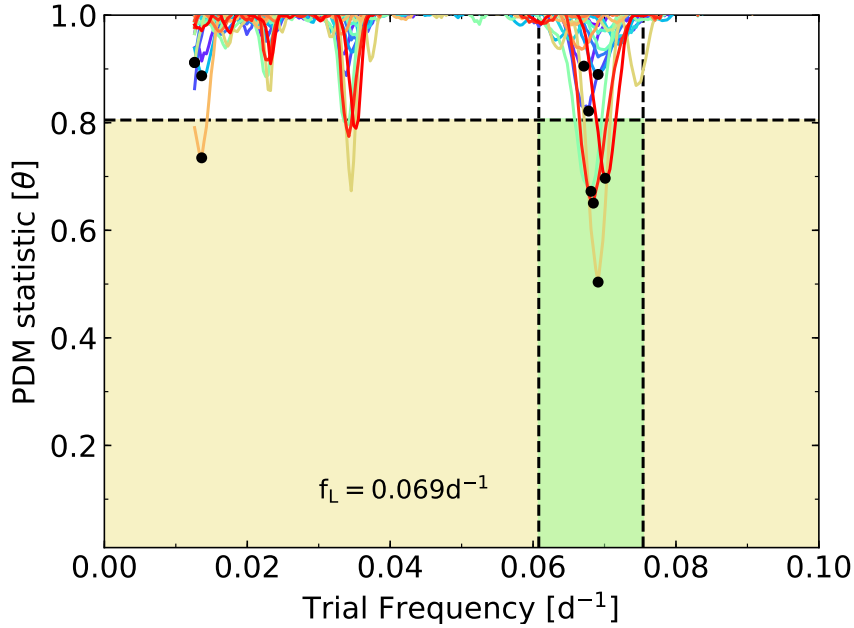


FIGURE 2.10: The PDM statistic θ measured at each trial frequency bin for light curves having an MF QPO signal mixed with red noise having an unbroken power-law model of slope $\beta = 2.6$ of $\log(P_{\text{rat}}) = 2$, on using the PDM while neglecting the lower frequency bins corresponding to $\sim 1/3$ duration. The black points represent the lowest minimum (θ_{min}) for a given PDM periodogram, and the green shaded region is the 99.9 per cent contour limits of the “ideal signal” in the θ –frequency space expected for the MF QPO signal.

of $\log(P_{\text{rat}}) \sim 4, 5$ exhibits reliable detection of 99.7 per cent only for $\beta \lesssim 1.8, 2.4$ respectively. Among this $>85\text{--}90$ per cent of the simulations possess $\theta_{\text{min}} < 0.65$. Next, for the HF QPO, values of $\log(P_{\text{rat}}) \sim 4, 5$ yields 99.7 per cent significance detections for $\beta \lesssim 1.6, 2.0$ respectively. Comparatively, the $\log(P_{\text{rat}}) \sim 3$ only approaches reliable detections of approximately 99.7 per cent when $\beta \lesssim 1.0$. For the HF QPO signals mixed with red noise case, more than 30–40 per cent of the simulations with reliable detections have $\theta_{\text{min}} < 0.65$.

The above analysis was performed considering values of θ_{min} occurring at any frequency while excluding all frequencies less than $\sim 0.012 \text{ d}^{-1}$, which corresponds to one-third of the duration. We also repeated the analysis including the lowest-frequency bins, but this action did not yield significant changes to the results of significant detection of the period. In fact, excluding the lowest bins helps only in reducing the detection inaccuracy error of registering θ_{min} at the wrong frequency (i.e, towards the lower bins) further explained in Section 2.3.3.

False negatives and detection inaccuracy errors

Type II Error (false negative): H1 is inferred false incorrectly when a QPO is intrinsically present.

We label a trial as false negative if the value of θ_{min} does not drop below the upper limit threshold calculated from the “ideal” scenario (irrespective of frequency). For instance, in Fig. 2.10, some of the black points that denote the lowest minimum (θ_{min}) for a given PDM periodogram computed

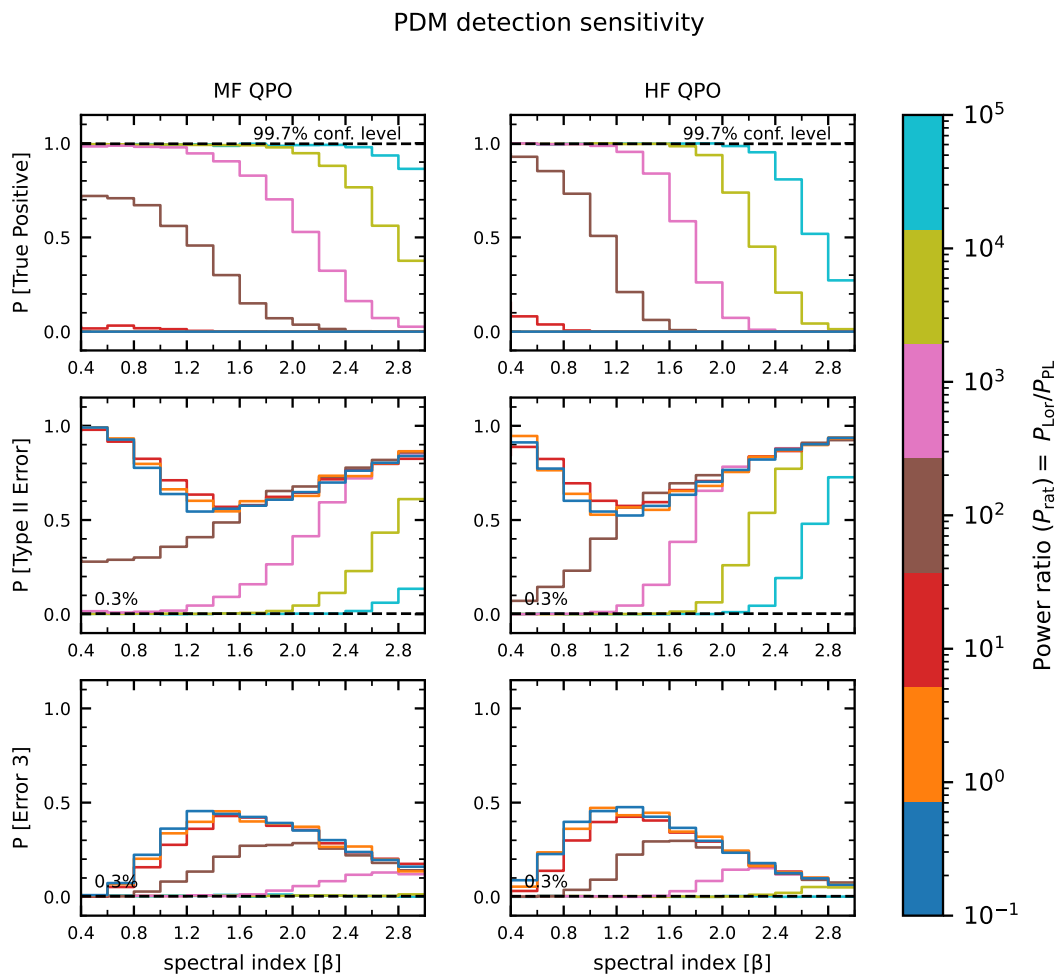


FIGURE 2.11: Top panel: The probability of detecting the first harmonics of the periodic signal in the expected frequency range, Middle panel: The probability of detecting the first harmonics of the quasi-periodic signal in the wrong frequency range, Bottom panel: The probability of detecting false negative of the first harmonics of the quasi-periodic signal all as a function of power ratio P_{rat} and red noise PSD power-law slope β for the MF & HF QPO using PDM.

for light curves with MF QPO mixed with red noise and lies above the upper limit of θ (0.805), below which MF QPO signals are expected. Hence, they are registered as false negatives.

As illustrated in Fig. 2.11, the type II error rate for the MF QPO is less than ~ 0.3 per cent for values of $\log(P_{\text{rat}}) \sim 5$, or 4 when $\beta \lesssim 2.4$, or 2.0 respectively. Furthermore, for the HF QPO, the false negative rate is less than 0.3 per cent for values of $\log(P_{\text{rat}}) \sim 5, 4, 3$ when $\beta \lesssim 2.0, 1.6, 1.0$ respectively. We observe that the rate of false negatives increases with a decrease in $\log(P_{\text{rat}})$ and/or an increase in the steepness β . We observe that at $\log(P_{\text{rat}}) \lesssim 2$, the rate of false negatives increases towards the lower spectral slopes of $\beta \lesssim 1.4$. This is because at the lower power values of QPO against the red noise, the probability of finding a minimum θ at the expected contours for the MF & HF signals decreases which in turn increases the rate of false negatives around these regions.

Detection inaccuracy error (Error 3): H1 is intrinsically true and also registered as true, but the QPO is detected at the wrong frequency.

When θ_{\min} goes below the upper limits obtained in the "ideal" situation but falls outside the predicted frequency region, then we record it as a detection inaccuracy error. In Fig. 2.10, the black dots that represent the lowest minimum (θ_{\min}) for a certain PDM periodogram, derived for light curves with MF QPO mixed with red noise, lie below the upper limit on θ (0.805) but do not fit within the predicted frequency range for MF QPO. As a result, when we have θ_{\min} of the PDM periodogram occurring in the yellow-shaded region, it is registered as Error 3.

When searching blindly for θ_{\min} across all the frequencies, especially considering the lowest-frequency bins, the likelihood of encountering a detection inaccuracy error is usually very high. This probability grows with higher β or lower $\log(P_{\text{rat}})$ values. Now, when we neglect these lower frequency bins, the rate of finding the θ_{\min} at the wrong frequency bins decreases both along the $\log(P_{\text{rat}})$ and the spectral index slope values. In Fig. 2.11, we see that even though the rate of detection inaccuracy error is > 0.3 per cent, it is still significantly low ($\lesssim 1$ per cent) at $\log(P_{\text{rat}}) \sim 4-5$, for $\beta \lesssim 2.6$ for both the MF & HF QPO.

2.4 Realistic uneven Sampling test using PDM

The AGN light curves acquired from observations are typically unevenly sampled, have data gaps, and/or have an irregular sampling. Thus, while employing the ACF and PDM for the purpose of looking for periodic signals, it is crucial to investigate the implications of sampling patterns. It is not possible to look at every possible sampling pattern, so we chose ones that could probably be seen by ground-based optical large-area surveys like LSST, PanSTARRS, ATLAS, etc., which are involved in the continuous monitoring almost on a regular basis, but with yearly sun-gaps of a few months. Ground-based radio surveys like OVRO are involved in continuous monitoring most of the year, with no significant gaps but somewhat irregular amplitudes. We evaluate how irregular sampling and regular gaps, such as yearly sun gaps, have an impact on pure red noise process signatures and impact the identification of a QPO when mixed with red noise.

We perform Monte Carlo simulations of 10-year light curves analogous to those obtained from a generic optical survey like LSST or ATLAS. We start testing evenly sampled data, with and without yearly sun gaps. Then, we try out several irregular sampling patterns, both with and without the yearly sun gaps. This section aims to analyse the impact of only the fundamental facets of irregular data sampling. Therefore, we only carry out the analysis for a subset of the parameters examined above. We highly recommend the readers to perform their respective simulations based on our work as a reference, especially for more sophisticated data sampling patterns.

2.4.1 PDM test for Lorentzian profile with uneven sampling

We do the same analysis as in Section 2.3, starting with the ideal case of only QPOs, modelled with simple Lorentzians with a quality factor of $Q = 30$. We begin with uniformly sampled data, considering that the light curves are 10 years long with a sampling rate of one point per day.

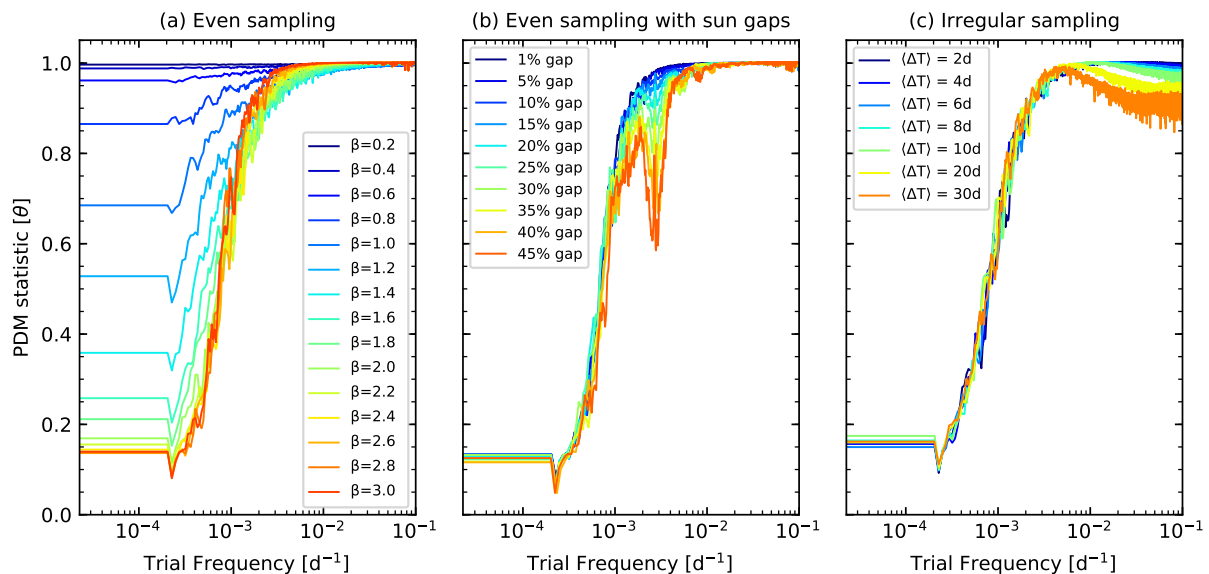


FIGURE 2.12: The distribution of the 99.9 per cent lower limit of the PDM statistic value θ at each test frequency of pure red noise 10 year long LSST type light curve for (a) Evenly sampled data at different spectral index slopes, (b) Evenly sampled data with yearly sun gaps of 45 per cent data gap for $\beta = 2.0$, (c) Irregularly sampled data with different average sampling rate for red noise slope $\beta = 2.0$.

Instead of performing tests with possible QPOs over all the frequencies between $1/(3650 \text{ days})$ and the Nyquist frequency of $1/(2 \text{ days})$, we select the following frequencies f_L : 1.3, 5.77, and $22.04 \times 10^{-8} \text{ Hz}$, as our three test frequency. These frequencies correspond to timescales of 2.3, 0.55, and 0.14 years, and they span 4.3, 18.2, and 69.5 cycles, respectively; we refer to these frequencies as low-, medium-, and high-frequency (LF, MF, and HF) QPOs.

We begin by simulating light curves to determine the region of frequency— θ space where the "ideal" signal occurs. We determine the 99.9 per cent confidence limits on θ_{\min} (upper limits): 0.705, 0.769, and 0.864 for the LF, MF and HF QPOs, respectively; for $\nu_{\theta_{\min}}$ (lower, upper bounds) are: (0.0005, 0.0014), (0.0045, 0.0055), and (0.0181, 0.0204) for the LF, MF and HF QPO respectively. When we analyse mixtures of a QPO and red noise, these values delineate the ranges within which to search for signatures of QPOs

In a similar way, we calculate the 99.9 per cent confidence limits on θ_{\min} and $\nu_{\theta_{\min}}$ firstly for the unevenly sampled data having different average sampling rates of 2—10 days in steps of 2 days, 20 days, and 30 days. After that, we calculate it for data that are evenly sampled and are irregularly sampled (average sampling rate of 8 days) with various values of sun gaps (36.5 d, 0.5 – 4.5 yrs in steps of 0.5 yrs). We find that the range of frequency— θ limits are roughly the same, having a ~ 4 –6 per cent divergence from the results for evenly sampled data.

2.4.2 The behaviour of the PDM for pure red noise processes with uneven sampling

We execute MCS for each of the various sampling patterns of the red noise process of the unbroken power-law PSD model, and we examine the influence of the sampling pattern on the PDM compared to the evenly sampled data.

Even sampling pattern: We again produce pure red noise light curves with an unbroken power-law PSD model over a broad range of slope values β (0.2–3.0), in incremental steps of $\Delta\beta=0.2$. At each step, we simulate 1000 light curves, which are evenly sampled and have a duration of 10 years, consisting of one point every day, and measure their PDMs.

Fig. 2.12 illustrates the 99.9 per cent confidence lower limits on θ obtained at each trial frequency. The figure shows that the PDM looks similar for the evenly sampled data as that of Section 2.3.2, where θ approaches extremely low values. We observe a turnover in the values of the statistic minimum at time scales of approximately one-third to one-fourth of the duration of the light curve, where it begins to fall below 0.85–0.8 and with increasing time scale. At a considerably longer duration (\lesssim one-half the duration), the statistic minimum can reach below 0.5, and at PSD slopes of $\gtrsim 1.8$, it can even fall below 0.2.

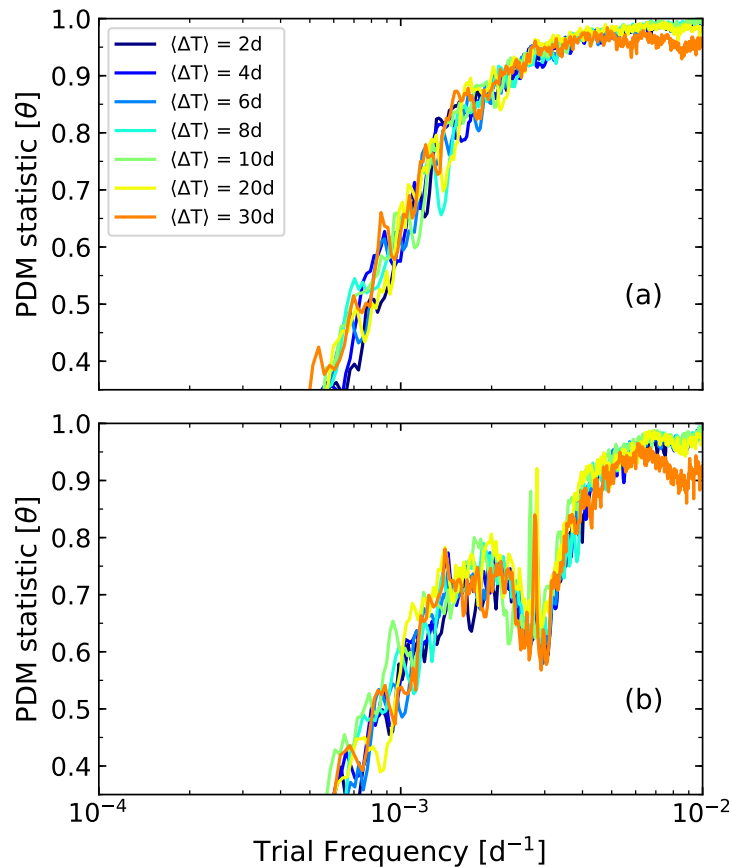


FIGURE 2.13: The distribution of the 99.9 per cent lower limit of the PDM statistic value θ at each test frequency for a randomly sampled pure red noise light curve having spectral index slope $\beta \sim 2.0$ with (a) 10 per cent yearly gap and (b) 45 per cent yearly gap for different average sampling rates.

Even sampling with yearly sun gaps: Now we examine the effect on PDM due to yearly sun gaps in the evenly sampled light curves. In order to show the impacts of sun gaps, we generate 1000 light curves of unbroken power-law PSD models with slopes of $\beta = 2.0$ for each different range of gaps. The gaps vary from 1 per cent of the duration, corresponding to 0.1 years, and gradually increase in increments of 5 per cent of the duration, corresponding to a range of 0.5–4.5 years of

gap in the 10-year long data. We plot the 99.9 per cent lower confidence limits for θ at each trial frequency for each different data gap in Fig. 2.12. We find that as the proportion of gaps in the data increases, it creates a new feature, where there is a sudden dip in the θ_{\min} , which can drop below 0.7 at frequency $\sim 1/(365\text{d})$ when the gaps are higher than 35 per cent of the total data, excluding the deep minimum seen at lowest frequencies ($\lesssim 1/3$ of the duration), which are not affected considerably by the sun gaps.

Again to analyse the impact of various red noise slopes with data gaps in the PDM, we generate red noise light curves employing an unbroken power-law PSD model over a broad range of slopes β (0.4–3.0), in increments of $\Delta\beta=0.2$ with a 45 per cent gap in the data. We simulate 1000 light curves at each step and determine the 99.9 per cent confidence lower limits on θ at each trial frequency for the various spectral slopes. The dip at a frequency of $1/(365\text{d})$ gets more pronounced for substantially higher PSD slopes, such as for values of β steeper than ~ 1.2 , where it falls below ~ 0.8 .

As a result, we suggest avoiding the frequency ranges corresponding to less than $1/3$ – $1/4$ of the duration of the light curve. Additionally, it is equally crucial to avoid other evident timescale ranges that correspond to the period of the gaps because these timescales could exhibit spurious deep minimum characteristics in the PDM.

Irregular sampling: Here, we examine the consequences of irregular sampling in the absence of significant data gaps. We construct 10-year-long light curves once again with daily sampling, but this time we resample by randomly choosing points every ΔT days and investigate average values of $\langle\Delta T\rangle = 2, 4, 6, 8, 10, 20,$ and 30 days. In order to calculate the 99.9 per cent confidence lower limits on θ at each trial frequency, we again generate 1000 light curves assuming $\beta = 2.0$, plotted in Fig. 2.12. Here, it is the relatively higher temporal frequencies that are affected. Specifically for $\langle\Delta T\rangle \sim 20$ – 30 days, θ_{\min} consistently deviates from just under unity to roughly 0.95–0.87 for frequencies corresponding to timescales smaller than approximately about $1/20$ of the duration. However, no narrow-band artifacts are induced.

Irregular sampling with yearly sun gaps: We examine the effects in the PDM when irregular sampling and yearly data gaps are present together. We calculate the 99.9 per cent confidence lower limits on θ at each trial frequency for an input unbroken power-law PSD model with $\beta = 2.0$ for each different average sampling rate with data gaps of 10 per cent and 45 per cent. The 45 per cent wide data gap is not uncommon for several ground-based optical programmes for targets near the equator). As seen in Fig. 2.13, there is no variation in the PDM for the 10 per cent wide gap scenario with irregular sampling compared to that when there are no data gaps. We see the spurious dip close to timescales of $1/(365\text{d})$ once again for the 45 per cent wide data gaps.

2.4.3 The behaviour of PDMs for QPOs mixed with red noise

We carry out MCS for the sum of a $Q = 30$ Lorentzian and an unbroken power-law red noise continuum, with slopes ranging 0.4–3.0 in increments of $\Delta\beta = 0.2$ and power ratios $\log(P_{\text{rat}})$ ranging from -1 to $+5$ in increments of $\Delta\log(P_{\text{rat}}) = 1$. For the sake of brevity, we have only tested the MF QPO. However, the findings were qualitatively identical for the HF QPOs.

We find that the MFQPO has a detection sensitivity range of significant detection of 99.7 per cent only at

We analyse the detection probability along the various spectral index slopes and power ratios by assuming a light curve extending for 10 years and consisting of one point each day. We find that the MFQPO has a detection sensitivity range of significant detection of 99.7 per cent only at $\log(P_{\text{rat}}) \gtrsim 5$.

We investigate the detection probability along the various spectral index slopes and power ratios for the 10-year light curve using three distinct irregular sampling patterns: (a) Even sampling with yearly sun gaps of 40 per cent, (b) Random sampling pattern with an average sampling rate of 8 days (c) Random sampling pattern with an average sampling rate of 8 days with yearly sun gaps of 40 per cent. We see that the detection sensitivity for the various sampling patterns is identical to that observed for the evenly sampled condition. Hence based on our findings, we infer that sampling artifacts do not significantly affect true-positive QPO detection sensitivity for the PDM regardless of the sampling pattern used.

2.5 Discussion

We empirically examined the regions of parameter space where a (true positive) detection of a QPO is most probable and statistically robust using ACF and PDM through extensive Monte Carlo simulations of quasi-periodic processes and mixtures of quasi-periodic and red noise processes.

Additionally, using the ACF and the PDM, we empirically investigated the signatures created by pure red noise processes and evaluated the region of parameter space where false positives are most likely to be encountered.

The light-curve sampling patterns which we investigated are indeed few. However, they are essential to long-term (multi-year) observing programmes with sustained monitoring and with sampling patterns relatively poorer than those needed for a DFT. With these sampling patterns, we generally find the following:

- In studying the effect of pure-red noise processes in the ACF, assuming an unbroken power-law PSD model and evenly sampled data, we find that all the investigated values of the spectral index slope produce false positives at a rate of more than 0.3 per cent determined across the time lag, which is too high to be ignored. For example, at $\beta \gtrsim 1.4$, the correlation coefficient of the first peak (period of the signal) can easily exceed 0.5—0.7, and at steeper slopes of $\beta \gtrsim 2.2$, it can attain even higher values (~ 0.9). The second peak following the zero time lag determined across the time lags independently can also exhibit a correlation value of ~ 0.7 at $\beta \gtrsim 1.0$ and can easily be mistaken for a QPO signal at these associated time lags.

When searching for a QPO signal mixed with red noise, it is possible to robustly eliminate peaks with correlation coefficients over 0.45-0.5 generated by pure red noise by restricting one's search to lags smaller than about 1/3 of the duration of the light curve. It makes the

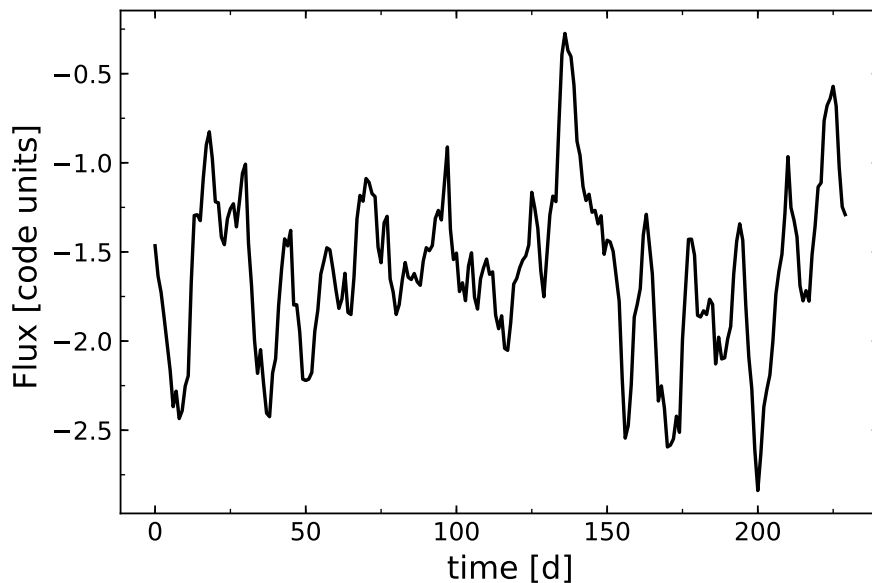


FIGURE 2.14: A sample light curve corresponding to power spectra of MF QPO signal of $\log(P_{\text{rat}}) = 2$ against the red noise continuum having $\beta = 1.8$, where mild features of quasi-periodicity are visually evident in the light curve. However, such a light curve would very likely (likelihood) yield no detection with an ACF or PDM.

false positive rate across the time lag $< 0.3\%$. The results remain qualitatively identical for broken power-law input PSD (for example, breaking from slopes of $\beta = 2.0$ to $\gamma = 1.0$ or to 0.0).

- In the analysis of pure red noise processes in the PDM, considering an unbroken power-law PSD model and evenly sampled data, we see that towards the lower frequency bins — corresponding to timescales longer than roughly one-third of the duration — θ consistently dips below 0.8 – 0.85 . It comes out that around 99.7 per cent of pure red noise simulations with a PSD slope of $\beta \gtrsim 2.4$ can produce θ_{\min} values less than 0.6 . Hence, we emphasise that low values of θ in a specific PDM do not necessarily imply the presence of a QPO, especially at low frequencies.

We notice that for all of the studied combinations of broken and unbroken power-law PSD models, only fewer than 1 per cent of the red noise-only trials acquire a value of $\theta_{\min} < 0.6$ after omitting lowest frequency bins (which correspond to longer than $1/3$ of the duration). *Therefore, a simple method to reduce false positive detections is to ignore the lower frequency bins in the PDM.*

- We investigated the detection sensitivity ranges in the ACF and PDM for a wide variety of red noise slopes and QPO strengths relative to the red noise (quantified by $\log(P_{\text{rat}})$) by considering mixtures of red noise processes and a QPO of quality factor $Q = 30$. After neglecting timescales $> 1/3$ duration, we find that :
 - The factors which predominantly govern the detection of a period with appropriate

statistical significance ($\gtrsim 99.7\%$) are the strength of the QPO relative to the red noise and the steepness of the red noise PSD slope. The probability of detecting a signal at the correct period generally decreases with steepening of the red noise slope and with a decrease in QPO's power against the red noise.

- Significantly high $\log(P_{\text{rat}})$ values are essential for robust detections of a QPO in both the ACF and PDM, and this is especially true for quite steep PSD slopes.
- For illustration, in Fig. 2.14, we have the light curve corresponding to the power spectra of the MF QPO signal having $\log(P_{\text{rat}}) = 2$ against the red noise continuum having $\beta = 1.8$. These power values of QPO would probably not register a true positive detection in the ACF or PDM at any time scale, even if slight signs of quasi-periodicity were visible in the light curves. The likelihood of not registering a true positive detection is 52.3% in ACF and 86% in PDM.
- With the ACF, we generally find that QPOs are detected robustly only when $\log(P_{\text{rat}}) \gtrsim 5$ for $\beta \gtrsim 2.4/2.2$ for a MF/HF QPO, respectively. Detections at values of $\log(P_{\text{rat}}) \sim 3$ are attainable only at lower spectral index slopes, $\beta \lesssim 1.2$.
- For the PDM, we require $\log(P_{\text{rat}}) \sim 4, 5$ for $\beta \lesssim 1.8, 2.4$ even for a 99 per cent detection for MF QPO. Detections at values of $\log(P_{\text{rat}}) \sim 4, 5$ are possible for $\beta \lesssim 1.6, 2.0$ for the HF QPO.
- We explore the effects of regular data gaps and irregular sampling in the PDM. Irregular data sampling causes θ_{min} to become low (~ 0.95) across broad swaths of frequencies, but true-positive detection rates for mixtures of QPOs with red noise are not significantly impacted after removing the lower bins. When a regular data gap such as a yearly sun gap is included, it produces a relatively narrow-band feature that is confined to e.g. $1/(365\text{d})$.

When there is a claim of a QPO signal from AGN in the literature, then one should be able to not just articulate its frequency & RMS, but also the form of the underlying red noise continuum and the uncertainties related to these parameters. In the case of ACF/PDM, it is not easy to determine the underlying PSD shape. We conclude that since the ACF/PDM tend to produce false alarm rates greater than 0.3% and given the general quality of AGN data gathered so far, it is advisable that the community should be cautious and refrain from publishing claims of QPO using the ACF/PDM (until they have a reliable and significant detection considering proper null hypothesis) since the detection rate is generally low and not significant until one reaches very high values of power of QPO against the red noise continuum.

The key issues impacting several periodicity assertions regarding AGNs in the literature are briefly covered in Section 2.5.1. In short, they include (1) sampling too few cycles of a “signal”, as red noise can produce spurious sinusoid-like trends on the longest timescales, and/or (2) mistreatment of the null hypothesis: white noise, or red noise with insufficient steep power-law slope, is assumed; the likelihood of false positives tends to increase towards steeper PSD slopes.

However, another problem with assertions in the literature is that the inferred RMS or RMS/mean (hereafter referred to as just RMS for convenience) of the claimed periodic signal is seldom mentioned. The RMS of the QPO contains physical information about the variability mechanism, just as the value of the period does. If the parameter limitations from previous studies are known, a consistency check may further assist in determining whether or not the claimed QPO is genuine. In Section 2.5.2, we expand on this topic and briefly provide some applications.

2.5.1 Some of the claims in the literature and basic pitfalls regarding ACF and PDM usage

One major caveat in searching for QPOs against a red-noise background, as pointed out by e.g. Vaughan et al. (2016), is that pure red noise processes, particularly those with relatively steep PSD slopes ($\beta > \sim 2$), can produce quasi-sinusoid-like, “W-shaped” segments of light curves for three or four “cycles.”

For observations of a finite length of a red noise process, the dominant trends on timescales longer than (very roughly) one-third of the full duration may be quasi-sinusoidal. These trends can potentially “trick” any period-searching method — ACF, PDM, fitting sinusoidal functions to light curves — into falsely identifying a period, without a proper calibration against a null hypothesis in place (e.g. Press 1978).

In this work, we empirically quantify how the pure red noise processes can yield deceptive signatures in the ACF and the PDM resembling those generated by a pure Lorentzian signal — strong correlation peaks in the ACF, and dips in θ_{\min} in the PDM — especially over timescales longer than about a third of the light curve duration.

The problem of observing too-few cycles couldn’t be resolved by extending observations. For example, Graham et al. (2015) claimed a period of ~ 1900 days in an optical light curve of the quasar PG 1302–102 by the sinusoidal fitting of a ~ 10 -year light curve; Vaughan et al. (2016) demonstrated the light curve’s consistency with pure red noise. Moreover, an additional five years’ monitoring reported by Liu et al. (2018) failed to confirm this period.

A second major caveat is that developing and testing a proper null hypothesis (pure red noise, no QPO) is critical for testing the statistical significance of a candidate period (especially in the absence of having the luxury of being able to extend monitoring). Testing against a null hypothesis consisting of Poisson (instrumental) noise only is clearly insufficient; some papers such as Li et al. (2009) do not attempt any such significance test. We empirically see that with both the ACF and PDM, the likelihood of encountering a false positive from a pure red noise process is extremely sensitive to the value of the underlying power-law PSD slope, and false positives can be significant in number, particularly for $\beta > \sim 2$. We recognize that it can be difficult to measure a periodogram and obtain an unbiased fit when data sampling is poor, but having at least a roughly accurate idea of β is thus critical for being able to form a proper null hypothesis.

Below, we provide a short explanation of these cautions concerning the use of the ACF and PDM and specific instances of incorrect interpretation from the literature. Our objective is not to single out specific authors; instead, we want to highlight only common errors, presenting just a few examples from the literature. A caveat is that data sampling in these cited publications is always not exactly the same as in our simulations in terms of the dynamic range of frequencies explored, frequency resolution, number and size of data gaps, and the irregularity of data sampling. Additionally, reliable estimates of the power-law slope β are often challenging since data are occasionally insufficient for a periodogram fit. Nevertheless, we believe the sampling disparity should not substantially influence our qualitative conclusions about these works. Also, the data sampling employed in all of these publications is such that the ratios of maximum to minimum temporal frequencies are usually of order a few hundred, somewhat comparable to what we investigated in this work.

General issues with ACF, with a few select examples:

As illustrated in Section 2.2.2, one fundamental difficulty in using the ACF to search for periods is that pure red noise processes can cause spurious bumps and wiggles at all timescales (particularly at considerably longer timescales and with $\beta > \sim 1.5$) which can be misidentified for a QPO signature.

ACFs in citations claiming a QPO frequently do not show the clear cosine-like behavior expected when a QPO dominates; both Li et al. (2009) and Fan et al. (2002), for instance, simply identify multiple local peaks in their ACFs as candidate signals, but these are likely artifacts of red noise, e.g. with $\beta \sim 1 - 2$.

Raiteri et al. (2001), Liu et al. (2011) and Raiteri et al. (2021) each claim QPO signatures in peaks occurring at timescales $> 1/3 - \sim 1/2$ of the light curve durations, with values of r_{corr} peaking at $\sim 0.5-0.7$.

However, we demonstrated that for both unbroken power-law PSDs with $\beta > 1.4$ and broken power-law PSDs, r_{corr} can frequently peak above 0.7 (and r_{corr} can even frequently peak above 0.9 when $\beta > \sim 2.2$ very easily, especially at timescales $> 1/3$ of the duration. The primary problem in the case of Liu et al. (2011) is that their light curve samples 2.5 cycles of a sinusoid-like trend (a "W-shape"), and this behaviour is compatible with red noise and presumably corresponds to a highly steep PSD slope (possibly $\beta \sim 2$ or 3).

General issues with PDM, with a few select examples:

One basic issue with attempting to use the PDM for period searching was demonstrated in Section 2.3.2: pure red-noise processes yield spuriously low values of θ_{min} at relatively low frequencies / long timescales e.g. $> \sim 1/3$ of the light curve duration. For example, even in the limit of perfect data sampling, red noise processes across all ranges of β tested can cause θ_{min} to drop to below values of typically e.g. $\sim 0.80-0.85$ below a frequency corresponding to ~ 30 per cent of the duration for the sampling patterns and red noise slopes simulated in this paper.

TABLE 2.3: The values of RMS/mean estimated from the light curves of highly-inclined SMBH binary systems, based on the flare emission profiles in DD18. Listed here are values for two selected values of mass ratio, four selected values of N_E , the fraction of an Einstein radius separating the lens and the source at closest approach, and two wavebands, NUV and V. Also listed in parentheses are estimates of $\log(P_{\text{rat}})$ assuming a mixture of a $Q = 30$ QPO at the MF QPO frequency, 8.0×10^{-7} Hz, and a continuum PSD with $\beta = 2.3$ and a normalization of 20 Hz^{-1} at 10^{-6} Hz.

N_E	Mass ratio $q = 0.05$		Mass ratio $q = 0.5$	
	NUV	V	NUV	V
0.05	0.752 (5.67)	0.471 (5.27)	0.784 (5.70)	0.504 (5.33)
0.1	0.471 (5.27)	0.281 (4.82)	0.504 (5.33)	0.307 (4.89)
0.5	0.095 (3.87)	0.074 (3.66)	0.105 (3.96)	0.082 (3.75)
1.0	0.030 (2.88)	0.030 (2.88)	0.033 (2.96)	0.033 (2.96)

Localized minima in the PDM are the basis for the claimed periods in the literature. However, these minima often occur on long timescales, $> \sim 1/3$ – $1/4$ of the duration, as observed in Fan et al. (2002), Liu et al. (2011), and Peñil et al. (2020).

It is worth noting that the Jurkevich (1971) technique, which has been utilized in Liu et al. (2011) and Fan et al. (2002), is numerically connected to the PDM: both compute the sample variance inside each test phase bin and consider the sum of those variances. However, the PDM is normalized by the overall variance in the light curve. Fan et al. (2002) and Li et al. (2009) employed a renormalized Jurkevich parameter V_m^2 as per accordance with Kidger et al. (1992), defining a fraction $f \equiv (1 - V_m^2)/V_m^2$. However, this method does not account for the number of degrees of freedom. As a result, the expectation value in the absence of any periodicity can differ significantly from 1.

Since the Jurkevich approach is not particularly simulated in this work, it isn't easy to directly compare our obtained values of θ_{\min} to those of V_m^2 as a function of timescale. However, given the properties of pure red noise processes, assertions of periods occurring over long timescales using either technique must be viewed with some skepticism.

2.5.2 Application to the detection of periods for selected physical situations

In emission from a source when there is a periodic signal that coexists with red noise and if the red noise power spectral characteristics can be estimated, then, for a given sampling pattern and a given test frequency, the threshold values of power ratio required for successful detection of a periodic signal with statistical significance using PDM or ACF can be translated into threshold values of RMS for the periodic component.

Such threshold values can be used to define the regions of parameter space for a given physical system where a periodic signal can be detected with the PDM or ACF. Alternately, for a given input set of parameters for a periodically-induced signal, one can estimate the RMS and then power ratio of the signal against the red noise continuum, and compare to threshold values of $\log(P_{\text{rat}})$ that can be detected with the PDM or ACF. Moreover, given the *high minimum values of $\log(P_{\text{rat}})$ needed for detection as demonstrated by this work*, when one claims detection of a periodic signal using the ACF or PDM, they are implicitly claiming a minimum value for $\log(P_{\text{rat}})$ and thus RMS — and these values have implications for the physical parameters of a given system.

Here, we briefly discuss the application to periodically self-lensing SMBH binaries in highly-inclined systems using the results from ACF & PDM.

Highly-inclined self-lensing SMBH binaries

We consider highly-inclined supermassive black hole (SMBH) binary systems following the framework of D’Orazio et al. (2018); hereafter DD18. Emission from the accretion disk around the primary black hole is periodically gravitationally lensed and magnified by the secondary. For simplicity, we assume that our simulation results derived assuming QPOs with a very high-quality factor, are applicable to such strictly-periodic systems. SMBH binary systems could additionally have quasi-periodic emission, potentially. Hydrodynamic simulations of accretion onto SMBH binaries from circumbinary disks can yield quasi-periodic fluctuations in accretion rate through the circumbinary disk (e.g. Farris et al. 2014; Farris et al. 2015). If such variations in accretion rate directly yield variations in luminosity when that material accretes onto the black holes, then quasi-periodic components contributing to observed emission might be expected.

However, tests incorporating mixtures of QPOs and red noise (including that generated in the two accretion mini-disks) would be difficult, because predicting the degree and PSD shape of the contaminating red noise is quite challenging: there could be additional modes of variability not present in stable/ more persistently-accreting disks; one would need to know the radii over which those variability mechanisms are triggered, taking into account e.g. tidal truncation of the outer disks (e.g. Paczynski 1977; Nguyen et al. 2016). Consequently, consideration of red noise (from mini-disks) with QPO mixtures in this context is beyond the scope of our work.

Our analysis focuses only on the optical and UV emission from the inner accretion disc. We utilize Fig. 5.3 of Breedt (2009) as an empirical reference for optical PSD slopes and normalization. The V-band unbroken power-law PSDs for seven Seyferts are published in Breedt (2009); we use the average slope value ($\beta = 2.3$) and normalization (20 Hz^{-1} at 10^{-6} Hz) from this work.

This study does not consider any potential evolution with the mass of black hole (M_{BH}) or accretion rate relative to Eddington $L_{\text{Bol}}/L_{\text{Edd}}$, as observed for broadband X-ray PSDs of nearby Seyferts McHardy et al. (2006). SMBH binary system can consist of black holes of different masses. In case both the black holes of binary are accreting, the $L_{\text{Bol}}/L_{\text{Edd}}$ can also differ and produce different individual PSD shapes and/or normalizations, and the sum of their variability characteristics will appear on our measurement of the single optical PSD shape. Therefore, we ignore these effects for extreme simplicity and presumptively assume that the single PSD shape depicts the intensity of red noise emission from both systems.

We incorporate from DD18 the magnification factors for binary systems with mass ratios of $q = 0.05$ and $q = 0.5$ and almost edge-on accretion disk, with an inclination of $J = 0.2$ rad with respect to the line of sight. We look into the NUV and V bands, with the former being the more "optimistic" case because of the magnification. We use the waveforms shown in Fig.3 of DD18 to calculate the RMS or mean for four different binary orbital inclinations to the line of sight, expressed in terms of the number of Einstein radii, N_E , which quantifies the angular separation between the source and the lens at nearest approach and is equal to $N_E = 0.05, 0.1, 0.5, \text{ and } 1.0$, respectively. Since the

incoming flux from the accretion disk is stochastic and will fluctuate over time, a magnification factor is not the same as a change in flux. We ignore this effect for simplicity. In Table 2.3, the values of RMS/mean are given.

We simulate continuous monitoring light curves, which are 250 days long and evenly sampled. Simulated adopting a $Q = 30$ QPO at the MF frequency used in Sections 2.2–2.4, 8×10^{-7} Hz, and taking into account values of RMS/mean for each inclination/waveband/mass ratio combination, mixed with a $\beta = 2.3$ continuum PSD as per the specifications stated above. In order to keep things simple, we make an assumption that the continuum PSD parameters are the same in the V and NUV bands. Table 2.3 shows the calculated values of $\log(P_{\text{rat}})$, which range from around 2.9 in the $N_E = 1.0$ cases up to 5.7 for the $N_E = 0.05$ cases.

If we recall, to get reliable true positive detections at about 99.7 per cent confidence for the MF QPO, in Fig. 2.11, we see that the $\log(P_{\text{rat}})$ values of 5 are necessary when using the PDM presented in Section 2.3.3. Furthermore, for the ACF, for significant true positive detections at $\gtrsim 99.7$ per cent confidence, $\log(P_{\text{rat}})$ values of 5 are necessary, and the $N_E = 0.05$ and 0.1 cases would thus likely be detected. (Note: Given the significant uncertainties and suppositions surrounding the form of the continuum PSD as described above, we choose to remain approximate in our conclusions herein.)

As a note, we mention that we are only commenting on the likelihood of detections in individual systems. This study does not attempt to estimate the frequency of occurrence of systems whose orbital characteristics meet these criteria and is beyond the scope of this work.

Chapter 3

An X-ray flaring event and a variable soft X-ray excess detected with eROSITA

Contents

3.1 X-ray Instrumentation	58
3.1.1 eROSITA	58
3.1.2 XMM-Newton	59
3.1.3 NICER	60
3.2 Source detection, follow-up observations, and data reduction	60
3.2.1 eROSITA data reduction and results	60
3.2.2 XMM-Newton data reduction	61
3.2.3 NICER data reduction	62
3.2.4 Optical & IR photometry	63
3.2.5 Optical spectroscopic observations	63
3.3 X-ray data analysis	64
3.3.1 XMM-Newton observations	64
3.3.2 NICER observations	68
3.3.3 eROSITA observations	69
3.4 Modeling the optical to X-ray SED	69
3.4.1 Warm Comptonization with AGNSED	70
3.4.2 Double Comptonization with THCOMP*ZBBODY	73
3.5 Optical spectroscopic analysis	74
3.6 Discussions	76
3.6.1 Summary of main observations:	76
3.6.2 Origin of the soft-excess	77
3.6.3 Determining the possible origin of the flare: Characteristic variability timescales	79
3.6.4 Disk instability models	79
3.6.5 Tidal Disruption Event	80
3.6.6 Alternative models	81
3.6.7 Diagnostics of the Broad Line Region	81

In this Chapter, we will discuss the Seyfert galaxy eRASSt_J040846.1–385132 (J0408–38 from now) detected by the eROSITA telescope to display major X-ray flux variations between successive eRASS scans. We subsequently triggered programmes on space-based telescopes (XMM-Newton and NICER), to make multi-wavelength observations in the optical, UV, and X-ray bands. Combined with public photometry data, we determined that the source was flaring in the X-ray, UV, and optical bands simultaneously. We also obtained optical spectroscopic monitoring to track the BLR. Here, we discuss the emission mechanism and finally discuss candidate mechanisms for driving the observed flaring.

3.1 X-ray Instrumentation

3.1.1 eROSITA

eROSITA (extended ROentgen Survey with an Imaging Telescope Array) is the primary instrument on the Russian Spectrum-Roentgen-Gamma (SRG) mission developed by a German consortium led by Max Planck Institute for extraterrestrial physics (MPE). It was launched successfully on July 13, 2019, from the Baikonur cosmodrome, Kazakhstan. eROSITA is a highly sensitive wide-field X-ray telescope, capable of delivering sharp, deep images over the entire sky. eROSITA consists of seven identical Wolter-I geometry mirror modules shown in Fig. 3.1 with each consisting of 54 mirror shells having an outer diameter of 358 mm, which provides a high effective area of $\sim 1500 \text{ cm}^2$ at 1.5 keV. It has a wide active field of view $\sim 1^\circ$ and the on-axis Point-Spread Function (or the Half Energy Width; HEW) of $15''$ provides an effective angular resolution of $25''$ – $30''$. Multiple mirror system has a short focal length and has reduced pileup when observing bright sources (Merloni et al. 2012). The primary mission of eROSITA, which began in December 2019, is to conduct eight deep 0.2-10 keV all-sky surveys (eRASS1–8). It is roughly 25 times more sensitive than the ROSAT all-sky survey in the soft X-ray band (0.2-2.3 keV), and it will offer the first-ever real imaging scan of the sky at the hard energy band (2.3-8 keV). The telescope scans the sky in great circles with one full circle completed every 4 hours and the entire sky covered every 6 months. The wide active X-ray view of the sky enables the study of the cosmological evolution of large-scale structures where eROSITA detects 50 – 100 thousand clusters of galaxies up to a redshift of $z \sim 1.3$. Additionally, it yields roughly 10^6 AGN samples covering a broad range of luminosities. The German eROSITA consortium has full and immediate access to survey data at Galactic longitudes $180^\circ < l < 360^\circ$ where a single sky scan yields almost half a million AGN sources to study.

While eROSITA is unprecedented in detecting these very rare events, its sensitivity per all-sky scan is limited when it is in scanning mode, as a given object is covered for only $\sim 240 \text{ s}$ every six months. We present the instrumentation used particularly for X-ray follow-up for this source namely *XMM-Newton* and *NICER* below.

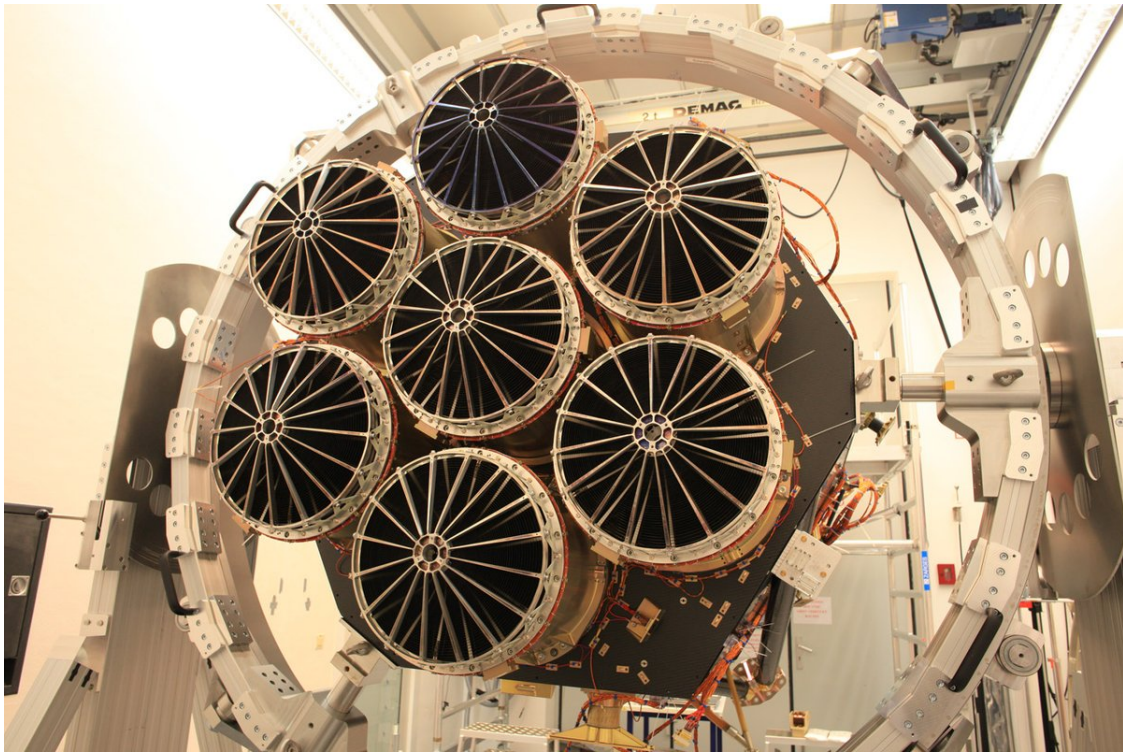


FIGURE 3.1: eROSITA telescope consisting of seven identical Wolter-I geometry mirror modules. Image credits: MPE/Predehl et al. (2021).

3.1.2 XMM-Newton

The *XMM-Newton* (X-ray Multi-Mirror Mission) observatory was launched by the European Space Agency (ESA) on December 1999. The satellite holds three X-ray telescopes each consisting of 58 Wolter-I type shells with a combined collecting area of 0.4425 m^2 at 1.5 keV and the telescope has a focal length of 7.5 m. It has three instruments aboard: spectroscopic imaging with the three European Photon Imaging Cameras (EPIC-pn, EPIC-MOS1, EPIC-MOS2), high-resolution dispersive spectroscopy with two reflection grating spectrometers (RGS-1, RGS-2), the Optical/UV Monitor Telescope (OM). EPIC cameras which is the primary instrument perform sensitive imaging over 30 arcmins field of view (FOV) in the energy range of 0.2–12 keV. It has an angular resolution of 6 arcsecs full-width half maximum (FWHM) and spectral resolution of $E/\Delta E \sim 20 - 50$. The EPIC-pn is composed of twelve identical charge-coupled devices (pn-CCDs) on a single silicon wafer each made of 64×189 pixels that are back-illuminated, while the EPIC-MOS (Metal Oxide Semiconductor) consists of seven identical CCD chips made of 600×600 pixels that are front-illuminated. The two RGS gratings are composed of an array of reflection gratings that diffracts the X-rays to the array of nine dedicated large back-illuminated CCDs. The OM telescope provides coverage between 170–650 nm of the central 17 arcmin^2 region of the X-ray field of view allowing multiwavelength observations of *XMM* targets simultaneously in the X-rays and UV/optical bands.

Deeper exposures are required to characterize X-ray spectra during transitions. Hence, we obtained monitoring with *XMM-Newton* EPIC to track the X-ray corona and simultaneous UV data from the OM to understand the evolution of the accretion disk.

TABLE 3.1: Observation log of the X-ray data from the eROSITA detected ignition event along with the X-ray follow-up observational campaign

Telescope/Instrument	Obs. start (UTC)	Exp. ^a	$f_{0.2-5.0\text{keV}}^b$
eRASS1	2020-02-11–00:00:00	0.58	$0.34^{+0.11}_{-0.05}$
eRASS2	2020-08-09–00:00:00	0.52	$1.35^{+0.15}_{-0.12}$
eRASS3	2021-01-29–12:00:00	0.38	$0.84^{+0.11}_{-0.09}$
eRASS4	2021-08-06–00:00:00	0.39	$4.83^{+0.27}_{-0.24}$
XMM-Newton EPIC	2021-08-21–20:24:47	26.40	$5.36^{+0.02}_{-0.05}$
NICER	2021-08-24–23:45:54	7.42	$5.83^{+0.08}_{-0.06}$
NICER	2021-11-25–16:35:40	21.58	$4.00^{+0.03}_{-0.04}$
eRASS5	2022-01-31–19:50:60	0.42	$1.64^{+0.14}_{-0.11}$
XMM-Newton EPIC	2022-03-10–01:49:25	25.65	$2.14^{+0.02}_{-0.07}$

^(a)Net exposure in ks. ^(b)Flux over 0.2–5.0 keV in units of $10^{-12}\text{erg cm}^{-2}\text{s}^{-1}$

3.1.3 NICER

The Neutron star Interior Composition ExploreR (*NICER*) is an X-ray timing and spectroscopy instrument launched by NASA to the International Space Station in June 2017. It consists of 56 X-ray concentrators (XRC) optics that concentrate X-ray light onto a restricted FOV of 30 arcmin^2 . Each XRC consists of 24 nested parabolic gold-coated thin foil mirrors. The instrument performs in the bandpass of 0.2–12.0 keV and has a moderate spectral resolution of $E/\Delta E \sim 6 - 80$ from 0.5 keV to 8 keV. It has a large effective area $\sim 1900\text{ cm}^2$. *NICER* was suitable to provide X-ray monitoring as part of the intensive follow-up campaign of this source.

3.2 Source detection, follow-up observations, and data reduction

3.2.1 eROSITA data reduction and results

The position of J0408–38 was observed by eROSITA during each of the five started All Sky Surveys. All eROSITA data of the source were obtained by the German eROSITA consortium (*eROSITA_DE*). Data products were extracted using the *eROSITA* data analysis software eSASS version *21121_0_4* (Predehl et al. 2021). The eSASS tasks *evtool* and *srctool* were employed to handle the event data and extract the source products, respectively. The data processing version *c020* was used and spectra were extracted using appropriate regions, which were varied in size depending on the brightness of the source and the number of background sources, which were cheesed from the used background regions.

The source was detected by eROSITA during its ignition phase where there was an increase in the X-ray flux determined by comparison of the eROSITA All-Sky Survey scans. The flux increased by a factor of 4 over a period of 6 months from $f_{0.2-5.0} = 0.84^{+0.11}_{-0.09} 10^{-12}\text{ erg cm}^{-2}\text{ s}^{-1}$ in eRASS3 (January 2021) to $f_{0.2-5.0} = 4.83^{+0.27}_{-0.24} 10^{-12}\text{ erg cm}^{-2}\text{ s}^{-1}$ in eRASS4 (August 2021) and then dropped back to lower flux levels. The eROSITA fluxes along with the other X-ray flux values from our follow-up programme are listed in Table 3.1. The position of the object is at R.A., dec.: X-ray coordinates at 62.19204, -38.85875 with a positional uncertainty of $\sim 1.0\text{ arcsec}$. The closest counterpart in the optical/IR bands is the Seyfert galaxy WISEA J040846.10–385131.0 =

LCRS B040659.9–385922, with optical coordinates of (RA, dec) = (62.192, 38.8587), at a redshift of $z = 0.0574$. The source had X-ray follow-up observations using *XMM-Newton* during its flaring state on 2021 August (XMM1) having ~ 25 ks exposure time and then during the post-flare state on 2022 March (XMM2) having ~ 22 ks exposure time where the X-ray flux of the source had decreased significantly back to the same flux levels before the flaring.

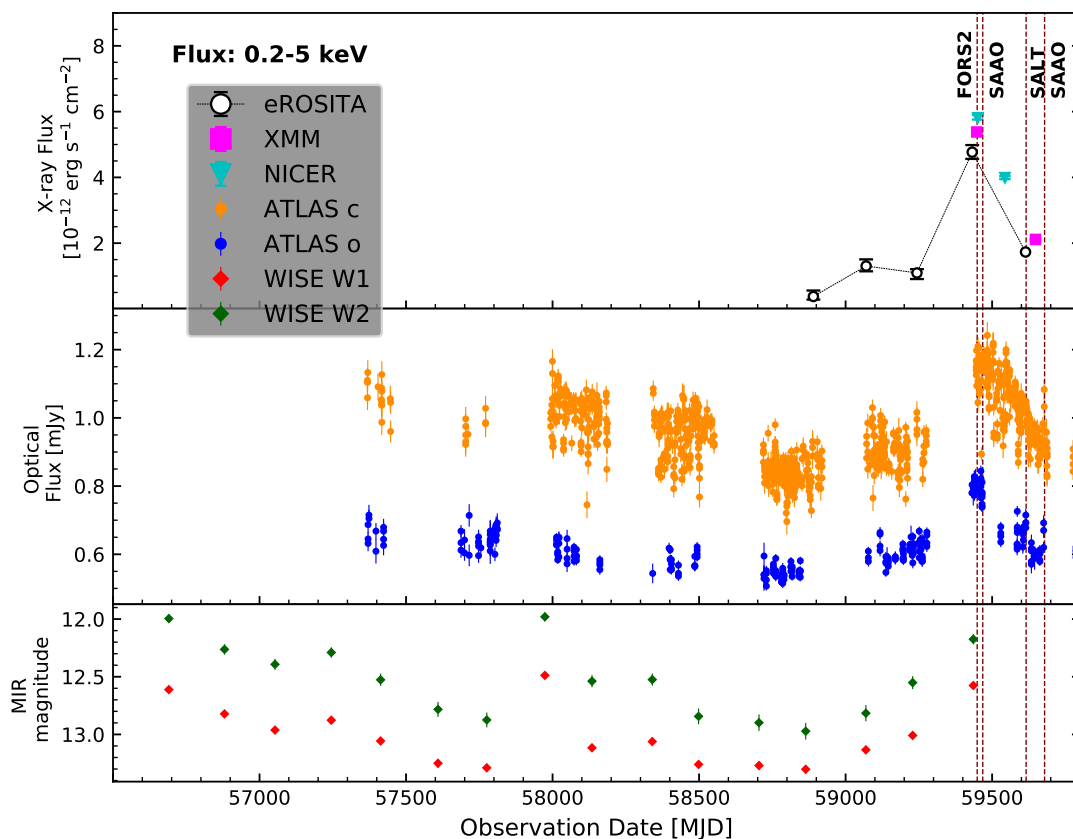


FIGURE 3.2: Multi-wavelength light curves of eRASSt_J040846.1-385132 along with the epochs of the optical spectroscopy shown by vertical dotted lines. In the top panel, we have the X-ray flux obtained for 0.2–5 keV from the XMM-Newton observations, five eRASS scans of eROSITA, and the two NICER observations. In the middle panel, we have the optical light curve from the ATLAS photometry database observed in the cyan filter (c, covering 420–650 nm) and orange (o, 560–820 nm) filters. In the bottom panel, the MIR light curve from WISE is observed in W1 & W2 bands. We can see the source to be flaring about the same epochs in multi-wavelengths.

3.2.2 XMM-Newton data reduction

The EPIC-pn and MOS camera were operating in Small Window and Partial Window imaging modes respectively in the 2021 observation and both the cameras were operating in the Large Window imaging mode during the 2022 observation. The data were reprocessed using the XMM-Newton science analysis system (SAS) version 19.1.0, applying the latest calibration files and using the HEASOFT (v.6.28). We followed the standard procedure for processing the EPIC-pn and MOS

data using EPPROC & EMPROC task within SAS respectively. Then we remove the time bins having a high background in the light curve by creating a Good Time Interval (GTI) file using the task TABGTIGEN. The source and background spectrum were extracted using a circular region of 35 arcsec radius for both observations. The spectra were rebinned by GRPPHA with a minimum of 20 counts per bin to ensure the use of χ^2 statistics. The data do not show any significant pile-up as indicated by the SAS task EPATPLOT. For the pn, we extracted single (pattern 0) and double (patterns 1–4) spectra separately (hereafter pn0 and pn14). Redistribution matrices and ancillary response files were generated with the SAS tasks RMFGEN and ARFGEN.

In both observations, *XMM-Newton*'s Optical Monitor imaged J0408–38 using the M2 filter (effective wavelength 2310 Å). Data were taken in both "image" and "fast" modes and reduced using the XMM_SAS routines OMICHAIN and OMFCHAIN, respectively. These routines apply all necessary calibrations (including flat-fielding and correcting exposures for deadtime), and they perform point-source aperture photometry. We obtain AB magnitudes of 17.464 ± 0.008 for XMM1, and 18.906 ± 0.022 for XMM2, but these values are not yet corrected for Galactic extinction. We corrected for Galactic extinction using $E(B-V) = 0.0081$ at the sky position of J0408–38 (Schlegel et al. 1998), and use $R \equiv A_V/E(B-V) = 3.1$, which yields $A_V = 0.025$ mag. We use the Galactic extinction curve of Cardelli et al. (1989) to estimate the extinction near M2 as $A_{M2} = 2.1 \times A_V = 0.053$ mags. The corrected AB magnitudes are thus 17.411 ± 0.008 for XMM1, and 18.853 ± 0.022 for XMM2. The corresponding extinction-corrected flux densities are $22.125 \pm 0.159 \times 10^{-16} \text{ erg cm}^{-2} \text{ s}^{-1} \text{ Å}^{-1}$ ($0.394 \pm 0.003 \text{ mJy}$) for XMM1, and $5.861 \pm 0.114 \times 10^{-16} \text{ erg cm}^{-2} \text{ s}^{-1} \text{ Å}^{-1}$ ($0.104 \pm 0.002 \text{ mJy}$) for XMM2.

3.2.3 NICER data reduction

NICER observed J0408–38 twice, once in August 2021 (three days after the first *XMM-Newton* observation) and again in November 2021, as summarized in Table 3.1. Extraction of source spectra, background spectra, response files, and ancillary response files all followed standard procedures using the NICER data reduction pipeline. Background spectra were based on the 3C50 background estimator. Counts from the two noisy detectors, 14 and 34, were not excluded, although we verified that their inclusion or exclusion did not impact results. To screen out periods of extreme optical loading impacting energies above 0.3 keV, we rejected time intervals when the detector undershoot rate — detector resets caused when incoming optical photons trigger a release of the accumulated charge (Remillard et al 2002) — exceeded 150 ct s^{-1} . We also filtered against periods of high-energy particle rates by screening out time intervals when the overshoot rate exceeded 1.5 ct s^{-1} . We also applied a background hard band count rate cut of 0.5 ct s^{-1} .

In all spectral fits described in Section 3.3.2, we ignore the data below 0.4 keV due to the effects of optical loading affecting the softest energy bins, and we can obtain good model constraints fitting up to 5 keV. Spectra are grouped to a minimum of 20 ct bin^{-1} .

3.2.4 Optical & IR photometry

As part of this study, we use the publicly available photometric data from the ATLAS survey, which were obtained by running forced photometry on the reduced images (Tonry et al. 2018; Smith et al. 2020). The observations from ATLAS are done using the orange (o, 560–820 nm) and cyan (c, 420–650 nm) filters. The resulting photometrically calibrated fluxes are reported in Fig. 3.2 in Janskys. We obtain infrared photometry taken using the *WISE* telescope’s NEOWISE-R project, using the NASA IRSA archives. The WISE bands W1 and W2 are centered on 3.368 and 4.618 microns, respectively. We use the fluxes generated by the automated forced photometry pipeline. As shown in the figure Fig. 3.2, the optical and IR data show similar variability to the X-ray data. The object exhibits a sudden increase and then decrease in flux at all continuum wavelengths probed, with both the increase and decrease lasting of order six months.

3.2.5 Optical spectroscopic observations

We obtained a total of five optical spectra of the counterpart of J0408-3851 as part of our multi-wavelength follow-up campaign. A single spectrum was taken using the FORS2 instrument (Apenzeller et al., 1998), installed on the UT1 telescope of the ESO 8.2m Very Large Telescope in Chile. The target was observed with a 1.3-arcsecond slit, using three grism+filter configurations: G14OOV (spectral resolution $R=2100$; 1000s exposure), G300V + GG435+81 ($R=440$, 600s exposure), and G300I + OG590+32 ($R=660$, 400s exposure) and combined these exposures to produce a single high-quality spectrum. The FORS2 spectrum was taken on 23 August 2021, during the flaring phase of the AGN. A further spectrum was taken using the Robert Stobie Spectrograph (RSS; Burgh et al., 2003; Kobulnicky et al., 2003) mounted on the 10m Southern African Large Telescope (Buckley et al., 2006, SALT,), situated at the South African Astronomical Observatory (SAAO) in the Northern Cape province of South Africa.

Finally, three spectra were taken with the SpUpNIC spectrograph (Crause et al., 2019) at the 1.9m telescope, also located at the SAAO. We made use of grating 7 at an angle of 16.5 degrees, resulting in wavelength coverage of 3500–8500 Å and $R=500$. Observations were made on 11 September 2021, 10 April 2022, and 4 September 2022, with a total integration time of approximately 2400s for each observation. All spectra were reduced using standard bias corrections, flat-fielding, and wavelength calibration using arc-lamp spectra taken on the night. Spectrophotometric calibrations were performed using a standard star taken on the night in the case of the VLT and SAAO 1.9m observations, and a standard star taken within the past year in the case of the SALT spectrum.

Continuum variability overview

Here, we briefly discuss the continuum light curve overview, presented in Fig. 3.2. The 0.2–5 keV X-ray fluxes derived from *XMM-Newton*, *NICER*, and *eROSITA* are discussed in Sections 3.3.1, 3.3.2, and 3.3.3, respectively.

The X-ray and optical continuum display roughly consistent behavior: both show mild increases from \sim early 2020 through \sim early 2021. Both bands experience data gaps, e.g., due to Sunblock for the optical bands, from Feb./Mar. 2021 through Aug. 2021. After the data gaps, in Aug. 2021,

both bands are sampled at the highest fluxes we measure (including eRASS4). Then, both optical and X-ray, along with the UV M2 band, all decrease through Spring 2022, although we caution that X and UV M2 lack good time sampling here. Both ATLAS bands are relatively monotonic in their decreases. The X-ray and optical bands are consistent with zero lag (as per visual inspection). However, due to the data gaps in both light curves, we cannot establish if any non-zero lag up to a timescale of very roughly six months exists.

3.3 X-ray data analysis

The spectral analysis for the X-ray observations was performed using XSPEC (v.12.11.1) package (Arnaud, 1996) and used the χ^2 statistics for the model fitting. The uncertainties on the best-fit parameters are estimated at the 90% confidence level ($\Delta\chi^2 = 2.71$) as derived from the MCMC using Goodman–Weare algorithm. We include the absorption model in the fitting to describe the Galactic absorption having the hydrogen column density fixed at $N_{\text{H}} = 1.27 \times 10^{20} \text{ cm}^{-2}$ (Willingale et al., 2013), using the photoelectric cross sections of Verner et al. (1996), and solar abundances from Wilms et al. (2000).

We perform combined spectral fitting to the pn0, pn14, MOS1, and MOS2 for both observations. We have used the redshift value $z = 0.05737$ of the source. For both observations, we use the energy range of 0.25–10 keV for pn0; 0.2–10 keV for MOS1 & MOS2. Since the double-events spectrum has calibration issues below 0.4 keV while using the small window mode, we use the energy range of 0.4–10 keV for pn14. In all models, we apply a “constant” term to account for cross-instrumental systematics. We left the value for pn0 frozen at unity; values for other instruments were always extremely close to unity.

3.3.1 XMM-Newton observations

The X-ray primary continuum of an AGN can be roughly described by a simple power-law model, hence we first fit the spectra with a simple absorbed red-shifted power law model (TBABS \times ZPOWERLW) to check for the emission and absorption components in the residual of the fit. This does not give a good fit for both the observations as illustrated from the data-to-model ratio in Fig. 3.3 (c) & (d) respectively, suggesting the presence of extra components in the spectra. A soft excess is evident from the positive residuals towards the lower X-ray energies ($\lesssim 1$ keV). One of the best-fitting phenomenological models was the double power law model (TBABS \times [ZPOWERLW + ZPOWERLW]) for both observations. In XMM1, we found the photon index of the power law fit of the soft X-ray was very steep ($\Gamma_{\text{SX}} = 2.79 \pm 0.04$) and the photon index of the power law fit of the hard X-ray component was flatter ($\Gamma_{\text{HX}} = 1.28^{+0.08}_{-0.10}$). This model had $\chi^2/dof = 1630.75/1638$, with the two model components crossing over at ~ 2.1 keV. In XMM2, we find that the soft X-ray component (SX) has hardened, now fitted with a power law of photon index $\Gamma_{\text{SX}} = 2.19^{+0.08}_{-0.06}$ and the hard X-ray component (HX) with flatter photon index ($\Gamma_{\text{HX}} = 1.12^{+0.15}_{-0.18}$). This model had $\chi^2/dof = 958.66/1014$ with the two components crossing over at ~ 4.0 keV. In both spectra, the soft component is very power-law-like with no obvious strong curvature and extends up to \sim

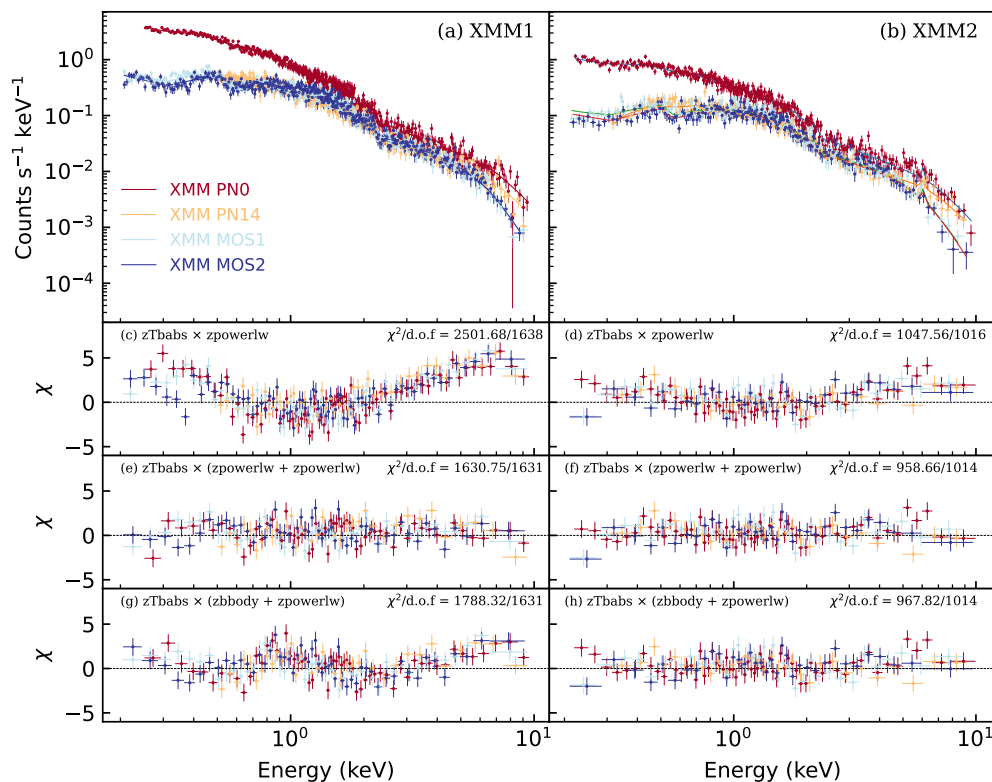


FIGURE 3.3: XMM-Newton X-ray spectrum of J0408-38 (a) XMM1: taken during the flaring of the event, (b) XMM2: taken after the flare subsided along with the fit residuals for a (c) & (d) red-shifted absorbed power-law model which does not give a good fit for both the observations and suggests the presence of extra components in the spectra (XMM1: $\chi^2/\text{d.o.f} = 2501.68/1638$; XMM2: $\chi^2/\text{d.o.f} = 1047.56/1016$); (e) & (f) are the fit residuals for a red-shifted double power-law model for the respective observations. They show a good fit (XMM1: $\chi^2/\text{d.o.f} = 1630.75/1631$; XMM2: $\chi^2/\text{d.o.f} = 958.66/1014$); (g) & (h) are the fit residuals for an absorbed black-body fit to soft X-ray and power-law model fit towards the hard energy band for the respective observations. We see that for XMM1 it does not show a good fit compared to XMM2 (XMM1: $\chi^2/\text{d.o.f} = 1788.32/1631$; XMM2: $\chi^2/\text{d.o.f} = 967.82/1014$).

2 & 4 keV in XMM1 & XMM2, respectively. However, it is important to note that it has varied dramatically in both normalization and spectral shape.

We check for narrow emission Fe-K α line at $E \sim 6.4$ keV by adding ZGAUSS to the best-fit model with Gaussian width σ fixed to 1 eV. We do not detect the line with high significance in any of the observations. The upper limit on the Gaussian component using the (TBABS \times [ZPOWERLW + ZPOWERLW + ZGAUSS]) model was found to be 45 eV and 155 eV in XMM1 and XMM2, respectively.

Physically motivated models: We try both phenomenological and physically motivated models to explain the soft excess. Some of the tested models χ^2 and the fit values are tabulated in Table 3.2. We first fit the spectra with a red-shifted hard X-ray power law and a single blackbody to the

TABLE 3.2: Simultaneous fit of *XMM-Newton* spectra of the two XMM observations over the energy range of 0.2–10 keV.

Component	Parameters	2021 August XMM1	2022 March XMM2
Model 1 – $constant \times tbabs \times (zpowerlw + zpowerlw)$			
SXPL	Γ_{SX}	2.79 ± 0.04	$2.19^{+0.08}_{-0.06}$
	$norm (\times 10^{-4})$	$9.59^{+0.52}_{-0.49}$	$4.17^{+0.35}_{-0.36}$
HXPL	Γ_{HX}	$1.28^{+0.08}_{-0.10}$	$1.12^{+0.15}_{-0.18}$
	$norm (\times 10^{-4})$	$2.67^{+0.43}_{-0.48}$	0.79 ± 0.32
	$\chi^2/d.o.f$	1630.75/1631	958.66/1014
	χ^2_{red}	0.99	0.96
Model 2 – $constant \times tbabs \times (zbody + zpowerlw)$			
BB	kT_e (KeV)	0.095 ± 0.003	$0.112^{+0.011}_{-0.015}$
	$norm (\times 10^{-5})$	2.46 ± 0.09	$0.32^{+0.06}_{-0.08}$
HXPL	Γ_{HX}	$2.03^{+0.03}_{-0.02}$	$1.84^{+0.03}_{-0.01}$
	$norm (\times 10^{-3})$	1.08 ± 0.02	$0.46^{+0.02}_{-0.01}$
	$\chi^2/d.o.f$	1788.32/1631	967.82/1014
	χ^2_{red}	1.09	0.95
Model 3 – $constant \times tbabs \times (compTT + zpowerlw)$			
compTT	T_0 (eV)	20 (F)	20 (F)
	kT (keV)	2 (F)	2 (F)
	τ (keV)	4.28 ± 0.11	$5.92^{+0.15}_{-0.26}$
	$norm (\times 10^{-2})$	4.58 ± 0.27	$0.62^{+0.03}_{-0.04}$
HXPL	Γ_{HX}	$1.34^{+0.08}_{-0.07}$	$0.99^{+0.23}_{-0.12}$
	$norm (\times 10^{-4})$	$3.31^{+0.57}_{-0.47}$	$0.77^{+0.49}_{-0.19}$
	$\chi^2/d.o.f$	1788.32/1631	967.82/1014
	χ^2_{red}	1.09	0.95
Model 4 – $constant \times tbabs \times (thcomp * zbody + zpowerlw)$			
Thcomp	Γ_{SX}	$2.79^{+0.07}_{-0.02}$	$2.54^{+0.28}_{-0.22}$
	kT_e (keV)	$0.50^{+0.23}_{-0.01}$	$0.50^{+0.72}_{-0.01}$
	$cov.frac.$	$0.76^{+0.13}_{-0.05}$	$0.79^{+0.18}_{-0.21}$
BB	kT_e (keV)	0.06 ± 0.01	$0.08^{+0.02}_{-0.01}$
	$norm (\times 10^{-5})$	$5.51^{+0.73}_{-0.65}$	$0.75^{+0.26}_{-0.22}$
PL	Γ_{HX}	$1.61^{+0.05}_{-0.08}$	$1.62^{+0.03}_{-0.13}$
	$norm (\times 10^{-4})$	$6.09^{+0.45}_{-0.90}$	$3.46^{+0.11}_{-0.92}$
	$\chi^2/d.o.f$	1613.66/1638	942.87/1015
	χ^2_{red}	0.98	0.93

Hydrogen column density is fixed to the Galactic value of $1.27 \times 10^{20} \text{ cm}^{-2}$ and the redshift of the source is fixed at $z = 0.05737$; (F) means that the parameter is frozen. $norm$ here is the value of the power law at 1 keV in units of $\text{ph/cm}^2/\text{s/keV}$

TABLE 3.3: Model fit of the two NICER spectra over the energy range of 0.4–5 keV.

Component	Parameters	2021 August NICER1	2021 November NICER2
Model 1 – $tbabs \times pegpwrlw$			
single PL	Γ	2.22 ± 0.002	$2.07^{+0.38}_{-0.08}$
	$norm$	$2.58^{+0.52}_{-0.49}$	$1.84^{+0.09}_{-0.71}$
	$\chi^2/d.o.f$	363.97/283	531.44/432
	χ^2_{red}	1.29	1.23
Model 2 – $tbabs \times (pegpwrlw + pegpwrlw)$			
SXPL	Γ_{SX}	$2.78^{+0.37}_{-0.24}$	$2.27^{+0.27}_{-0.12}$
	$norm$	$1.46^{+0.56}_{-0.58}$	$4.17^{+0.35}_{-0.36}$
HXPL	Γ_{HX}	$1.49^{+0.27}_{-0.43}$	$1.08^{+0.41}_{-0.92}$
	$norm$	$1.25^{+0.23}_{-0.31}$	0.798 ± 0.322
	$\chi^2/d.o.f$	275.54/281	485.88/430
	χ^2_{red}	0.99	0.96

Hydrogen column density is fixed to the Galactic value of $1.27 \times 10^{20} \text{ cm}^{-2}$ and the redshift of the source is fixed at $z = 0.05737$.

soft excess. We see that in XMM1, the soft X-ray component could not simply be modeled using a single black-body component and yields bad residuals as illustrated in Fig. 3.3. (g) having $\chi^2/dof = 1788.32/1631$, whereas it shows a good fit to XMM2 observations having the soft excess fit with red-shifted single black-body (ZBBODY) of $kT_e \sim 0.11^{+0.01}_{-0.02}$ keV and the hard X-ray power-law of photon index $\Gamma_{HX} = 1.84^{+0.03}_{-0.01}$ with $\chi^2/dof = 967.82/1014$ as shown in Fig. 3.3 (h). We also tried fitting DISKBB & DISKPBB which simply couldn't fit the soft component and/or yielded very bad residuals with high χ^2/dof for the XMM1 observation. We try the physically motivated comptonization model (compTT) described in Titarchuk (1994), for the soft energy band having the seed photon temperature (T_0) fixed to a low energy value of 20 eV and the plasma temperature (kT_e) fixed to a low energy value of 2 keV for both the observations, which produces a good fit with optical depth $\tau = 4.28 \pm 0.11$ (XMM1) & $\tau = 5.92^{+0.15}_{-0.26}$ (XMM2) and with a hard X-ray photon index $\Gamma_{HX} = 1.34^{+0.08}_{-0.07}$ (XMM1) & $\Gamma_{HX} = 0.99^{+0.23}_{-0.12}$ (XMM2).

The ionized reflection models for the soft component using `relxill` (García et al. 2014) produce a good fit for both observations. The good fit parameter values having the inclination angle frozen to 45 deg for both observations: (a) for the XMM1 observation: we get $\Gamma_{HX} \sim 1.45$ and with the reflection parameters of $\Gamma_{SX} \sim 2.85$ with highly ionized accretion disk of value $\log \xi = 4.7$; (b) for the XMM2 observation: we get $\Gamma_{HX} \sim 1.17$ and with the reflection parameters of $\Gamma_{SX} \sim 2.03$ with ionized accretion disk of value $\log \xi = 3.7$. In both cases, black hole spin a^* pegs at 0.998. However, we find that certain model parameter values – namely, the very high ionization and the black hole spin pegging at 0.998 – to be “extreme,” and needed to fit the extreme observed smoothness of the soft X-ray component, so `relxill` thus seems to us somewhat contrived. For soft X-ray excess, `compTT` works the best of the models we tried.

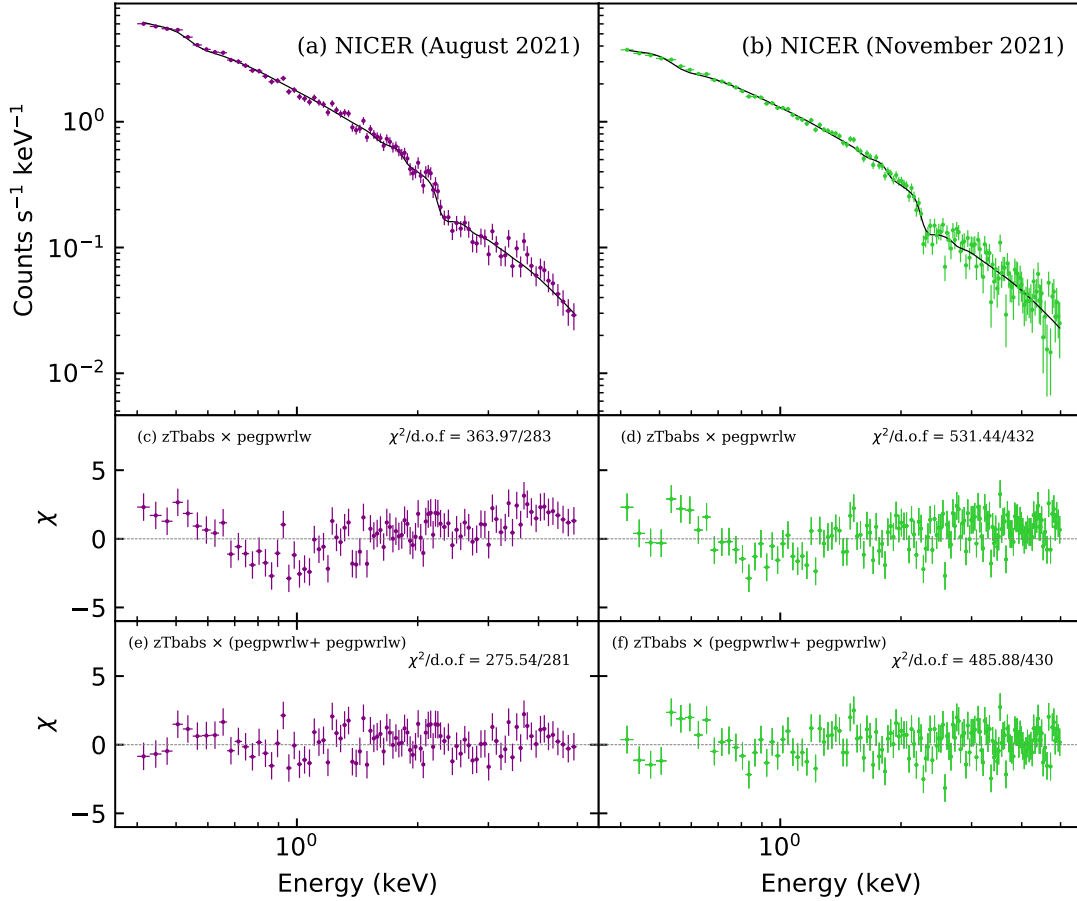


FIGURE 3.4: NICER X-ray spectrum of J0408-38 (a) NICER observation on August 2021 taken during the flaring of the event, (b) NICER observation on November 2021 taken after the flare subsided. The fit residuals for a (c) & (d) simple power law which does not give a good fit for both the observations and suggest the presence of extra components in the spectra; (e) & (f) are the good fit residuals using a double power-law model for the respective observations, in qualitative agreement with fits to the XMM-Newton EPIC spectra.

3.3.2 NICER observations

We fit the August 2021 and November 2021 spectra separately shown in Fig. 3.4. We first applied a simple power law, but in each case, we obtained values of χ^2/dof above 1.2, with broadband concave data/model residuals similar to those seen in the EPIC data when a single power law was applied. For each spectrum, we instead obtained an excellent fit with a dual power-law model, qualitatively consistent with the XMM-Newton EPIC fits. Results are summarized in Table 3.3. We do not include any systematic uncertainties associated with incomplete background modeling; typically, for background systematics of $\pm 2\%$, Γ_{SX} , pegged power-law flux $F(0.5-2)$, and $F(2-5)$ are shifted by up to 0.01, 0.03×10^{-12} erg cm $^{-2}$ s $^{-1}$, and $<0.01 \times 10^{-12}$ erg cm $^{-2}$ s $^{-1}$, respectively. Γ_{HX} is shifted by up to 0.03 (August 2021) or 0.10 (November 2021).

We note that the 0.2-5.0 keV flux measured from the August 2021 NICER spectrum obtained

TABLE 3.4: Model fit of the five eRASS spectra over the energy range of 0.2–3 keV

Component	Parameters	eRASS1	eRASS2	eRASS3	eRASS4	eRASS5
Model 1 – $tbabs \times zpowerlw$						
single PL	Γ	$1.82^{+0.70}_{-0.84}$	$1.99^{+0.53}_{-1.01}$	$2.28^{+0.24}_{-1.30}$	$2.41^{+0.11}_{-1.43}$	$1.94^{+0.58}_{-0.97}$
	$norm \times 10^{-4}$	$0.79^{+0.21}_{-0.28}$	$3.26^{+0.21}_{-0.28}$	$2.08^{+0.21}_{-0.28}$	$11.85^{+0.21}_{-0.28}$	$3.94^{+0.21}_{-0.28}$
	$\chi^2/d.o.f$	6.41/8	23.25/40	26.67/24	86.01/111	58.78/53
	χ^2_{red}	0.80	0.58	1.11	0.77	1.11

Hydrogen column density is fixed to the Galactic value of $1.27 \times 10^{20} \text{ cm}^{-2}$ and the redshift of the source is fixed at $z = 0.05737$.

from dual power-law model fit ($\chi^2/d.o.f = 275.54/281$) extrapolated from 0.4 down to 0.2 keV is $f_{0.2-5.0} = 5.83^{+0.08}_{-0.06} 10^{-12} \text{ erg cm}^{-2} \text{ s}^{-1}$, with the soft and hard power-law photon indices: $\Gamma_{\text{SX}} = 2.78^{+0.37}_{-0.24}$ and $\Gamma_{\text{HX}} = 1.49^{+0.27}_{-0.43}$ respectively. These values are roughly consistent with the fit values from August 2021 XMM-Newton EPIC spectrum. In addition, the flux from the November 2021 NICER spectrum from dual power-law model fit ($\chi^2/d.o.f = 485.88/430$) is $f_{0.2-5.0} = 4.0^{+0.03}_{-0.04} 10^{-12} \text{ erg cm}^{-2} \text{ s}^{-1}$ and is roughly consistent with the interpolation of fluxes between the August 2021 and March 2022 XMM-Newton spectra. the soft and hard power-law photon indices: $\Gamma_{\text{SX}} = 2.27^{+0.27}_{-0.12}$ and $\Gamma_{\text{HX}} = 1.08^{+0.41}_{-0.92}$ respectively.

3.3.3 eROSITA observations

All spectra of the eRASS observations fit moderately well by simple steep power laws given the spectral resolution, over the energy range of 0.2–3.0 keV tabulated in Tab. 3.4, and thus consistent with being completely dominated by the soft excess observed in XMM. In Fig. 3.5, we have the data and the model along with the fit residuals. As the flux increases from eRASS2 to eRASS4, we see that the value of the photon index obtained from the power-law fit changes from $\Gamma = 1.99^{+0.53}_{-1.01}$ to $\Gamma = 2.41^{+0.11}_{-1.43}$. Then in eRASS5, flux levels have decreased, and the photon index became $\Gamma = 1.94^{+0.58}_{-0.97}$, which is consistent with the results from the XMM observations.

3.4 Modeling the optical to X-ray SED

We have the data at the flare peak and post-flare times, close to eRASS4/XMM1 and eRASS5/XMM2, respectively. However, we caution that it is not clear that eRASS4, XMM1, and the start of the ATLAS window in Summer 2021 sampled the true luminosity peak of the flare, (what we call ‘peak’ is the highest luminosity that we measure using XMM and the intrinsic luminosity may have been higher and we missed it) and it is not clear that the flare had completely concluded by XMM2 and eRASS5. For simplicity and brevity, we henceforth refer to the two SEDs as “peak” and “post-flare”, bearing these caveats in mind.

We construct both SEDs from XMM EPIC, XMM OM, and ATLAS data. For ATLAS, we use data taken as close as possible to the two XMM observations, which occurred on MJD 59447 (peak) and 59656 (post-flare). For the flare peak, we average data taken within ± 8 days of XMM1: c-band: $810 \pm 18 \mu\text{Jy}$ and o-band: $1150 \pm 24 \mu\text{Jy}$. For the post-flare SED, ATLAS data only go up to MJD 59603 (o-band) and 59586 (c-band). We thus took data from the second half of the observing

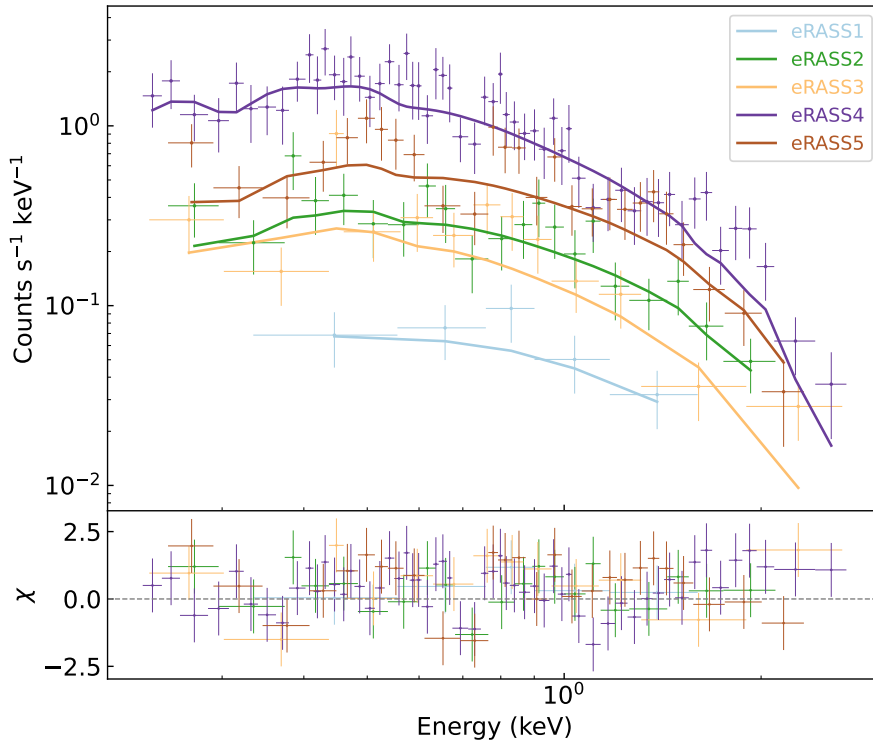


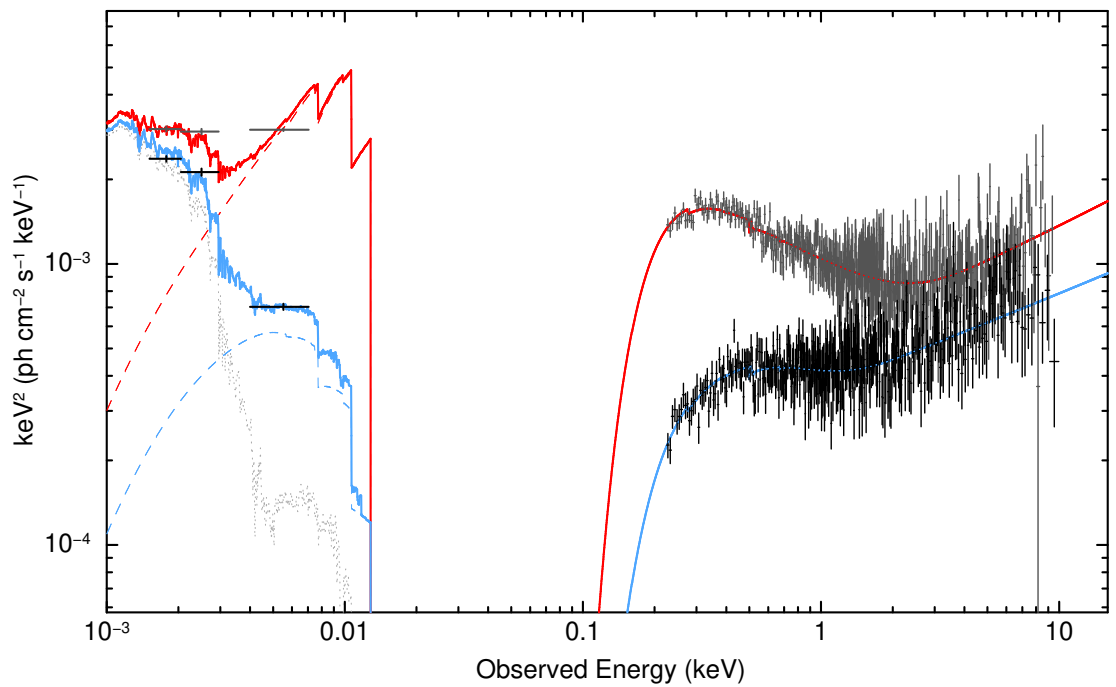
FIGURE 3.5: Simple red-shifted power-law model fit to the eRASS X-ray spectra along with the residuals

season (after MJD 59500), fit a linear regression, and extrapolated it to MJD 59656. Uncertainties on flux density are estimated from the most recent (closest in time to MJD 59656) cluster of data points: c-band: $581 \pm 17 \mu\text{Jy}$, o-band: $901 \pm 20 \mu\text{Jy}$. All SED fits were conducted in XSPEC.

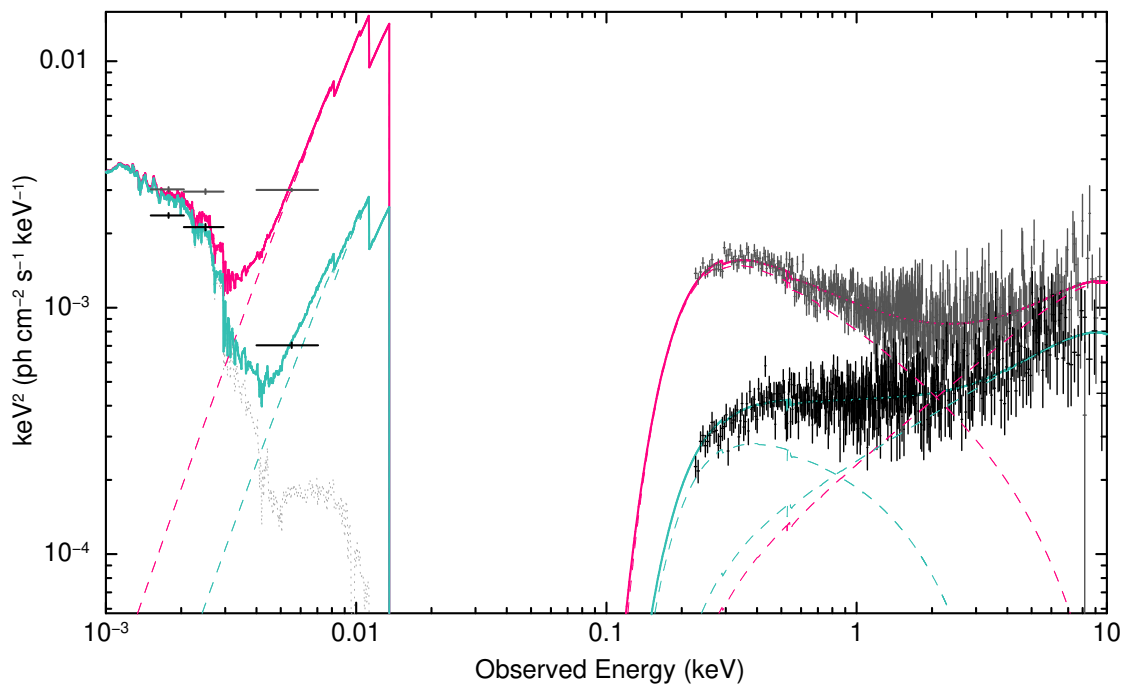
In all the SED fits to account for the host galaxy starlight contribution, we use the spectral template of an Sb galaxy from the *SWIRE* template library (Polletta et al., 2007) to model it. The Galactic dust reddening is modelled using REDDEN with the value of $E(B-V)$ fixed at 6.86×10^{-3} (Schlegel et al., 1998). The luminosity distance to the galaxy is 258 Mpc determined using Ned Wright’s cosmology calculator (Wright, 2006).

3.4.1 Warm Comptonization with AGNSED

For the multiwavelength SED fitting, we apply the AGNSED model (Kubota et al. 2018) which includes three emission regions: the standard outer disc region, warm Comptonizing region, and the inner hot Comptonizing region. The emission thermalizes locally as black body temperature or modified colour temperature corrected black body as in a standard disc only in the outer regions extended upto $R = R_{\text{out}}$. Inwards, from R_{hot} to R_{warm} , the disc emits as warm Comptonization rather than a black body to explain the steep UV downturn and the soft X-ray upturn (soft excess) observed in the AGN spectra (e.g., Davis et al. 2007). In this model, the authors consider a truncated disc geometry, where the inner hot Comptonization region extending up to R_{hot} producing



(A)



(B)

FIGURE 3.6: (A) The best-fitting AGNSED model and (B) the double Comptonized: THCOMP \times BBODY model fit the accretion disk in optical, UV and Comptonized emission from X-ray shown by the grey and black data points for the flaring and post-flaring states respectively in both the figures fit a super-massive black hole of mass of $2 \times 10^7 M_{\odot}$. The solid lines represent the total model and the dashed lines represent the model fit to the data. The dashed grey line represents the host galaxy template from the *SWIRE* library.

TABLE 3.5: The best-fitting parameters of two broad-band SEDs for J0408–38, using two models

Comp.	Par.	2021 August XMM1	2022 March XMM2
Tbabs	$N_{\text{H,Gal}}$ (10^{22}cm^{-2})	0.0127 (F)	0.0127 (F)
redden	$E_{B-V,\text{Gal}}$	0.0069 (F)	0.0069 (F)
redshift	z	0.0574 (F)	0.0574 (F)
Model 1 – AGNSED			
agnsed	M_{BH} ($10^7 M_{\odot}$)	2.0 (F)	2.0 (F)
	$\log(\dot{m})$	−0.94	−1.40
	a_*	0 (F)	0 (F)
	$kT_{\text{e,hot}}$ (keV)	100 (F)	100 (F)
	$kT_{\text{e,warm}}$ (keV)	0.34	0.20
	Γ_{hot}	1.75	1.69
	Γ_{warm}	2.73	2.39
	R_{hot} (R_g)	22.77	92.255
	R_{warm} (R_g)	499.97	199.46
	H	10 (F)	10 (F)
	reprocess	1 (F)	1 (F)
	Norm	1 (F)	1 (F)
	$\chi^2/d.o.f$	503.52/491	347.97/385
	χ_{red}^2	1.02	0.90
Model 2 – Thcomp*bbbody			
thcomp1	Γ_{warm}	2.69	2.39
	$kT_{\text{e,warm}}$ (keV)	1.47	0.50
	cov. frac.	0.29	0.22
zbbbody	kT_{B} (keV)	0.01 (F)	0.01 (F)
thcomp2	Γ_{hot}	1.19	1.46
	$kT_{\text{e,hot}}$ (keV)	100.0 (F)	100.0 (F)
	cov. frac.	6.162×10^{-3}	4.757×10^{-2}
zbbbody	kT_{B} (keV)	0.01 (F)	0.01 (F)
	Norm	1.573×10^{-3}	2.86×10^{-4}
	$\chi^2/d.o.f$	632.01/491	425.91/385
	χ_{red}^2	1.29	1.11

(F) means that the parameter is frozen.

the primary hard X-ray emission, does not have an underlying disc component and has low optical depth. To model the reprocessing due to the hot corona as an extended source illuminating the warm Comptonization and the outer disc, they assume the lamppost geometry to calculate the reprocessed hard X-ray emission by having a spherical hot inner flow from a height H above on the spin axis from the black-hole.

We perform a simultaneous fit with $ZTBABS \times REDDEN \times (AGNSEED+SWS0TEMPLATE.FITS)$ to both SEDs. The main parameters of this model are the mass of the SMBH fixed to $M_{BH} = 2 \times 10^7 M_{\odot}$ estimated from the FWHM value of $H\beta$ emission line (see Section 3.5), the distance of the source (fixed to $D = 258$ Mpc), the Eddington ratio ($\log(\dot{m}) = \log L/L_{Edd}$), the dimensionless spin parameter of the black hole (a_*) fixed to zero, the electron temperature of the hot corona $kT_{e,hot}$ fixed at the default value of 100 keV, the electron temperature of the warm corona $kT_{e,warm}$, the radial size of the hot and warm corona R_{hot} , R_{warm} respectively. We assume the simple point source to accrete from height $H = 10R_g$ (fixed value) above the spin axis (Gardner et al., 2017). The inclination angle of the warm Comptonizing region and the outer disc is fixed at 30° . The only parameters allowed to vary between the two SEDs are $\log(\dot{m})$, $kT_{e,warm}$, Γ_{hot} , Γ_{warm} and all other parameters are tied between the two SEDs. The model produces a best-fitting value of $\chi^2/dof = 500.46/491$ and $347.97/385$ for the XMM1 & XMM2 observations respectively. The system parameters with best-fit values for the two XMM observations taken at different epochs are given in Table 3.5. From the best-fit parameters, we see that the radius of the hot corona region (R_{hot}) and the warm Comptonizing region (R_{warm}) has increased for the XMM2 observation taken post the flaring compared to XMM1 observations taken during the flaring state. Correspondingly the mass accretion rate \dot{m} has decreased from ~ 0.114 (in XMM1 observation) to ~ 0.0404 during the XMM2 observation i.e., \dot{m} has decreased by a factor of ~ 2.8 from flaring to post-flare state. The spectral index slopes and temperature values obtained from AGNSEED for the hot and warm Comptonizing region observed in (a) XMM1 observation: $\Gamma_{hot} = 1.77$, $\Gamma_{warm} = 2.74$, $kT_{e,warm} = 0.335$ keV; (b) XMM2 observation: $\Gamma_{hot} = 1.69$, $\Gamma_{warm} = 2.39$, $kT_{e,warm} = 0.201$ keV. These values of the spectral index determined for the hot and warm corona regions are closer to the best-fit values for the hard & soft X-ray photon index slopes respectively obtained from the phenomenological model fit to the XMM-Newton X-ray data in Section 3.3.1.

3.4.2 Double Comptonization with THCOMP*ZBBODY

We use the thermal Comptonization model Thcomp (Zdziarski et al., 2020) to describe the broadband X-ray continuum and estimate the variations in the coronal properties during the high flux state and low flux state of the source. We assume that the accretion disk having a simple black body emission provides the required seed photons for thermal Comptonization in the hot and warm corona. Thus, two comptonized components using $[reden \times TBabs \times (thcomp \times ztbody + thcomp \times ztbody)]$, to model respectively the “soft-excess” (THCOMP1, BBODY) and the X-ray emission above ~ 1 keV (THCOMP2, BBODY). The hard X-ray temperature is fixed to 100 keV and the temperature of the black body emission from the disc is fixed at 0.01 keV for the comptonization to give the soft and the hard X-ray photons. The best-fit of the model has $\chi^2/dof = 632.01/491$ and $425.91/385$ for the XMM1 & XMM2 respectively. The photon index of

warm Comptonization region (a) for XMM1 is $\Gamma_{\text{warm}} = 2.69$ and for XMM2 is $\Gamma_{\text{warm}} = 2.39$; the temperature of the Comptonization region (a) for XMM1 is $kT_{e,\text{warm}} = 1.4$ keV and (b) for XMM2 is $kT_{e,\text{warm}} = 0.5$ keV. The covering fraction of the warm corona region decreases from $\sim 30\%$ to $\sim 20\%$ from the flaring state to the post-flare state.

3.5 Optical spectroscopic analysis

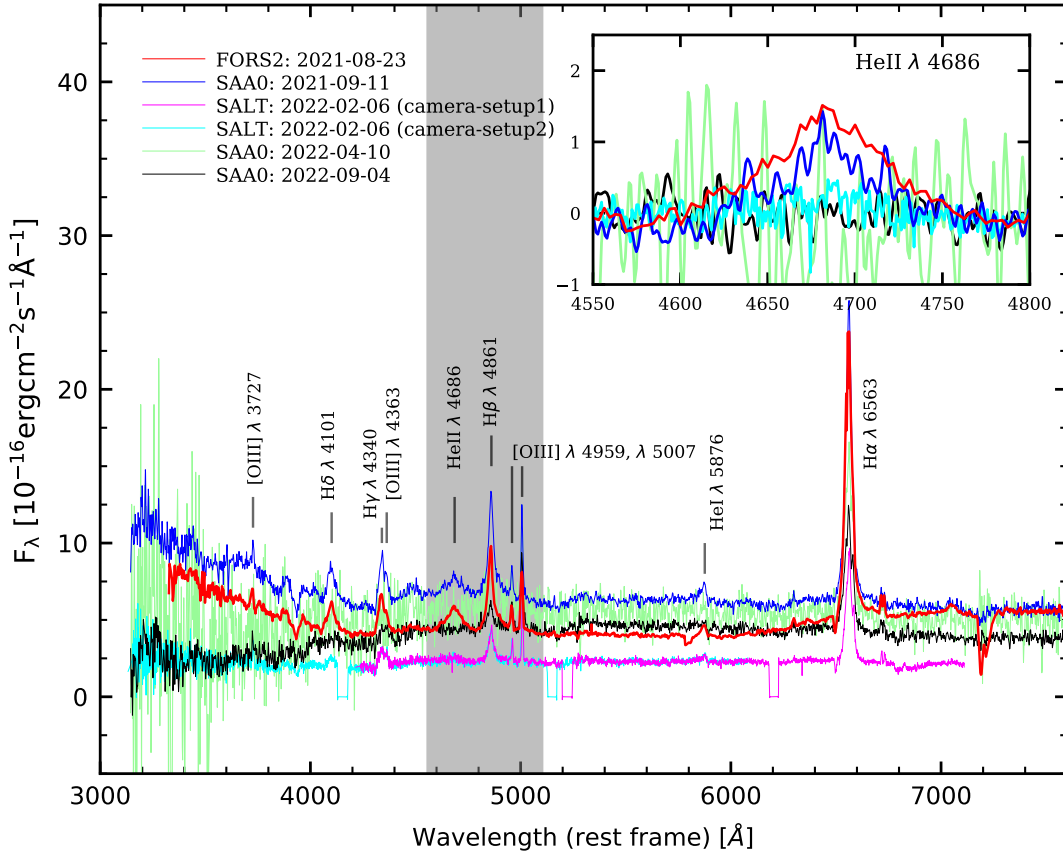


FIGURE 3.7: Optical spectrum of J0408 taken with FORS2, SAAOA, and SALT telescope at the different epochs of flaring and post-flare state of the AGN noted with the different emission lines. In the inset figure shown for the window range of 4550-4800 \AA , we see that the HeII $\lambda 4686$ emission line fading over the course of the observations roughly tracking the X-ray optical continuum.

A quasar continuum typically contains the following components that need to be accounted for while performing the spectral fitting: the blue continuum approximated by a simple power law, the FeII emission, and contamination components by the host galaxy. We use the empirical template presented in Bruhweiler et al. (2008) for the FeII emission and the spectrum generated by Bruzual et al. (2003) for the host galaxy template. There is no indication of a strong contribution from FeII. We apply the de-reddening factor and also apply the extinction factor for all the spectral fits (Schlafly et al. 2011). We perform the spectral analysis using `lmfit` python programme which

implements the least-square fitting for the continuum and phenomenological line fitting. The fitting was split and performed in the three windows: 3800–4400 Å, 4400–5050 Å, and 5200–6800 Å in the rest frame at which the continuum is fit locally. We use Gaussian profiles to model the different emission line features of the spectra.

TABLE 3.6: Results from the spectral line fitting procedure

MJD ^a (d)	Instrument	HeII flux $10^{-16}\text{erg cm}^{-2}\text{s}^{-1}$	HeII FWHM km s^{-1}	H β_n flux $10^{-16}\text{erg cm}^{-2}\text{s}^{-1}$	H β_n FWHM km s^{-1}	H β_b flux $10^{-16}\text{erg cm}^{-2}\text{s}^{-1}$	H β_b FWHM km s^{-1}
59449.0	FORS2 (spectrum #1)	100.099	4573.928	31.410	689.762	147.714	2761.524
59468.0	SAAO (spectrum #2)	56.55	3733.167	25.046	551.444	181.063	2316.628
59616.0	SALT (spectrum #3)	8.761	2276.006	5.9927	431.562	54.008	2054.181
59679.0	SAAO (spectrum #4)	–	–	46.202	689.785	–	–
59826.0	SAAO (spectrum #5)	< 0.27	–	12.007	727.201	41.383	2923.993

^aModified Julian Day of observations. The subscripts n and b indicate the narrow and broad components of the emission lines, respectively.

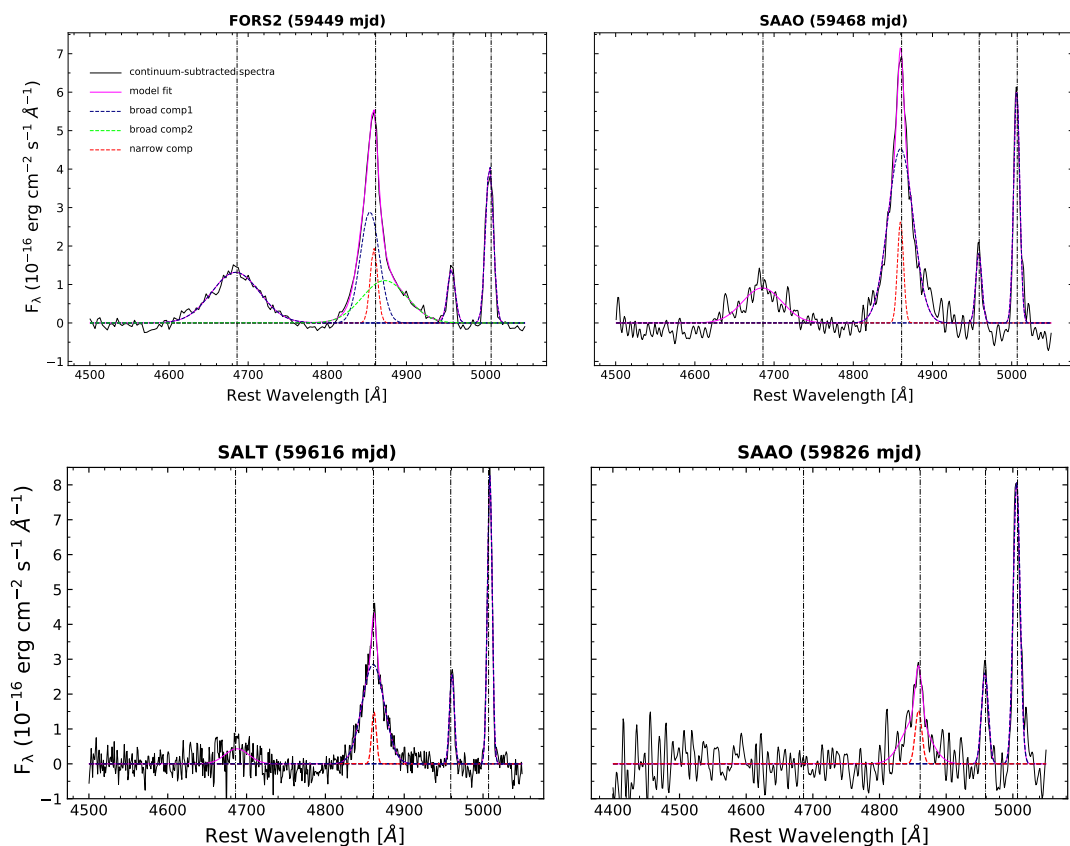


FIGURE 3.8: The fit residuals represented by the continuous black line after the continuum subtraction accounting for the Galactic continuum and the power-law for the emission lines: HeII $\lambda 4686$, H β $\lambda 4861$ and O[III] $\lambda 4959$, $\lambda 5007$. The magenta line marks the fit of the whole spectrum including all components.

We use the continuum subtracted spectra to locally fit the regions around the characteristic emission line features around H α and H β in the wavelength range of 6450–6700 Å and 4800–4920 Å respectively. We fit the narrow [OIII] $\lambda 4959$, $\lambda 5007$ lines using a single Gaussian for each line in all four spectra. All of the narrow-line components in each object are fixed to have the same velocity width as the [OIII] $\lambda 5007$. We observed the HeII $\lambda 4686$ emission line fading over the course of observations taken from the flaring state to the post-flaring state which is roughly tracking the optical and X-ray continuum as shown in Fig. 3.7. In the detailed spectral fitting for the window

range 4400–5050 Å consisting of the HeII λ 4686, H β λ 4861 and [OIII] λ 4959, λ 5007 emission lines as shown in Fig. 3.8, we noticed an extra red-shifted broad wing in the H β profile present only in the first two spectral observations. Therefore, two Gaussians are used to model the broad H β emission line in FORS2 (MJD 59449) and SAAO (MJD 59468) shown in Fig. 3.8.

We calculated the flux of the emission line intensities by integrating the best fit gaussian profiles for the corresponding wavelength ranges given in Table 3.6. We see that the HeII line flux decreases from 100.099×10^{-16} erg cm $^{-2}$ s $^{-1}$ to 8.76×10^{-16} erg cm $^{-2}$ s $^{-1}$ from spectrum #1 to spectrum #3, and then to being non-detected in spectrum #5, with an upper limit of 2.745×10^{-17} erg cm $^{-2}$ s $^{-1}$.

We calculated the emission line intensities by integrating the best fit gaussian profiles for the broad components (excluding the redshifted broad component for H β); these intensities are listed in Table 3.6. Overall, H β and HeII intensities decrease roughly monotonically from spectra #1 and 2 to spectrum #5 (we ignore the low-signal/noise spectrum #4 in this statement), concurrent with the X-ray, UV, and optical continuum flux decreases. From spectra #1 and 2 to spectrum #5, H β intensity decreases by a factor of roughly 3 (the same as the UV 2 emission). However, HeII displays a much sharper drop, ~ 30 . In the Discussion, we discuss BLR diagnostics based on these measured line and continuum variability behaviors.

We can obtain virial estimates for both the radial location of the H β -emitting region of the BLR, R_{BLR} , and the black hole mass, M_{BH} , using the empirical relation between optical luminosity and BLR radius R_{BLR} in nearby Seyferts (Bentz et al. 2013). From the optical spectral fits, we find an average flux density of λF_{5100} to be 4.18×10^{-16} erg cm $^{-2}$ s $^{-1}$ Å $^{-1}$, which for a luminosity distance of 258 Mpc corresponds to a monochromatic luminosity of $\lambda L_{5100} = 1.8 \times 10^{43}$ erg s $^{-1}$. We use the average value of H β FWHM velocity across all spectral fits, 2514 km s $^{-1}$. We apply the $\lambda L_{5100} - R_{\text{BLR}}$ relation of Bentz et al. (2013), $\log(R_{\text{BLR}}, \text{lt-dy}) = K + \alpha \log(\lambda L_{5100} / (10^{44}))$, with their best-fitting values of $K = 1.56$ and $\alpha = 0.55$. We obtain $R_{\text{BLR}} = 3.7 \times 10^{16}$ cm = 14.1 lt-days. Assuming a virial factor f of 1.0, we obtain $M_{\text{BH}} = f R_{\text{BLR}} v_{\text{FWHM}}^2 G^{-1} = 2.1 \times 10^7 M_{\odot}$. We assign an uncertainty of ~ 0.13 dex to R_{BLR} , M_{BH} , and L_{Edd} , based on the scatter in the $\lambda L_{5100} - R_{\text{BLR}}$ relation of Bentz et al. (2013).

3.6 Discussions

3.6.1 Summary of main observations:

- The source was observed to be flaring where the X-ray flux was increasing over roughly six months where the X-rays increased by a factor of ~ 6 and the total optical continuum emission (AGN + host galaxy contamination) increased by ~ 25 –30 percent, as observed via ATLAS photometry.
- The source started to fade again, where the X-ray decreased by a factor ~ 3 over a period of roughly six months. As inferred from SED fits, the AGN's optical emission decreased by ~ 4 .

- The spectral shape of the SX-excess was found to be varying between the bright and the faint state of the source. XMM-Newton EPIC spectra reveal that the photon index of the soft X-ray band is very steep during the peak of the flare ($\Gamma \sim 2.8$) and flattens considerably by the end of the flare six months later ($\Gamma \sim 2.2$). Ionized disk reflection models lead to extreme/contrived regions of parameter space, and are disfavored.
- We model the broadband optical/UV-X-ray SED both near the flare peak, and during post-flare times, We find support for thermal Comptonization models using AGNSED. The soft excess here is consistent with warm Comptonization.
- The SED modeling implies that, from near the flare peak (XMM1) to post-flare times (XMM2), the total luminosity drops by a factor of 3–4, and the value of $L_{\text{Bol}}/L_{\text{Edd}}$ decreases from $\sim 2\%$ to $\sim 0.5\%$.
- From the optical spectral observations, we see that the HeII λ 4686 emission line present during the flaring state of the sources fades gradually with the subsequent observations of the source, roughly tracking the optical/UV and X-ray continuum.
- Correspondingly the presence of a red-shifted broad component in H β emission line disappears over the successive spectral observation of the source from flaring to post-flaring state. This red-shifted broad component could be associated with the in-flow of material onto the SMBH.

3.6.2 Origin of the soft-excess

In the context of varying soft X-ray excess between the observations it has been identified that the soft X-ray excess can vary independently, and sometimes more slowly than, the hard X-ray coronal power law (e.g., Markowitz et al. 2009a, NGC 3227; Turner et al. 2001, Ark 564; Edelson et al. 2002, Ton S180). The soft excess variability has been found to be independent of the hard X-ray variability also on a longer (\sim years) timescale (Mehdipour et al. 2011; Petrucci et al. 2013). Moreover, strong variations in the strength of the soft X-ray excess have been seen, and it can even disappear between observations (Markowitz et al. 2009b, Rivers et al. 2012, Noda et al. 2018). Below we discuss the flare in the context of several models, with a focus on the strong spectral variation observed in the soft X-ray excess.

In many Seyferts, the soft excess is modeled well by the “warm” Comptonization model where the optical/UV thermal photons are upscattered in a Comptonizing medium which is optically thicker and lower in temperature compared to the hot corona which is responsible for the primary X-ray emission. This model has been successfully applied to many sources such as NGC 5548 (Magdziarz et al., 1998), RE J1034+396 (Middleton et al., 2009), RX J0136.9-3510 (Jin et al., 2009), Ark 120 (Matt et al., 2014) and 1H 0419-577 (Di Gesu et al., 2014). The comptonization model is supported by strong similarities between optical-UV and soft X-ray variability. Correlated variability between the X-ray, UV, and optical bands is in agreement with the inverse Compton processes (Edelson et al. 1996; Marshall et al. 1997, etc.). In more recent work, the multiwavelength monitoring campaign of the bright Seyfert galaxy Mrk 509 (Kaastra et al., 2011) also provided

evidence for such a strong correlation. As one typical example, Petrucci et al. (2013) used ten simultaneous XMM-Newton and INTEGRAL observations of Mrk 509 to find that a hot ($kT \sim 100$ keV), optically-thin ($\tau \sim 0.5$) corona is producing the primary continuum and that the soft excess can be modeled well by a warm ($kT \sim 1$ keV), optically-thick ($\tau \sim 10 - 20$) plasma.

In the AGNSED model, the high-energy hot corona region which produces the hard X-rays extends from R_{isco} to R_{hot} and the warm corona region producing the soft excess extends from R_{hot} to R_{warm} . In this model, the warm Comptonization is associated with the optically thick, geometrically thin accretion disc, while the hot component is part of an optically thin, geometrically thick accretion flow. From the best-fitting parameters to our source J0408-38 discussed in Section 4.1, we detected a varying soft-excess from the outburst phase to the declining phase with the photon index varying from $\Gamma_{\text{warm}} \sim 2.7$ to 2.4. The temperature of the warm corona decreased from $kT_{e,\text{warm}} \sim 0.33$ keV to ~ 0.201 keV. The radius of the warm corona decreased after the outburst. We estimate the optical depth of the warm and hot Comptonizing regions using their respective best-fit electron temperature and the X-ray power law photon-index values using the following equation (Zdziarski et al. 1996) :

$$\tau = \sqrt{\frac{9}{4} + \frac{3}{\theta_e[(\Gamma + \frac{3}{2})^2 - \frac{9}{4}]}} - \frac{3}{2} \quad (3.1)$$

where $\theta_e = kT_e/m_e c^2$ and Γ is the spectral index slope. The optical depth values estimated both for the warm corona from the Eq. 3.1: (a) XMM1: $\tau_{\text{hot}} \sim 2.73$, $\tau_{\text{warm}} \sim 15.62$; (b) XMM2: $\tau_{\text{hot}} \sim 0.529$, $\tau_{\text{warm}} \sim 22.8$. Due to poor spectral constraints the values from our best fits likely should not be taken literally, just qualitatively. The optical depth of the warm corona increased from $\tau_{\text{warm}} \sim 22.7$ to 33.85. The shrinking of the warm corona caused the expansion of the hot corona region. All of these parameter changes are associated with, and likely caused by, variations in the Eddington ratio, $L_{\text{Bol}}/L_{\text{Edd}}$, which decreased from 2% during the peak of outburst to 0.5% over a period of ~ 6 months in the declining phase. The X-ray power law photon index changed only slightly as a result of decreasing optical depth and increasing temperature of the corona.

In the context of the "thcomp" model, the best-fitting parameters indicate that warm Comptonization plasma has $kT \gtrsim 1.0$ keV during the flare peak. Optical depth for warm Comptonization (τ_{warm}) increases from ~ 11 at flare peak up to ~ 24 during the post-flare/baseline. The warm Comptonization component has a marginally higher covering fraction during the flare peak (30%) compared to the post-flare/baseline (21%). The broadband spectra fitted with the thermal Comptonization model suggest that the flux changes in response to both the change in accretion rate and the change in warm medium size.

In the case of J0408, the Compton up-scattering of a burst of UV thermal emission from the disk could have produced a corresponding burst of X-ray emission. This could have effectively cooled the corona, leading to a steepening in the spectral slope. As the disk emission fades, the corona receives an input of heating and/or does not cool as effectively (e.g., the optical depth could increase), leading to the soft X-ray slope getting flatter again.

3.6.3 Determining the possible origin of the flare: Characteristic variability timescales

We review the accretion disks and variability timescales described in the Introduction in Section 1.6.1 namely: the light crossing time-scale (t_{lc}), the dynamical or orbital timescale (t_{orb}), the thermal timescale (t_{th}) and the viscous timescale (t_{vis}) associated with accreting SMBHs having a thin disk, to understand the possible origins of the flaring observed in this source. On the assumption that the high flux point is observed to be the maximum flux state of the outburst, we approximately consider the rise and decay time of the outburst to be ~ 170 and 190 days obtained roughly from Fig.3.2. We calculate the timescales at the radial distance of $r \sim 100R_g$ which is the typical inner emitting region of the optical band. We assume the viscous parameter to be $\alpha = 0.03$ and set H/R (the ratio of the height of the disk to radial distance) to 0.05 . The mass of the black hole at $M_{BH} = 2 \times 10^7 M_\odot$.

- $t_{lc} \sim r/c \approx 2.73$ hours
- $t_{orb} \sim \left(\frac{r^3}{GM_{BH}}\right)^{1/2} \approx 3.219$ days
- $t_{th} \sim (\alpha)^{-1} \times t_{orb} \approx 107.3$ days
- $t_{vis} \sim \left(\frac{H}{R}\right)^{-2} \times t_{th} \approx 3.53$ years

The light-crossing time scale is too short and the viscous timescale for the accretion disk is usually too long to be comparable to the variability timescale observed in this source. The thermal timescale is the closest to the observation. We discuss some of the scenarios or disk instability models below that could possibly cause variabilities at timescales shorter than the viscous timescale expected from the standard thin accretion disk.

3.6.4 Disk instability models

Some of the accreting black holes display much stronger variability patterns which are different from the stochastic variations. Instabilities in the accretion disk can produce these kind of variability and flares:

(i) Radiation pressure instability is attributed to cause flares observed in several galactic sources (e.g., Belloni et al. 1997, GRS 1915+105; Cannizzo 1996, GRO J1744-28 and Pahari et al. 2013, IGR 17091-3624). The mechanisms involve four stages: a quiescent phase, a rising phase, the outburst phase, and the decay phase. Initially, the inner accretion disk is empty or filled with an insignificant amount of gas up to the truncation radius (R_{trunc}). Diffusion causes the matter from the outer disk to flow into the inner disk, and during this stage, the X-ray luminosity does not increase appreciably. When the radiation pressure exceeds the gas pressure, a heat wave propagation occurs from the inner disk to R_{trunc} , enhancing the local viscosity, H/R , and accretion rate (M_\odot). In this phase, the luminosity increases quickly and is referred to as the rising phase. An outburst phase follows this and is dominated by the thermal emissions from the hot and bright disk. The slow supply to the inner disk fails to compensate for the pace at which the inner disk gets accreted onto the black hole. Hence the luminous phase fades as the internal disk gets empty. However, the next flare can originate after the inner disk is refilled. Therefore, in this mechanism, recurring

flares are possible. The time of the flares can be approximately estimated using the refilling time of the inner accretion. In addition, the time taken for thoroughly heating the internal disk gives clues on the rise time. Since the luminous phase lasts until the inner accretion disk empties, the flare decay time ought to be more than the orbital period.

(ii) Sniegowska et al. (2020) adopted a simple toy model in which an unstable intermediate zone due to radiation pressure instability exists between the outer cold stable disk and inner hot advection-dominated accretion flows. The model parameters include the accretion rate (\dot{M}), the radius (R), the thickness of the unstable zone (ΔR), and the viscosity parameter α . Furthermore, it predicts that the spectrum should be bluer at outbursts, X-rays should be of larger amplitudes, also semi-periodic variations. However, due to its simplicity, it misses out on the complex effects of real disks and does not result in an outburst shape consistent with the observations.

(iii) Another interesting scenario that can cause flares is the H-ionization disk instability in the outer accretion disk. The mass accumulated at the circularization radius is initially quite cold, and the temperature is below H ionization. However, the surface density and temperature build up over time. H gets ionized when 3000K is reached; at this stage, the free electrons and photons are produced and trapped. This continues, and once all H gets ionized, the temperature shoots to 10^4 K. Such temperatures enhance the c_s and local accretion, causing the heating front to propagate inwards. When the outer disk temperature falls below 10^4 K, a cooling front propagates that turns ionized to neutral H. The growth of mass accretion onto black holes occurs enormously by several orders and proceeds on the time scale of days for the heating front. However, the reduction of mass accretion is governed by the viscous time of the outer disc and occurs quite slowly. In the case of AGNs, the radiation pressure is an essential factor, and the sound speed is also faster in these systems. In addition, the hot accretion flow ($H/R \approx 1$) so the viscous timescale is close to the thermal timescale.

Thus, disk instability is an exciting mechanism that can generate flares in accreting black hole systems. For our object under study, we only have one flare observed and it is too early to speculate regarding the periodicity of J0408. In Conclusions, we (the community) should continue to monitor J0408-38 over the next years to see if additional flares occur, which could support a recurring disk instability mechanism, or a TDE with material getting stripped off periodically/regularly (e.g., Saxton et al. 2015; Grupe et al. 2015; Parker et al. 2019).

3.6.5 Tidal Disruption Event

Stars passing close to supermassive black holes can get tidally disrupted. For $< 10^8 M_\odot$ black hole, the tidal radius lies outside the black hole's event horizon, and the debris produced from disruption on falling onto the black hole can produce emissions, primarily in soft X-rays and ultraviolet (Drake et al., 2011). Such emissions could decay over weeks to months. The event rate is estimated to be about $\approx 10^{-5} \text{ galaxy}^{-1} \text{ yr}^{-1}$ (Wang et al., 2004). These events can occur in the galaxy with the right mass range for a central black hole and dynamic inner regions. TDEs in quiescent galaxies tend to have asymmetric light curves with a fast rise and a slow decay, with

optical/UV thermal emission from stellar streams usually peaking months before X-ray emission from circularized material appears. This scenario does not seem to apply to J0408–38. However, there are cases of TDEs occurring in already-active AGNs. Stellar debris can impact the accretion disk, heating it, thus causing excess thermal emission, while also supplying extra material for accretion, temporarily increasing $L_{\text{bol}}/L_{\text{Edd}}$. For example, the transient PS16dtm is associated with the nucleus of a Seyfert 1 galaxy with a $10^6 M_{\odot}$ black hole (Blanchard et al., 2017). It is suggested to originate from a tidal disruption event wherein the accretion debris powers the optical/UV emission and obscures the X-ray-emitting region. Homan et al. (A&A, *subm.*) reported on an SMBH transient event detected with eROSITA and GAIA: its optical/X-ray continuum variability properties (fast rise, slow decay) and ultra-soft X-ray spectrum ($\Gamma \sim 5$) categorize it as a TDE. However, the optical spectral properties (broad Balmer lines, strong [O III], [N II], and [S II]) categorize the object as a low-luminosity AGN. Another high-redshift example is that of the $z = 1.1$ quasar SDSS J014124+010306, wherein variability associated with a TDE is claimed to be separated from the AGN continuum variability (Zhang 2022). Finally, in the local Seyfert 1ES 1927+654, the X-ray emission disappeared following major changes in the optical spectral type (Ricci et al. 2020). After the optical and UV outburst, the power law component produced in the X-ray spectrum vanished, and the blackbody component appeared. It is hypothesized that the event of tidal disruption of a star by the accreting black hole caused depletion of the inner regions of the accretion flow affecting the magnetic field that powers the X-ray corona.

3.6.6 Alternative models

There are some alternative models to explain the large amplitude variability at optical to X-ray wavelengths observed in many Seyfert galaxies and luminous quasars. Even though these variations imply changes in the global accretion rate the variations are too rapid to be explained by the inflow in a thin standard accretion disc. Therefore, one such method to explain the short inflow and large amplitude variability can be caused due to the thermal instabilities caused in the geometrically thick disc supported by magnetic pressure (e.g., Dexter et al. 2019). The variability mechanism is majorly due to changes in mass accretion rate or thermal fluctuations (Kelly et al. 2009; Ruan et al. 2014). In Zhong et al. (2013) they present a new scenario to explain the soft excess as a result of magnetic reconnection which creates a shock wave and turbulence on the surface of the accretion disc over a thin layer causing the electrons to accelerate. These electrons in turn undergo Compton scattering with photons from the accretion disk and emit X-rays which contributes to the soft excess.

3.6.7 Diagnostics of the Broad Line Region

Here, we briefly discuss the potential diagnostics of J0408–38’s BLR from the $H\beta$ $\lambda 4861$ and HeII $\lambda 4686$ emission lines. We focus on potential reasons why the decrease in observed HeII intensity from spectrum #1 to spectrum #5 (factor of at least ~ 30 as it fades to becoming undetected by spectrum #5) is so much greater than that for $H\beta$ (factor of ~ 3) during the same time.

First, we consider the possibility that the divergence in behavior between the two lines is driven by evolution in the extreme UV (EUV) continuum, since hydrogen and HeII emission are driven

by continuum emission above 1 Ryd (13.6 eV) and 4 Ryd (54.4 eV), respectively. We hypothesize that as the flare fades, the >54.4 eV continuum emission fades more sharply than the continuum emission above 13.6 eV.

For example, if both >13.6 and >54.4 eV continuum are both dominated by thermal disk emission, then this is a reasonable hypothesis, given the well-established observations of "bluer-when-brighter" behavior of Seyferts across the optical to UV bands (e.g., Paltani et al. 1994; Vanden Berk et al. 2004).

We take the fluxes corresponding to the best-fitting AGNSED models from Section 3.4.1. The 13.6 eV – 10 keV continuum flux drops from 3.72×10^{-11} erg cm $^{-2}$ s $^{-1}$ in the high-flux state to 4.54×10^{-12} erg cm $^{-2}$ s $^{-1}$ in the low-flux state, a drop of 8.2. Meanwhile, the 54.4 eV – 10 keV continuum drops from 1.76×10^{-11} to 3.97×10^{-12} erg cm $^{-2}$ s $^{-1}$, a drop of 4.4. That is, the ratio of > 54.4 eV to > 13.6 eV model flux actually increases as the flare subsides. This is because as one increases in energy from the optical/near UV range to the EUV range, in the context of our best-fitting AGNSED fits, the continuum emission becomes dominated by the Comptonized component above ~ 10 eV as it connects the EUV regime to the soft X-ray excess. It is thus not clear that evolution in the EUV continuum slope can be responsible for the diverging behavior in the HeII and H β lines. However, we must caution that our observations of J0408–38 completely lack any rest-frame energy coverage between 2185 Å (5.7 eV) and 66 Å (211 eV), and this exercise is consequently a strongly model-dependent extrapolation.

We now consider that the two emission lines are likely probing different radial regions of the BLR, by a factor that may be as much as an order of magnitude. Reverberation-mapping campaigns on several nearby Seyferts have revealed that reverberation lags for HeII are generally shorter than those for H β , thus supporting radial ionization stratification in the BLR. For example, Kollatschny et al. (2001) and Grier et al. (2012) found HeII lags to be shorter than those for H β by factors of roughly 6–8 in Mkn 110 and Mkn 335, respectively. Moreover, these works found support for HeII emission to arise in the same virial structure as H β emission, just emanating at smaller radii, at least in these two objects. In addition to empirical support, photoionization calculations support that the emission-weighted radii of these two emission lines can differ by roughly an order of magnitude (Korista et al. 2004).

In the case of J0408–38, the observation of HeII emission varying much more strongly than H β emission could, speculatively, indicate diverging physical conditions (geometry, density, or illumination) between the two radially distinct emission regions. As a purely speculative example, there could conceivably have existed some temporary, vertically-extended structure in the inner, highly-ionized region of the BLR only. Such a structure could have created a larger covering factor for the HeII-emitting radii than for the larger radii where H β is created, being most prominent during optical spectrum #1.

Finally, however, an alternate, simpler explanation that does not require different covering factors at different radii are based on HeII and H β emission having divergent "responsivities." Following Korista et al. (2004), responsivity is defined qualitatively as how much a given line's intensity varies for a given variation in ionizing continuum flux; it is defined quantitatively as

$\eta \equiv \Delta \log(F_{\text{line}}) / \Delta \log(\Phi)$, where F_{line} denotes line intensity and Φ denotes the number of ionizing photons (eqs. 1 and 2 in Korista et al. 2004).

Responsivities vary with distance, generally getting larger towards larger radii for a given emission line. However, different atomic species can yield vastly different responsivities, depending on local conditions such as density, as well as the number of ionizing photons and how variable the input continuum is. Consequently, there can exist physical conditions where HeII's responsivity is substantially stronger than that for H β .

From spectrum #1 to spectrum #5, the ionizing continuum drops by a factor of roughly 8 (0.9 in the log), considering the 13.6 eV – 10 keV continuum emission fluxes from the best-fitting AGNSED models fits to the broadband SED. Meanwhile, H β intensity drops by roughly 3 (0.5 in the log), yielding $\eta \sim 0.5$. Comparison to Fig. 4 of (Korista et al. 2004) indicates that such a responsivity is typical for typical BLR number densities ($\log(n, \text{cm}^{-3}) \gtrsim 10$). HeII intensity drops by at least 30 (1.5 in the log), yielding $\eta \gtrsim 1.7$. Such a responsivity in HeII is reasonably achieved towards relatively higher values of n , e.g., $\log(n) \sim 11 - 12$.

Finally, we briefly discuss the broad, redshifted emission component detected in the H β profile in spectrum #1. This feature can be modeled with a Gaussian with an energy centroid suggesting gas inflowing with a bulk velocity of order $\sim 3618 \text{ km s}^{-1}$. Such a red wing qualitatively resembles those observed in the H β profiles of some nearby reverberation-mapped Seyferts, including Arp 151 (Pancoast et al. 2014) and 3C 120 (Grier et al. 2013). Though such a feature implies some bulk inflow motion, it is not clear if there is any direct connection between the continuum flare and the presence of this inflow, or if the two are merely coincidental. Moreover, it is not clear if this red wing arises from a kinematic component that is physically separate and distinct from the BLR. Nor is it clear whether this feature indicates that the BLR itself contains a kinematic component associated with bulk infall, as measured in several nearby reverberation-mapped Seyferts (Grier et al. 2013; Pancoast et al. 2014). However, the transient nature of this red wing combined with the relative stability of the other broad H β component ("broad component 1") seems to favor a component physically distinct from the BLR.

The infalling component could, speculatively, be associated with a "Failed Radiatively Accelerated Dusty Outflow" (FRADO; Czerny et al. 2011; Naddaf et al. 2021). In such models, the BLR is formed as a dusty wind flowing upwards from the disk and pushed radially outwards by radiation pressure. However, after the gas is heated by the radiation to the point where dust sublimates, the driving force subsides, and the cloud falls ballistically back down to the accretion disk, forming a "failed" wind. The dynamical simulations of Naddaf et al. (2021) predict that wind heights and velocities depend on source accretion rate, but infall velocities of hundreds to thousands of km s^{-1} are plausible. In J0408-38, the energy centroid of the broad redshifted component suggests an infall velocity of $\sim 3618 \text{ km s}^{-1}$. It is (speculatively) possible that the FORS2 spectrum caught emission from such an infalling component, which then faded or impacted into the accretion disk by spectrum #2, 19 days later.

Chapter 4

Conclusions

Contents

4.1 Summary and conclusions on the study of detection of periodic signals using the statistical tools: ACF & PDM	85
4.2 Summary and conclusions on the results on the multi-wavelength campaign on a flaring Seyfert detected with eROSITA	88

4.1 Summary and conclusions on the study of detection of periodic signals using the statistical tools: ACF & PDM

We present the findings of an empirical analysis of the behaviour of two statistical tools, the ACF and the PDM when employed to identify a QPO in light curves containing stochastic red noise variability.

These methods have been put to use for the identification of periodic signals in AGN light curves. However, characteristics that may be mistaken for a QPO are also readily mimicked by pure red-noise processes. Guidance is necessary for avoiding false-positive QPO claims and supporting true-positive detections, especially considering that the astronomical community has or will soon access databases with vast numbers of monitoring light curves obtained from present and proposed ground-based monitoring programmes such as LSST.

We carry out Monte Carlo simulations with various red noise power-law PSD slopes and QPO strengths for a selected number of light curve sampling patterns. We empirically examine both true-positive QPO detections in the presence of a mixture of broadband red noise and a narrow-band QPO, as well as false positive detections in cases where a QPO is absent and solely red noise is present (the null hypothesis model).

After testing for a wide variety of power-law slopes over the complete timescale range, we find that pure red noise light curves can generate false positive signals in the ACF more than 0.3 per cent of the time. False-positive peaks commonly exhibit correlation coefficients of 0.5 or above. The proportion of false positives stays ≥ 0.3 per cent at power-law slopes $\beta \gtrsim 2.6$ when limiting our analysis to delays that are smaller than one-third of the total duration. However, the maximum correlation coefficients remain at 0.55. We conclude that the signal is most likely genuine

when a peak is present with a correlation coefficient of >0.5 when using lags of no more than a third of the whole period and for evenly sampled data.

In the PDM, pure red-noise processes lead to drops in the PDM test statistic θ (e.g., $\theta \sim 0.6$), especially for frequencies corresponding to timescales higher than about one-third of the duration. For all the tested slopes, the percentage of false positives is larger than 0.3 per cent, and on considerably steeper slopes $\beta \gtrsim 1.4$, the rate of false positives approaches 99.9 per cent. However, suppose we exclude the lowest frequencies (timescales higher than about a third of the period). In that case, the rate of false positives is still more than 0.3 per cent for all slopes, although the probability of having the PDM statistic θ less than 0.65 is < 0.3 per cent. Therefore, ignoring the lower frequency bins in the PDM is a simple approach to minimize false positive detections.

These findings provide empirical evidence that, when employing the ACF or PDM, and when variability is caused by pure red noise process with an unbroken power-law PSD shape, the ad-hoc approach of basically discarding timescales greater than $\sim 1/3$ of the total duration is an efficient procedure to eliminate false positives (However, we strongly emphasise that such a criterion of one-third is only intended to be very approximate and may vary depending on factors like the steepness of the power-law slope, data sampling). Furthermore, they imply that the characteristics at the longest timescales/lowest frequencies in previously published periodicity claims using ACFs or PDMs may have been consistent with pure red noise rather than being attributable to QPOs, as was previously suggested.

When QPOs are present alongside pure red noise in evenly sampled data, the sensitivity of true-positive detection in the ACF and PDM naturally relies significantly on the steepness of the red noise's PSD slope in addition to the relative strengths of the QPO and the noise ($\log(P_{\text{rat}})$). Without the pre-filtering approach mentioned in Sections 2.2.3 and 2.3.3, we find that very large $\log(P_{\text{rat}})$ values such as 4–5 are usually necessary for a 99.7 per cent true-positive detection rate at PSD slope values of $\beta < \sim 2$.

We remind here that we have not included the Poisson noise in our simulated light curves. Doing so would probably make it much more challenging to detect a true positive. As a result, our findings are essentially lower limits on the values of $\log(P_{\text{rat}})$.

We reiterate that any assertion that a QPO was discovered using the ACF or PDM entails the detection of a signal with a very high signal-to-noise ratio. Depending on the model used for interpretation, high $\log(P_{\text{rat}})$ and RMS values may signify extreme regions of model parameter space.

In the particular scenario of periodically self-lensing black holes in gravitationally closed binary systems on a steeply inclined orbit, which we discussed in Section 2.5.2, for $\log(P_{\text{rat}})$ to be $\gtrsim 5$ (assuming no light curve filtering) in optical/UV emission from the inner disks the source and lens must be separated by only $N_E \sim 0.05$ at the closest approach (DD18).

We also looked at a limited number of different sampling patterns, considering yearly sun gaps, which is typical in ground-based optical observing programmes and irregular but continuous

sampling to see how they affected the true-positive and false-positive detection rates in the PDM. The true-positive detection rates do not change substantially for given values of $\log(P_{\text{rat}})$ and β .

For QPO-seeking readers with light curves with sampling patterns similar to those we simulated, we recommend utilising our simulations and plots as guidelines to determine if specific characteristics in their own ACFs/PDMs are suggestive of any QPO or are consistent with a single pure red noise process.

For the readers dealing with light curves having different sampling patterns and/or intending to test a null hypothesis model that is more sophisticated than the basic unbroken power law, we advise them to conduct their simulations, including examining the range of behaviour that may be displayed under the appropriate null hypothesis model, based on the slope of the underlying red noise process (and its uncertainty). Readers should test a broad range of slopes **if the slope is not known precisely** in order to be cautious. Lastly, it's important to note that our simulations here did not account for the impacts of Poisson noise, so readers should keep that in mind when running their simulations.

It is worth analysing if a periodogram, as opposed to the ACF or PDM, is more effective at clearly distinguishing broadband continuum noise from a narrow-band QPO for a specific sampling pattern. The approach of Vaughan (2005) is appropriate for QPO identification in a periodogram for evenly-sampling data, and the behaviour of the periodogram (probability distribution of powers, biases, the degree to which the neighbouring temporal frequency are independent, etc.) has been effectively understood (see references in, e.g. Vaughan 2005). However, for a particular RMS strength, the $\log(P_{\text{rat}})$ value required to identify a QPO depends on variables such as temporal frequency spacing and the quality factor Q . Other issues, such as the effect of aliasing at high temporal frequencies, dependent on the spectral slope and data sampling, come into the picture for unevenly-sampled data for all detection methods. Since such in-depth discussions are beyond the purview and objectives of the current study, we encourage readers who have a particular sample pattern in mind to run simulations for all approaches to assist estimate detection rates of both true and false positives. The presence of red noise can make the ACF and PDM values significantly self-correlated. Therefore, we want to caution the users that they cannot use these tools to consistently separate a narrow-band signal from the red noise continuum and characterise the form of that continuum.

We, therefore, urge the community to take into account the testing of alternative approaches, such as Bayesian fits (e.g. CARMA; Zhu et al. 2020) and the creation of automated light curve classifiers (for example, Sánchez-Sáez et al. 2021), which may be able to quantify departures from pure-red noise behaviour. However, it is beyond the purview of the present research to compare how different approaches, whether modern or classical ones (such as ACF, PDM, and periodogram), perform better in maximising the true positive detections and decreasing false detections.

Finally, irrespective of the statistical approach utilized, we strongly recommend readers disclose the inferred value of the RMS (or, equivalently, RMS/mean) of the QPO together with the timescale in any of the QPO findings they make ahead. The RMS contains extra information regarding the

physical characteristics of the periodic process and/or variability mechanism (for example, observer viewing angles, jet angle parameters, and energy dependency of a variability mechanism). However, this information is often overlooked in publications on QPO claims.

If additional avenues and methods (imaging, spectroscopy) are available, it is expected that, hopefully, the physical characteristics inferred by the QPO strength will be compatible with the physical information acquired from other ways.

4.2 Summary and conclusions on the results on the multi-wavelength campaign on a flaring Seyfert detected with eROSITA

Drastic variability is observed in the AGN emission on all timescales and at all wavelengths. In a small number of Seyferts and quasars, drastic changes are observed in the X-ray and/or optical flux which leads to significant changes in their spectral properties. These variations are significantly greater than the "normal" stochastic variations associated with persistent accretion. There are various physical processes, many of which still remain poorly understood, that can trigger mass flow onto the supermassive black hole (SMBH) igniting or shutting down the AGN. The accretion phase of AGN is likely episodic and hence, the study of these extremely variable sources will help to improve our understanding of accretion processes and AGN duty cycles. So far only a few samples of such Changing Look AGNs have been discovered.

eROSITA performs all-sky X-ray surveys every six months, monitoring roughly about half a million AGN and is capable of identifying these rare, accretion ignition/shut-down events as they occur. The regular, multi-year monitoring of such a large AGN sample helps to gather a huge database of AGN X-ray variability. Multi-wavelength follow-up programmes are used to systematically track the evolution of individual X-ray spectral components, UV/optical accretion disk, and the illumination of the broad-line region (BLR) responding to major changes in the accretion rate and flux changes. In this work, we presented a study on a flaring AGN detected with eROSITA, where the source was caught flaring where there was a sudden increase and then a decrease in the X-ray flux (0.2–5 keV) over a period of approximately six months. Multi-wavelength follow-up observations with XMM-Newton (EPIC+OM) and NICER were made during the flaring and post-flaring times of the source along with simultaneous optical monitoring using VLT (FORIS2), SALT, SAAO at different epochs of the flaring and decaying stages of the source to constrain the rate and extent of these drastic flux changes and yield crucial constraints on how the different structural AGN components respond to changes in the accretion rate. The source also flared in the optical and infrared bands, as determined by public photometry from ATLAS and WISE's NEOWISE scans.

We modelled and compared the X-ray spectra taken during the outburst and during the declining flux state of the source to understand the nature and the underlying reason for the sudden increase in luminosity at the multi-wavelength continuum. Fitting the XMM-Newton spectra revealed the soft excess present in both observations. We fit the 0.2–10 keV data with the phenomenological

model and then quantify the soft excess below 2 keV with respect to this model. A simple power-law model was found to be the best fit phenomenological model for the soft excess, where its photon index varied between the two epochs from $\Gamma_{\text{SX}} \sim 2.78 \pm 0.04$ to $\Gamma_{\text{SX}} \sim 2.2 \pm 0.07$. The spectra of the soft X-ray photons were softer during the flaring state and got harder as the source went back to lower flux levels.

We demonstrated that the broadband SED of J0408–38, from optical to X-rays (and including the soft X-ray excess), could be modeled with thermal Comptonization models. We used both the AGNSED model and a double thermal-Comptonization model. In the AGNSED model, we assume a hot, optically-thin corona/truncated-disc geometry where the optically thicker and colder outer disc is covered by a warm corona extending until the truncation radius. From the best-fitting parameters, we observe the radial distance of the hot corona region to increase from $R_{\text{hot}} \sim 23$ to $92R_g$ from the outburst to the declining flux state. Meanwhile, the warm Comptonizing region decreases; the temperature is noticed to decrease from $kT_{\text{e,warm}} \sim 0.36$ to 0.20 keV and with the photon index changing from $\Gamma_{\text{warm}} \sim 2.73$ to $\Gamma_{\text{warm}} \sim 2.38$ from the flaring state to the post-flaring state. The nature of the soft excess in our source from the best-fit models supports the origin due to warm Comptonization.

In the context of the AGNSED model, the multi-wavelength flaring is the result of a change in the accretion rate \dot{m} , i.e., the accretion rate decreases between the two XMM-Newton observations, as the UV flux tracks the disk output, and this change of \dot{m} goes along with a change of the truncation radius. On the other hand, the decrease in the accretion rate and increase in the truncation radius naturally decreases the temperature of the warm corona. The increase in mass accretion inward through the accretion disk increases the optical luminosity, then in UV luminosity as local \dot{m} travels inward and reaches inner flow, and it drives an increase in corona X-ray luminosity with cooling of corona and spectral steepening which is consistent with XMM spectral observations for J0408-38. But the fluctuations would travel at the viscous timescale which is typical of order decades–centuries for a standard geometrically thin, an optically-thick disk which is too long. However, if the disk is geometrically thick (H/R approaches one) yet still emits thermally, then the viscous timescale becomes much shorter (tending towards the thermal timescale) and either way, there will be an associated time delay from optical to UV to X-ray. Future works having multi-wavelength campaigns and observations can shed light on any recurrent flaring and support the disk instability mechanisms.

The simultaneous optical spectroscopic monitoring of the source at different epochs during the outburst phase and declining phase reveals the dimming HeII line which gradually disappears roughly tracking the optical/UV and X-ray continuum. We calculated the flux of the emission line intensities by integrating the best fit gaussian profiles for the corresponding wavelength ranges and see that the HeII line flux decreases (from 100.099×10^{-16} erg cm⁻² s⁻¹ to 8.76×10^{-16} erg cm⁻² s⁻¹) and then vanishes (upper limit of 2.745×10^{-17} erg cm⁻² s⁻¹).

The HeII and H β emission lines could likely arise from the same virial structure but at different radial regions of the BLR. In the case of J0408–38, the observation of HeII emission varying much

more strongly than $H\beta$ emission could, speculatively, indicate diverging physical conditions (geometry, density, or illumination) between the two radially distinct emission regions. An alternate explanation could be that the HeII and $H\beta$ emissions have divergent responsivities which define qualitatively how much the intensity of the emission lines varies for a given variation in the ionization continuum flux.

We observe a broad, redshifted emission component in the optical spectrum taken during the flaring state (spectrum #1- FORS2) of J0408-38 modeled with a Gaussian with the energy centroid suggesting the gas inflowing with a bulk velocity of order $\sim 3618 \text{ km s}^{-1}$. It is not clear if the bulk inflow could directly be associated with the flaring continuum. However, the transient nature of this red wing combined with the relative stability of the other broad $H\beta$ component ("broad component 1") seems to favor a component physically distinct from the BLR. The inflow of matter could be speculatively be associated with a "Failed Radiatively Accelerated Dusty Outflow" (FRADO; Czerny et al. 2011; Naddaf et al. 2021) where the BLR is formed as a dusty wind flowing upwards from the disk and pushed radially outwards by radiation pressure. The dynamical simulations of Naddaf et al. (2021) predict that wind heights and velocities depend on the accretion rate of the source, but infall velocities could range between hundreds to thousands of km s^{-1} . It is (speculatively) possible that the FORS2 spectrum caught emission from such an infalling component, which then faded or impacted into the accretion disk by spectrum #2, 19 days later.

Chapter 5

Acknowledgements

First project in Chapter 2

SK, Co-author AM, and Co-author ASC acknowledge support from Narodowe Centrum Nauki (NCN) grant 2016/23/B/ST9/03123. SK and Co-author AM also acknowledge partial support from NCN grant 2018/31/G/ST9/03224. SK and Co-author AM thank T. Bogdanovic for useful discussions on applications to physical systems.

Second project in Chapter 3

SK, Co-author AM, and Co-author TS acknowledge partial support from Narodowe Centrum Nauki (NCN) grants 2016/23/B/ST9/03123 and 2018/31/G/ST9/03224. Co-author AM also acknowledges partial support from NCN grant 2019/35/B/ST9/03944. Co-author DH acknowledges support from DLR grant FKZ 50 OR 2003. Co-author MK is supported by DFG grant KR 3338/4-1. Co-author SH is supported by the German Science Foundation (DFG grant number WI 1860/14-1). This work is based on data from eROSITA, the soft X-ray instrument aboard SRG, a joint Russian-German science mission supported by the Russian Space Agency (Roskosmos), in the interests of the Russian Academy of Sciences represented by its Space Research Institute (IKI), and the Deutsches Zentrum für Luft und Raumfahrt (DLR). The SRG spacecraft was built by Lavochkin Association (NPOL) and its subcontractors and is operated by NPOL with support from the Max Planck Institute for Extraterrestrial Physics (MPE). The development and construction of the eROSITA X-ray instrument were led by MPE, with contributions from the Dr. Karl Remeis Observatory Bamberg & ECAP (FAU Erlangen-Nuernberg), the University of Hamburg Observatory, the Leibniz Institute for Astrophysics Potsdam (AIP), and the Institute for Astronomy and Astrophysics of the University of Tübingen, with the support of DLR and the Max Planck Society. The Argelander Institute for Astronomy of the University of Bonn and the Ludwig Maximilians Universität Munich also participated in the science preparation for eROSITA. The eROSITA data shown here were processed using the eSASS software system developed by the German eROSITA consortium. Some of the observations reported in this work were obtained with the Southern African Large Telescope (SALT) under programs 2020-2-MLT-008 and 2021-2-MLT-003. Polish participation in SALT is funded by grant No. MEiN nr 2021/WK/01. This research has made

use of data and/or software provided by the High Energy Astrophysics Science Archive Research Center (HEASARC), which is a service of the Astrophysics Science Division at NASA/GSFC.

Bibliography

- Abbott, BP et al. (2016a). “GW151226: observation of gravitational waves from a 22-solar-mass binary black hole coalescence”. In: *Physical review letters* 116.24, p. 241103.
- Abbott, BP et al. (2017). “GW170814: a three-detector observation of gravitational waves from a binary black hole coalescence”. In: *Physical review letters* 119.14, p. 141101.
- Abbott, BP et al. (2016b). “Observation of gravitational waves from a binary black hole merger”. In: *Physical review letters* 116.6, p. 061102.
- Abbott, R et al. (2020a). “GW190412: Observation of a binary-black-hole coalescence with asymmetric masses”. In: *Physical Review D* 102.4, p. 043015.
- (2020b). “GW190521: a binary black hole merger with a total mass of 150 M_{\odot} ”. In: *Physical review letters* 125.10, p. 101102.
- Abraham, Z. (Mar. 2000). “Precession, beaming and the periodic light curve of OJ287”. In: *Astronomy & Astrophysics* 355, pp. 915–921.
- Abramowicz, M. A. and W. Kluźniak (Aug. 2001). “A precise determination of black hole spin in GRO J1655-40”. In: *Astronomy & Astrophysics* 374, pp. L19–L20. DOI: [10.1051/0004-6361:20010791](https://doi.org/10.1051/0004-6361:20010791). arXiv: [astro-ph/0105077](https://arxiv.org/abs/astro-ph/0105077) [astro-ph].
- Abramowicz, MA et al. (1988). “Slim accretion disks”. In: *The Astrophysical Journal* 332, pp. 646–658.
- Acciari, V. A. et al. (Sept. 2011). “TeV and Multi-wavelength Observations of Mrk 421 in 2006-2008”. In: *The Astrophysical Journal* 738.1, 25, p. 25. DOI: [10.1088/0004-637X/738/1/25](https://doi.org/10.1088/0004-637X/738/1/25). arXiv: [1106.1210](https://arxiv.org/abs/1106.1210) [astro-ph.HE].
- Ackermann, M. et al. (Nov. 2015). “Multiwavelength Evidence for Quasi-periodic Modulation in the Gamma-Ray Blazar PG 1553+113”. In: *The Astrophysical Journal, Letters* 813.2, L41, p. L41. DOI: [10.1088/2041-8205/813/2/L41](https://doi.org/10.1088/2041-8205/813/2/L41). arXiv: [1509.02063](https://arxiv.org/abs/1509.02063) [astro-ph.HE].
- Adams, David J et al. (2004). *An introduction to galaxies and cosmology*. Cambridge University Press.
- Alexander, D. M. et al. (Oct. 2005). “The X-Ray Spectral Properties of SCUBA Galaxies”. In: *The Astrophysical Journal* 632.2, pp. 736–750. DOI: [10.1086/444342](https://doi.org/10.1086/444342). arXiv: [astro-ph/0506608](https://arxiv.org/abs/astro-ph/0506608) [astro-ph].

- Alexander, Tal (Feb. 2013). "Improved AGN light curve analysis with the z-transformed discrete correlation function". In: *arXiv e-prints*, arXiv:1302.1508, arXiv:1302.1508. arXiv: [1302.1508](#) [[astro-ph.IM](#)].
- Alston, W. N. et al. (Nov. 2014). "Detection of a QPO in five XMM-Newton observations of RE J1034+396." In: *Monthly Notices of the Royal Astronomical Society* 445, pp. L16–L20. DOI: [10.1093/mnras1/slu127](#). arXiv: [1407.7657](#) [[astro-ph.HE](#)].
- Alston, W. N. et al. (May 2015). "Discovery of an ~ 2 -h high-frequency X-ray QPO and iron $K\alpha$ reverberation in the active galaxy MS 2254.9-3712". In: *Monthly Notices of the Royal Astronomical Society* 449.1, pp. 467–476. DOI: [10.1093/mnras/stv351](#). arXiv: [1411.0684](#) [[astro-ph.HE](#)].
- Alston, W. N. et al. (2019). "The remarkable X-ray variability of IRAS 13224-3809 - I. The variability process". In: *Monthly Notices of the Royal Astronomical Society* 482.2, pp. 2088–2106. DOI: [10.1093/mnras/sty2527](#). arXiv: [1803.10444](#) [[astro-ph.HE](#)].
- Anderson, James M. and James S. Ulvestad (July 2005). "The Size of the Radio-Emitting Region in Low-Luminosity Active Galactic Nuclei". In: *The Astrophysical Journal* 627.2, pp. 674–700. DOI: [10.1086/430463](#). arXiv: [astro-ph/0504066](#) [[astro-ph](#)].
- Antonucci, R. R. J. and J. S. Miller (Oct. 1985). "Spectropolarimetry and the nature of NGC 1068." In: *The Astrophysical Journal* 297, pp. 621–632. DOI: [10.1086/163559](#).
- Antonucci, Robert (Jan. 1993). "Unified models for active galactic nuclei and quasars." In: *Annual Review of Astronomy Astrophysics* 31, pp. 473–521. DOI: [10.1146/annurev.aa.31.090193.002353](#).
- Appenzeller, I. et al. (Dec. 1998). "Successful commissioning of FORS1 - the first optical instrument on the VLT." In: *The Messenger* 94, pp. 1–6.
- Arcodia, R. et al. (Apr. 2021). "X-ray quasi-periodic eruptions from two previously quiescent galaxies". In: 592.7856, pp. 704–707. DOI: [10.1038/s41586-021-03394-6](#). arXiv: [2104.13388](#) [[astro-ph.HE](#)].
- Arnaud, K. A. (Jan. 1996). "XSPEC: The First Ten Years". In: *Astronomical Data Analysis Software and Systems V*. Ed. by George H. Jacoby and Jeannette Barnes. Vol. 101. Astronomical Society of the Pacific Conference Series, p. 17.
- Arnaud, K. A. et al. (Nov. 1985). "EXOSAT observations of a strong soft X-ray excess in MKN 841." In: *Monthly Notices of the Royal Astronomical Society* 217, pp. 105–113. DOI: [10.1093/mnras/217.1.105](#).
- Ashton, Dominic I. and Matthew J. Middleton (Mar. 2021). "Searching for energy-resolved quasi-periodic oscillations in AGN". In: *Monthly Notices of the Royal Astronomical Society* 501.4, pp. 5478–5499. DOI: [10.1093/mnras/staa4024](#). arXiv: [2101.01194](#) [[astro-ph.HE](#)].
- Avni, Y. and H. Tananbaum (June 1986). "X-Ray Properties of Optically Selected QSOs". In: *The Astrophysical Journal* 305, p. 83. DOI: [10.1086/164230](#).

- Axelsson, M., L. Borgonovo, and S. Larsson (Aug. 2005). "Evolution of the 0.01-25 Hz power spectral components in Cygnus X-1". In: *Astronomy & Astrophysics* 438.3, pp. 999–1012. DOI: [10.1051/0004-6361:20042362](https://doi.org/10.1051/0004-6361:20042362). arXiv: [astro-ph/0504446](https://arxiv.org/abs/astro-ph/0504446) [astro-ph].
- Baade, W. and R. Minkowski (Jan. 1954). "On the Identification of Radio Sources." In: *The Astrophysical Journal* 119, p. 215. DOI: [10.1086/145813](https://doi.org/10.1086/145813).
- Ballantyne, D. R., R. R. Ross, and A. C. Fabian (Oct. 2001). "X-ray reflection by photoionized accretion discs". In: *Monthly Notices of the Royal Astronomical Society* 327.1, pp. 10–22. DOI: [10.1046/j.1365-8711.2001.04432.x](https://doi.org/10.1046/j.1365-8711.2001.04432.x). arXiv: [astro-ph/0102040](https://arxiv.org/abs/astro-ph/0102040) [astro-ph].
- Bannikova, E Yu et al. (2021). "Dynamical model of an obscuring clumpy torus in AGNs–I. Velocity and velocity dispersion maps for interpretation of ALMA observations". In: *Monthly Notices of the Royal Astronomical Society* 503.1, pp. 1459–1472.
- Barvainis, Richard (Sept. 1987). "Hot Dust and the Near-Infrared Bump in the Continuum Spectra of Quasars and Active Galactic Nuclei". In: *The Astrophysical Journal* 320, p. 537. DOI: [10.1086/165571](https://doi.org/10.1086/165571).
- Barvainis, Richard et al. (Jan. 2005). "Radio Variability of Radio-quiet and Radio-loud Quasars". In: *The Astrophysical Journal* 618.1, pp. 108–122. DOI: [10.1086/425859](https://doi.org/10.1086/425859). arXiv: [astro-ph/0409554](https://arxiv.org/abs/astro-ph/0409554) [astro-ph].
- Beckmann, V. and C. Shrader (Jan. 2012). "The AGN phenomenon: open issues". In: *Proceedings of "An INTEGRAL view of the high-energy sky (the first 10 years)" - 9th INTEGRAL Workshop and celebration of the 10th anniversary of the launch (INTEGRAL 2012). 15-19 October 2012. Bibliotheque Nationale de France*, 69, p. 69. DOI: [10.22323/1.176.0069](https://doi.org/10.22323/1.176.0069). arXiv: [1302.1397](https://arxiv.org/abs/1302.1397) [astro-ph.HE].
- Belloni, T. et al. (Apr. 1997). "An Unstable Central Disk in the Superluminal Black Hole X-Ray Binary GRS 1915+105". In: *The Astrophysical Journal, Letters* 479.2, pp. L145–L148. DOI: [10.1086/310595](https://doi.org/10.1086/310595). arXiv: [astro-ph/9702048](https://arxiv.org/abs/astro-ph/9702048) [astro-ph].
- Belloni, Tomaso, Dimitrios Psaltis, and Michiel van der Klis (June 2002). "A Unified Description of the Timing Features of Accreting X-Ray Binaries". In: *The Astrophysical Journal* 572.1, pp. 392–406. DOI: [10.1086/340290](https://doi.org/10.1086/340290). arXiv: [astro-ph/0202213](https://arxiv.org/abs/astro-ph/0202213) [astro-ph].
- Beloborodov, Andrei M (1999). "Electron-positron outflows from gamma-ray emitting accretion discs". In: *Monthly Notices of the Royal Astronomical Society* 305.1, pp. 181–189.
- Bentz, Misty C. et al. (Apr. 2013). "The Low-luminosity End of the Radius-Luminosity Relationship for Active Galactic Nuclei". In: *The Astrophysical Journal* 767.2, 149, p. 149. DOI: [10.1088/0004-637X/767/2/149](https://doi.org/10.1088/0004-637X/767/2/149). arXiv: [1303.1742](https://arxiv.org/abs/1303.1742) [astro-ph.CO].
- Berti, Emanuele (2006). "LISA observations of massive black hole mergers: event rates and issues in waveform modelling". In: *Classical and Quantum Gravity* 23.19, S785.

- Best, PN et al. (2005). "The host galaxies of radio-loud active galactic nuclei: mass dependences, gas cooling and active galactic nuclei feedback". In: *Monthly Notices of the Royal Astronomical Society* 362.1, pp. 25–40.
- Bianchi, Stefano et al. (2008). "NGC 3147: a 'true'type 2 Seyfert galaxy without the broad-line region". In: *Monthly Notices of the Royal Astronomical Society* 385.1, pp. 195–199.
- Blanchard, P. K. et al. (July 2017). "PS16dtm: A Tidal Disruption Event in a Narrow-line Seyfert 1 Galaxy". In: *The Astrophysical Journal* 843.2, 106, p. 106. DOI: [10.3847/1538-4357/aa77f7](https://doi.org/10.3847/1538-4357/aa77f7). arXiv: [1703.07816](https://arxiv.org/abs/1703.07816) [astro-ph.HE].
- Blandford, RD and CF McKee (1982a). "Reverberation mapping of the emission line regions of Seyfert galaxies and quasars". In: *The Astrophysical Journal* 255, pp. 419–439.
- Blandford, RD and DG Payne (1982b). "Hydromagnetic flows from accretion discs and the production of radio jets". In: *Monthly Notices of the Royal Astronomical Society* 199.4, pp. 883–903.
- Blandford, Roger D and Roman L Znajek (1977). "Electromagnetic extraction of energy from Kerr black holes". In: *Monthly Notices of the Royal Astronomical Society* 179.3, pp. 433–456.
- Blustin, A. J. et al. (Apr. 2007). "The mass-energy budget of the ionised outflow in NGC 7469". In: *Astronomy & Astrophysics* 466.1, pp. 107–118. DOI: [10.1051/0004-6361:20066883](https://doi.org/10.1051/0004-6361:20066883). arXiv: [astro-ph/0702311](https://arxiv.org/abs/astro-ph/0702311) [astro-ph].
- Blustin, A. J. et al. (Feb. 2005). "The nature and origin of Seyfert warm absorbers". In: *Astronomy & Astrophysics* 431, pp. 111–125. DOI: [10.1051/0004-6361:20041775](https://doi.org/10.1051/0004-6361:20041775). arXiv: [astro-ph/0411297](https://arxiv.org/abs/astro-ph/0411297) [astro-ph].
- Bolton, J. G., G. J. Stanley, and O. B. Slee (July 1949). "Positions of Three Discrete Sources of Galactic Radio-Frequency Radiation". In: 164.4159, pp. 101–102. DOI: [10.1038/164101b0](https://doi.org/10.1038/164101b0).
- Bon, E. et al. (Aug. 2016). "Evidence for Periodicity in 43 year-long Monitoring of NGC 5548". In: *The Astrophysical Journal, Supplement* 225.2, 29, p. 29. DOI: [10.3847/0067-0049/225/2/29](https://doi.org/10.3847/0067-0049/225/2/29). arXiv: [1606.04606](https://arxiv.org/abs/1606.04606) [astro-ph.HE].
- Breedt, Elme Brredt (2009). "The relationship between the x-ray and optical variability in Seyfert Galaxies". PhD thesis. University of Southampton. URL: <https://eprints.soton.ac.uk/161201/>.
- Britzen, S. et al. (Aug. 2018). "OJ287: deciphering the 'Rosetta stone of blazars'". In: *Monthly Notices of the Royal Astronomical Society* 478.3, pp. 3199–3219. DOI: [10.1093/mnras/sty1026](https://doi.org/10.1093/mnras/sty1026).
- Bruhweiler, F. and E. Verner (Mar. 2008). "Modeling Fe II Emission and Revised Fe II (UV) Empirical Templates for the Seyfert 1 Galaxy I Zw 1". In: *The Astrophysical Journal* 675.1, pp. 83–95. DOI: [10.1086/525557](https://doi.org/10.1086/525557).
- Bruzual, G. and S. Charlot (Oct. 2003). "Stellar population synthesis at the resolution of 2003". In: *Monthly Notices of the Royal Astronomical Society* 344.4, pp. 1000–1028. DOI: [10.1046/j.1365-8711.2003.06897.x](https://doi.org/10.1046/j.1365-8711.2003.06897.x). arXiv: [astro-ph/0309134](https://arxiv.org/abs/astro-ph/0309134) [astro-ph].

- Buchner, Johannes and Franz E. Bauer (Mar. 2017). "Galaxy gas as obscurer - II. Separating the galaxy-scale and nuclear obscurers of active galactic nuclei". In: *Monthly Notices of the Royal Astronomical Society* 465.4, pp. 4348–4362. DOI: [10.1093/mnras/stw2955](https://doi.org/10.1093/mnras/stw2955). arXiv: [1610.09380](https://arxiv.org/abs/1610.09380) [astro-ph.HE].
- Buckley, David A. H., Gerhard P. Swart, and Jacobus G. Meiring (June 2006). "Completion and commissioning of the Southern African Large Telescope". In: *Society of Photo-Optical Instrumentation Engineers (SPIE) Conference Series*. Ed. by Larry M. Stepp. Vol. 6267. Society of Photo-Optical Instrumentation Engineers (SPIE) Conference Series, 62670Z, 62670Z. DOI: [10.1117/12.673750](https://doi.org/10.1117/12.673750).
- Burgh, Eric B. et al. (Mar. 2003). "Prime Focus Imaging Spectrograph for the Southern African Large Telescope: optical design". In: *Instrument Design and Performance for Optical/Infrared Ground-based Telescopes*. Ed. by Masanori Iye and Alan F. M. Moorwood. Vol. 4841. Society of Photo-Optical Instrumentation Engineers (SPIE) Conference Series, pp. 1463–1471. DOI: [10.1117/12.460312](https://doi.org/10.1117/12.460312).
- Burtscher, L. et al. (Oct. 2013). "A diversity of dusty AGN tori. Data release for the VLTI/MIDI AGN Large Program and first results for 23 galaxies". In: *Astronomy & Astrophysics* 558, A149, A149. DOI: [10.1051/0004-6361/201321890](https://doi.org/10.1051/0004-6361/201321890). arXiv: [1307.2068](https://arxiv.org/abs/1307.2068) [astro-ph.CO].
- Cannizzo, John K. (July 1996). "The Nature of the Giant Outbursts in the Bursting Pulsar GRO J1744-28". In: *The Astrophysical Journal, Letters* 466, p. L31. DOI: [10.1086/310167](https://doi.org/10.1086/310167). arXiv: [astro-ph/9605127](https://arxiv.org/abs/astro-ph/9605127) [astro-ph].
- Cardelli, Jason A., Geoffrey C. Clayton, and John S. Mathis (Oct. 1989). "The Relationship between Infrared, Optical, and Ultraviolet Extinction". In: *The Astrophysical Journal* 345, p. 245. DOI: [10.1086/167900](https://doi.org/10.1086/167900).
- Carrara, E. A. et al. (Nov. 1993). "The milliarcsecond structure of the quasar 3C 279." In: *Astronomy & Astrophysics* 279, pp. 83–89.
- Carroll, Sean M (2004). "An introduction to general relativity: spacetime and geometry". In: *Addison Wesley* 101, p. 102.
- Casella, P. et al. (2004). "A study of the low-frequency quasi-periodic oscillations in the X-ray light curves of the black hole candidate <ASTROBJ>XTE J1859+226</ASTROBJ>". In: *Astronomy & Astrophysics* 426, pp. 587–600. DOI: [10.1051/0004-6361:20041231](https://doi.org/10.1051/0004-6361:20041231). arXiv: [astro-ph/0407262](https://arxiv.org/abs/astro-ph/0407262) [astro-ph].
- Chakraborty, Joheen et al. (Nov. 2021). "Possible X-Ray Quasi-periodic Eruptions in a Tidal Disruption Event Candidate". In: *The Astrophysical Journal, Letters* 921.2, L40, p. L40. DOI: [10.3847/2041-8213/ac313b](https://doi.org/10.3847/2041-8213/ac313b). arXiv: [2110.10786](https://arxiv.org/abs/2110.10786) [astro-ph.HE].
- Chan, Chi-Ho et al. (Aug. 2019). "Tidal Disruption Events in Active Galactic Nuclei". In: *The Astrophysical Journal* 881.2, 113, p. 113. DOI: [10.3847/1538-4357/ab2b40](https://doi.org/10.3847/1538-4357/ab2b40). arXiv: [1904.12261](https://arxiv.org/abs/1904.12261) [astro-ph.HE].

- Charisi, M. et al. (2016). "A population of short-period variable quasars from PTF as supermassive black hole binary candidates". In: *Monthly Notices of the Royal Astronomical Society* 463.2, pp. 2145–2171. DOI: [10.1093/mnras/stw1838](https://doi.org/10.1093/mnras/stw1838). arXiv: [1604.01020](https://arxiv.org/abs/1604.01020) [astro-ph.GA].
- Chatterjee, Ritaban et al. (June 2018). "Possible Accretion Disk Origin of the Emission Variability of a Blazar Jet". In: *The Astrophysical Journal, Letters* 859.2, L21, p. L21. DOI: [10.3847/2041-8213/aac48a](https://doi.org/10.3847/2041-8213/aac48a). arXiv: [1805.06222](https://arxiv.org/abs/1805.06222) [astro-ph.HE].
- Corral, A. et al. (June 2011). "The X-ray spectral properties of the AGN population in the XMM-Newton bright serendipitous survey". In: *Astronomy & Astrophysics* 530, A42, A42. DOI: [10.1051/0004-6361/201015227](https://doi.org/10.1051/0004-6361/201015227). arXiv: [1104.2173](https://arxiv.org/abs/1104.2173) [astro-ph.CO].
- Couto, J. D. et al. (Dec. 2016). "New Insights into the Spectral Variability and Physical Conditions of the X-Ray Absorbers in NGC 4151". In: *The Astrophysical Journal* 833.2, 191, p. 191. DOI: [10.3847/1538-4357/833/2/191](https://doi.org/10.3847/1538-4357/833/2/191). arXiv: [1610.05689](https://arxiv.org/abs/1610.05689) [astro-ph.GA].
- Crause, Lisa A. et al. (Apr. 2019). "SpUpNIC (Spectrograph Upgrade: Newly Improved Cassegrain): a versatile and efficient low- to medium-resolution, long-slit spectrograph on the South African Astronomical Observatory's 1.9-m telescope". In: *J. Astron. Telescopes, Instruments, and Systems* 5, p. 024007. DOI: [10.1117/1.JATIS.5.2.024007](https://doi.org/10.1117/1.JATIS.5.2.024007).
- Crummy, J. et al. (Feb. 2006). "An explanation for the soft X-ray excess in active galactic nuclei". In: *Monthly Notices of the Royal Astronomical Society* 365.4, pp. 1067–1081. DOI: [10.1111/j.1365-2966.2005.09844.x](https://doi.org/10.1111/j.1365-2966.2005.09844.x). arXiv: [astro-ph/0511457](https://arxiv.org/abs/astro-ph/0511457) [astro-ph].
- Czerny, B. and K. Hryniewicz (Jan. 2011). "The origin of the broad line region in active galactic nuclei". In: *Astronomy & Astrophysics* 525, L8, p. L8. DOI: [10.1051/0004-6361/201016025](https://doi.org/10.1051/0004-6361/201016025). arXiv: [1010.6201](https://arxiv.org/abs/1010.6201) [astro-ph.CO].
- Dai, Xinyu et al. (Apr. 2004). "A Study of Quasar Evolution in the X-Ray Band with the Aid of Gravitational Lensing". In: *The Astrophysical Journal* 605.1, pp. 45–57. DOI: [10.1086/382205](https://doi.org/10.1086/382205). arXiv: [astro-ph/0401013](https://arxiv.org/abs/astro-ph/0401013) [astro-ph].
- Dauser, T et al. (2010). "Broad emission lines for a negatively spinning black hole". In: *Monthly Notices of the Royal Astronomical Society* 409.4, pp. 1534–1540.
- Davis, Shane W., Jong-Hak Woo, and Omer M. Blaes (Oct. 2007). "The UV Continuum of Quasars: Models and SDSS Spectral Slopes". In: *The Astrophysical Journal* 668.2, pp. 682–698. DOI: [10.1086/521393](https://doi.org/10.1086/521393). arXiv: [0707.1456](https://arxiv.org/abs/0707.1456) [astro-ph].
- De Marco, B. et al. (Dec. 2015). "The evolution of the disc variability along the hard state of the black hole transient GX 339-4". In: *Monthly Notices of the Royal Astronomical Society* 454.3, pp. 2360–2371. DOI: [10.1093/mnras/stv1990](https://doi.org/10.1093/mnras/stv1990). arXiv: [1509.00043](https://arxiv.org/abs/1509.00043) [astro-ph.HE].
- Dexter, Jason and Mitchell C. Begelman (Feb. 2019). "Extreme AGN variability: evidence of magnetically elevated accretion?" In: *Monthly Notices of the Royal Astronomical Society* 483.1, pp. L17–L21. DOI: [10.1093/mnrasl/sly213](https://doi.org/10.1093/mnrasl/sly213). arXiv: [1807.03314](https://arxiv.org/abs/1807.03314) [astro-ph.GA].

- Di Gesu, L. et al. (Mar. 2014). “Simultaneous XMM-Newton and HST-COS observation of 1H 0419-577. II. Broadband spectral modeling of a variable Seyfert galaxy”. In: *Astronomy & Astrophysics* 563, A95, A95. DOI: [10.1051/0004-6361/201322916](https://doi.org/10.1051/0004-6361/201322916). arXiv: [1401.5614](https://arxiv.org/abs/1401.5614) [astro-ph.HE].
- Dicken, D. et al. (Mar. 2009). “The Origin of the Infrared Emission in Radio Galaxies. II. Analysis of Mid- to Far-Infrared Spitzer Observations of the 2Jy Sample”. In: *The Astrophysical Journal* 694.1, pp. 268–285. DOI: [10.1088/0004-637X/694/1/268](https://doi.org/10.1088/0004-637X/694/1/268). arXiv: [0810.5675](https://arxiv.org/abs/0810.5675) [astro-ph].
- Done, C. et al. (Oct. 2007). “The Origin of the Soft Excess in AGN”. In: *The Central Engine of Active Galactic Nuclei*. Ed. by L. C. Ho and J. W. Wang. Vol. 373. Astronomical Society of the Pacific Conference Series, p. 121. arXiv: [astro-ph/0703449](https://arxiv.org/abs/astro-ph/0703449) [astro-ph].
- D’Orazio, Daniel J. and 2018MNRAS.474.2975D Di Stefano Rosanne (Mar. 2018). “Periodic self-lensing from accreting massive black hole binaries”. In: *Monthly Notices of the Royal Astronomical Society* 474.3, pp. 2975–2986. DOI: [10.1093/mnras/stx2936](https://doi.org/10.1093/mnras/stx2936). arXiv: [1707.02335](https://arxiv.org/abs/1707.02335) [astro-ph.HE].
- Drake, A. J. et al. (July 2011). “The Discovery and Nature of the Optical Transient CSS100217:102913+404220”. In: *The Astrophysical Journal* 735.2, 106, p. 106. DOI: [10.1088/0004-637X/735/2/106](https://doi.org/10.1088/0004-637X/735/2/106). arXiv: [1103.5514](https://arxiv.org/abs/1103.5514) [astro-ph.CO].
- Ebrero, J. et al. (Jan. 2009). “The XMM-Newton serendipitous survey. VI. The X-ray luminosity function”. In: *Astronomy & Astrophysics* 493.1, pp. 55–69. DOI: [10.1051/0004-6361:200810919](https://doi.org/10.1051/0004-6361:200810919). arXiv: [0811.1450](https://arxiv.org/abs/0811.1450) [astro-ph].
- Eckart, A. and R. Genzel (Oct. 1996). “Observations of stellar proper motions near the Galactic Centre”. In: 383.6599, pp. 415–417. DOI: [10.1038/383415a0](https://doi.org/10.1038/383415a0).
- (Jan. 1997). “Stellar proper motions in the central 0.1 PC of the Galaxy”. In: *Monthly Notices of the Royal Astronomical Society* 284.3, pp. 576–598. DOI: [10.1093/mnras/284.3.576](https://doi.org/10.1093/mnras/284.3.576).
- Edelson, R. et al. (Jan. 2019). “The First Swift Intensive AGN Accretion Disk Reverberation Mapping Survey”. In: *The Astrophysical Journal* 870.2, 123, p. 123. DOI: [10.3847/1538-4357/aaf3b4](https://doi.org/10.3847/1538-4357/aaf3b4). arXiv: [1811.07956](https://arxiv.org/abs/1811.07956) [astro-ph.HE].
- Edelson, R. A. and J. H. Krolik (Oct. 1988). “The Discrete Correlation Function: A New Method for Analyzing Unevenly Sampled Variability Data”. In: *The Astrophysical Journal* 333, p. 646. DOI: [10.1086/166773](https://doi.org/10.1086/166773).
- Edelson, R. A. et al. (Oct. 1996). “Multiwavelength Observations of Short-Timescale Variability in NGC 4151. IV. Analysis of Multiwavelength Continuum Variability”. In: *The Astrophysical Journal* 470, p. 364. DOI: [10.1086/177872](https://doi.org/10.1086/177872). arXiv: [astro-ph/9605082](https://arxiv.org/abs/astro-ph/9605082) [astro-ph].
- Edelson, Rick and Kirpal Nandra (Apr. 1999). “A Cutoff in the X-Ray Fluctuation Power Density Spectrum of the Seyfert 1 Galaxy NGC 3516”. In: *The Astrophysical Journal* 514.2, pp. 682–690. DOI: [10.1086/306980](https://doi.org/10.1086/306980). arXiv: [astro-ph/9810481](https://arxiv.org/abs/astro-ph/9810481) [astro-ph].

- Edelson, Rick et al. (Apr. 2002). "X-Ray Spectral Variability and Rapid Variability of the Soft X-Ray Spectrum Seyfert 1 Galaxies Arakelian 564 and Ton S180". In: *The Astrophysical Journal* 568.2, pp. 610–626. DOI: [10.1086/323779](https://doi.org/10.1086/323779). arXiv: [astro-ph/0108387](https://arxiv.org/abs/astro-ph/0108387) [[astro-ph](#)].
- Elitzur, Moshe (2012). "On the unification of active galactic nuclei". In: *The Astrophysical Journal Letters* 747.2, p. L33.
- (2006). "The obscuring torus in AGN". In: *New Astronomy Reviews* 50.9-10, pp. 728–731.
- Elitzur, Moshe and Luis C Ho (2009). "On the disappearance of the broad-line region in low-luminosity active galactic nuclei". In: *The Astrophysical Journal* 701.2, p. L91.
- Emmanoulopoulos, D., I. M. McHardy, and I. E. Papadakis (Aug. 2013). "Generating artificial light curves: revisited and updated". In: *Monthly Notices of the Royal Astronomical Society* 433.2, pp. 907–927. DOI: [10.1093/mnras/stt764](https://doi.org/10.1093/mnras/stt764). arXiv: [1305.0304](https://arxiv.org/abs/1305.0304) [[astro-ph.IM](#)].
- Esin, Ann A, Jeffrey E McClintock, and Ramesh Narayan (1997). "Advection-dominated accretion and the spectral states of black hole X-ray binaries: application to Nova Muscae 1991". In: *The Astrophysical Journal* 489.2, p. 865.
- Esin, Ann A et al. (1998). "Spectral transitions in cygnus X-1 and other black hole X-ray binaries". In: *The Astrophysical Journal* 505.2, p. 854.
- Fabian, A. C. et al. (Sept. 2000). "Broad Iron Lines in Active Galactic Nuclei". In: *Publications of the Astronomical Society of the Pacific* 112.775, pp. 1145–1161. DOI: [10.1086/316610](https://doi.org/10.1086/316610). arXiv: [astro-ph/0004366](https://arxiv.org/abs/astro-ph/0004366) [[astro-ph](#)].
- Fabian, A. C. et al. (Aug. 2015). "Properties of AGN coronae in the NuSTAR era". In: *Monthly Notices of the Royal Astronomical Society* 451.4, pp. 4375–4383. DOI: [10.1093/mnras/stv1218](https://doi.org/10.1093/mnras/stv1218). arXiv: [1505.07603](https://arxiv.org/abs/1505.07603) [[astro-ph.HE](#)].
- Fabian, A. C. et al. (May 2017). "Properties of AGN coronae in the NuSTAR era - II. Hybrid plasma". In: *Monthly Notices of the Royal Astronomical Society* 467.3, pp. 2566–2570. DOI: [10.1093/mnras/stx221](https://doi.org/10.1093/mnras/stx221). arXiv: [1701.06774](https://arxiv.org/abs/1701.06774) [[astro-ph.HE](#)].
- Fabian, Andrew C. and Giovanni Miniutti (July 2005). "The X-ray spectra of accreting Kerr black holes". In: *arXiv e-prints*, [astro-ph/0507409](https://arxiv.org/abs/astro-ph/0507409), [astro-ph/0507409](https://arxiv.org/abs/astro-ph/0507409). arXiv: [astro-ph/0507409](https://arxiv.org/abs/astro-ph/0507409) [[astro-ph](#)].
- Falcke, H., E. Körding, and S. Markoff (Feb. 2004). "A scheme to unify low-power accreting black holes. Jet-dominated accretion flows and the radio/X-ray correlation". In: *Astronomy & Astrophysics* 414, pp. 895–903. DOI: [10.1051/0004-6361:20031683](https://doi.org/10.1051/0004-6361:20031683). arXiv: [astro-ph/0305335](https://arxiv.org/abs/astro-ph/0305335) [[astro-ph](#)].
- Fan, J. H. et al. (Jan. 2002). "Optical periodicity analysis for radio selected BL Lacertae objects (RBLs)". In: *Astronomy & Astrophysics* 381, pp. 1–5. DOI: [10.1051/0004-6361:20011356](https://doi.org/10.1051/0004-6361:20011356).
- Farris, B. D. et al. (Jan. 2015). "Characteristic signatures in the thermal emission from accreting binary black holes." In: *Monthly Notices of the Royal Astronomical Society* 446, pp. L36–L40. DOI: [10.1093/mnrasl/slu160](https://doi.org/10.1093/mnrasl/slu160). arXiv: [1406.0007](https://arxiv.org/abs/1406.0007) [[astro-ph.HE](#)].

- Farris, Brian D. et al. (2014). “Binary Black Hole Accretion from a Circumbinary Disk: Gas Dynamics inside the Central Cavity”. In: *The Astrophysical Journal* 783.2, 134, p. 134. DOI: [10.1088/0004-637X/783/2/134](https://doi.org/10.1088/0004-637X/783/2/134). arXiv: [1310.0492](https://arxiv.org/abs/1310.0492) [astro-ph.HE].
- Fath, Edward Arthur (Jan. 1909). “The spectra of some spiral nebulae and globular star clusters”. In: *Lick Observatory Bulletin* 149, pp. 71–77. DOI: [10.5479/ADS/bib/1909LicOB.5.71F](https://doi.org/10.5479/ADS/bib/1909LicOB.5.71F).
- Ferrarese, Laura and David Merritt (Aug. 2000). “A Fundamental Relation between Supermassive Black Holes and Their Host Galaxies”. In: *The Astrophysical Journal, Letters* 539.1, pp. L9–L12. DOI: [10.1086/312838](https://doi.org/10.1086/312838). arXiv: [astro-ph/0006053](https://arxiv.org/abs/astro-ph/0006053) [astro-ph].
- Finke, Justin D. (Oct. 2016). “External Compton Scattering in Blazar Jets and the Location of the Gamma-Ray Emitting Region”. In: *The Astrophysical Journal* 830.2, 94, p. 94. DOI: [10.3847/0004-637X/830/2/94](https://doi.org/10.3847/0004-637X/830/2/94).
- Fisher, R. A. (Aug. 1929). “Tests of Significance in Harmonic Analysis”. In: *Proceedings of the Royal Society of London Series A* 125.796, pp. 54–59. DOI: [10.1098/rspa.1929.0151](https://doi.org/10.1098/rspa.1929.0151).
- Gallo, L. C. et al. (July 2013). “1ES 1927+654: a bare Seyfert 2”. In: *Monthly Notices of the Royal Astronomical Society* 433.1, pp. 421–433. DOI: [10.1093/mnras/stt735](https://doi.org/10.1093/mnras/stt735). arXiv: [1304.7155](https://arxiv.org/abs/1304.7155) [astro-ph.HE].
- García, J. et al. (Feb. 2014). “Improved Reflection Models of Black Hole Accretion Disks: Treating the Angular Distribution of X-Rays”. In: *The Astrophysical Journal* 782.2, 76, p. 76. DOI: [10.1088/0004-637X/782/2/76](https://doi.org/10.1088/0004-637X/782/2/76). arXiv: [1312.3231](https://arxiv.org/abs/1312.3231) [astro-ph.HE].
- García, Javier A. et al. (Jan. 2019). “Implications of the Warm Corona and Relativistic Reflection Models for the Soft Excess in Mrk 509”. In: *The Astrophysical Journal* 871.1, 88, p. 88. DOI: [10.3847/1538-4357/aaf739](https://doi.org/10.3847/1538-4357/aaf739). arXiv: [1812.03194](https://arxiv.org/abs/1812.03194) [astro-ph.HE].
- Gardner, Emma and Chris Done (Sept. 2017). “The origin of the UV/optical lags in NGC 5548”. In: *Monthly Notices of the Royal Astronomical Society* 470.3, pp. 3591–3605. DOI: [10.1093/mnras/stx946](https://doi.org/10.1093/mnras/stx946). arXiv: [1603.09564](https://arxiv.org/abs/1603.09564) [astro-ph.HE].
- Gaskell, C Martin, René W Goosmann, and Elizabeth S Klimek (2008). “Structure and kinematics of the broad-line region and torus of Active Galactic Nuclei”. In: *arXiv preprint arXiv:0807.2889*.
- George, I. M. and A. C. Fabian (Mar. 1991). “X-ray reflection from cold matter in Active Galactic Nuclei and X-ray binaries.” In: *Monthly Notices of the Royal Astronomical Society* 249, p. 352. DOI: [10.1093/mnras/249.2.352](https://doi.org/10.1093/mnras/249.2.352).
- George, I. M. et al. (Jan. 1998). “ASCA Observations of Seyfert 1 Galaxies. III. The Evidence for Absorption and Emission Due to Photoionized Gas”. In: *The Astrophysical Journal, Supplement* 114.1, pp. 73–120. DOI: [10.1086/313067](https://doi.org/10.1086/313067). arXiv: [astro-ph/9708046](https://arxiv.org/abs/astro-ph/9708046) [astro-ph].
- Ghez, A. M. et al. (Dec. 1998). “High Proper-Motion Stars in the Vicinity of Sagittarius A*: Evidence for a Supermassive Black Hole at the Center of Our Galaxy”. In: *The Astrophysical Journal* 509.2, pp. 678–686. DOI: [10.1086/306528](https://doi.org/10.1086/306528). arXiv: [astro-ph/9807210](https://arxiv.org/abs/astro-ph/9807210) [astro-ph].

- Gierliński, Marek and Chris Done (Mar. 2004). "Is the soft excess in active galactic nuclei real?" In: *Monthly Notices of the Royal Astronomical Society* 349.1, pp. L7–L11. DOI: [10.1111/j.1365-2966.2004.07687.x](https://doi.org/10.1111/j.1365-2966.2004.07687.x). arXiv: [astro-ph/0312271](https://arxiv.org/abs/astro-ph/0312271) [astro-ph].
- Gierliński, Marek et al. (2008). "A periodicity of ~ 1 hour in X-ray emission from the active galaxy RE J1034+396". In: 455.7211, pp. 369–371. DOI: [10.1038/nature07277](https://doi.org/10.1038/nature07277).
- Gilli, R. et al. (Mar. 2000). "The variability of the Seyfert galaxy NGC 2992: the case for a revived AGN". In: *Astronomy & Astrophysics* 355, pp. 485–498. arXiv: [astro-ph/0001107](https://arxiv.org/abs/astro-ph/0001107) [astro-ph].
- Giustini, Margherita, Giovanni Miniutti, and Richard D. Saxton (Apr. 2020). "X-ray quasi-periodic eruptions from the galactic nucleus of RX J1301.9+2747". In: *Astronomy & Astrophysics* 636, L2, p. L2. DOI: [10.1051/0004-6361/202037610](https://doi.org/10.1051/0004-6361/202037610). arXiv: [2002.08967](https://arxiv.org/abs/2002.08967) [astro-ph.HE].
- Goyal, A. et al. (Aug. 2018). "Stochastic Modeling of Multiwavelength Variability of the Classical BL Lac Object OJ 287 on Timescales Ranging from Decades to Hours". In: *The Astrophysical Journal* 863.2, 175, p. 175. DOI: [10.3847/1538-4357/aad2de](https://doi.org/10.3847/1538-4357/aad2de). arXiv: [1709.04457](https://arxiv.org/abs/1709.04457) [astro-ph.HE].
- Goyal, Arti (Aug. 2019). "PKS 2155-304: A Case Study of Blazar Variability Power Spectrum at the Highest Energies and on the Longest Timescales". In: *Galaxies* 7.3, p. 73. DOI: [10.3390/galaxies7030073](https://doi.org/10.3390/galaxies7030073).
- Goyal, Arti et al. (Mar. 2017). "Multiwavelength Variability Study of the Classical BL Lac Object PKS 0735+178 on Timescales Ranging from Decades to Minutes". In: *The Astrophysical Journal* 837.2, 127, p. 127. DOI: [10.3847/1538-4357/aa6000](https://doi.org/10.3847/1538-4357/aa6000). arXiv: [1702.02504](https://arxiv.org/abs/1702.02504) [astro-ph.HE].
- Graham, Matthew J. et al. (2015). "A possible close supermassive black-hole binary in a quasar with optical periodicity". In: 518.7537, pp. 74–76. DOI: [10.1038/nature14143](https://doi.org/10.1038/nature14143). arXiv: [1501.01375](https://arxiv.org/abs/1501.01375) [astro-ph.GA].
- Green, Paul J. et al. (Jan. 2009). "A Full Year's Chandra Exposure on Sloan Digital Sky Survey Quasars from the Chandra Multiwavelength Project". In: *The Astrophysical Journal* 690.1, pp. 644–669. DOI: [10.1088/0004-637X/690/1/644](https://doi.org/10.1088/0004-637X/690/1/644). arXiv: [0809.1058](https://arxiv.org/abs/0809.1058) [astro-ph].
- Grier, C. J. et al. (Jan. 2012). "A Reverberation Lag for the High-ionization Component of the Broad-line Region in the Narrow-line Seyfert 1 Mrk 335". In: *The Astrophysical Journal, Letters* 744.1, L4, p. L4. DOI: [10.1088/2041-8205/744/1/L4](https://doi.org/10.1088/2041-8205/744/1/L4). arXiv: [1110.6179](https://arxiv.org/abs/1110.6179) [astro-ph.CO].
- Grier, C. J. et al. (Feb. 2013). "The Structure of the Broad-line Region in Active Galactic Nuclei. I. Reconstructed Velocity-delay Maps". In: *The Astrophysical Journal* 764.1, 47, p. 47. DOI: [10.1088/0004-637X/764/1/47](https://doi.org/10.1088/0004-637X/764/1/47). arXiv: [1210.2397](https://arxiv.org/abs/1210.2397) [astro-ph.CO].
- Grinberg, V. et al. (May 2014). "Long term variability of Cygnus X-1. VI. Energy-resolved X-ray variability 1999-2011". In: *Astronomy & Astrophysics* 565, A1, A1. DOI: [10.1051/0004-6361/201322969](https://doi.org/10.1051/0004-6361/201322969). arXiv: [1402.4485](https://arxiv.org/abs/1402.4485) [astro-ph.HE].

- Grupe, Dirk, S. Komossa, and Richard Saxton (Apr. 2015). "IC 3599 Did It Again: A Second Outburst of the X-Ray Transient Seyfert 1.9 Galaxy". In: *The Astrophysical Journal, Letters* 803.2, L28, p. L28. DOI: [10.1088/2041-8205/803/2/L28](https://doi.org/10.1088/2041-8205/803/2/L28). arXiv: [1504.01389](https://arxiv.org/abs/1504.01389) [astro-ph.HE].
- Guainazzi, M., G. Matt, and G. C. Perola (Dec. 2005). "X-ray obscuration and obscured AGN in the local universe". In: *Astronomy & Astrophysics* 444.1, pp. 119–132. DOI: [10.1051/0004-6361:20053643](https://doi.org/10.1051/0004-6361:20053643). arXiv: [astro-ph/0508265](https://arxiv.org/abs/astro-ph/0508265) [astro-ph].
- Guainazzi, M. et al. (Oct. 2001). "X-ray absorption in Seyfert 2 galaxies". In: *Monthly Notices of the Royal Astronomical Society* 327.1, pp. 323–328. DOI: [10.1046/j.1365-8711.2001.04710.x](https://doi.org/10.1046/j.1365-8711.2001.04710.x). arXiv: [astro-ph/0106150](https://arxiv.org/abs/astro-ph/0106150) [astro-ph].
- Guilbert, P. W. and M. J. Rees (July 1988). "'Cold' material in non-thermal sources." In: *Monthly Notices of the Royal Astronomical Society* 233, pp. 475–484. DOI: [10.1093/mnras/233.2.475](https://doi.org/10.1093/mnras/233.2.475).
- Gupta, Alok C., A. K. Srivastava, and Paul J. Wiita (Jan. 2009). "Periodic Oscillations in the Intra-Day Optical Light Curves of the Blazar S5 0716+714". In: *The Astrophysical Journal* 690.1, pp. 216–223. DOI: [10.1088/0004-637X/690/1/216](https://doi.org/10.1088/0004-637X/690/1/216). arXiv: [0808.3630](https://arxiv.org/abs/0808.3630) [astro-ph].
- Haardt, F. and L. Maraschi (Oct. 1991). "A Two-Phase Model for the X-Ray Emission from Seyfert Galaxies". In: *The Astrophysical Journal, Letters* 380, p. L51. DOI: [10.1086/186171](https://doi.org/10.1086/186171).
- Haardt, Francesco, Laura Maraschi, and Gabriele Ghisellini (Sept. 1994). "A Model for the X-Ray and Ultraviolet Emission from Seyfert Galaxies and Galactic Black Holes". In: *The Astrophysical Journal, Letters* 432, p. L95. DOI: [10.1086/187520](https://doi.org/10.1086/187520). arXiv: [astro-ph/9405059](https://arxiv.org/abs/astro-ph/9405059) [astro-ph].
- Halpern, J. P. (June 1984). "Variable X-ray absorption in the QSO MR 2251-178." In: *The Astrophysical Journal* 281, pp. 90–94. DOI: [10.1086/162077](https://doi.org/10.1086/162077).
- Harrison, C. (2014). "Observational constraints on the influence of active galactic nuclei on the evolution of galaxies". In: *The Astrophysical Journal, Letters* 539.1, pp. L9–L12. DOI: [10.1086/312838](https://doi.org/10.1086/312838). arXiv: [astro-ph/0006053](https://arxiv.org/abs/astro-ph/0006053) [astro-ph].
- Heinz, S. and R. A. Sunyaev (Aug. 2003). "The non-linear dependence of flux on black hole mass and accretion rate in core-dominated jets". In: *Monthly Notices of the Royal Astronomical Society* 343.3, pp. L59–L64. DOI: [10.1046/j.1365-8711.2003.06918.x](https://doi.org/10.1046/j.1365-8711.2003.06918.x). arXiv: [astro-ph/0305252](https://arxiv.org/abs/astro-ph/0305252) [astro-ph].
- Heisler, Charlene A., Stuart L. Lumsden, and Jeremy A. Bailey (Feb. 1997). "Visibility of scattered broad-line emission in Seyfert 2 galaxies". In: 385.6618, pp. 700–702. DOI: [10.1038/385700a0](https://doi.org/10.1038/385700a0).
- Herrnstein, J. R. et al. (Aug. 1999). "A geometric distance to the galaxy NGC4258 from orbital motions in a nuclear gas disk". In: 400.6744, pp. 539–541. DOI: [10.1038/22972](https://doi.org/10.1038/22972). arXiv: [astro-ph/9907013](https://arxiv.org/abs/astro-ph/9907013) [astro-ph].
- Ho, Luis C. and James S. Ulvestad (Mar. 2001). "Radio Continuum Survey of an Optically Selected Sample of Nearby Seyfert Galaxies". In: *The Astrophysical Journal, Supplement* 133.1, pp. 77–118. DOI: [10.1086/319185](https://doi.org/10.1086/319185). arXiv: [astro-ph/0102506](https://arxiv.org/abs/astro-ph/0102506) [astro-ph].

- Hopkins, Philip F. and Martin Elvis (Jan. 2010). "Quasar feedback: more bang for your buck". In: *Monthly Notices of the Royal Astronomical Society* 401.1, pp. 7–14. DOI: [10.1111/j.1365-2966.2009.15643.x](https://doi.org/10.1111/j.1365-2966.2009.15643.x). arXiv: [0904.0649](https://arxiv.org/abs/0904.0649) [astro-ph.CO].
- Hoyle, F. and William A. Fowler (Feb. 1963). "Nature of Strong Radio Sources". In: 197.4867, pp. 533–535. DOI: [10.1038/197533a0](https://doi.org/10.1038/197533a0).
- Ingram, Adam and Chris Done (2012). "Modelling variability in black hole binaries: linking simulations to observations". In: *Monthly Notices of the Royal Astronomical Society* 419.3, pp. 2369–2378. DOI: [10.1111/j.1365-2966.2011.19885.x](https://doi.org/10.1111/j.1365-2966.2011.19885.x). arXiv: [1108.0789](https://arxiv.org/abs/1108.0789) [astro-ph.HE].
- Jester, Sebastian (2005). "A simple test for the existence of two accretion modes in active galactic nuclei". In: *The Astrophysical Journal* 625.2, p. 667.
- Jin, Chichuan et al. (Sept. 2009). "The Seyfert AGN RX J0136.9-3510 and the spectral state of super Eddington accretion flows". In: *Monthly Notices of the Royal Astronomical Society* 398.1, pp. L16–L20. DOI: [10.1111/j.1745-3933.2009.00697.x](https://doi.org/10.1111/j.1745-3933.2009.00697.x). arXiv: [0903.4698](https://arxiv.org/abs/0903.4698) [astro-ph.CO].
- Jones, T. W., S. L. O'Dell, and W. A. Stein (Mar. 1974). "Physics of Compact Nonthermal Sources. I. Theory of Radiation Processes". In: *The Astrophysical Journal* 188, pp. 353–368. DOI: [10.1086/152724](https://doi.org/10.1086/152724).
- Jurkevich, I. (Sept. 1971). "A Method of Computing Periods of Cyclic Phenomena". In: *Astrophysics & Space Science* 13.1, pp. 154–167. DOI: [10.1007/BF00656321](https://doi.org/10.1007/BF00656321).
- Kaastra, J. S. et al. (Oct. 2011). "Multiwavelength campaign on Mrk 509. I. Variability and spectral energy distribution". In: *Astronomy & Astrophysics* 534, A36, A36. DOI: [10.1051/0004-6361/201116869](https://doi.org/10.1051/0004-6361/201116869). arXiv: [1107.0656](https://arxiv.org/abs/1107.0656) [astro-ph.CO].
- Kakkad, D et al. (2018). "Spatially resolved electron density in the narrow line region of $z < 0.02$ radio AGNs". In: *Astronomy & Astrophysics* 618, A6.
- Kaspi, Shai et al. (Aug. 2002). "The Ionized Gas and Nuclear Environment in NGC 3783. I. Time-averaged 900 Kilosecond Chandra Grating Spectroscopy". In: *The Astrophysical Journal* 574.2, pp. 643–662. DOI: [10.1086/341113](https://doi.org/10.1086/341113). arXiv: [astro-ph/0203263](https://arxiv.org/abs/astro-ph/0203263) [astro-ph].
- Keenan, Mary et al. (Aug. 2021). "The relativistic jet dichotomy and the end of the blazar sequence". In: *Monthly Notices of the Royal Astronomical Society* 505.4, pp. 4726–4745. DOI: [10.1093/mnras/stab1182](https://doi.org/10.1093/mnras/stab1182). arXiv: [2007.12661](https://arxiv.org/abs/2007.12661) [astro-ph.GA].
- Kelly, Brandon C., Jill Bechtold, and Aneta Siemiginowska (June 2009). "Are the Variations in Quasar Optical Flux Driven by Thermal Fluctuations?" In: *The Astrophysical Journal* 698.1, pp. 895–910. DOI: [10.1088/0004-637X/698/1/895](https://doi.org/10.1088/0004-637X/698/1/895). arXiv: [0903.5315](https://arxiv.org/abs/0903.5315) [astro-ph.CO].
- Kidger, M., L. Takalo, and A. Sillanpaa (Oct. 1992). "A new analysis of the 11-year period in OJ 287 : confirmation of its existence." In: *Astronomy & Astrophysics* 264, pp. 32–36.

- King, Andrew (Oct. 2003). "Black Holes, Galaxy Formation, and the $M_{BH}-\sigma$ Relation". In: *The Astrophysical Journal, Letters* 596.1, pp. L27–L29. DOI: [10.1086/379143](https://doi.org/10.1086/379143). arXiv: [astro-ph/0308342](https://arxiv.org/abs/astro-ph/0308342) [[astro-ph](#)].
- Kishimoto, M. et al. (Dec. 2009). "Exploring the inner region of type 1 AGNs with the Keck interferometer". In: *Astronomy & Astrophysics* 507.3, pp. L57–L60. DOI: [10.1051/0004-6361/200913512](https://doi.org/10.1051/0004-6361/200913512). arXiv: [0911.0666](https://arxiv.org/abs/0911.0666) [[astro-ph.CO](#)].
- Kishimoto, M. et al. (Mar. 2011). "The innermost dusty structure in active galactic nuclei as probed by the Keck interferometer". In: *Astronomy & Astrophysics* 527, A121, A121. DOI: [10.1051/0004-6361/201016054](https://doi.org/10.1051/0004-6361/201016054). arXiv: [1012.5359](https://arxiv.org/abs/1012.5359) [[astro-ph.CO](#)].
- Kobulnicky, Henry A. et al. (Mar. 2003). "Prime focus imaging spectrograph for the Southern African large telescope: operational modes". In: *Instrument Design and Performance for Optical/Infrared Ground-based Telescopes*. Ed. by Masanori Iye and Alan F. M. Moorwood. Vol. 4841. Society of Photo-Optical Instrumentation Engineers (SPIE) Conference Series, pp. 1634–1644. DOI: [10.1117/12.460315](https://doi.org/10.1117/12.460315).
- Kocsis, Bence, Zoltan Haiman, and Kristen Menou (2008). "Premerger localization of gravitational wave standard sirens with LISA: triggered search for an electromagnetic counterpart". In: *The Astrophysical Journal* 684.2, p. 870.
- Kollatschny, W. et al. (Nov. 2001). "Short-term emission line and continuum variations in Mrk 110". In: *Astronomy & Astrophysics* 379, pp. 125–135. DOI: [10.1051/0004-6361:20011323](https://doi.org/10.1051/0004-6361:20011323). arXiv: [astro-ph/0109470](https://arxiv.org/abs/astro-ph/0109470) [[astro-ph](#)].
- Korista, Kirk T. and Michael R. Goad (May 2004). "What the Optical Recombination Lines Can Tell Us about the Broad-Line Regions of Active Galactic Nuclei". In: *The Astrophysical Journal* 606.2, pp. 749–762. DOI: [10.1086/383193](https://doi.org/10.1086/383193). arXiv: [astro-ph/0402506](https://arxiv.org/abs/astro-ph/0402506) [[astro-ph](#)].
- Kormendy, John and Douglas Richstone (1995). "Inward Bound—The Search For Supermassive Black Holes In Galactic Nuclei". In: *Annual Review of Astronomy and Astrophysics* 33, p. 581.
- Kozłowski, Szymon et al. (2010). "Quantifying Quasar Variability as Part of a General Approach to Classifying Continuously Varying Sources". In: *The Astrophysical Journal* 708.2, pp. 927–945. DOI: [10.1088/0004-637X/708/2/927](https://doi.org/10.1088/0004-637X/708/2/927). arXiv: [0909.1326](https://arxiv.org/abs/0909.1326) [[astro-ph.CO](#)].
- Krishnan, S. et al. (Dec. 2021). "Detection of periodic signals in AGN red noise light curves: empirical tests on the Auto-Correlation Function and Phase Dispersion Minimization". In: *Monthly Notices of the Royal Astronomical Society* 508.3, pp. 3975–3994. DOI: [10.1093/mnras/stab2839](https://doi.org/10.1093/mnras/stab2839). arXiv: [2110.14454](https://arxiv.org/abs/2110.14454) [[astro-ph.HE](#)].
- Krolik, Julian H. and Mitchell C. Begelman (June 1988). "Molecular Tori in Seyfert Galaxies: Feeding the Monster and Hiding It". In: *The Astrophysical Journal* 329, p. 702. DOI: [10.1086/166414](https://doi.org/10.1086/166414).
- Krolik, Julian H. and Gerard A. Kriss (Nov. 2001). "Warm Absorbers in Active Galactic Nuclei: A Multitemperature Wind". In: *The Astrophysical Journal* 561.2, pp. 684–690. DOI: [10.1086/323442](https://doi.org/10.1086/323442).

- Kubota, Aya and Chris Done (Oct. 2018). "A physical model of the broad-band continuum of AGN and its implications for the UV/X relation and optical variability". In: *Monthly Notices of the Royal Astronomical Society* 480.1, pp. 1247–1262. DOI: [10.1093/mnras/sty1890](https://doi.org/10.1093/mnras/sty1890). arXiv: [1804.00171](https://arxiv.org/abs/1804.00171) [astro-ph.HE].
- LaMassa, Stephanie M. et al. (Feb. 2015). "The Discovery of the First "Changing Look" Quasar: New Insights Into the Physics and Phenomenology of Active Galactic Nucleus". In: *The Astrophysical Journal* 800.2, 144, p. 144. DOI: [10.1088/0004-637X/800/2/144](https://doi.org/10.1088/0004-637X/800/2/144). arXiv: [1412.2136](https://arxiv.org/abs/1412.2136) [astro-ph.GA].
- Laor, Ari and Hagai Netzer (June 1989). "Massive thin accretion discs. - I. Calculated spectra." In: *Monthly Notices of the Royal Astronomical Society* 238, pp. 897–916. DOI: [10.1093/mnras/238.3.897](https://doi.org/10.1093/mnras/238.3.897).
- Lawrence, A. et al. (Feb. 1987). "Low-frequency divergent X-ray variability in the Seyfert galaxy NGC4051". In: 325.6106, pp. 694–696. DOI: [10.1038/325694a0](https://doi.org/10.1038/325694a0).
- Leahy, D. A. et al. (Mar. 1983). "On searches for pulsed emission with application to four globular cluster X-ray sources : NGC 1851, 6441, 6624 and 6712." In: *The Astrophysical Journal* 266, pp. 160–170. DOI: [10.1086/160766](https://doi.org/10.1086/160766).
- Lee, Chin-Fei et al. (2018). "ALMA observations of the very young Class 0 protostellar system HH211-mms: A 30 au dusty disk with a disk wind traced by SO?" In: *The Astrophysical Journal* 863.1, p. 94.
- Lehto, Harry J. and Mauri J. Valtonen (1996). "OJ 287 Outburst Structure and a Binary Black Hole Model". In: *The Astrophysical Journal* 460, p. 207. DOI: [10.1086/176962](https://doi.org/10.1086/176962).
- Leighly, Karen M. (Dec. 1999). "A Comprehensive Spectral and Variability Study of Narrow-Line Seyfert 1 Galaxies Observed by ASCA. I. Observations and Time Series Analysis". In: *The Astrophysical Journal, Supplement* 125.2, pp. 297–316. DOI: [10.1086/313277](https://doi.org/10.1086/313277). arXiv: [astro-ph/9907294](https://arxiv.org/abs/astro-ph/9907294) [astro-ph].
- Li, H. Z. et al. (Nov. 2009). "The Periodicity Analysis of the Light Curve of 3C 279 and Implications for the Precession Jet". In: *Publications of the Astronomical Society of the Pacific* 121.885, p. 1172. DOI: [10.1086/648433](https://doi.org/10.1086/648433).
- Li, Ruancun et al. (July 2022). "The Host Galaxy and Rapidly Evolving Broad-line Region in the Changing-look Active Galactic Nucleus 1ES 1927+654". In: *The Astrophysical Journal* 933.1, 70, p. 70. DOI: [10.3847/1538-4357/ac714a](https://doi.org/10.3847/1538-4357/ac714a). arXiv: [2208.01797](https://arxiv.org/abs/2208.01797) [astro-ph.GA].
- Lightman, Alan P. and Douglas M. Eardley (Jan. 1974). "Black Holes in Binary Systems: Instability of Disk Accretion". In: *The Astrophysical Journal, Letters* 187, p. L1. DOI: [10.1086/181377](https://doi.org/10.1086/181377).
- Lightman, Alan P. and Timothy R. White (Dec. 1988). "Effects of Cold Matter in Active Galactic Nuclei: A Broad Hump in the X-Ray Spectra". In: *The Astrophysical Journal* 335, p. 57. DOI: [10.1086/166905](https://doi.org/10.1086/166905).

- Lin, D. N. C. and G. A. Shields (June 1986). "Accretion Disks and Periodic Outbursts of Active Galaxies Nuclei". In: *The Astrophysical Journal* 305, p. 28. DOI: [10.1086/164225](https://doi.org/10.1086/164225).
- Liu, Tingting, Suvi Gezari, and M. Coleman Miller (May 2018). "Did ASAS-SN Kill the Supermassive Black Hole Binary Candidate PG1302-102?" In: *The Astrophysical Journal, Letters* 859.1, L12, p. L12. DOI: [10.3847/2041-8213/aac2ed](https://doi.org/10.3847/2041-8213/aac2ed). arXiv: [1803.05448](https://arxiv.org/abs/1803.05448) [astro-ph.HE].
- Liu, Tingting et al. (2015). "A PERIODICALLY VARYING LUMINOUS QUASAR ATz= 2 FROM THE PAN-STARRS1 MEDIUM DEEP SURVEY: A CANDIDATE SUPERMASSIVE BLACK HOLE BINARY IN THE GRAVITATIONAL WAVE-DRIVEN REGIME". In: *The Astrophysical Journal* 803.2, p. L16. DOI: [10.1088/2041-8205/803/2/116](https://doi.org/10.1088/2041-8205/803/2/116).
- Liu, Y. et al. (June 2011). "Methods for the Quasi-Periodic Variability Analysis in Blazars". In: *Journal of Astrophysics and Astronomy* 32.1-2, pp. 79–86. DOI: [10.1007/s12036-011-9059-7](https://doi.org/10.1007/s12036-011-9059-7).
- López-Gonzaga, N. et al. (June 2016). "Mid-infrared interferometry of 23 AGN tori: On the significance of polar-elongated emission". In: *Astronomy & Astrophysics* 591, A47, A47. DOI: [10.1051/0004-6361/201527590](https://doi.org/10.1051/0004-6361/201527590). arXiv: [1602.05592](https://arxiv.org/abs/1602.05592) [astro-ph.GA].
- Lusso, E. et al. (Sept. 2012). "Bolometric luminosities and Eddington ratios of X-ray selected active galactic nuclei in the XMM-COSMOS survey". In: *Monthly Notices of the Royal Astronomical Society* 425.1, pp. 623–640. DOI: [10.1111/j.1365-2966.2012.21513.x](https://doi.org/10.1111/j.1365-2966.2012.21513.x). arXiv: [1206.2642](https://arxiv.org/abs/1206.2642) [astro-ph.CO].
- Lusso, E. et al. (Nov. 2013). "The Obscured Fraction of Active Galactic Nuclei in the XMM-COSMOS Survey: A Spectral Energy Distribution Perspective". In: *The Astrophysical Journal* 777.2, 86, p. 86. DOI: [10.1088/0004-637X/777/2/86](https://doi.org/10.1088/0004-637X/777/2/86). arXiv: [1309.0814](https://arxiv.org/abs/1309.0814) [astro-ph.CO].
- Magdziarz, Pawel et al. (Nov. 1998). "A spectral decomposition of the variable optical, ultraviolet and X-ray continuum of NGC 5548". In: *Monthly Notices of the Royal Astronomical Society* 301.1, pp. 179–192. DOI: [10.1046/j.1365-8711.1998.02015.x](https://doi.org/10.1046/j.1365-8711.1998.02015.x).
- Maiolino, R., A. Marconi, and E. Oliva (Jan. 2001). "Dust in active nuclei. II. Powder or gravel?" In: *Astronomy & Astrophysics* 365, pp. 37–48. DOI: [10.1051/0004-6361:20000012](https://doi.org/10.1051/0004-6361:20000012). arXiv: [astro-ph/0010066](https://arxiv.org/abs/astro-ph/0010066) [astro-ph].
- Malizia, A. et al. (Feb. 2014). "The INTEGRAL High-energy Cut-off Distribution of Type 1 Active Galactic Nuclei". In: *The Astrophysical Journal, Letters* 782.2, L25, p. L25. DOI: [10.1088/2041-8205/782/2/L25](https://doi.org/10.1088/2041-8205/782/2/L25). arXiv: [1401.3647](https://arxiv.org/abs/1401.3647) [astro-ph.HE].
- Malkan, M. A. and W. L. W. Sargent (Mar. 1982). "The ultraviolet excess of Seyfert 1 galaxies and quasars." In: *The Astrophysical Journal* 254, pp. 22–37. DOI: [10.1086/159701](https://doi.org/10.1086/159701).
- Malkan, Matthew A, Varoujan Gorjian, and Raymond Tam (1998). "A Hubble Space Telescope* Imaging Survey of Nearby Active Galactic Nuclei". In: *The Astrophysical Journal Supplement Series* 117.1, p. 25.

- Malyali, A. et al. (Mar. 2021). "AT 2019avd: a novel addition to the diverse population of nuclear transients". In: *Astronomy & Astrophysics* 647, A9, A9. DOI: [10.1051/0004-6361/202039681](https://doi.org/10.1051/0004-6361/202039681). arXiv: [2101.08760](https://arxiv.org/abs/2101.08760) [astro-ph.HE].
- Marchese, E. et al. (Apr. 2012). "NGC 454: unveiling a new 'changing look' active galactic nucleus". In: *Monthly Notices of the Royal Astronomical Society* 421.2, pp. 1803–1812. DOI: [10.1111/j.1365-2966.2012.20445.x](https://doi.org/10.1111/j.1365-2966.2012.20445.x). arXiv: [1201.2169](https://arxiv.org/abs/1201.2169) [astro-ph.CO].
- Markoff, Sera, Michael A Nowak, and Jörn Wilms (2005). "Going with the flow: can the base of jets subsume the role of compact accretion disk coronae?" In: *The Astrophysical Journal* 635.2, p. 1203.
- Markowitz, A. and R. Edelson (Feb. 2001). "An RXTE Survey of Long-Term X-Ray Variability in Seyfert 1 Galaxies". In: *The Astrophysical Journal* 547.2, pp. 684–692. DOI: [10.1086/318402](https://doi.org/10.1086/318402). arXiv: [astro-ph/0009422](https://arxiv.org/abs/astro-ph/0009422) [astro-ph].
- Markowitz, A. et al. (Feb. 2009a). "A Comprehensive X-Ray Spectral Analysis of the Seyfert 1.5 NGC 3227". In: *The Astrophysical Journal* 691.2, pp. 922–945. DOI: [10.1088/0004-637X/691/2/922](https://doi.org/10.1088/0004-637X/691/2/922). arXiv: [0810.1249](https://arxiv.org/abs/0810.1249) [astro-ph].
- Markowitz, A. et al. (Aug. 2003). "X-Ray Fluctuation Power Spectral Densities of Seyfert 1 Galaxies". In: *The Astrophysical Journal* 593.1, pp. 96–114. DOI: [10.1086/375330](https://doi.org/10.1086/375330). arXiv: [astro-ph/0303273](https://arxiv.org/abs/astro-ph/0303273) [astro-ph].
- Markowitz, A. G. and J. N. Reeves (Nov. 2009b). "A Suzaku Observation of NGC 4593: Illuminating the Truncated Disk". In: *The Astrophysical Journal* 705.1, pp. 496–508. DOI: [10.1088/0004-637X/705/1/496](https://doi.org/10.1088/0004-637X/705/1/496). arXiv: [0910.1110](https://arxiv.org/abs/0910.1110) [astro-ph.HE].
- Markowitz, AG, Mirko Krumpe, and Robert Nikutta (2014). "First X-ray-based statistical tests for clumpy-torus models: eclipse events from 230 years of monitoring of Seyfert AGN". In: *Monthly Notices of the Royal Astronomical Society* 439.2, pp. 1403–1458.
- Marshall, H. L. et al. (Apr. 1997). "The Variability and Spectrum of NGC 5548 in the Extreme Ultraviolet". In: *The Astrophysical Journal* 479.1, pp. 222–230. DOI: [10.1086/303850](https://doi.org/10.1086/303850).
- Matt, G. (Mar. 2000). "Dust lanes, thick absorbers, and the unification model for Seyfert galaxies". In: *Astronomy & Astrophysics* 355, pp. L31–L33. arXiv: [astro-ph/0002427](https://arxiv.org/abs/astro-ph/0002427) [astro-ph].
- Matt, G., A. C. Fabian, and C. S. Reynolds (July 1997). "Geometrical and chemical dependence of K-shell X-ray features". In: *Monthly Notices of the Royal Astronomical Society* 289.1, pp. 175–184. DOI: [10.1093/mnras/289.1.175](https://doi.org/10.1093/mnras/289.1.175).
- Matt, G., G. C. Perola, and L. Piro (July 1991). "The iron line and high energy bump as X-ray signatures of cold matter in Seyfert 1 galaxies." In: *Astronomy & Astrophysics* 247, p. 25.
- Matt, G. et al. (Apr. 2014). "The soft-X-ray emission of Ark 120. XMM-Newton, NuSTAR, and the importance of taking the broad view". In: *Monthly Notices of the Royal Astronomical Society* 439.3, pp. 3016–3021. DOI: [10.1093/mnras/stu159](https://doi.org/10.1093/mnras/stu159). arXiv: [1401.5235](https://arxiv.org/abs/1401.5235) [astro-ph.HE].

- Matt, Giorgio, Matteo Guainazzi, and Roberto Maiolino (June 2003). “Changing look: from Compton-thick to Compton-thin, or the rebirth of fossil active galactic nuclei”. In: *Monthly Notices of the Royal Astronomical Society* 342.2, pp. 422–426. DOI: [10.1046/j.1365-8711.2003.06539.x](https://doi.org/10.1046/j.1365-8711.2003.06539.x). arXiv: [astro-ph/0302328](https://arxiv.org/abs/astro-ph/0302328) [astro-ph].
- McConnell, Nicholas J. and Chung-Pei Ma (Feb. 2013). “Revisiting the Scaling Relations of Black Hole Masses and Host Galaxy Properties”. In: *The Astrophysical Journal* 764.2, 184, p. 184. DOI: [10.1088/0004-637X/764/2/184](https://doi.org/10.1088/0004-637X/764/2/184). arXiv: [1211.2816](https://arxiv.org/abs/1211.2816) [astro-ph.CO].
- McHardy, I. M. et al. (Dec. 2006). “Active galactic nuclei as scaled-up Galactic black holes”. In: 444.7120, pp. 730–732. DOI: [10.1038/nature05389](https://doi.org/10.1038/nature05389). arXiv: [astro-ph/0612273](https://arxiv.org/abs/astro-ph/0612273) [astro-ph].
- McHardy, I. M. et al. (Dec. 2007). “Discovery of multiple Lorentzian components in the X-ray timing properties of the Narrow Line Seyfert 1 Ark 564”. In: *Monthly Notices of the Royal Astronomical Society* 382.3, pp. 985–994. DOI: [10.1111/j.1365-2966.2007.12411.x](https://doi.org/10.1111/j.1365-2966.2007.12411.x). arXiv: [0709.0262](https://arxiv.org/abs/0709.0262) [astro-ph].
- McHardy, Ian and Bozena Czerny (Feb. 1987). “Fractal X-ray time variability and spectral invariance of the Seyfert galaxy NGC5506”. In: 325.6106, pp. 696–698. DOI: [10.1038/325696a0](https://doi.org/10.1038/325696a0).
- McKernan, B., T. Yaqoob, and C. S. Reynolds (Aug. 2007). “A soft X-ray study of type I active galactic nuclei observed with Chandra high-energy transmission grating spectrometer”. In: *Monthly Notices of the Royal Astronomical Society* 379.4, pp. 1359–1372. DOI: [10.1111/j.1365-2966.2007.11993.x](https://doi.org/10.1111/j.1365-2966.2007.11993.x). arXiv: [0705.2542](https://arxiv.org/abs/0705.2542) [astro-ph].
- Mehdipour, M. et al. (Oct. 2011). “Multiwavelength campaign on Mrk 509. IV. Optical-UV-X-ray variability and the nature of the soft X-ray excess”. In: *Astronomy & Astrophysics* 534, A39, A39. DOI: [10.1051/0004-6361/201116875](https://doi.org/10.1051/0004-6361/201116875). arXiv: [1107.0659](https://arxiv.org/abs/1107.0659) [astro-ph.CO].
- Merloni, A. et al. (Sept. 2015). “A tidal disruption flare in a massive galaxy? Implications for the fuelling mechanisms of nuclear black holes”. In: *Monthly Notices of the Royal Astronomical Society* 452.1, pp. 69–87. DOI: [10.1093/mnras/stv1095](https://doi.org/10.1093/mnras/stv1095). arXiv: [1503.04870](https://arxiv.org/abs/1503.04870) [astro-ph.HE].
- Merloni, A. et al. (Sept. 2012). “eROSITA Science Book: Mapping the Structure of the Energetic Universe”. In: *arXiv e-prints*, arXiv:1209.3114, arXiv:1209.3114. DOI: [10.48550/arXiv.1209.3114](https://doi.org/10.48550/arXiv.1209.3114). arXiv: [1209.3114](https://arxiv.org/abs/1209.3114) [astro-ph.HE].
- Merloni, Andrea, Sebastian Heinz, and Tiziana di Matteo (Nov. 2003). “A Fundamental Plane of black hole activity”. In: *Monthly Notices of the Royal Astronomical Society* 345.4, pp. 1057–1076. DOI: [10.1046/j.1365-2966.2003.07017.x](https://doi.org/10.1046/j.1365-2966.2003.07017.x). arXiv: [astro-ph/0305261](https://arxiv.org/abs/astro-ph/0305261) [astro-ph].
- Middleton, Matthew et al. (Mar. 2009). “RE J1034+396: the origin of the soft X-ray excess and quasi-periodic oscillation”. In: *Monthly Notices of the Royal Astronomical Society* 394.1, pp. 250–260. DOI: [10.1111/j.1365-2966.2008.14255.x](https://doi.org/10.1111/j.1365-2966.2008.14255.x). arXiv: [0807.4847](https://arxiv.org/abs/0807.4847) [astro-ph].
- Miller, L., T. J. Turner, and J. N. Reeves (May 2008). “An absorption origin for the X-ray spectral variability of MCG-6-30-15”. In: *Astronomy & Astrophysics* 483.2, pp. 437–452. DOI: [10.1051/0004-6361:200809590](https://doi.org/10.1051/0004-6361:200809590). arXiv: [0803.2680](https://arxiv.org/abs/0803.2680) [astro-ph].

- Miniutti, G. et al. (Sept. 2019). “Nine-hour X-ray quasi-periodic eruptions from a low-mass black hole galactic nucleus”. In: 573.7774, pp. 381–384. DOI: [10.1038/s41586-019-1556-x](https://doi.org/10.1038/s41586-019-1556-x). arXiv: [1909.04693](https://arxiv.org/abs/1909.04693) [astro-ph.HE].
- Miniutti, G. et al. (Jan. 2014). “The properties of the clumpy torus and BLR in the polar-scattered Seyfert 1 galaxy ESO 323-G77 through X-ray absorption variability”. In: *Monthly Notices of the Royal Astronomical Society* 437.2, pp. 1776–1790. DOI: [10.1093/mnras/stt2005](https://doi.org/10.1093/mnras/stt2005). arXiv: [1310.7701](https://arxiv.org/abs/1310.7701) [astro-ph.HE].
- Miyamoto, Sigenori et al. (Dec. 1991). “X-Ray Variability of GX 339-4 in Its Very High State”. In: *The Astrophysical Journal* 383, p. 784. DOI: [10.1086/170837](https://doi.org/10.1086/170837).
- Miyoshi, Makoto et al. (Jan. 1995). “Evidence for a black hole from high rotation velocities in a sub-parsec region of NGC4258”. In: 373.6510, pp. 127–129. DOI: [10.1038/373127a0](https://doi.org/10.1038/373127a0).
- Moderski, R., M. Sikora, and M. Błażejowski (Aug. 2003). “Numerical simulations of radiation from blazar jets”. In: *Astronomy & Astrophysics* 406, pp. 855–865. DOI: [10.1051/0004-6361:20030794](https://doi.org/10.1051/0004-6361:20030794). arXiv: [astro-ph/0205228](https://arxiv.org/abs/astro-ph/0205228) [astro-ph].
- Motta, S. E. et al. (2015). “Geometrical constraints on the origin of timing signals from black holes”. In: *Monthly Notices of the Royal Astronomical Society* 447.2, pp. 2059–2072. DOI: [10.1093/mnras/stu2579](https://doi.org/10.1093/mnras/stu2579). arXiv: [1404.7293](https://arxiv.org/abs/1404.7293) [astro-ph.HE].
- Mullaney, J. R. et al. (June 2011). “Defining the intrinsic AGN infrared spectral energy distribution and measuring its contribution to the infrared output of composite galaxies”. In: *Monthly Notices of the Royal Astronomical Society* 414.2, pp. 1082–1110. DOI: [10.1111/j.1365-2966.2011.18448.x](https://doi.org/10.1111/j.1365-2966.2011.18448.x). arXiv: [1102.1425](https://arxiv.org/abs/1102.1425) [astro-ph.CO].
- Naddaf, Mohammad-Hassan, Bożena Czerny, and Ryszard Szczerba (Oct. 2021). “The Picture of BLR in 2.5D FRADO: Dynamics and Geometry”. In: *The Astrophysical Journal* 920.1, 30, p. 30. DOI: [10.3847/1538-4357/ac139d](https://doi.org/10.3847/1538-4357/ac139d). arXiv: [2102.00336](https://arxiv.org/abs/2102.00336) [astro-ph.GA].
- Nagar, Neil M, Heino Falcke, and Andrew S Wilson (2005). “Radio sources in low-luminosity active galactic nuclei-IV. Radio luminosity function, importance of jet power, and radio properties of the complete Palomar sample”. In: *Astronomy & Astrophysics* 435.2, pp. 521–543.
- Nandra, K. and K. A. Pounds (May 1994). “GINGA observations of the X-ray spectra of Seyfert galaxies.” In: *Monthly Notices of the Royal Astronomical Society* 268, pp. 405–429. DOI: [10.1093/mnras/268.2.405](https://doi.org/10.1093/mnras/268.2.405).
- Nandra, K. et al. (Feb. 1997). “ASCA Observations of Seyfert 1 Galaxies. I. Data Analysis, Imaging, and Timing”. In: *The Astrophysical Journal* 476.1, pp. 70–82. DOI: [10.1086/303600](https://doi.org/10.1086/303600).
- Narayan, Ramesh and Insu Yi (1994). “Advection-dominated accretion: Underfed black holes and neutron stars”. In: *arXiv preprint astro-ph/9411059*.
- Nayakshin, Sergei (2000). “On the X-Ray-heated Skin of Accretion Disks”. In: *The Astrophysical Journal* 534.2, p. 718.

- Netzer, H (2006). "Active galactic nuclei: Basic physics and main components". In: *Physics of Active Galactic Nuclei at all Scales*. Springer, pp. 1–38.
- Netzer, Hagai (2015). "Revisiting the unified model of active galactic nuclei". In: *arXiv preprint arXiv:1505.00811*.
- Netzer, Hagai and Ari Laor (1993). "Dust in the narrow-line region of active galactic nuclei". In: *The Astrophysical Journal* 404, pp. L51–L54.
- Netzer, Hagai and Bradley M Peterson (1997). "Reverberation mapping and the physics of active galactic nuclei". In: *Astronomical Time Series*, pp. 85–108.
- Nguyen, Khai and Tamara Bogdanović (Sept. 2016). "Emission Signatures from Sub-parsec Binary Supermassive Black Holes. I. Diagnostic Power of Broad Emission Lines". In: *The Astrophysical Journal* 828.2, 68, p. 68. DOI: [10.3847/0004-637X/828/2/68](https://doi.org/10.3847/0004-637X/828/2/68). arXiv: [1605.09389](https://arxiv.org/abs/1605.09389) [astro-ph.HE].
- Noda, Hirofumi and Chris Done (Nov. 2018). "Explaining changing-look AGN with state transition triggered by rapid mass accretion rate drop". In: *Monthly Notices of the Royal Astronomical Society* 480.3, pp. 3898–3906. DOI: [10.1093/mnras/sty2032](https://doi.org/10.1093/mnras/sty2032). arXiv: [1805.07873](https://arxiv.org/abs/1805.07873) [astro-ph.GA].
- Novikov, I. D. and K. S. Thorne (Jan. 1973). "Astrophysics of black holes." In: *Black Holes (Les Astres Occlus)*, pp. 343–450.
- Nowak, M. A. (Oct. 2000). "Are there three peaks in the power spectra of GX 339-4 and Cyg X-1?" In: *Monthly Notices of the Royal Astronomical Society* 318.2, pp. 361–367. DOI: [10.1046/j.1365-8711.2000.03668.x](https://doi.org/10.1046/j.1365-8711.2000.03668.x). arXiv: [astro-ph/0005232](https://arxiv.org/abs/astro-ph/0005232) [astro-ph].
- Osterbrock, D. E. (Oct. 1981). "Seyfert galaxies with weak broad H alpha emission lines". In: *The Astrophysical Journal* 249, pp. 462–470. DOI: [10.1086/159306](https://doi.org/10.1086/159306).
- Packham, Christopher et al. (Jan. 2005). "The Extended Mid-Infrared Structure of the Circinus Galaxy". In: *The Astrophysical Journal, Letters* 618.1, pp. L17–L20. DOI: [10.1086/427691](https://doi.org/10.1086/427691).
- Paczynski, B. (Sept. 1977). "A model of accretion disks in close binaries." In: *The Astrophysical Journal* 216, pp. 822–826. DOI: [10.1086/155526](https://doi.org/10.1086/155526).
- Padovani, P. and P. Rafanelli (Oct. 1988). "Mass-luminosity relationships and accretion rates for Seyfert 1 galaxies and quasars." In: *Astronomy & Astrophysics* 205, pp. 53–70.
- Padovani, P. et al. (Aug. 2017). "Active galactic nuclei: what's in a name?" In: *Astronomy & Astrophysics Reviews* 25.1, 2, p. 2. DOI: [10.1007/s00159-017-0102-9](https://doi.org/10.1007/s00159-017-0102-9). arXiv: [1707.07134](https://arxiv.org/abs/1707.07134) [astro-ph.GA].
- Pahari, Mayukh et al. (Dec. 2013). "Interpreting the large amplitude X-ray variation of GRS 1915+105 and IGR J17091-3624 as modulations of an accretion disc". In: *Monthly Notices of the Royal Astronomical Society* 436.3, pp. 2334–2345. DOI: [10.1093/mnras/stt1732](https://doi.org/10.1093/mnras/stt1732). arXiv: [1310.1186](https://arxiv.org/abs/1310.1186) [astro-ph.HE].
- Paltani, S. and T. J. L. Courvoisier (Nov. 1994). "Systematic study of the ultraviolet variability of active galactic nuclei." In: *Astronomy & Astrophysics* 291, pp. 74–88.

- Pancoast, Anna et al. (Dec. 2014). "Modelling reverberation mapping data - II. Dynamical modelling of the Lick AGN Monitoring Project 2008 data set". In: *Monthly Notices of the Royal Astronomical Society* 445.3, pp. 3073–3091. DOI: [10.1093/mnras/stu1419](https://doi.org/10.1093/mnras/stu1419). arXiv: [1311.6475](https://arxiv.org/abs/1311.6475) [astro-ph.CO].
- Papadakis, I. E. and A. Lawrence (Apr. 1993). "Improved Methods for Power Spectrum Modelling of Red Noise". In: *Monthly Notices of the Royal Astronomical Society* 261, p. 612. DOI: [10.1093/mnras/261.3.612](https://doi.org/10.1093/mnras/261.3.612).
- Parker, M. L. et al. (Feb. 2019). "X-ray spectra reveal the reawakening of the repeat changing-look AGN NGC 1566". In: *Monthly Notices of the Royal Astronomical Society* 483.1, pp. L88–L92. DOI: [10.1093/mnrasl/sly224](https://doi.org/10.1093/mnrasl/sly224). arXiv: [1811.10289](https://arxiv.org/abs/1811.10289) [astro-ph.HE].
- Peñil, P. et al. (June 2020). "Systematic Search for γ -Ray Periodicity in Active Galactic Nuclei Detected by the Fermi Large Area Telescope". In: *The Astrophysical Journal* 896.2, 134, p. 134. DOI: [10.3847/1538-4357/ab910d](https://doi.org/10.3847/1538-4357/ab910d). arXiv: [2002.00805](https://arxiv.org/abs/2002.00805) [astro-ph.HE].
- Perola, G. C. et al. (July 2002). "Compton reflection and iron fluorescence in BeppoSAX observations of Seyfert type 1 galaxies". In: *Astronomy & Astrophysics* 389, pp. 802–811. DOI: [10.1051/0004-6361:20020658](https://doi.org/10.1051/0004-6361:20020658). arXiv: [astro-ph/0205045](https://arxiv.org/abs/astro-ph/0205045) [astro-ph].
- Peterson, Bradley M (1997). *An introduction to active galactic nuclei*. Cambridge University Press.
- Peterson, Bradley M. et al. (June 1998). "On Uncertainties in Cross-Correlation Lags and the Reality of Wavelength-dependent Continuum Lags in Active Galactic Nuclei". In: *Publications of the Astronomical Society of the Pacific* 110.748, pp. 660–670. DOI: [10.1086/316177](https://doi.org/10.1086/316177). arXiv: [astro-ph/9802103](https://arxiv.org/abs/astro-ph/9802103) [astro-ph].
- Petrucci, P. O. et al. (Jan. 2013). "Multiwavelength campaign on Mrk 509. XII. Broad band spectral analysis". In: *Astronomy & Astrophysics* 549, A73, A73. DOI: [10.1051/0004-6361/201219956](https://doi.org/10.1051/0004-6361/201219956). arXiv: [1209.6438](https://arxiv.org/abs/1209.6438) [astro-ph.HE].
- Piconcelli, E. et al. (Oct. 2007). "The XMM-Newton view of IRAS 09104+4109: evidence for a changing-look Type 2 quasar?" In: *Astronomy & Astrophysics* 473.1, pp. 85–89. DOI: [10.1051/0004-6361:20077630](https://doi.org/10.1051/0004-6361:20077630). arXiv: [0707.2465](https://arxiv.org/abs/0707.2465) [astro-ph].
- Piconcelli, E. et al. (Mar. 2005). "The XMM-Newton view of PG quasars. I. X-ray continuum and absorption". In: *Astronomy & Astrophysics* 432.1, pp. 15–30. DOI: [10.1051/0004-6361:20041621](https://doi.org/10.1051/0004-6361:20041621). arXiv: [astro-ph/0411051](https://arxiv.org/abs/astro-ph/0411051) [astro-ph].
- Pier, Edward A. and Julian H. Krolik (Dec. 1992). "Infrared Spectra of Obscuring Dust Tori around Active Galactic Nuclei. I. Computational Method and Basic Trends". In: *The Astrophysical Journal* 401, p. 99. DOI: [10.1086/172042](https://doi.org/10.1086/172042).
- Pihajoki, P., M. Valtonen, and S. Ciprini (Oct. 2013). "Short time-scale periodicity in OJ 287". In: *Monthly Notices of the Royal Astronomical Society* 434.4, pp. 3122–3129. DOI: [10.1093/mnras/stt1233](https://doi.org/10.1093/mnras/stt1233). arXiv: [1307.1113](https://arxiv.org/abs/1307.1113) [astro-ph.HE].

- Piro, L., G. Matt, and R. Ricci (Dec. 1997). "Soft excesses of hard X-ray selected Seyfert 1 galaxies studied with the ROSAT-PSPC". In: 126, pp. 525–535. DOI: [10.1051/aas:1997280](https://doi.org/10.1051/aas:1997280).
- Poisson, Eric and Clifford M Will (2014). *Gravity: Newtonian, post-newtonian, relativistic*. Cambridge University Press.
- Polletta, M. et al. (July 2007). "Spectral Energy Distributions of Hard X-Ray Selected Active Galactic Nuclei in the XMM-Newton Medium Deep Survey". In: *The Astrophysical Journal* 663.1, pp. 81–102. DOI: [10.1086/518113](https://doi.org/10.1086/518113). arXiv: [astro-ph/0703255](https://arxiv.org/abs/astro-ph/0703255) [[astro-ph](#)].
- Polletta, M. et al. (Oct. 2000). "The far-infrared emission of radio loud and radio quiet quasars". In: *Astronomy & Astrophysics* 362, pp. 75–96. arXiv: [astro-ph/0006315](https://arxiv.org/abs/astro-ph/0006315) [[astro-ph](#)].
- Porquet, D. et al. (July 2004). "XMM-Newton EPIC observations of 21 low-redshift PG quasars". In: *Astronomy & Astrophysics* 422, pp. 85–95. DOI: [10.1051/0004-6361:20047108](https://doi.org/10.1051/0004-6361:20047108). arXiv: [astro-ph/0404385](https://arxiv.org/abs/astro-ph/0404385) [[astro-ph](#)].
- Potschmidt, K. et al. (Sept. 2003). "Long term variability of Cygnus X-1. I. X-ray spectral-temporal correlations in the hard state". In: *Astronomy & Astrophysics* 407, pp. 1039–1058. DOI: [10.1051/0004-6361:20030906](https://doi.org/10.1051/0004-6361:20030906). arXiv: [astro-ph/0202258](https://arxiv.org/abs/astro-ph/0202258) [[astro-ph](#)].
- Pounds, K. A. et al. (Nov. 2003). "A high-velocity ionized outflow and XUV photosphere in the narrow emission line quasar PG1211+143". In: *Monthly Notices of the Royal Astronomical Society* 345.3, pp. 705–713. DOI: [10.1046/j.1365-8711.2003.07006.x](https://doi.org/10.1046/j.1365-8711.2003.07006.x). arXiv: [astro-ph/0303603](https://arxiv.org/abs/astro-ph/0303603) [[astro-ph](#)].
- Predehl, P. et al. (Mar. 2021). "The eROSITA X-ray telescope on SRG". In: *Astronomy & Astrophysics* 647, A1, A1. DOI: [10.1051/0004-6361/202039313](https://doi.org/10.1051/0004-6361/202039313). arXiv: [2010.03477](https://arxiv.org/abs/2010.03477) [[astro-ph.HE](#)].
- Press, W. H. (Jan. 1978). "Flicker noises in astronomy and elsewhere." In: *Comments on Astrophysics* 7.4, pp. 103–119.
- Raiteri, C. M. et al. (Oct. 2001). "Optical and radio variability of the BL Lacertae object <ASTROBJ>AO 0235+16</ASTROBJ>: A possible 5-6 year periodicity". In: *Astronomy & Astrophysics* 377, pp. 396–412. DOI: [10.1051/0004-6361:20011112](https://doi.org/10.1051/0004-6361:20011112). arXiv: [astro-ph/0108165](https://arxiv.org/abs/astro-ph/0108165) [[astro-ph](#)].
- Raiteri, C. M. et al. (Feb. 2021). "The dual nature of blazar fast variability: Space and ground observations of S5 0716+714". In: *Monthly Notices of the Royal Astronomical Society* 501.1, pp. 1100–1115. DOI: [10.1093/mnras/staa3561](https://doi.org/10.1093/mnras/staa3561). arXiv: [2011.06493](https://arxiv.org/abs/2011.06493) [[astro-ph.HE](#)].
- Rees, MJ (1966). "Appearance of relativistically expanding radio sources". In: *Nature* 211.5048, pp. 468–470.
- Reeves, James et al. (Mar. 2008). "On why the iron K-shell absorption in AGN is not a signature of the local warm/hot intergalactic medium". In: *Monthly Notices of the Royal Astronomical Society* 385.1, pp. L108–L112. DOI: [10.1111/j.1745-3933.2008.00443.x](https://doi.org/10.1111/j.1745-3933.2008.00443.x). arXiv: [0801.1587](https://arxiv.org/abs/0801.1587) [[astro-ph](#)].
- Remillard, Ronald A and Jeffrey E McClintock (2006). "X-ray properties of black-hole binaries". In: *Annu. Rev. Astron. Astrophys.* 44, pp. 49–92.

- Remillard, Ronald A. et al. (Sept. 1999). "RXTE Observations of 0.1-300 HZ Quasi-periodic Oscillations in the Microquasar GRO J1655-40". In: *The Astrophysical Journal* 522.1, pp. 397–412. DOI: [10.1086/307606](https://doi.org/10.1086/307606).
- Ricci, C. et al. (Mar. 2016). "IC 751: A New Changing Look AGN Discovered by NuSTAR". In: *The Astrophysical Journal* 820.1, 5, p. 5. DOI: [10.3847/0004-637X/820/1/5](https://doi.org/10.3847/0004-637X/820/1/5). arXiv: [1602.00702](https://arxiv.org/abs/1602.00702) [astro-ph.HE].
- Ricci, C. et al. (July 2020). "The Destruction and Recreation of the X-Ray Corona in a Changing-look Active Galactic Nucleus". In: *The Astrophysical Journal, Letters* 898.1, L1, p. L1. DOI: [10.3847/2041-8213/ab91a1](https://doi.org/10.3847/2041-8213/ab91a1). arXiv: [2007.07275](https://arxiv.org/abs/2007.07275) [astro-ph.HE].
- Rindler, W. (Jan. 1956). "Visual horizons in world models". In: *Monthly Notices of the Royal Astronomical Society* 116, p. 662. DOI: [10.1093/mnras/116.6.662](https://doi.org/10.1093/mnras/116.6.662).
- Risaliti, G. and M. Elvis (Aug. 2004). "A Panchromatic View of AGN". In: *Supermassive Black Holes in the Distant Universe*. Ed. by A. J. Barger. Vol. 308. Astrophysics and Space Science Library, p. 187. DOI: [10.1007/978-1-4020-2471-9_6](https://doi.org/10.1007/978-1-4020-2471-9_6). arXiv: [astro-ph/0403618](https://arxiv.org/abs/astro-ph/0403618) [astro-ph].
- Risaliti, G, M Elvis, and F Nicastro (2002). "Ubiquitous variability of X-ray-absorbing column densities in Seyfert 2 galaxies". In: *The Astrophysical Journal* 571.1, p. 234.
- Rivers, Elizabeth et al. (Nov. 2012). "A Suzaku Observation of Mkn 590 Reveals a Vanishing Soft Excess". In: *The Astrophysical Journal* 759.1, 63, p. 63. DOI: [10.1088/0004-637X/759/1/63](https://doi.org/10.1088/0004-637X/759/1/63). arXiv: [1210.3330](https://arxiv.org/abs/1210.3330) [astro-ph.HE].
- Ross, Nicholas P. et al. (Nov. 2018). "A new physical interpretation of optical and infrared variability in quasars". In: *Monthly Notices of the Royal Astronomical Society* 480.4, pp. 4468–4479. DOI: [10.1093/mnras/sty2002](https://doi.org/10.1093/mnras/sty2002). arXiv: [1805.06921](https://arxiv.org/abs/1805.06921) [astro-ph.GA].
- Rowan-Robinson, Michael (Feb. 1995). "A new model for the infrared emission of quasars". In: *Monthly Notices of the Royal Astronomical Society* 272.4, pp. 737–748. DOI: [10.1093/mnras/272.4.737](https://doi.org/10.1093/mnras/272.4.737).
- Ruan, John J. et al. (Mar. 2014). "Evidence for Large Temperature Fluctuations in Quasar Accretion Disks from Spectral Variability". In: *The Astrophysical Journal* 783.2, 105, p. 105. DOI: [10.1088/0004-637X/783/2/105](https://doi.org/10.1088/0004-637X/783/2/105). arXiv: [1401.1211](https://arxiv.org/abs/1401.1211) [astro-ph.HE].
- Ruan, John J et al. (2019). "The analogous structure of accretion flows in supermassive and stellar mass black holes: new insights from faded changing-look quasars". In: *The Astrophysical Journal* 883.1, p. 76.
- Rusinek-Abarca, Katarzyna and Marek Sikora (2021). "The dependence of the fraction of radio luminous quasars on redshift and its theoretical implications". In: *The Astrophysical Journal* 922.2, p. 202.
- Salpeter, E. E. (Aug. 1964). "Accretion of Interstellar Matter by Massive Objects." In: *The Astrophysical Journal* 140, pp. 796–800. DOI: [10.1086/147973](https://doi.org/10.1086/147973).

- Sams, Bruce J., Andreas Eckart, and Rashid Sunyaev (July 1996). "Near-infrared jets in the Galactic microquasar GRS1915+105". In: 382.6586, pp. 47–49. DOI: [10.1038/382047a0](https://doi.org/10.1038/382047a0).
- Sánchez-Sáez, P. et al. (Mar. 2021). "Alert Classification for the ALerCE Broker System: The Light Curve Classifier". In: *The Astronomical Journal* 161.3, 141, p. 141. DOI: [10.3847/1538-3881/abd5c1](https://doi.org/10.3847/1538-3881/abd5c1). arXiv: [2008.03311](https://arxiv.org/abs/2008.03311) [astro-ph.IM].
- Sanders, D. B. et al. (Dec. 1989). "Continuum Energy Distributions of Quasars: Shapes and Origins". In: *The Astrophysical Journal* 347, p. 29. DOI: [10.1086/168094](https://doi.org/10.1086/168094).
- Sandrinelli, A. et al. (2016). "Quasi-periodicities at Year-like Timescales in Blazars". In: *The Astronomical Journal* 151.3, 54, p. 54. DOI: [10.3847/0004-6256/151/3/54](https://doi.org/10.3847/0004-6256/151/3/54). arXiv: [1512.04561](https://arxiv.org/abs/1512.04561) [astro-ph.GA].
- Saxton, R. D. et al. (Dec. 2015). "Was the soft X-ray flare in NGC 3599 due to an AGN disc instability or a delayed tidal disruption event?" In: *Monthly Notices of the Royal Astronomical Society* 454.3, pp. 2798–2803. DOI: [10.1093/mnras/stv2160](https://doi.org/10.1093/mnras/stv2160). arXiv: [1509.05193](https://arxiv.org/abs/1509.05193) [astro-ph.GA].
- Scepi, Nicolas, Mitchell C. Begelman, and Jason Dexter (Mar. 2021). "Magnetic flux inversion in a peculiar changing look AGN". In: *Monthly Notices of the Royal Astronomical Society* 502.1, pp. L50–L54. DOI: [10.1093/mnras/1/slab002](https://doi.org/10.1093/mnras/1/slab002). arXiv: [2011.01954](https://arxiv.org/abs/2011.01954) [astro-ph.HE].
- Schartmann, M. et al. (Mar. 2009). "The effect of stellar feedback on the formation and evolution of gas and dust tori in AGN". In: *Monthly Notices of the Royal Astronomical Society* 393.3, pp. 759–773. DOI: [10.1111/j.1365-2966.2008.14220.x](https://doi.org/10.1111/j.1365-2966.2008.14220.x). arXiv: [0811.1425](https://arxiv.org/abs/0811.1425) [astro-ph].
- Schlafly, Edward F. and Douglas P. Finkbeiner (Aug. 2011). "Measuring Reddening with Sloan Digital Sky Survey Stellar Spectra and Recalibrating SFD". In: *The Astrophysical Journal* 737.2, 103, p. 103. DOI: [10.1088/0004-637X/737/2/103](https://doi.org/10.1088/0004-637X/737/2/103). arXiv: [1012.4804](https://arxiv.org/abs/1012.4804) [astro-ph.GA].
- Schlegel, David J., Douglas P. Finkbeiner, and Marc Davis (June 1998). "Maps of Dust Infrared Emission for Use in Estimation of Reddening and Cosmic Microwave Background Radiation Foregrounds". In: *The Astrophysical Journal* 500.2, pp. 525–553. DOI: [10.1086/305772](https://doi.org/10.1086/305772). arXiv: [astro-ph/9710327](https://arxiv.org/abs/astro-ph/9710327) [astro-ph].
- Schmidt, M. (Mar. 1963). "3C 273 : A Star-Like Object with Large Red-Shift". In: 197.4872, p. 1040. DOI: [10.1038/1971040a0](https://doi.org/10.1038/1971040a0).
- Schwarzenberg-Czerny, A. (1997). "The Correct Probability Distribution for the Phase Dispersion Minimization Periodogram". In: *The Astrophysical Journal* 489.2, pp. 941–945. DOI: [10.1086/304832](https://doi.org/10.1086/304832).
- Seyfert, Carl K. (Jan. 1943). "Nuclear Emission in Spiral Nebulae." In: *The Astrophysical Journal* 97, p. 28. DOI: [10.1086/144488](https://doi.org/10.1086/144488).
- Shakura, N. I. and R. A. Sunyaev (Jan. 1973). "Black holes in binary systems. Observational appearance." In: *Astronomy & Astrophysics* 24, pp. 337–355.

- Shappee, B. J. et al. (June 2014). "The Man behind the Curtain: X-Rays Drive the UV through NIR Variability in the 2013 Active Galactic Nucleus Outburst in NGC 2617". In: *The Astrophysical Journal* 788.1, 48, p. 48. DOI: [10.1088/0004-637X/788/1/48](https://doi.org/10.1088/0004-637X/788/1/48). arXiv: [1310.2241](https://arxiv.org/abs/1310.2241) [astro-ph.HE].
- Shemmer, Ohad et al. (July 2006). "The Hard X-Ray Spectral Slope as an Accretion Rate Indicator in Radio-quiet Active Galactic Nuclei". In: *The Astrophysical Journal, Letters* 646.1, pp. L29–L32. DOI: [10.1086/506911](https://doi.org/10.1086/506911). arXiv: [astro-ph/0606389](https://arxiv.org/abs/astro-ph/0606389) [astro-ph].
- Shen, Yue (Nov. 2021). "Extreme Variability and Episodic Lifetime of Quasars". In: *The Astrophysical Journal* 921.1, 70, p. 70. DOI: [10.3847/1538-4357/ac1ce4](https://doi.org/10.3847/1538-4357/ac1ce4). arXiv: [2108.05381](https://arxiv.org/abs/2108.05381) [astro-ph.GA].
- Shi, Yong et al. (2010). "Unobscured type 2 active galactic nuclei". In: *The Astrophysical Journal* 714.1, p. 115.
- Shields, G. A. (Apr. 1978). "Thermal continuum from accretion disks in quasars". In: 272.5655, pp. 706–708. DOI: [10.1038/272706a0](https://doi.org/10.1038/272706a0).
- Sikora, M. (Feb. 2009). "Radio bimodality: Spin, accretion mode, or both?" In: *Astronomische Nachrichten* 330.2, p. 291. DOI: [10.1002/asna.200811178](https://doi.org/10.1002/asna.200811178). arXiv: [0811.3105](https://arxiv.org/abs/0811.3105) [astro-ph].
- Singh, K. P., G. P. Garmire, and J. Nousek (Oct. 1985). "Observations of Soft X-Ray Spectra from a Seyfert 1 and a Narrow Emission-Line Galaxy". In: *The Astrophysical Journal* 297, p. 633. DOI: [10.1086/163560](https://doi.org/10.1086/163560).
- Slipher, V. M. (Jan. 1917). "The spectrum and velocity of the nebula N.G.C. 1068 (M 77)". In: *Lowell Observatory Bulletin* 3, pp. 59–62.
- Smith, Alex G. and A. D. Nair (Sept. 1995). "Timescales of Long-Term Optical Base-Level Fluctuations in Three Classes of AGN". In: *Publications of the Astronomical Society of the Pacific* 107, p. 863. DOI: [10.1086/133634](https://doi.org/10.1086/133634).
- Smith, K. W. et al. (Aug. 2020). "Design and Operation of the ATLAS Transient Science Server". In: *Publications of the Astronomical Society of the Pacific* 132.1014, 085002, p. 085002. DOI: [10.1088/1538-3873/ab936e](https://doi.org/10.1088/1538-3873/ab936e). arXiv: [2003.09052](https://arxiv.org/abs/2003.09052) [astro-ph.IM].
- Sniegowska, M. et al. (Sept. 2020). "Possible mechanism for multiple changing-look phenomena in active galactic nuclei". In: *Astronomy & Astrophysics* 641, A167, A167. DOI: [10.1051/0004-6361/202038575](https://doi.org/10.1051/0004-6361/202038575). arXiv: [2007.06441](https://arxiv.org/abs/2007.06441) [astro-ph.GA].
- Sołtan, A. (July 1982). "Masses of quasars." In: *Monthly Notices of the Royal Astronomical Society* 200, pp. 115–122. DOI: [10.1093/mnras/200.1.115](https://doi.org/10.1093/mnras/200.1.115).
- Stellingwerf, R. F. (Sept. 1978). "Period determination using phase dispersion minimization." In: *The Astrophysical Journal* 224, pp. 953–960. DOI: [10.1086/156444](https://doi.org/10.1086/156444).
- Suganuma, Masahiro et al. (2006). "Reverberation measurements of the inner radius of the dust torus in nearby Seyfert 1 galaxies". In: *The Astrophysical Journal* 639.1, p. 46.

- Sun, Wei-Hsin and Matthew A. Malkan (Nov. 1989). "Fitting Improved Accretion Disk Models to the Multiwavelength Continua of Quasars and Active Galactic Nuclei". In: *The Astrophysical Journal* 346, p. 68. DOI: [10.1086/167986](https://doi.org/10.1086/167986).
- Tavecchio, Fabrizio, Laura Maraschi, and Gabriele Ghisellini (Dec. 1998). "Constraints on the Physical Parameters of TeV Blazars". In: *The Astrophysical Journal* 509.2, pp. 608–619. DOI: [10.1086/306526](https://doi.org/10.1086/306526). arXiv: [astro-ph/9809051](https://arxiv.org/abs/astro-ph/9809051) [astro-ph].
- Thorne, Kip S. (July 1974). "Disk-Accretion onto a Black Hole. II. Evolution of the Hole". In: *The Astrophysical Journal* 191, pp. 507–520. DOI: [10.1086/152991](https://doi.org/10.1086/152991).
- Timmer, J. and M. Koenig (Aug. 1995). "On generating power law noise." In: *Astronomy & Astrophysics* 300, p. 707.
- Titarchuk, Lev (Oct. 1994). "Generalized Comptonization Models and Application to the Recent High-Energy Observations". In: *The Astrophysical Journal* 434, p. 570. DOI: [10.1086/174760](https://doi.org/10.1086/174760).
- Titarchuk, Lev and Yuriy Lyubarskij (1995). "Power-law spectra as a result of comptonization of the soft radiation in a plasma cloud". In: *The Astrophysical Journal* 450, p. 876.
- Tombesi, F. et al. (Oct. 2010). "Evidence for ultra-fast outflows in radio-quiet AGNs. I. Detection and statistical incidence of Fe K-shell absorption lines". In: *Astronomy & Astrophysics* 521, A57, A57. DOI: [10.1051/0004-6361/200913440](https://doi.org/10.1051/0004-6361/200913440). arXiv: [1006.2858](https://arxiv.org/abs/1006.2858) [astro-ph.HE].
- Tombesi, F. et al. (Apr. 2013). "Unification of X-ray winds in Seyfert galaxies: from ultra-fast outflows to warm absorbers". In: *Monthly Notices of the Royal Astronomical Society* 430.2, pp. 1102–1117. DOI: [10.1093/mnras/sts692](https://doi.org/10.1093/mnras/sts692). arXiv: [1212.4851](https://arxiv.org/abs/1212.4851) [astro-ph.HE].
- Tonry, J. L. et al. (Nov. 2018). "The ATLAS All-Sky Stellar Reference Catalog". In: *The Astrophysical Journal* 867.2, 105, p. 105. DOI: [10.3847/1538-4357/aae386](https://doi.org/10.3847/1538-4357/aae386). arXiv: [1809.09157](https://arxiv.org/abs/1809.09157) [astro-ph.IM].
- Trakhtenbrot, Benny et al. (Sept. 2019). "1ES 1927+654: An AGN Caught Changing Look on a Timescale of Months". In: *The Astrophysical Journal* 883.1, 94, p. 94. DOI: [10.3847/1538-4357/ab39e4](https://doi.org/10.3847/1538-4357/ab39e4). arXiv: [1903.11084](https://arxiv.org/abs/1903.11084) [astro-ph.GA].
- Trippe, M. L. et al. (June 2008). "Long-Term Variability in the Optical Spectrum of the Seyfert Galaxy NGC 2992". In: *The Astronomical Journal* 135.6, pp. 2048–2054. DOI: [10.1088/0004-6256/135/6/2048](https://doi.org/10.1088/0004-6256/135/6/2048). arXiv: [0804.1381](https://arxiv.org/abs/0804.1381) [astro-ph].
- Tristram, K. R. W. et al. (July 2009). "Parsec-scale dust distributions in Seyfert galaxies. Results of the MIDI AGN snapshot survey". In: *Astronomy & Astrophysics* 502.1, pp. 67–84. DOI: [10.1051/0004-6361/200811607](https://doi.org/10.1051/0004-6361/200811607). arXiv: [0903.4892](https://arxiv.org/abs/0903.4892) [astro-ph.CO].
- Tristram, K. R. W. et al. (Nov. 2007). "Resolving the complex structure of the dust torus in the active nucleus of the Circinus galaxy". In: *Astronomy & Astrophysics* 474.3, pp. 837–850. DOI: [10.1051/0004-6361:20078369](https://doi.org/10.1051/0004-6361:20078369). arXiv: [0709.0209](https://arxiv.org/abs/0709.0209) [astro-ph].

- Turner, T. J. and L. Miller (Mar. 2009). "X-ray absorption and reflection in active galactic nuclei". In: *Astronomy & Astrophysics Reviews* 17.1, pp. 47–104. DOI: [10.1007/s00159-009-0017-1](https://doi.org/10.1007/s00159-009-0017-1). arXiv: [0902.0651](https://arxiv.org/abs/0902.0651) [astro-ph.HE].
- Turner, T. J. and K. A. Pounds (Oct. 1989). "The EXOSAT spectral survey of AGN." In: *Monthly Notices of the Royal Astronomical Society* 240, pp. 833–880. DOI: [10.1093/mnras/240.4.833](https://doi.org/10.1093/mnras/240.4.833).
- Turner, T. J. et al. (Nov. 2001). "Multiwavelength Monitoring of the Narrow-Line Seyfert 1 Galaxy Arakelian 564. I. ASCA Observations and the Variability of the X-Ray Spectral Components". In: *The Astrophysical Journal* 561.1, pp. 131–145. DOI: [10.1086/323232](https://doi.org/10.1086/323232). arXiv: [astro-ph/0105283](https://arxiv.org/abs/astro-ph/0105283) [astro-ph].
- Turner, T. J. et al. (Oct. 1999). "On X-Ray Variability in Seyfert Galaxies". In: *The Astrophysical Journal* 524.2, pp. 667–673. DOI: [10.1086/307834](https://doi.org/10.1086/307834). arXiv: [astro-ph/9906050](https://arxiv.org/abs/astro-ph/9906050) [astro-ph].
- Urry, C. Megan and Paolo Padovani (Sept. 1995). "Unified Schemes for Radio-Loud Active Galactic Nuclei". In: *Publications of the Astronomical Society of the Pacific* 107, p. 803. DOI: [10.1086/133630](https://doi.org/10.1086/133630). arXiv: [astro-ph/9506063](https://arxiv.org/abs/astro-ph/9506063) [astro-ph].
- Urry, M. (Jan. 2003). "The AGN Paradigm for Radio-Loud Objects". In: *Active Galactic Nuclei: From Central Engine to Host Galaxy*. Ed. by Suzy Collin, Francoise Combes, and Isaac Shlosman. Vol. 290. Astronomical Society of the Pacific Conference Series, p. 3. arXiv: [astro-ph/0301309](https://arxiv.org/abs/astro-ph/0301309) [astro-ph].
- Uttley, P., I. M. McHardy, and I. E. Papadakis (May 2002). "Measuring the broad-band power spectra of active galactic nuclei with RXTE". In: *Monthly Notices of the Royal Astronomical Society* 332.1, pp. 231–250. DOI: [10.1046/j.1365-8711.2002.05298.x](https://doi.org/10.1046/j.1365-8711.2002.05298.x). arXiv: [astro-ph/0201134](https://arxiv.org/abs/astro-ph/0201134) [astro-ph].
- Valtonen, M. J. et al. (2006). "The 2005 November Outburst in OJ 287 and the Binary Black Hole Model". In: *The Astrophysical Journal, Letters* 643.1, pp. L9–L12. DOI: [10.1086/505039](https://doi.org/10.1086/505039).
- van der Klis, M. (Jan. 1997). "Quantifying Rapid Variability in Accreting Compact Objects". In: *Statistical Challenges in Modern Astronomy II*. Ed. by G. Jogesh Babu and Eric D. Feigelson, p. 321. arXiv: [astro-ph/9704273](https://arxiv.org/abs/astro-ph/9704273) [astro-ph].
- Vanden Berk, Daniel E. et al. (Feb. 2004). "The Ensemble Photometric Variability of ~25,000 Quasars in the Sloan Digital Sky Survey". In: *The Astrophysical Journal* 601.2, pp. 692–714. DOI: [10.1086/380563](https://doi.org/10.1086/380563). arXiv: [astro-ph/0310336](https://arxiv.org/abs/astro-ph/0310336) [astro-ph].
- Vasudevan, R. V. and A. C. Fabian (Nov. 2007). "Piecing together the X-ray background: bolometric corrections for active galactic nuclei". In: *Monthly Notices of the Royal Astronomical Society* 381.3, pp. 1235–1251. DOI: [10.1111/j.1365-2966.2007.12328.x](https://doi.org/10.1111/j.1365-2966.2007.12328.x). arXiv: [0708.4308](https://arxiv.org/abs/0708.4308) [astro-ph].
- Vaughan, S. (Feb. 2005). "A simple test for periodic signals in red noise". In: *Astronomy & Astrophysics* 431, pp. 391–403. DOI: [10.1051/0004-6361:20041453](https://doi.org/10.1051/0004-6361:20041453). arXiv: [astro-ph/0412697](https://arxiv.org/abs/astro-ph/0412697) [astro-ph].

- Vaughan, S., A. C. Fabian, and K. Nandra (Mar. 2003). "X-ray continuum variability of MCG-6-30-15". In: *Monthly Notices of the Royal Astronomical Society* 339.4, pp. 1237–1255. DOI: [10.1046/j.1365-8711.2003.06285.x](https://doi.org/10.1046/j.1365-8711.2003.06285.x). arXiv: [astro-ph/0211421](https://arxiv.org/abs/astro-ph/0211421) [astro-ph].
- Vaughan, S. and P. Uttley (2005). "Where are the X-ray quasi-periodic oscillations in active galaxies?" In: *Monthly Notices of the Royal Astronomical Society* 362.1, pp. 235–244. DOI: [10.1111/j.1365-2966.2005.09296.x](https://doi.org/10.1111/j.1365-2966.2005.09296.x). arXiv: [astro-ph/0506455](https://arxiv.org/abs/astro-ph/0506455) [astro-ph].
- Vaughan, S. et al. (2016). "False periodicities in quasar time-domain surveys". In: *Monthly Notices of the Royal Astronomical Society* 461.3, pp. 3145–3152. DOI: [10.1093/mnras/stw1412](https://doi.org/10.1093/mnras/stw1412). arXiv: [1606.02620](https://arxiv.org/abs/1606.02620) [astro-ph.IM].
- Verner, D. A. et al. (July 1996). "Atomic Data for Astrophysics. II. New Analytic FITS for Photoionization Cross Sections of Atoms and Ions". In: *The Astrophysical Journal* 465, p. 487. DOI: [10.1086/177435](https://doi.org/10.1086/177435). arXiv: [astro-ph/9601009](https://arxiv.org/abs/astro-ph/9601009) [astro-ph].
- Véron-Cetty, M. P. and P. Véron (Aug. 2006). "A catalogue of quasars and active nuclei: 12th edition". In: *Astronomy & Astrophysics* 455.2, pp. 773–777. DOI: [10.1051/0004-6361:20065177](https://doi.org/10.1051/0004-6361:20065177).
- Villata, M. and C. M. Raiteri (1999). "Helical jets in blazars. I. The case of MKN 501". In: *Astronomy & Astrophysics* 347, pp. 30–36.
- Wallinder, F. H. (Jan. 1993). "Towards Understanding Active Galactic Nuclei". In: *Comments on Astrophysics* 16, p. 331.
- Walter, R. and H. H. Fink (July 1993). "The ultraviolet to soft X-ray bump of Seyfert 1 type active galactic nuclei." In: *Astronomy & Astrophysics* 274, p. 105.
- Wang, Jianxiang and David Merritt (Jan. 2004). "Revised Rates of Stellar Disruption in Galactic Nuclei". In: *The Astrophysical Journal* 600.1, pp. 149–161. DOI: [10.1086/379767](https://doi.org/10.1086/379767). arXiv: [astro-ph/0305493](https://arxiv.org/abs/astro-ph/0305493) [astro-ph].
- Ward, Martin et al. (Apr. 1987). "The Continuum of Type 1 Seyfert Galaxies. I. A Single Form Modified by the Effects of Dust". In: *The Astrophysical Journal* 315, p. 74. DOI: [10.1086/165115](https://doi.org/10.1086/165115).
- Webb, James R. et al. (Feb. 1988). "Optical Observations of 22 Violently Variable Extragalactic Sources: 1968-1986". In: *The Astronomical Journal* 95, p. 374. DOI: [10.1086/114641](https://doi.org/10.1086/114641).
- White, Russell J. and Bradley M. Peterson (Aug. 1994). "Comments on Cross-Correlation Methodology in Variability Studies of Active Galactic Nuclei". In: *Publications of the Astronomical Society of the Pacific* 106, p. 879. DOI: [10.1086/133456](https://doi.org/10.1086/133456).
- Wijnands, Rudy, Jeroen Homan, and Michiel van der Klis (1999). "The Complex Phase-Lag Behavior of the 3-12 HZ Quasi-Periodic Oscillations during the Very High State of XTE J1550-564". In: *The Astrophysical Journal, Letters* 526.1, pp. L33–L36. DOI: [10.1086/312365](https://doi.org/10.1086/312365). arXiv: [astro-ph/9909515](https://arxiv.org/abs/astro-ph/9909515) [astro-ph].
- Wilkins, DR et al. (2022). "Acceleration and cooling of the corona during X-ray flares from the Seyfert galaxy I Zw 1". In: *Monthly Notices of the Royal Astronomical Society* 512.1, pp. 761–775.

- Wilkins, DR et al. (2017). "Revealing structure and evolution within the corona of the Seyfert galaxy I Zw 1". In: *Monthly Notices of the Royal Astronomical Society* 471.4, pp. 4436–4451.
- Willingale, R. et al. (May 2013). "Calibration of X-ray absorption in our Galaxy". In: *Monthly Notices of the Royal Astronomical Society* 431.1, pp. 394–404. DOI: [10.1093/mnras/stt175](https://doi.org/10.1093/mnras/stt175). arXiv: [1303.0843](https://arxiv.org/abs/1303.0843) [astro-ph.HE].
- Willott, Chris J. et al. (Mar. 2002). "A submillimetre difference between radio galaxies and radio quasars: evidence for quasar-heated dust and synchronized submillimetre and radio source activity". In: *Monthly Notices of the Royal Astronomical Society* 331.2, pp. 435–444. DOI: [10.1046/j.1365-8711.2002.05209.x](https://doi.org/10.1046/j.1365-8711.2002.05209.x). arXiv: [astro-ph/0111559](https://arxiv.org/abs/astro-ph/0111559) [astro-ph].
- Wills, B. J., H. Netzer, and D. Wills (Jan. 1985). "Broad emission features in QSOs and active galactic nuclei. II. New observations and theory of Fe II and HI emission." In: *The Astrophysical Journal* 288, pp. 94–116. DOI: [10.1086/162767](https://doi.org/10.1086/162767).
- Wilms, J., A. Allen, and R. McCray (Oct. 2000). "On the Absorption of X-Rays in the Interstellar Medium". In: *The Astrophysical Journal* 542.2, pp. 914–924. DOI: [10.1086/317016](https://doi.org/10.1086/317016). arXiv: [astro-ph/0008425](https://arxiv.org/abs/astro-ph/0008425) [astro-ph].
- Wilson, A. S. and T. M. Heckman (Jan. 1985). "The narrow line region and associated radio emission in active galactic nuclei". In: *Astrophysics of Active Galaxies and Quasi-Stellar Objects*. Ed. by J. S. Miller, pp. 39–109.
- Winter, Lisa M. et al. (Jan. 2009). "X-Ray Spectral Properties of the BAT AGN Sample". In: *The Astrophysical Journal* 690.2, pp. 1322–1349. DOI: [10.1088/0004-637X/690/2/1322](https://doi.org/10.1088/0004-637X/690/2/1322). arXiv: [0808.0461](https://arxiv.org/abs/0808.0461) [astro-ph].
- Wright, E. L. (Dec. 2006). "A Cosmology Calculator for the World Wide Web". In: *Publications of the Astronomical Society of the Pacific* 118.850, pp. 1711–1715. DOI: [10.1086/510102](https://doi.org/10.1086/510102). arXiv: [astro-ph/0609593](https://arxiv.org/abs/astro-ph/0609593) [astro-ph].
- Wu, Qingwen and Minfeng Gu (2008). "The X-ray spectral evolution in X-ray binaries and its application to constrain the black hole mass of ultraluminous X-ray sources". In: *The Astrophysical Journal* 682.1, p. 212.
- Young, AJ, AS Wilson, and PL Shopbell (2001). "A Chandra X-ray study of NGC 1068. I. Observations of extended emission". In: *The Astrophysical Journal* 556.1, p. 6.
- Zamorani, G. et al. (Apr. 1981). "X-ray studies of quasars with the Einstein Observatory II." In: *The Astrophysical Journal* 245, pp. 357–374. DOI: [10.1086/158815](https://doi.org/10.1086/158815).
- Zdziarski, A. A., W. N. Johnson, and P. Magdziarz (Nov. 1996). "Broad-band γ -ray and X-ray spectra of NGC 4151 and their implications for physical processes and geometry." In: *Monthly Notices of the Royal Astronomical Society* 283.1, pp. 193–206. DOI: [10.1093/mnras/283.1.193](https://doi.org/10.1093/mnras/283.1.193). arXiv: [astro-ph/9607015](https://arxiv.org/abs/astro-ph/9607015) [astro-ph].

- Zdziarski, Andrzej A. et al. (Mar. 2020). "Spectral and temporal properties of Compton scattering by mildly relativistic thermal electrons". In: *Monthly Notices of the Royal Astronomical Society* 492.4, pp. 5234–5246. DOI: [10.1093/mnras/staa159](https://doi.org/10.1093/mnras/staa159). arXiv: [1910.04535](https://arxiv.org/abs/1910.04535) [astro-ph.HE].
- Zhang, Xue-Guang (Oct. 2022). "A new candidate for central tidal disruption event in SDSS J014124 + 010306 with broad Mg II line at $z = 1.06$ ". In: *Monthly Notices of the Royal Astronomical Society* 516.1, pp. L66–L71. DOI: [10.1093/mnrasl/slac092](https://doi.org/10.1093/mnrasl/slac092).
- Zhong, Xiaogu and Jiancheng Wang (Aug. 2013). "A Magnetic Reconnection Origin for the Soft X-Ray Excess in an Active Galactic Nucleus". In: *The Astrophysical Journal* 773.1, 23, p. 23. DOI: [10.1088/0004-637X/773/1/23](https://doi.org/10.1088/0004-637X/773/1/23). arXiv: [1305.7326](https://arxiv.org/abs/1305.7326) [astro-ph.HE].
- Zhu, Xing-Jiang and Eric Thrane (Sept. 2020). "Toward the Unambiguous Identification of Supermassive Binary Black Holes through Bayesian Inference". In: *The Astrophysical Journal* 900.2, 117, p. 117. DOI: [10.3847/1538-4357/abac5a](https://doi.org/10.3847/1538-4357/abac5a). arXiv: [2004.10944](https://arxiv.org/abs/2004.10944) [astro-ph.HE].
- Zoła, S and W Ogłóza (2001). "Accretion disk in the binary system V367 Cygni". In: *Astronomy & Astrophysics* 368.3, pp. 932–938.